GHENT
UNIVERSITY

Sensitivity of IceCube Cosmic Ray measurements to the hadronic interaction models

SAM DE RIDDER

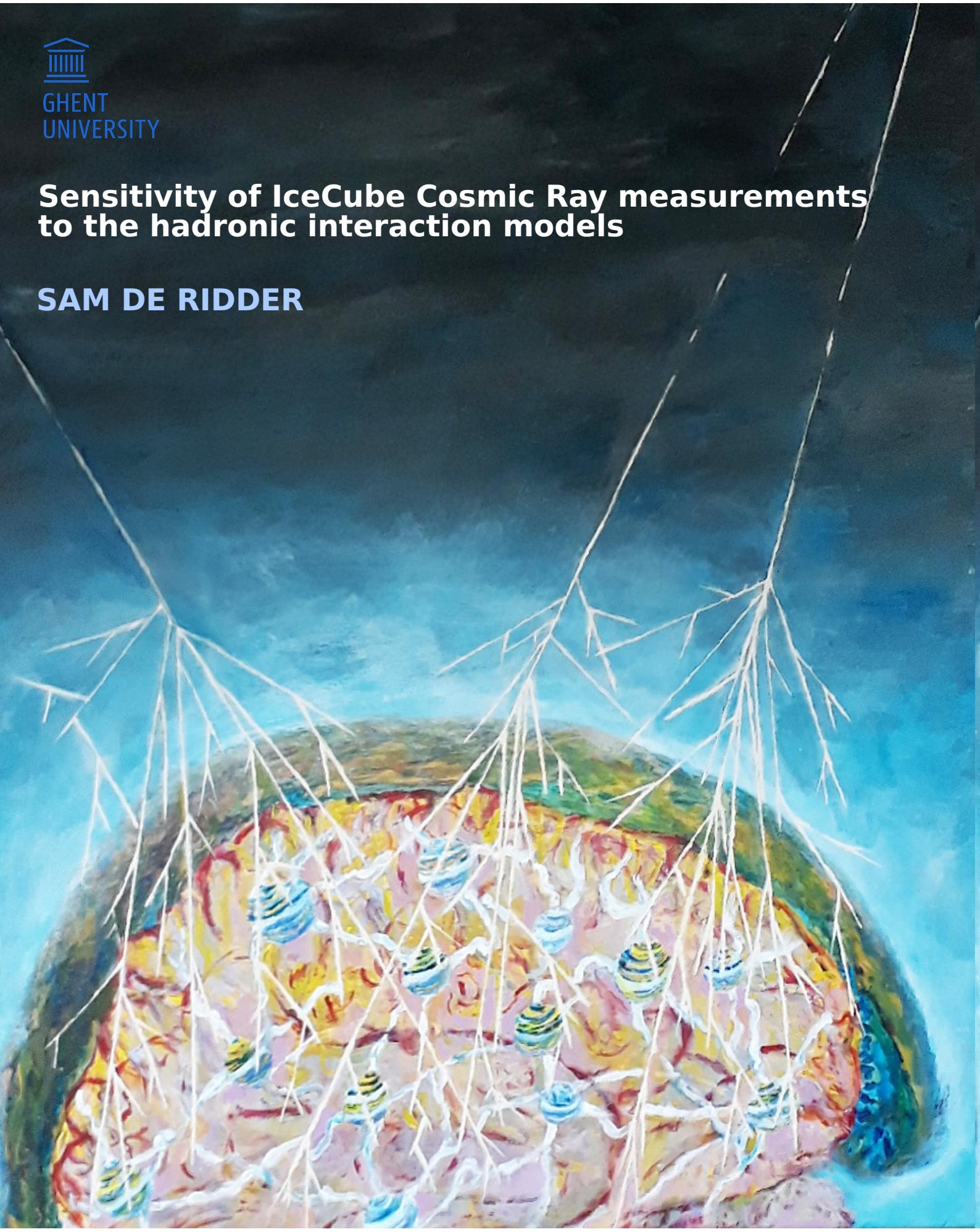

Sensitivity of IceCube Cosmic Ray measurements to the hadronic interaction models

SAM DE RIDDER

Promotor: Dirk Ryckbosch

Proefschrift ingediend tot het behalen van de academische graad van
Doctor in de Wetenschappen: Fysica

Universiteit Gent
Faculteit Wetenschappen
Vakgroep Fysica en Sterrenkunde
2012 - 2019

MEMBERS OF THE EXAMINATION COMMITTEE

Chair

Prof. dr. Natalie Jachowicz (Universiteit Gent)

Promotor

Prof. dr. Dirk Ryckbosch (Universiteit Gent)

Committee members

Prof. dr. Maarten Baes (Universiteit Gent)
Prof. dr. Didar Dobur (Universiteit Gent)
Prof. dr. Karen Andeen (Marquette University, Wisconsin, USA)
Dr. Andreas Haungs (Karlsruhe Institute of Technology, Germany)
Prof. dr. Alexander Sevrin (Vrije Universiteit Brussel)

Cover design: *An Van Praet*

Dankwoord - Acknowledgements

If I have seen further it is by standing on the shoulders of Giants.

Isaac Newton

Dit werk wordt opgedragen aan al de reuzen in mijn leven.

This work is dedicated to all the giants in my life.

Mijn ouders, broer en zus, vriendin, familie, vrienden en collega's. Kortom, iedereen rondom mij. Voor een kleine jongeman zoals ik zijn jullie allemaal reuzen. Niet alleen letterlijk, maar vooral figuurlijk. Allemaal hebbben jullie me de voorbije jaren, maar ook alle jaren ervoor, uitstekend ondersteund. Jullie omringden me met liefde en plezier en ik kon me steeds aan jullie optrekken. Een grote dank, van mij, voor jullie allemaal.

I explicitely want to express my gratitude to my promotor, Dirk Ryckbosch, for offering me a PhD position in his group. It was a great adventure in which I learned a lot and had many amazing and interesting opportunities. Going to South Pole is only one such an example. I also wish to thank all members of the IceCube collaboration, especially the cosmic ray working group. Working within such a nice group was a great pleasure.

Contents

Nederlandstalige samenvatting

De bal van Maradonna, balancerend op zijn voet.
Het potlood van Picasso, dat het soms niet meer zijn moet.
Isaac Newton zag een appel, en dacht zie ik dat goed?
Het is niet wat het is, het is wat je d'r mee doet.

Bart Peeters - Het is niet wat het is

Jij, ik, wij allemaal, staan voortdurend blootgesteld aan straling die zoveel energie heeft dat ze elektronen kan losmaken van de atomen waar ze rond draaien. In de fysica noemen we dit ioniserende straling. Deze straling kunnen we niet zien, ruiken of voelen. Het zijn kleine atomaire of subatomaire deeltjes, of energetische elektromagnetische straling. Ionisatie van atomen in ons lichaam kan ons DNA beschadigen en hierdoor ziektes veroorzaken zoals bijvoorbeeld kanker. Aan de positieve kant is de straling ook waarschijnlijk deels verantwoordelijk voor mutaties, waardoor soorten kunnen evolueren. De straling is er altijd al geweest. Sinds de industriële ontwikkeling is een deel van de straling die we ontvangen veroorzaakt door de mens, maar -gemiddeld gezien- is de meeste straling van natuurlijke oorsprong. Iets meer dan 100 jaar geleden, kort na de ontdekking van deze ioniserende straling, werd ontdekt dat ongeveer 30 % van de natuurlijke achtergrondstraling niet van de aarde komt, maar uit de ruimte. De aarde wordt voortdurend gebombardeerd door energetische deeltjes uit het heelal: kosmische straling.

Met de ontdekking van kosmische straling ontstond een nieuw onderzoeksveld in de fysica: astrodeeltjesfysica, waarbij atomaire deeltjes gebruikt worden om gebeurtenissen in het heelal te bekijken of onderzoeken. Maar wat zijn deze deeltjes? En voornamelijk, waar komen ze vandaan? Worden ze gecreëerd in onze eigen melkweg of in verre andere sterrenstelsels? Door ontploffende sterren, in de buurt van actieve kernen van sterrenstelsels, of... ? En wat gebeurt ermee op hun reis naar de aarde?
Tijdens de voorbije honderd jaar gebeurde er uitgebreid onderzoek naar dit fenomeen, zowel theoretisch als experimenteel. Op dit moment begrijpen we ruwweg wat deze kosmische straling is. Het zijn hoogenergetische deeltjes, voornamelijk geladen, die gecreëerd worden buiten ons zonnestelsel. Het gevolg van het feit dat ze geladen zijn is dat ze beïnvloed worden door magnetische velden en dus helaas niet terugwijzen naar hun bron. Iedereen kent wel de bekende mooie beelden van het poollicht of aurora's, dewelke veroorzaakt worden door elektronen uitgestoten door de zon. Kosmische straling is hetzelfde fenomeen, maar dan met andere deeltjes en hogere energieën. Ze moeten dus ook versneld worden in meer energetische omgevingen. We meten ook dat met toenemende energie van de kosmische straling er minder en minder deeltjes zijn, maar er zelfs kosmische stralingsdeeltjes gemeten worden met een energie van wel[1] 10^{20} eV. Dit is een enorme hoeveelheid energie in zo één klein deeltje. Om even te vergelijken: de hoogste energie dat we kunnen bereiken in deeltjesversnellers gebouwd door de mens, meerbepaald de Large Hadron Collider van het CERN, is momenteel $6.5 \cdot 10^{12}$ eV. Dit is iets meer dan 10 miljoen keer lager dan de hoogste energiën in kosmische stralingsdeeltjes. Verder weten we ook uit welke elementen de laag-energetische kosmische straling bestaat. Net zoals in het zonnestelsel bestaat deze straling voornamelijk uit waterstof en

[1] De elektronvolt (eV) is de meest gebruikte eenheid in de deeltjesfysica. Dit is de energieverandering die een deeltje met de lading van één elektron (e) ondergaat wanneer het in een elektrisch veld een weg aflegt zodat het een potentiaalverandering van 1 V ondergaat.
1 eV= $1.602 \cdot 10^{-19}$ J

helium, maar ook uit zwaardere deeltjes. We zien echter ook interessante verschillen tussen de samenstelling van kosmische straling en die in het zonnestelsel, waaruit we bijvoorbeeld proberen te schatten hoe lang deze deeltjes onderweg zijn alvorens wij ze meten.
Ondanks het uitgebreide onderzoek uitgevoerd tijdens de voorbije honderd jaar, hebben we nog geen antwoord kunnen geven op het merendeel van bovenstaande vragen. Hiervoor zal het nodig zijn om nog meer gedetailleerdere metingen te doen en de resultaten te vergelijken met metingen van andere boodschapper- ("messenger") deeltjes: fotonen, neutrino's en zwaartekrachtsgolven. De recente technologische vooruitgang stuwt de multi-messenger astronomie enorm vooruit. Het is duidelijk dat er interessante tijden op komst zijn in de astrodeeltjesfysica.

Één van de experimenten actief in de multi-messenger astronomie is het IceCube Neutrino Observatorium ("IceCube"). Deze unieke telescoop, de grootste ter wereld, gebruikt het ijs van Antarctica om op zoek te gaan naar neutrino's uit het heelal. Deze zouden geproduceerd worden waar ook kosmische stralingsdeeltjes worden versneld. Het voordeel van neutrino's is dat ze ongeladen zijn, waardoor zij wel recht naar de bron wijzen. Echter, aangezien ze zwak interageren, is het moeilijk om deze neutrino's te vangen en is er dus een groot volume voor nodig. IceCube gebruikt hiervoor 5160 detector modules gespreid over één kubieke kilometer tussen ongeveer 1.5 en 2.5 km onder het ijsoppervlak, vlakbij de geografische zuidpool. Over het 1 km^2 oppervlak boven de IceCube detector werden verder ook 182 detector tanks gebouwd. Dit onderdeel wordt dan ook "IceTop" genoemd.

In dit thesiswerk werd het IceCube Neutrino Observatorium gebruikt om kosmische straling te bestuderen. De combinatie van de IceTop en IceCube component maken van het IceCube Neutrino Observatorium dan ook een unieke kosmische stralingsdetector. Deze telescoop bereikt zijn volle efficiëntie voor de meting van kosmische stralingsenergiën tussen 10^{15} eV en 10^{18} eV.
Een telescoop op het aardoppervlak, zoals IceCube, meet kosmische stralingsdeeltjes van deze energieën echter niet rechtstreeks. Wanneer de energetische deeltes vanuit de ruimte onze atmosfeer binnendringen, botsen ze snel met (voornamelijk) zuurstof- of stikstofmoleculen in de atmosfeer. Aangezien de deeltjes zoveel energie bevatten, creëren ze in deze botsingen nieuwe deeltjes, die op hun beurt weer zullen botsen en extra deeltjes maken. Zo ontstaat er een heuse waterval aan deeltes richting het aardoppervlak. Deze kunnen weliswaar een lage energie hebben, maar zijn dan wel met miljoenen. Het zijn deze deeltes die hier voor ons voor de natuurlijke kosmische achtergrondstraling zorgen die er voortdurend is. Trouwens, gelukkig voor ons is de atmosfeer er, tezamen met het magnetisch veld van de aarde, om ons te beschermen voor die energetische straling! Voor ruimtereizigers zorgt deze straling echter voor een enorm gezondheidsrisico.

Observatoria zoals IceCube detecteren deze secundaire straling en moeten hieruit proberen de eigenschappen van het originele deeltje te reconstrueren. Aangezien er heel wat gedetailleerde processen uit de deeltjesfysica aan te pas komen tijdens de ontwikkeling van zo een deeltjeswaterval, is dit een enorm complex proces. Om de relaties te vinden tussen de waarnemingen en de eigenschappen van het oorspronkelijke deeltje worden hiervoor computersimulaties gebruikt. Deze simuleren het gehele proces van de ontwikkeling van alle deeltjes in de atmosfeer. De eerste botsingen gebeuren echter bij energieën hoger dan diegene die bereikt worden in deeltjesversnellers, waardoor er een grote onzekerheid heerst over hoe die botsingen exact moeten gemodelleerd worden. Hierdoor zijn ook de relaties tussen de metingen en de eigenschappen van het originele deeltje onzeker. En dan hangt het er verder ook nog vanaf aan welke secundaire deeltjes je experiment gevoelig is: verschillende experimenten meten verscheidene soorten secundaire deeltes.
Onlangs presenteerde het IceCube Neutrino Observatorium zijn resultaten van het energiespectrum en de samenstelling van kosmische straling, voor energieën tussen 10^{15} eV en 10^{18} eV. Het energiespectrum was het meest gedetailleerde ooit gemeten in dit energiegebied, en het vertoonde interessante details. Net zoals andere experimenten zagen we met IceCube dat de gemiddelde massa van de deeltjes zwaarder werd tot een energie van ruwweg 10^{17} eV. In de energieregio tussen 10^{17} eV en 10^{18} eV verkreeg IceCube echter een gemiddeld zwaardere massa in vergelijking met andere experimenten in dit energiegebied. Dit is één van de

belangrijkste discussiepunten bij de onrechtstreekse metingen van kosmische straling.

De analyse uitgevoerd in deze thesis heeft als doel na te gaan of het feit dat IceCube een ander deel van de deeltjeslawine gebruikt om de massa van het originele deeltje te reconstrueren, de reden kan zijn voor het verschil met andere experimenten. Dit zou mogelijk zijn wanneer de simulaties, meerbepaald het modelleren van de hoogenergetische hadronische botsingen, niet perfect zijn. Hiervoor voerden we simulaties uit met verschillende modellen die de botsingen beschrijven, zogenaamde hadronische interactiemodellen. We reconstrueerden de massa op twee onafhankelijke manieren en bekeken vervolgens voor elk van de modellen of de massa verkregen met beide manieren dezelfde was. Twee van de vier modellen leverden consistente, dus goede, resultaten op. Voor twee andere modellen zagen we een waarneembaar verschil, wat wijst op fouten binnen deze modellen. Dit toont aan dat de simulaties nog moeten verbeteren indien we betrouwbare conclusies willen kunnen trekken over de samenstelling van kosmische straling bij deze hoge energieën.
Het tweede doel gerealiseerd binnen dit thesiswerk is de ontwikkeling van een standaard software pakket dat nu gebruikt wordt om kosmische stralingswaarnemingen met IceTop en IceCube te reconstrueren. Deze zorgt ervoor dat er een kwalitatieve reconstructie gebeurt, dewelke nu gebruikt wordt door collega's van het IceCube Neutrino Observatorium. Dit zal een verdere analyse van de data enorm ten goede komen.

Introduction

The matter with human beans is that they is absolutely refusing to believe in anything unless they is actually seeing it right in front of their own schnozzles.

Roald Dahl - The BFG

Earth is constantly bombarded with energetic particles from all directions out of the Universe: cosmic rays. This cosmic radiation is responsible for roughly 30 % of the natural background radiation we, humans, are exposed to. The discovery of cosmic rays dates back to 1912, when, in the search to find the sources of background radiation, Victor Hess performed a series of measurements at higher altitudes during balloon flights. He found that the amount of radiation increases with altitude: the radiation should come from above, from outer space.
With the discovery of cosmic rays, a new research field in physics was born: astroparticle physics, where atomic particles are used to investigate the Universe. A number of questions rose up: what are these cosmic particles? And especially, where do they come from? Are they created inside our own Milky Way, or at remote galaxies? Which objects in the Universe can create the extreme environments to accelerate particles to such high energies? And what affects their journey from the source to the Earth?
Extensive theoretical and experimental studies have been performed in the past century to try to answer these questions. Our current knowledge about cosmic rays is summarized in Chapter 1 of this thesis. From experiments we now have a solid overview of what they are, i.e. the steep power-law energy spectrum up to enormous energies is established and the composition is known for low-energetic cosmic rays. However, although experiments start to reveal or exclude possible sources, acceleration and propagation mechanisms, they largely remain a mystery. Now, in the last decades, modern techniques within multi-messenger astronomy developed rapidly, experiments started to compare and combine their results and measurements from various messenger particles are being merged. This yields that promising times lie ahead in astroparticle physics.

One of the experiments active in the field of multi-messenger astronomy is the IceCube Neutrino Observatory (”IceCube”). This unique telescope, the largest on Earth, uses the South Pole ice to hunt for neutrinos created at the same accelerating sites where cosmic rays are accelerated. These neutrinos are uncharged and interact only weakly, therefore they are the ideal messenger particles. However, catching them is hard and requires a large volume. To achieve this, IceCube uses roughly 5000 detector modules spread over one cubic kilometer. They are deployed at depths between $\sim$1.5 and $\sim$2.5 km below the Antarctic surface, close to the geographical South Pole. Over the 1 km^2 surface above the in-ice array detector tanks are deployed, called ”IceTop”.
In this work the IceCube Neutrino Observatory is used to study cosmic radiation. For cosmic ray analyses, the IceCube Neutrino Observatory is a unique experiment due to the combination of the IceTop surface component and the deep in-ice component. The IceCube Neutrino Observatory is therefore extensively described in Chapter 2. This yields a full description of the detector and data-taking procedures, without a specific focus towards cosmic ray physics.

The IceCube Neutrino Observatory is senstive to cosmic rays in the energy range between $\sim$1 PeV (10^{15} eV) and $\sim$1 EeV (10^{18} eV). Experiments on the surface of the Earth, like IceCube, however do not detect these

high-energetic cosmic rays directly. When cosmic rays of these energies rain on the Earth, they do not reach the surface, but soon collide with nuclei in the atmosphere. In these collisions the energy is split between the daughter particles, which on their turn collide and distribute the energy to the secondary particles created in these collisions. As such, a giant particle cascade or extensive air shower (EAS) is created, which is able to reach the detectors at the surface. The experiments thus measure the cosmic ray indirectly, via the secondary particles created in the air shower. The development of extensive air showers in the atmosphere is the subject of Chapter 3. At the end of this chapter an overview is provided of the current measurement techniques of the indirect air shower experiments and the most recent results.

Indirect air shower experiments try to relate their observations to the properties of the primary cosmic rays. Since the air shower development is such a complex process where millions of particles are involved, Monte Carlo simulations are used to establish the relationships between observations and primary particle properties. Experiments perform their own simulations of the development of the air shower in the atmosphere and the signal deposition in their detector. However, since the first interactions of the cosmic ray in the atmosphere occur at energies beyond reach of man-made accelerators facilities, the physics of these interactions is unsure. This thus introduces an important restriction in the simulations and, correspondingly, in the deduction of the primary cosmic ray properties. Several models to describe these high-energy hadronic interactions exist, which are all based on extrapolations from lower energies. The study and application of these models yields an important interaction between particle physics and cosmic ray studies. The details on the air shower and detector simulations performed for cosmic ray analyses with IceTop and IceCube are given in Chapter 4. This includes a description of the model for the atmosphere used in simulations that was developed during this thesis work, but also a discussion on the hadronic interaction models and the thinning and dethinning of air showers.

The main work presented in this thesis consists of two distinct parts. In the first part, described in Chapter 5, a full processing chain for cosmic ray analyses with IceTop and IceCube is developed. At the start of this chapter a description of the data-processing that is performed soon after the data is taken is given. For cosmic ray analyses, this data is however far from perfect and is not easily useable for analyzers. A further, more advanced, data reconstructrion was developed as part of this thesis work. It is primarily based on previous analyses, but now provides a standard processing to high-level data that is suitable for most cosmic ray analyses. The newest event selection, noise removal and reconstruction procedures are included for both detector arrays, as well as a description of the correction for the influence of snow on the data and the effects caused by atmospheric variations.

In the specific analysis performed in this thesis the sensitivity of cosmic ray measurements to the hadronic interaction models is studied. This was motivated by the discrepancy in the composition measurement between IceCube and other experiments in the region between 100 PeV and 1 EeV. While other experiments measure a decreasing or even light composition at these energies and slightly above, the composition reconstruction with IceCube indicates a heavier composition (although with large error bars). As one of the important discrepancies in indirect cosmic ray measurements, the aim is to find out whether this could be due to the fact that the experiments use various EAS components to reconstruct the composition. For the composition measurement with IceCube the signal deposition by the high-energy muon bundle in the in-ice detector is used, while other experiments for example use the number of low-energy muons at the surface or the depth of shower maximum. If the simulations are imperfect, possibly due to the description of the energetic collisions in the hadronic interaction models, these various observables could lead to a different conclusion with regard to the properties of the primary particle. In this work the reconstruction of the composition with the deep IceCube detector is compared to a sensitivity to the composition with the IceTop array. The details of the analysis are given in Chapter 6.
When both variables would result in a similar composition reconstruction, the simulations provide a consistent picture. This comparison is performed for simulations with the pre-LHC model Sibyll 2.1 and the

post-LHC models Sibyll 2.3, QGSJet-II.04 and EPOS-LHC. The results are shown in Chapter 7, together with an outlook for the analysis.
Chapter 8 finally provides a discussion of the work.

1

Cosmic rays

> *Equipped with his five senses, man explores the universe around him and calls the adventure "Science".*
>
> Edwin Hubble

Visible light has been the oldest known source of messengers from the universe. For our ancestors, the Sun and the Moon have been a source of religion, calenders, navigation and much more. The sky full of stars was overwhelming to them, and unexpected events like comets or "guest stars" (currently known as exploding stars or supernovae) are described in early books and paintings. Astronomy is possibly the first science that ever existed.

The early observational astronomy tried to find the place of the Earth within the Solar Sytem and subsequently in the Universe. In the 17th century, Galileo Galilei was among the first to use a telescope to study the Universe. More details became known. With the realization that the electromagnetic spectrum was broader than the visible part during the 19th century, a new window to the Universe opened. In 1931 Karl Jansky was -by accident- the first to observe extraterrestrial radio emission, while studying sources of radio emission at Earth for the Bell Telephone Laboratories [1]. In the 20th century more observatories were built, both at the Earth's surface and on board of satellites, which now gives us a broad view of the rich Universe in all of the (electromagnetic) wavelengths. At this moment, we know that our solar system is a part of the Milky Way, our own galaxy containing hundreds of billions of stars. Stars of various sizes and colours, newly born stars and dead ones. And that our galaxy is only one amongst the many, many galaxies in the giant universe.

Aside from photons, about 100 years ago scientists discovered that also other particles arrive at Earth. It was realized that the space between stars was not entirely empty, but particles of all kind were travelling through it all the time. The widely known auroras, or polar light, are created by charged particles transfered from the Sun to the Earth by solar winds. They are mostly electrons and protons that impact on our atmosphere and create this beautiful (ionisation) light. Those particles are very common in the region around the Earth, since they are produced by our Sun, but have rather low energies. More energetic phenomena in our universe produce particles higher in energy, which are less common but still present everywhere in the universe. These particles thus also reach our Earth. They are called "cosmic rays" (CR). This term is mainly used for energetic, massive and charged nuclei originating from outside of the Solar System. Highly energetic photons, quanta of electromagnetic radiation, are called "gamma rays".

Cosmic rays can provide important clues about the very energetic phenomena in our universe. Phenomena invisible for photon detection methods might be revealed by cosmic radiation, as illustrated in Figure 1.1. While photons are stopped by dust, cosmic rays are mostly unaffected by the dust clouds. A third messenger particle from the universe is a neutrino, which is hard to catch, but can easily traverse dust clouds. Like a photon, this neutrino is neutral and it will thus not be influenced by magnetic fields. Cosmic rays on

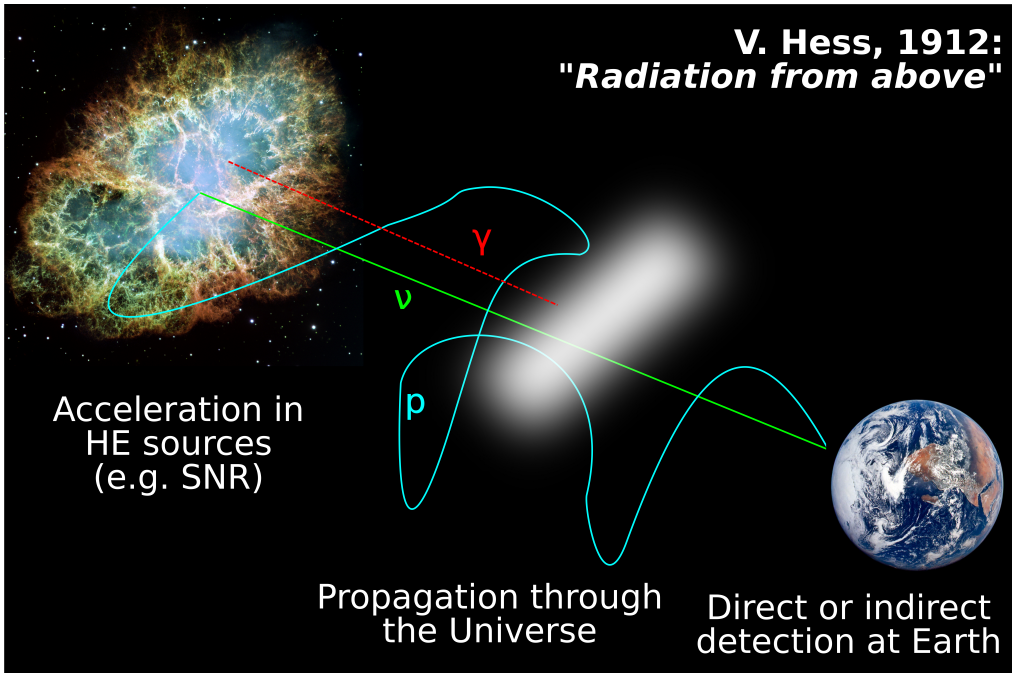

Figure 1.1: Sketch of the production, propagation and detection of charged particles (p, pale blue), neutrinos (ν, green) and photons (γ, red) in the universe. While photons can be stopped by dust, neutrinos can reach the Earth unaffected and point back to the source. Charged particles are bent by magnetic fields, thus yielding almost no direction information.

the other hand are mostly charged particles and they will be deflected on their path due to the presence of magnetic fields. Hence, all three kinds of messenger particles can provide unique insights in the outer space. A combination of the information of all messenger particles permits not only to study the broad diversity of phenomena in the universe, but also the environment encountered by particles during their propagation through galaxies and the intergalactic medium.

Furthermore, as will be shown, cosmic rays are the most energetic particles we know. For the first half of the twentieth century they have been the most important source for discoveries of new subatomic particles. And even now, they are still important in the field of high energy physics.

Section 1.1 provides a broad overview of our current knowledge of what cosmic rays exactly are. The route that has been travelled to get to this knowledge, the history of cosmic ray detection, is described in Section 1.2. The possible sources, production and propagation of these cosmic rays is then discussed in Sections 1.3 and 1.4. The terminology used in this work will be ”primary cosmic rays” or just ”cosmic rays” when it concerns the particles that are produced in the source and that bombard our atmosphere. As will be shown in Chapter 3, these primary cosmic rays can produce many ”secondary cosmic ray particles” in the atmosphere of the Earth.

1.1 What are cosmic rays?

About 100 years ago the name cosmic rays was given to *energetic particles coming from outer space* by Robert Millikan. In this section the nature of cosmic rays, or the answer to the question ”what are they?”, is broadly described. This provides a more detailed look to the cosmic rays and allows to better understand the history and discoveries of and with this cosmic radiation, described in the following section.
Here we specifically focus on the energy that these cosmic particles actually have, together their particle type. Aside from this, also the direction of the particles can be measured. However, due to the deflection by interstellar magnetic fields, for moderate energy cosmic rays the direction is unrelated to the original direction. Only cosmic rays of the highest energies can possibly contain some useful direction information. Hence, we here focus on the mass and energy of the cosmic rays.

1.1.1 Energy spectrum

Figure 1.2 provides a global view of the measured flux as function of the energy of the cosmic ray particles. This energy spectrum is shown from[1] $\sim$10 GeV to 10^{11} GeV.
Cosmic rays can thus possess enormous energies. As a comparison, protons at the large hadron collider (LHC) are currently accelerated up to $6.5 \cdot 10^3$ GeV. The indication of the LHC energy on this figure shows the design collision energy from two bundles ($14 \cdot 10^3$) converted to a situation where all energy is present in one particle and the other particle is at rest. An energy of 10^{11} GeV$\approx$[2] 16 J is equal to the energy contained in a tennis ball flying at roughly 80 km/h. However, in a cosmic ray all this energy is contained in a nucleus with a radius of the order of 10^{-15} m.

The most notible feature of this energy spectrum is its stable and steep flux decrease as function of energy. This spectrum can approximately be fitted as a power law spectrum with index -2.7 over its entire energy range:

$$\frac{dN}{dE} \sim E^{-2.7} \tag{1.1}$$

At $\sim$100 GeV the cosmic ray flux is about 1 particle per square meter per second. When the energy increases to $\sim$1 PeV, or 10^6 GeV, the flux decreases to roughly 1 particle per squared meter per year. Going to even higher energies, at $\sim$1 EeV (=10^9 GeV), the particle flux is only 1 particle per square kilometer per year. The apparent uniformity of the energy spectrum is modulated by the solar magnetic field at the lowest energies.
The steep flux decrease has a consequence for the detection mechanism at the various energies. A small sized, several square meter, detector will be able to gather enough statistics after several years of data taking up to energies of $\sim 200 \cdot 10^3$ GeV. At higher energies, larger detectors are required. It is not possible to take these large detectors to space, but they need to be at the surface of the Earth. A high-energy cosmic ray particle will, however, not make it to the ground but will instead collide with atmospheric nuclei and create a huge amount of secondary particles. Since the experiments on the surface of the Earth measure these secondary particles, they measure the cosmic ray ”indirectly”. In order to avoid interaction in the atmosphere, small sized detectors try to detect the particles above the atmosphere and provide ”direct” measurements of the primary cosmic rays.

Although the spectrum seems to have a close to uniform behaviour over the entire range, recent experiments revealed more details. By weighting the flux with the energy (E) to a certain power, these details become visible. In Figure 1.3, the energy spectrum as weighted with $E^{2.6}$. Direct measurements of individual masses are shown up to 200 TeV. At higher energies the total energy spectrum is plotted, where the features on top of the power law can be seen. The spectrum shows a clear steepening around $3 - 4 \cdot 10^6$ GeV. At this energy the spectral index of the power law changes from $\sim$-2.7 to $\sim$-3. Around 10^{10} GeV the spectrum flattens again

[1] 1 GeV is the energy that an electron acquires when it traverses a voltage difference of 10^9 V.
[2] 1 eV = $1.602 \cdot 10^{-19}$ J

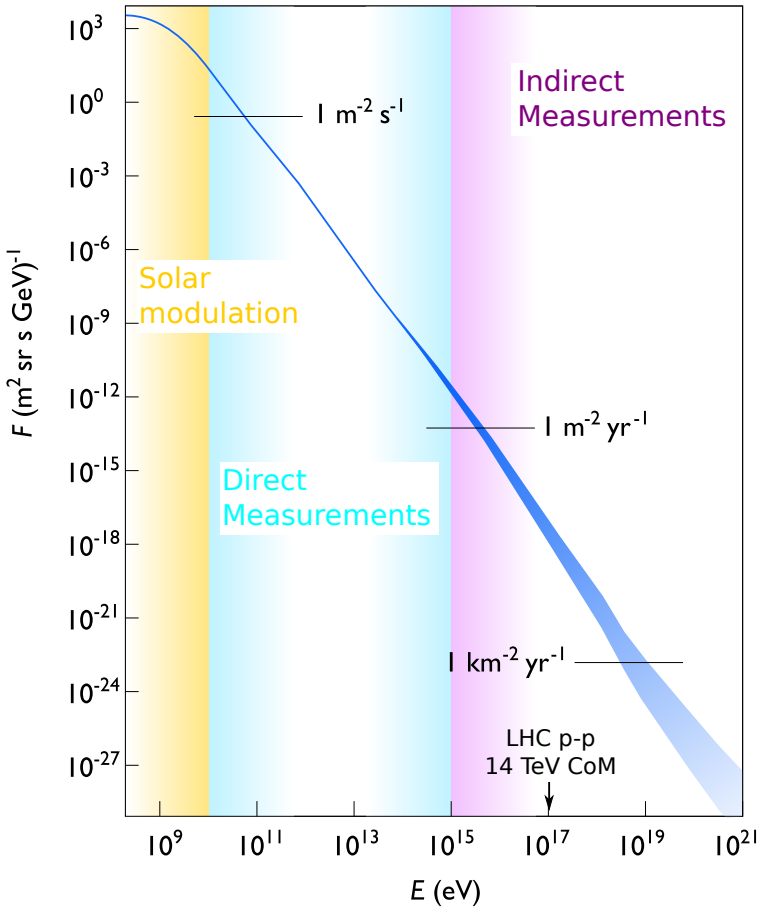

Figure 1.2: The cosmic ray energy spectrum over a broad energy range, from 1 GeV to about 1000 EeV. The steeply falling spectrum can be observed as the blue line or region. The broadness of the blue region shows the uncertainty in the measurements. Direct measurements extend up to 200 TeV - 1 PeV, where the indirect air shower measurements take over. Adapted from [2].

to a spectral index of ∼-2.6 . With some imagination one could overlay a human leg on top of the spectrum. The steepening around $3 - 4 \cdot 10^6$ GeV would then be the "knee" of the spectrum and the flattening around 10^{10} GeV is the "ankle". The most recent experiments revealed an extra, although less clear, feature around 10^8 GeV. Sometimes, this feature is called the "2nd knee".
The changes in the spectrum could possibly be related to a changing underlying source, as discussed in section 1.3. The energy spectrum seems to end with a cut-off of the flux at around $5 - 10 \cdot 10^{10}$ GeV. This cut-off is called the "GZK" cut-off, and is discussed in more detail in Section 1.4.

Energy density

From the measured flux ϕ_{cr}, the number of particles dN that travel through an area dA per time dt, the local cosmic ray density ρ_{cr} can be calculated:

$$\rho_{cr} = \frac{dN}{d^3x} = \frac{dN}{dldA} = \frac{dN}{\beta c dt dA} = \frac{1}{\beta c}\phi_{cr}\,(\mathrm{m}^{-2}\mathrm{s}^{-1}) \tag{1.2}$$

Here the volume d^3x is split in a length dl and area dA. β is the relativistic velocity and c the speed of light. The measured flux is often expressed per opening angle (or sterad sr). The density can then be calculated from:

$$\rho_{cr} = \frac{4\pi}{\beta c}\phi_{cr}\,(\mathrm{m}^{-2}\mathrm{s}^{-1}\mathrm{sr}^{-1}) \tag{1.3}$$

The energy density of CRs ρ_{cr}^{E} is obtained from the integration of the flux per energy interval over the entire energy range:

$$\rho_{cr}^{E} = 4\pi \int_{E_{min}}^{E_{max}} \frac{E}{\beta c} \frac{dN}{dE} dE \tag{1.4}$$

Due to the steep spectrum, in practice this means integrating over the lowest energies, with E_{min} ≈100 MeV and E_{max} ≈1 TeV. Here it has to be taken into account that this energy region is affected by solar modulation. In [3] the local energy density of cosmic ray nuclei is estimated to be 0.5 eV/cm^3. If one assumes that this local density is present in the entire galaxy, a total energy can be calculated that has to be produced by possible sources. If a certain group of possible sources does not produce enough CRs or the abundance of these source types is too low, they can probably be omitted as candidates for acceleration sites of CRs. Together with the requirement that a source should be able to produce particles of a high energy, also the energy density is thus considered when the sources are investigated (Section 1.3).

1.1.2 Composition

Which particles do in fact contribute to this spectrum? Is it dominated by protons? Or by other nuclei? Or are different nuclei important at different energies?
At energies up to 100 TeV the composition of cosmic rays is rather well known due to the direct detection. With the use of a magnetic spectrometer, these experiments can measure both the charge and energy of a particle.

Figure 1.4 shows a comparison of the relative abundance of nuclei for cosmic rays up to 100 TeV with the relative abundance of nuclei inside our solar system. Products of stellar nucleosynthesis, like carbon, oxygen and iron, show up as peaks in both the cosmic ray and solar system mass distribution. For two groups of elements (Li, Be, B and Sc, Ti, V, Cr and Mn) a larger abundance in cosmic rays is observed compared to the abundance in the solar system. These groups of elements have masses just below the abundant carbon (C) and oxygen (O) for the first group and iron (Fe) for the second. The elements are produced during the propagation of cosmic rays through the universe. These are spallation processes of the primary particles (like C, O or Fe) with the interstellar medium. The relative abundance of the spallation product compared to the primary particle can yield information about the time that CRs spend in the galaxy and the amount of matter they encounter. This led to the conclusion that galactic particles are often retained in the galaxy by its magnetic field. On top of this the spectra of the spallation products are found to be steeper than their parent particles, which teaches us that higher energetic particles escape out of the galaxy faster.

For higher energetic cosmic rays, the composition is unclear due to the inherent difficulty of the indirect measurement technique and the low flux. Some recent results are discussed in 3.4.3, but no conclusive results are reached yet. Recent global overviews of the composition try to fit the available data and/or build models based on some assumptions. As an example, Figure 1.3 shows a fit to the data available in 2016 [4]. This fit uses direct measurements for individual elements as a base to extrapolate to higher energies. New populations take over at higher energies in order to explain the observed spectrum. The knee, 2nd knee and ankle of the spectrum are linked to the upper threshold of a certain population or of individual elements inside this population.
The work presented here contributes in the composition measurement of cosmic rays in the region from the knee to the ankle.

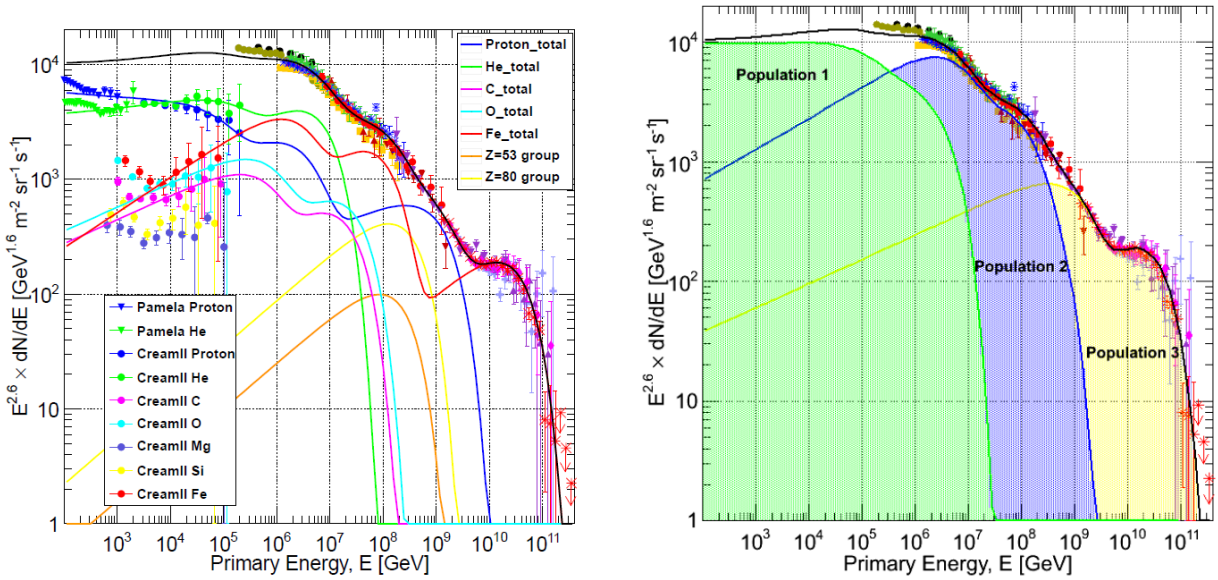

Figure 1.3: A detailed view of the cosmic ray energy spectrum, reweighted to $E^{2.6}$ to show its details. Several recent experimental results are used. The energy spectra of the individual elements are fitted at the lowest energies and extrapolated and modeled to higher energies to fit the air shower data. The right plot shows how different populations of various sources could contribute to the energy spectrum. [4]

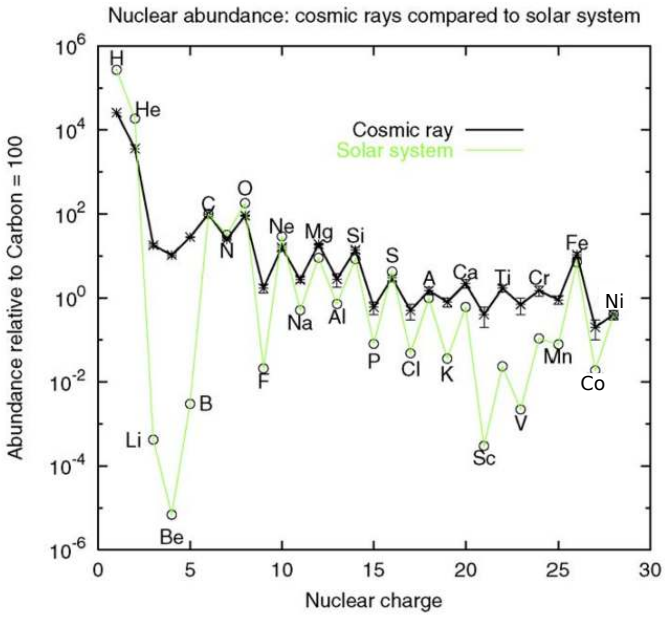

Figure 1.4: Cosmic ray composition for energies $<$ 100 TeV compared to the abundance of elements in the solar system, relative to carbon=100 [5].

1.2 History and discoveries

1.2.1 The discovery of cosmic radiation

While today we are wondering about the sources of cosmic rays or the composition above the knee of the spectrum, little more than 100 years ago one did not even know about their existence. A first hint of what later was identified as due to cosmic radiation was observed by C. A. Coulomb, as early as 1785 [6]. Coulomb was performing measurements of the electrostatic force between two charges (which resulted in his famous Coulomb law), when he noted that his electrometer discharged spontaneously by the action of air.
At the end of the 19th century an entire new and important research field in physics, chemistry and medicine was born: radioactivity. This new field would also reveal the reason of the spontaneous discharge of Coulomb's electrometers. In 1895, Wilhelm Röntgen systematically studied the properties of an unknown radiation emerging from discharge tubes. He was granted the first Nobel Prize in Physics (in 1901) for his important discovery of X-rays or Röntgen rays. Studying these newly discovered X-rays using uranium salts, Henri Becquerel subsequently found that the uranium salts themselves emit some kind of penetrating radiation. After further investigation, it seemed that he observed the spontaneous decay of the (uranium) nucleus. He had discovered radioactivity. Inspired by this, Pierre and Marie Curie decided to investigate more materials on their radioactive properties and thereby discovered the radioactive materials polonium and radium. At about the same time, shortly after 1896, Rutherford demonstrated that there were at least two types of radiation emitted from radioactive nuclei: alpha and beta radiation. The Nobel Prize in Physics in 1903 was shared between Becquerel and Pierre and Marie Curie, while Rutherford was awarded the Nobel Prize in Chemistry in 1908.

Soon it was proven that charged particles emitted by radioactive materials could discharge an electrometer. And thus these electroscopes could measure the level of radioactivity. Surprisingly it was observed that even without the presence of radioactive sources in the vicinity, an electroscope would discharge. There thus has to be some source of natural radioactivity. But where does this come from? Does it arise from the soil of the Earth itself? Or does it have an extraterrestrial origin? If so, would the sun be the dominant source? This gathered the interest of many scientists and several experiments were performed, although the first results were contradictory. Indeed, Charles T. R. Wilson performed measurements with an electrometer in a tunnel, and observed no significant change in the discharge rate compared to measurements above ground. In 1909 Theodor Wulf conducted measurements at the foot and top of the Eifel Tower. He measured a (not very significant) decrease of the radiation at the top (at a height of about 300 m) compared to the foot. This supported the leading idea among scientists at that time that the Earth would be the main source of this radiation. On the other hand, in 1910 Albert Gockel measured the ionization rate during a balloon flight up to 3000 m, and he observed no significant decrease with altitude. Possibly he was the first to coin the term "cosmic radiation". And the Italian physicst D. Pacini performed a measurement with his electrometer at a depth of 3 m in the sea. When he compared his result with measurements at ground, he observed less ionization during the underwater measurements. This made him conclude that the radiation must come from the atmosphere.
The measurements which are currently most quoted as the discovery of cosmic rays were performed by Victor Hess in 1912. He performed multiple balloon flights to measure the radiation at various altitudes with improved Wulf electroscopes on board. The highest meaurement went up to about 5300 m, during a near-solar eclipse. His meaurements (Figure 1.5) show a rise of the ionization rate as the height increases. He concluded that there was penetrating radiation "coming from above", thus extraterrestrial radiation entering Earth's atmosphere. This radiation contributes to the radiation measured at ground level and the sun is for sure not the only source of this radiation [7]. Hess received the Nobel prize in Physics in 1936.
In 1913 and 1914 W. Kolhörster confirmed the measurements of Hess during balloon flights going even up to 9200 m. These measurements are shown on the right of Figure 1.5. It was proven that "cosmic rays" are responsible for a significant fraction (~ 30 %)of the natural radiation present at ground level.

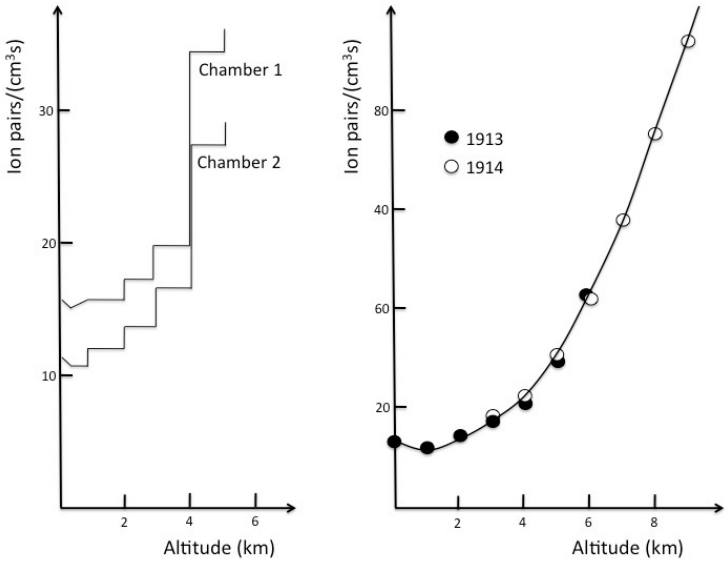

Figure 1.5: The measurements of Victor Hess (left) and Werner Kolhörster (right) during their balloon flights to measure the flux of cosmic radiation. [8]

Many studies of these cosmic rays followed, and especifically the development of the Geiger-Müller tube in 1928 made detailed measurements possible. When a large voltage difference is applied over a gas in a small tube, single ionizing events or particles can be detected with a good timing resolution. Using multiple geiger counters and lead plates with various thickness, Bruno Rossi showed that cosmic rays existed of both a soft component, which is easily absorbed, and a hard component going through a thick layer of lead. Furthermore, in 1930 Rossi demonstrated that cosmic rays are mostly positively charged particles, since more particles are detected from the west compared to the east, which is caused by the deflection in the Earth's magnetic field [9]. In the following decades, the overall composition of cosmic rays (Figure 1.4) was measured.
Rossi also noted that an unusual fraction of same-time discharges of his geiger counters occured, above the accidental rate, pointing to groups of particles arriving at the same time [10]. Pierre Auger investigated this effect in detail, when he commissioned several detectors high in the Alps, with a separation of 10 cm up to 75 m. He published his measurements in 1939, where he reported "extensive air showers": large cascades of secondary particles caused by one primary particle. He also concluded that some of these air showers were caused by primary particles with an energy as high as 10^{15} eV [11].

1.2.2 Particle discoveries using cosmic rays

The progress in cosmic ray studies also meant the rise of particle physics. Astrophysical sources provide very energetic particles that enter our atmosphere. From about 1930 to 1950 particle physics mainly consisted of studying these cosmic rays. Wilson's invention of the cloud chamber in 1911 was of great importance for particle physics: it allowed to display single (charged) particle tracks. Wilson was granted the Nobel Prize in physics in 1927. The passage of cosmic rays through these chambers revealed the existence of many new particles. After some time, these cloud chambers were connected to a geiger tube which triggered the camera when a picture needed to be taken.
The first particle discovered with cosmic radiation was a particle with the same mass as an electron, but an opposite (positive) charge. Figure 1.6 shows the first photograph of an anti-electron or positron passing through a cloud chamber placed in a uniform magnetic field, taken by Carl. D. Anderson in 1932. The Nobel Prize in 1936 was awarded to both Victor Hess and Carl Anderson. Only a few years later in 1937, Anderson and Seth Neddermeyer discovered the muon [13]. Because of its mass, for long this particle was mistakenly identified as the meso(tro)n predicted by Yukawa [14]. In 1947, the first "strange" particle, the

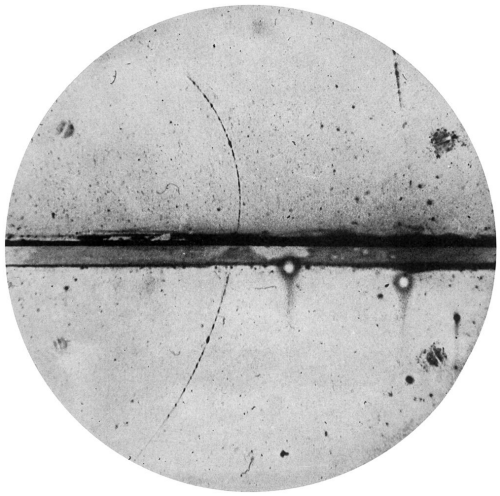

Figure 1.6: Cloud chamber photograph of the first positron ever observed, by Carl. D. Anderson [12].

K-meson or Kaon, was discovered in an experiment where many cloud chamber photographs were analyzed. On two of them, a particular unknown decay seemed to occur [15]. Photographs using cloud chambers furthermore led to the discovery of Δ, Ξ and Σ baryons. The development of photographic emulsion chambers, which could be exposed for a long time at high altitudes, was another important step in the visualization of charged particles. Aside from the confirmation of previous measurements, photographic emulsion chamber meaurements of cosmic rays led to the discovery of charged pions in 1948. These pions later appeared to be the real mesons predicted by Yukawa.
Up to the end of the first half of the twentieth century, cosmic ray studies were the source to find new particles. However, this changed significantly around 1950 when the first accelerator was built. In 1948 the cosmotron, a proton synchrotron at the Brookhaven National Laboratory, was constucted. Soon discoveries made in cosmic rays were confirmed, and unknown particles were found from the accelerator data. In Europe, this led to the important cosmic ray conference held in 1953 in Bagneres de Bigorre (Southern France). At this conference many (astro-)particle physists were present to discuss the status of particle physics and how to proceed. In the concluding remarks of the organizer, Leprince-Ringuet, it was stated that *in the future, we must use particle accelerators* [16]. One year later CERN was established as the European Organization for Nuclear Research. In the 2nd half of the twentieth century, many new particles were discovered. This zoo of particles can now be interpreted as fundamental particles or a composite of multiple quarks. They are the building blocks of the Standard Model of Particle Physics.

Further on in the concluding remarks of the 1953 conference, the future of cosmic ray physics is discussed. The importance of cosmic ray studies was questioned, since the discovery potential was superseded by accelerator experiments. However, Leprince-Ringuet concludes: *But probably this point of view should be tempered by the fact that we have the uniqueness of some phenomena, quite rare it is true, for which the energies are much larger*. Indeed, collider experiments became the leading experiments in particle physics, but cosmic ray experiments could keep adding new information due to its uniqueness and high energies. In 1998, cosmic ray studies have proven useful in the discovery of neutrino oscillations [17]. And the particle energies produced by man-made accelerators will probably never reach the energies produced by accelerators in the universe. Figure 1.2 shows the equivalent fixed-target energy reached by the Large Hadron collider (LHC) during proton-proton collisions at a center-of-mass (CoM) energy of 14 TeV. The interplay between cosmic ray physics and particle physics will remain important. Also in the work presented here it will play a major role.

1.3 Origin of cosmic rays

While it is clear that cosmic rays up to 0.1 - 1 GeV are solar particles, the nature of the cosmic accelerators for higher energy cosmic rays is a greater mystery. This should not be a big surprise in view of the complexity of the problem. The universe is huge and largely unexplored. Probably we are separated at least a few hunderd parsecs (pc) [3] from the nearest sources. The acceleration mechanism in the sources can only be modelled using Earthly knowledge and simulations. Moreover, during the propagation through the universe the properties of the cosmic ray particles could be altered. They might be further accelerated or could interact with matter encountered on their way to the Earth. Since they are charged, they are deflected by magnetic fields, and thus mostly do not point back to the sources. Hints about the sources could come from indirect neutral particles like neutrinos or gamma rays which are not influenced by magnetic fields, together with a correct explanation of the measured energy spectra and composition at Earth. Although the cosmic ray spectrum looks remarkably regular, it is probable that various types of accelerators contribute to different energy ranges, just as the sun only contributes to the energy spectrum up to a certain energy.
In this section some of the possible sources are discussed.

1.3.1 Supernovae remnants in our galaxy

In 1933, Walter Baade and Fritz Zwicky were responsible for one of the major breakthroughs in astronomy. They coined the term "super-novae"[4]: stars which explode, energetically sweap out material and transform into a densily packed neutron star. This was a major step in the understanding of the zoo of objects in the universe, but they also immediately identified these gigantic explosions as possible sources of cosmic rays. Their second paper, published at the same time as the first one [18], was named "Cosmic Rays from Super-Novae"[19]. They were probably wrong on some conclusions in their paper, like that supernovae responsible for the cosmic rays would be extragalactic. It seems nevertheless very plausible that supernovae remnants (SNR), the remainders of supernovae explosions, are responsible for at least a certain fraction of the galactic cosmic rays. Figure 1.7 shows the Crab Nebula, a famous supernova remnant.

Power

A great argument in favour of supernovae remnants as a source of galactic cosmic rays is that they can deliver the power needed to sustain the current cosmic ray energy density. Under the assumption that the local cosmic ray energy density (see part 1.1.1) is representative for the entire galaxy, the total energy of cosmic rays in the galaxy E_{cr}^{gal} can be calculated:

$$E_{cr}^{gal} = V^{gal} \cdot \rho_{cr}^{E} \tag{1.5}$$

If we approximate the galaxy as a cylindrical volume with radius 15 kpc and height 200 pc, the volume of the galaxy V^{gal} is π (15 kpc)^2(200pc) $\approx 4 \cdot 10^{66}$ cm^3. Thus the total cosmic ray energy in the galaxy is:

$$E_{cr}^{gal} \approx 2 \cdot 10^{66} \text{ eV} \tag{1.6}$$

In order to calculate the total power in galactic cosmic rays, we need to know the lifetime of cosmic rays in the galaxy. As discussed in section 1.1.2, the total amount of matter traversed could be deduced from the boron to carbon ratio. For the lowest cosmic ray energies, which dominate the total cosmic ray density, about 5 g/cm^2 of matter is traversed (X_{cr}) [3]. If we approximate that the particles travel at the speed of light, and assume a particle number density ρ_N^{gal} of 1 hydrogen atom per cm^3, we could calculate the lifetime of cosmic

[3] 1 pc= 1 parsec $\approx$ 3.26 ly. 1 light year (ly) is the distance travelled by light in one year. Thus 1 ly $\approx 300000 \frac{\text{km}}{\text{s}} \cdot 3600 \cdot 24 \cdot 365$ s $\approx 9.46 \cdot 10^{12}$ km and 1 pc = $3.08 \cdot 10^{13}$ km

[4] The name "super-novae" came from the fact that they were far more luminous objects then normal novae.

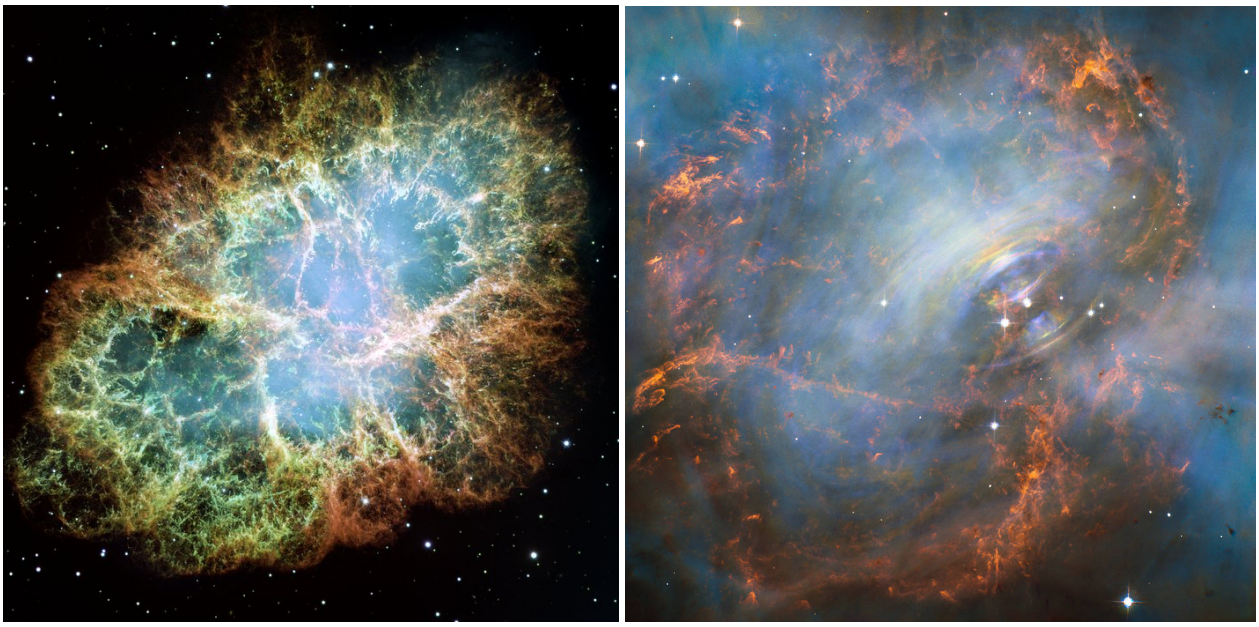

Figure 1.7: Left: Composite picture of the Crab Nebula, one of the best known supernovae remnants. The star explosion was observed in 1054 A.D. as a "sudden bright star" and is still visible with even a small telescope. The distance between the Earth and the nebula is about 6500 ly and it lies in the Perseus arm of our galaxy. Right: Zoom to the heart of the nebula, where a remaining neutron star spins with a rate of 30 times per second (the right most of the two stars close to the center of this image). Credits: NASA/ESA Hubble Space Telescope.

rays τ_{cr}:

$$\begin{aligned} \tau_{cr} &= \frac{X_{cr}}{\beta c \rho^{gal}} \\ &= \frac{X_{cr} N_A}{\beta c \rho_N^{gal} M_H} \\ &\approx 6 \cdot 10^6 \text{ years} \end{aligned} \tag{1.7}$$

Here N_A is the Avogadro constant and M_H the molar mass of hydrogen. Several approximations are used in this calculation but it gives the correct order of magnitude. A similar cosmic ray lifetime is obtained from so-called cosmic ray clocks: radioactive isotopes generated at the sources or during spallation [20].
Hence an estimation of the total power in galactic cosmic rays is:

$$P_{cr}^{gal} = \frac{E_{cr}^{gal}}{\tau_{cr}} \approx 7 \cdot 10^{51} \text{ eV/s} \approx 1 \cdot 10^{40} \text{ erg/s} \tag{1.8}$$

The erg is a common energy unit in astronomy. In 1961, Ginzburg and Syrovatsky [21] pointed out that the energy release in each supernova remnant could be of the order 10^{50} erg. Although the last 325 years no supernova explosion has been observed in our galaxy, the average supernova rate is assumed to be one every 30-100 years. SNR could thus be responsible for the acceleration of all galactic cosmic rays if the efficiency of the energy transer is $\sim 10\%$. This efficiency is subject to quite some uncertainties, and seems very efficient compared to standards on Earth, but might nonetheless be possible in space.

Acceleration

If supernovae want to qualify as CR-accelerating site, an efficient energy transfer from the supernova explosion to the particles is required. In 1949, Enrico Fermi proposed a mechanism where particles can gain energy by collisions with moving interstellar ionized gas clouds [22]. Afterwards it was realized that

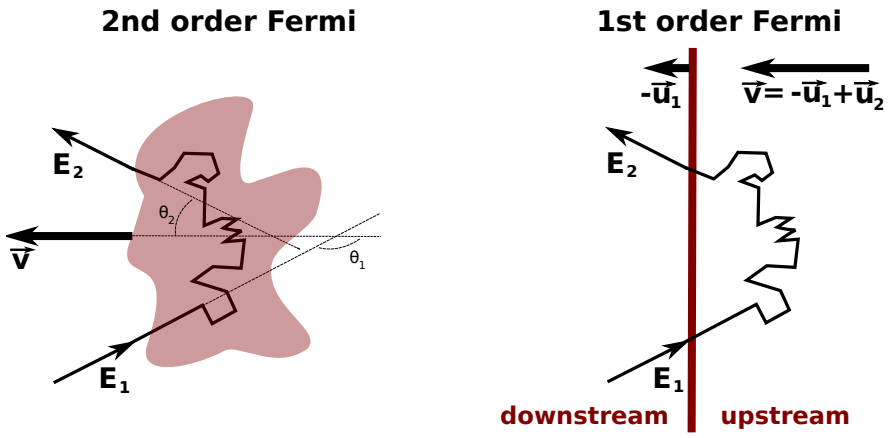

Figure 1.8: Illustration of 2nd order Fermi (or magnetic cloud) and 1st order Fermi (or shock) acceleration. In his original paper in 1949, E. Fermi proposed the encounters with magnetic clouds as possible particle acceleration regions.

particle acceleration via collisions with moving shock fronts, as present in supernova explosions, is even more efficient. As will be shown below, the former plasma cloud acceleration process is propotional to $\beta^2 = \left(\frac{v}{c}\right)^2$ and is thus called 2nd order Fermi acceleration (Figure 1.8 - left), while the latter shock acceleration gains energy proportional to β. Shock front acceleration is called 1st order Fermi acceleration (Figure 1.8 - right). This derivation is based on the one performed in [3].
To deduce the acceleration efficiency for the ionized cloud case, we could assume a test particle with energy $E_1 \approx p_1 c$ entering a cloud that moves with speed $\vec{v}$.
After multiple scatterings the particle eventually leaves the gas with energy E_2. In the reference frame of the gas cloud the initial particle energy E_1 is transformed to:

$$E_1^{'} = \sqrt{1-\beta^2} E_1 \left(1 - \beta \cos\theta_1\right) \tag{1.9}$$

with $\beta = v/c$ the velocity of the cloud. The lab frame energy of the particle after the encounter is:

$$E_2 = \sqrt{1-\beta^2} E_2^{'} \left(1 + \beta \cos\theta_2\right) \tag{1.10}$$

Inside the gas the particle energy does not change, thus $E_2^{'} = E_1^{'}$. Hence the relative energy gain ϵ per encounter, with angles θ_1 and θ_2 is given by:

$$\epsilon = \frac{\Delta E}{E_1} = \frac{E_2 - E_1}{E_1} = \frac{1 - \beta\cos\theta_1 + \beta\cos\theta_2 - \beta^2\cos\theta_1\cos\theta_2}{1-\beta^2} - 1 \tag{1.11}$$

The case of the shock front acceleration (right plot of Figure 1.8) results in the same equation, but now $\beta = v/c$ is the velocity of the shocked gas downstream from the shockfront. In this case the shock front moves with velocity -$\vec{u_1}$ and the shocked gas moves away from the shock front with a velocity of $\vec{u_2}$ with regard to the shock front ($|u_2| < |u_1|$).
Up to now this calculation is the same for the gas cloud and the shock. The difference between the two arises when the average over the zenith angles in Eq. 1.11 is taken:

- In the plasma cloud acceleration the scattered angle is uniform, thus $< \cos\theta_2 >= 0$. The probability for a particle to collide with the cloud depends on the velocity difference between the cloud and the particle:

  $$\frac{dn}{d\cos\theta_1} = \frac{1-\beta\cos\theta_1}{2} \text{ for } -1 \leqslant \cos\theta_1 \leqslant 1 \tag{1.12}$$

  Averaging over the zenith angles gives $< \cos\theta_1 >= -\frac{\beta}{3}$. Thus one obtains an average relative energy gain of:

  $$\epsilon = \frac{1+\beta^2/3}{1-\beta^2} - 1 \sim \frac{4}{3}\beta^2 \tag{1.13}$$

- In the shock wave both the distribution of encounter and scattering angles are the projection of an isotropic flux onto a plane:

$$\frac{dn}{d\cos\theta} = 2\cos\theta \tag{1.14}$$

with $1 \leqslant \cos\theta_1 \leqslant 1$ for the incoming angle and $-1 \leqslant \cos\theta_2 \leqslant 0$ for the scattered angle. Integrating over the angles gives $< \cos\theta_1 >= -2/3$ and $< \cos\theta_2 >= 2/3$, which results in an average relative energy gain of:

$$\epsilon = \frac{1 + \frac{4}{3}\beta + \frac{4}{9}\beta^2}{1-\beta^2} - 1 \sim \frac{4}{3}\beta = \frac{4}{3}\frac{u_2 - u_1}{c} \tag{1.15}$$

This illustrates that the energy increase in plasma clouds is of second order and first order for shock acceleration. Furthermore, since plasma clouds seem to have a relatively small velocity and also internal energy losses could occur, particle acceleration via plasma clouds seems improbable. Shock waves on the other hand would be an excellent candidate.

Even more important, and in favour of SNR as being particle acceleration sites, is the fact that many of such encounters would approximately result in the desired power law spectrum measured at Earth (Eq. 1.1). Assume a particle with initial energy E_0, and ϵ the particle acceleration efficiency with each encounter between the particle and the shock front (1st order) or ionized cloud (2nd order). The particle energy gain per encounter is $\Delta E = \epsilon E_0$. After n encounters the energy will be E_n:

$$E_n = E_0\,(1+\epsilon)^n \tag{1.16}$$

From which the number of encounters to reach the final particle energy E is obtained:

$$n = \frac{\ln(E/E_0)}{\ln(1+\epsilon)} \tag{1.17}$$

With each encounter there is a certain probability P_{esc} to escape the accelerating region. The probability that a particle remains in the region after n encounters is given by $(1-P_{esc})^n$. Thus the number of particles N which are able to reach at least an energy E is given by:

$$\begin{aligned} N(\geqslant E) &\sim \sum_{m=n}^{\infty}(1-P_{esc})^m = (1-P_{esc})^n \sum_{m=0}^{\infty}(1-P_{esc})^m = \frac{(1-P_{esc})^n}{P_{esc}} \\ &\sim \frac{1}{P_{esc}}\left(\frac{E}{E_0}\right)^{-\gamma} \end{aligned} \tag{1.18}$$

with:

$$\gamma = \frac{ln\left(\frac{1}{1-P_{esc}}\right)}{ln\,(1+\epsilon)} \approx \frac{P_{esc}}{\epsilon} \tag{1.19}$$

Hence, the energy spectrum naturally follows a power law distribution when multiple encounters between particles and the accelerating region occur and the escape probability is taken into account.

For the shock acceleration the outgoing flux Φ_{out}, the escape downstream from the shock front, is given by $\rho_{cr} \cdot u_2$, with ρ_{cr} the cosmic ray density. The incoming flux on the other hand is again given by the projection of an isotropic flux onto a plane:

$$\Phi_{in} = \int_0^1 d\cos\theta \int_0^{2\pi} \frac{c\rho_{cr}}{4\pi}\cos\theta d\phi = \frac{c\rho_{cr}}{4} \tag{1.20}$$

Now the escape chance can be computed:

$$P_{esc} = \frac{\Phi_{out}}{\Phi_{in}} = \frac{\rho_{cr}u_2}{c\rho_{cr}/4} = \frac{4u_2}{c} \tag{1.21}$$

If this is inserted in Eq. 1.19, together with the relative energy gain (Eq. 1.15), one obtains:

$$\gamma = \frac{3}{u_1/u_2 - 1} \tag{1.22}$$

From the conservation of mass, momentum and energy and the ratio of specific heats for a monoatomic gas ($c_p/c_v \approx 5/3$) one can obtain $u_1/u_2 \approx 1/4$ [3]. Thus $\gamma \approx 1$ is obtained. Hence, from Eq. 1.18 a power law spectrum with power -2 is obtained:

$$\frac{dN}{dE} \sim E^{-(\gamma+1)} \sim E^{-2} \tag{1.23}$$

This matches the observed power law spectrum at earth (Eq. 1.1), with only a difference between the predicted power law factor at the source and the one observed at the earth. This could be due to the propagation from the source and is discussed further in Section 1.4,

Maximum energy

Not only the relative energy gain (Eq. 1.15) per collision determines the maximal energy that can be reached, but also the number of encounters with the shock wave. This is determined by the total lifetime of the accelerating region τ, together with the time between two subsequent encounters T_{cycle}. The total energy gain or maximal energy is defined by:

$$dE = \frac{\epsilon E}{T_{cycle}} \cdot dt \tag{1.24}$$

One thus need to know the lifetime for the SNR and the time between subsequent accelerations T_{cycle}. The SNR evolution can be divided into several phases. Lagage and Cesarsky computed that the maximal energies can only be reached in the free expansion phase [23]. In this first phase of the SNR the expanding shock propagates freely through the ISM and accelerates, compresses and heats the interstellar gas. The end of this phase is reached when the mass of the heated interstellar material becomes of similar size compared to the mass of the expanding shock wave. At this point the interstellar material forms a reverse shock and decelerates the SNR shock wave. Lagage and Cesarsky showed that T_{cycle} is given by:

$$T_{cycle} \geqslant 20 \frac{E}{3u_1 ZeB} \tag{1.25}$$

with Ze the electric charge of the particle, and B the surrounding magnetic field. This dependency on E/ZeB is not surprising since this is the gyroradius of a highly relativistic particle, the radius of a circular motion of a charged particle in a magnetic field. Replacing it in Eq 1.24, together with the relative energy gain Eq. 1.15 and again $u_1/u_2 \approx 1/4$ results in a maximal energy of

$$E_{max} \leqslant \frac{3}{20}\frac{u_1}{c} ZeB(u_1\tau) = \frac{6}{20}\frac{ZeB}{c}\frac{E_{SNR}}{M_{SNR}}\tau \tag{1.26}$$

E_{SNR} and M_{SNR} are respectively the total energy in the SNR (10^{51} erg) and the mass (a few solar masses). The lifetime of the free expansion phase is thus defined by the time when the swept up gas has a mass of $\sim M_{SNR}$ and is ~ 1000 years. Using also the magnetic field of the surrounding interstellar medium (ISM) $\approx 3\mu G$, one obtains:

$$E_{max} \leqslant Z \cdot 3 \cdot 10^4 \text{ GeV} \tag{1.27}$$

In this diffusive shock acceleration SNR will only be able to accelerate protons up to 30 TeV and iron nuclei to 780 TeV. However, models exist which could increase these numbers by a factor 30-100, which would allow protons to be accelerated by SNR up to about the knee of the spectrum, and iron nuclei almost up to 100 PeV. This could be accomplished by increasing the magnetic field in the accelerating region (as can be seen from Eq. 1.26). Shock acceleration where the accelerated particles create an amplification of the

magnetic field themselves is called non-linear shock acceleration and proposed by T. Bell [24] and others. It should also be noted that probably a significant fraction of the cosmic rays remain trapped in the SNR after the free expansion phase and only diffuse outwards slowly. In these phases the particles will however not be accelerated further and might lose energy adiabatically due to the expansion of the shock front. It is therefore possible that SNR contribute to several "populations" in the cosmic ray particle spectrum.

Gamma rays from SNR

If SNR accelerate protons up to energies of several TeV, it is expected to see a typical π^0-decay signature in the γ-ray spectrum from SNR. Gamma rays are not deflected in magnetic fields and therefore point back to the SNR. The neutral pions are created through collisions of the accelerated protons with the ambient gas, mostly consisting of hydrogen atoms. π^0 particles decay for 99 % to 2 γ's, with each an energy of $\approx m_\pi/2 = 67.5$ MeV. Due to a background of γ-rays from electron bremsstrahlung the identification of this π^0-fingerprint is not straightforward. It was only recently, in 2013, that the Fermi-LAT collaboration reported on the detection of this typical γ-ray bump of π^0 decay [25]. It could be distinguished from the Bremsstrahlung photons due to an increase of the γ spectrum around the π^0-bump. This provides evidence that SNRs are regions where protons are accelerated. Up to which energy, however, remains a question.

1.3.2 Possible other galactic sources

From the gyroradius ($r_L = pc/ZeB$), and the known values of the radius and magnetic field of the Milky way, it can be deduced that particles up to 10^{18} eV= 1 EeV are retained in our galaxy. It is however unclear whether galactic accelerators are in fact responsible for cosmic rays up to this energy, or whether they run out of fuel at lower energies.
As shown above, it is not straightforward that SNR in our galaxy provide the necessary conditions to accelerate particles up to the PeV-EeV range, although it is not impossible. Other galactic objects that could possibly accelerate particles up to these high energies are less well known and studied. The required power of the sources to sustain cosmic rays with energies $>$ 10 PeV is of the order 10^{37} erg/s. Therefore they must not be as abundant as the source(s) for lower energetic cosmic rays. Possible candidates include neutron stars or pulsars, which are pulsating neutron stars, present as the compact remnant in the center of a SNR. They often generate intense magnetic fields (and could then be called 'magnetars') which could be an excellent environment for CR acceleration up to the highest energies. Only $\mathcal{O}(10)$ of them are known in our galaxy. One of them is the pulsar in the center of the Crab Nebula, as shown in Figure 1.7. Another candidate for galactic acceleration are binary systems with at least 1 very heavy partner. Furthemore, also an extreme class of supernova explosions, called superluminous supernovae or hypernovae could be interesting candidates.

1.3.3 Extragalactic sources

The highest energetic cosmic rays are probably not created within our own galaxy, but have an extragalactic origin. The abundance of the most energetic phenomena in the universe is very low in our own Milky Way and furthermore also particles with an energy exceeding 10^{18} eV are not contained in our galaxy.
A crucial limitation for the maximal energy that could be reached in SNR was that the gyroradius or Larmor radius of the particle could not exceed the radius of the essential part of the accelerating region. In other words, that the particle stays confined in the SNR. This requirement could actually serve as general demand for all accelerating sites. A.M. Hillas generalized this in his famous "Hillas plot", from which an updated version for protons can be seen in Figure 1.9. He plotted many possible accelerating sites on a magnetic field as function of radius ($B - R$) plot. The maximal energy that can be reached increases with either the magnetic field (B_{source}) or the radius of the source (R_{source}):

$$E_{max} \approx ZeB_{source}R_{source} \tag{1.28}$$

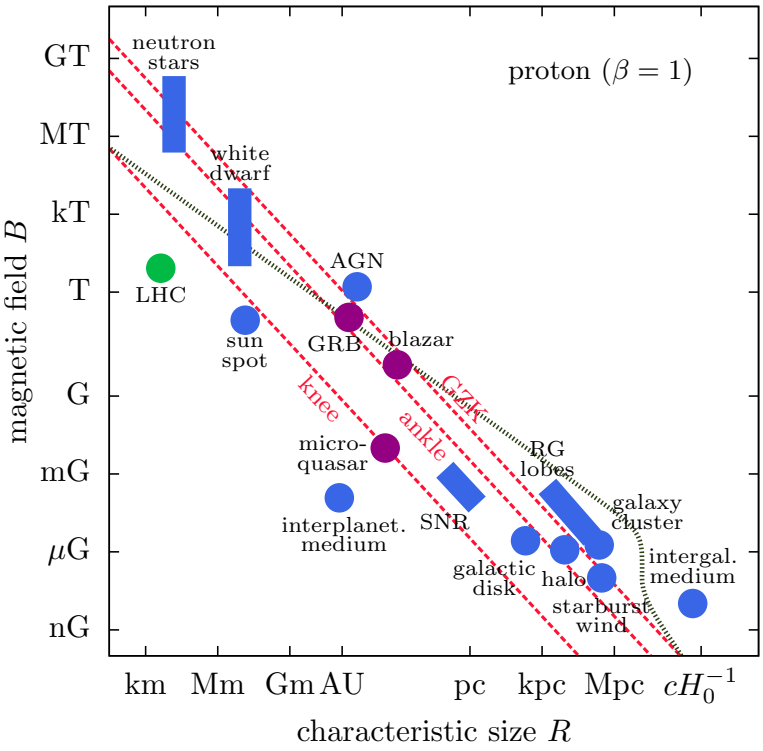

Figure 1.9: The famous Hillas plot, which illustrates the maximal energy that can be reached by protons, using the stringent requirement of confinement in a source with a certain magnetic field B and radius R. Astrophysical objects with their typical size and magnetic field are added to the figure. The knee ($\sim$ PeV), ankle ($\sim$ EeV) and GZK limit ($\sim$ 60 EeV) are indicated as the dashed red lines. The dashed black line shows the limit imposed by (synchrotron) energy loss in the source region itself and because of interaction with the CMB. [26, 27]

Equal-energy lines go from the top left to the bottom right on this plot. However, if the source moves towards us with a Lorentz factor Γ_{source} the upper bound of achievable energy is given by:

$$E_{max} \approx ZeB_{source}R_{source}\Gamma_{source} \tag{1.29}$$

It can be seen that neutron stars, active galactive nuclei (AGNs), gamma-ray bursts (GRBs), blazars and radio-galaxy lobes are among the possible sources to accelerate ultra-high-energy cosmic rays (UHECR, $E > 10^{18}$ GeV). However, if the magnetic field becomes too large, the protons start to lose more energy due to synchrotron radiation. For high magnetic fields the source region can therefore not be too large either, since particles should be able to escape from the source before they lose their energy. This synchrotron energy loss is thus placing another energy limit on the possible acceleration in sources. This is shown by the dashed black line. Synchrotron losses in the source thus essentially exclude neutron stars and also AGNs as sources of cosmic rays up to the GZK limit. However in certain conditions it might still be possible. At the highest radii this line shows another dip due to the interaction with the cosmic microwave background (CMB).
Heavier nuclei with an accordingly higher charge Z are easier to confine in the source, thus could be accelerated up to higher energies, as shown in Eq. 1.29. For these nuclei, effects like for example photo-disintegration might limit the maximal energy that can be reached.

Many energetic objects are observed in the universe: ranging from AGNs, blazars, quasars to radio galaxies, Seyfert galaxies, etc. These are, however, often (parts of) similar objects but observed from a different angle or at a different time. This unified picture is shown on the left plot of Figure 1.10 [29]. In general a galaxy consists of a black hole surrounded by an accretion disk and a large halo. Some galaxies have jets. A blazar galaxy is, for example, observed when the jets arising from the black hole point directly towards us. Quasars

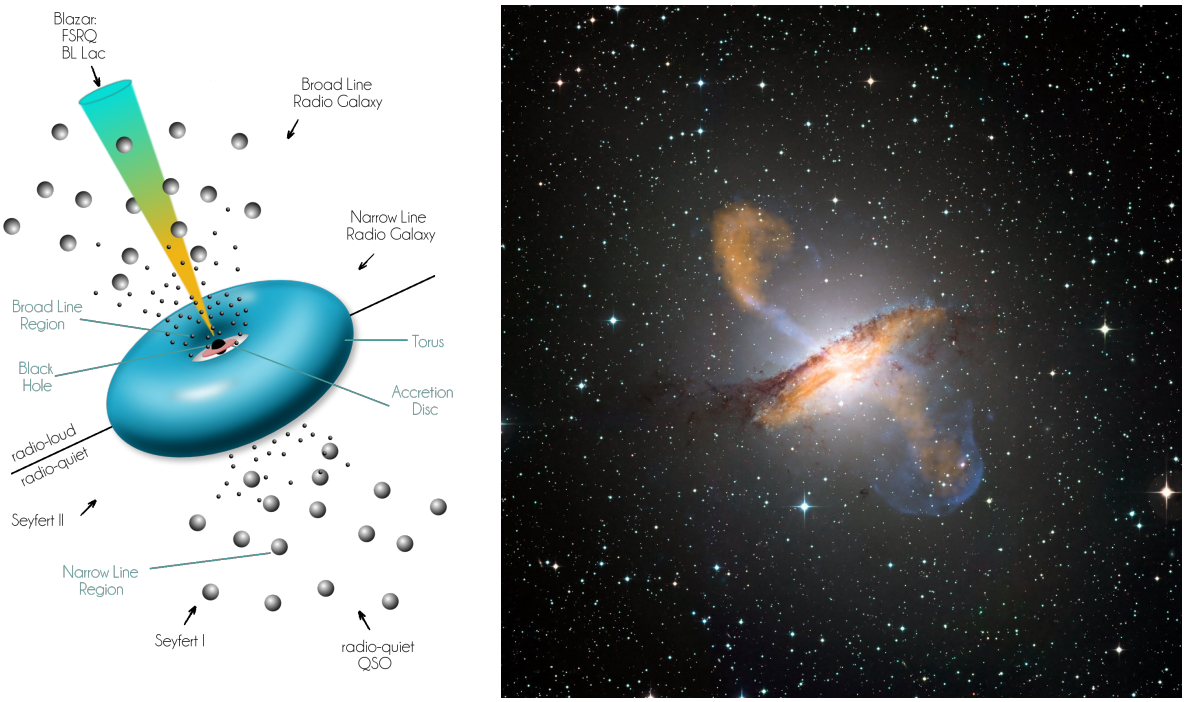

Figure 1.10: Left: Unified picture of Active Galactive Nuclei [28, 29]. Right: Composite image in various photon wavelengths of Centaurus A, the nearest radio-galaxy (at ∼3.8 Mpc) [30]. Submillimetre data, shown in orange, are from LABOCA on APEX; optical wavelengths from the Wild Field Imager on MPG/ESO 2.2 m in Chile are shown in their real colour; X-ray data are from the Chandra X-ray Observatory and is shown in blue. The radio lobes (in orange), jets and the torus of molecular gas are clearly visible.

are the most energetic objects in our universe, but all quasars are far away from us. This indicates that quasars are younger galaxies, and the black hole might become dormant over time, as happened in the case of the black hole in our Milky way. Alternatively, they might turn into radio or Seyfert galaxies.
The closest radio galaxy, Centaurus A, is shown on the right plot of Figure 1.10. Radio galaxies mainly emit photons of radio and other wavelengths between 10 MHz and 100 GHz, mostly arising from synchrotron losses (probably from electrons). Where the jet terminates in the intergalactic medium (IGM), often large radio lobes are observed, as is the case for Centaurus A.

Most of the regions inside such violent systems could be sites for UHECR acceleration. All of these sites have advantages and disadvantages. It is therefore even possible that only an interplay between the regions provides the right circumstances to accelerate UHECR. The core regions, close to the black hole, possess the large magnetic fields, but the escape probability seems low. From the radio lobes particles could probably escape easier, but the magnetic field might not suffice. The jets on the other hand are caused by spinning magnetic field lines and thus particle acceleration to huge energies could occur. Also the escape probability out of these jets seems to suffice, but adiabatic cooling might limit the maximal energy.
Obviously the dynamics are difficult, but this is a rapidly progressing field where many new theories develop ([31, 32, 33]) using input from the latest experimental data. Centaurus A seems to be an excellent candidate to study due to its proximity, and γ-ray observatories could play an important role to pinpoint the region(s) that might be responsible for the acceleration of the highest energy cosmic rays.

1.3.4 A variety of sources but smooth spectrum?

Supernova remnants appear to be an excellent candidate to be the source of galactic cosmic rays, at least up to $\mathcal{O}$(100 TeV), and possibly to somewhat higher energies. Nevertheless, it seems required that above these energies, at least one other source needs to contribute to the spectrum. It is even probable that several types of sources contribute to various energy ranges of the spectrum.
But how can different sources result in such a smooth energy spectrum over more than 10 orders of magnitude? In [34] B. Peters tried to answer this question. He wondered *"Can such separate sources dominate neighbouring energy intervals of the primary particle spectrum without introducing appreciable changes in slope or discontinuities in the size-frequency distribution of air showers?"*
Peters showed that this is actually possible, even if the sources differ in strength by a factor of $\mathcal{O}$(1000). The only requirement is that all or many chemical elements are present in each source and all of these elements should have rather similar spectra. It is probable that the flux decreases with increasing mass of the nucleus. It was shown before that particles are accelerated up to a certain magnetic rigidity, limited by the Larmor radius. Hence, with increasing charge of the nucleus, higher energies will be reached. This results in subsequent cut-offs of proton, helium, etc in the energy spectrum, up to iron. The iron cut-off is a factor of 26 higher compared to the proton cut-off. Assuming a steep spectrum with $E^{-2.7}$, this means that the iron flux can be a factor ∼6000 lower compared to protons. After the iron cut-off the second source, weaker but reaching higher in energy, would take over. This is shown for two hypothetical sources in Figure 1.11.

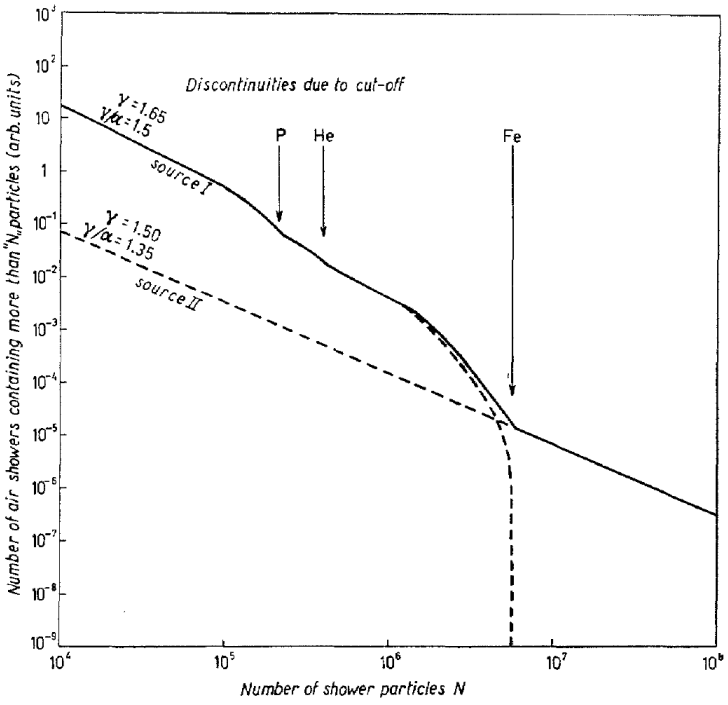

Figure 1.11: Illustration of a differential energy spectrum where two hypothetical sources contribute. [34]

The resulting spectrum would show small discontinuities at the elemental cut-offs, but no major jumps would be visible. This seems to be a plausible explanation for the very uniform energy spectrum.
With increasingly detailed measurements, these small discontinuities in the spectrum could become visible. This behaviour would also result in an increasing mean mass of the cosmic rays from the proton cut-off up to the iron cut-off, after which the mass would decrease again due to the proton-dominated second source. Such an increase and subsequent decrease in the average mass is a very distinct feature which would hint to consecutive cut-offs of a certain source. Since Peters was the first one to point this out, such behaviour is often called a 'Peters cycle'.

1.4 Propagation of cosmic rays

In the previous section some possible galactic and extragalactic sources have been described. One should, however, also consider that on their way from the source to the Earth, the particles are subject to the conditions of the medium that they traverse: particles are contained in the galaxy by magnetic deflection, some escape, spallation reactions could occur, particles could lose energy, etc. This could influence the measured spectrum at the Earth, which could then be different at the source. In this part some basic ideas and results about galactic and extragalactic propagation are covered.

1.4.1 Propagation in the galaxy

Leaky box model

The most basic approach to describe galactic propagation is a system in equilibrium (i.e a constant amount of cosmic particles) that has a uniform diffusion throughout the galaxy. There is a certain chance to escape the galaxy if the edge of the galaxy is crossed, and a uniform distribution of sources. This simple model is called the "leaky box model" [35, 3].
A general equation that could describe the particle number N at every position as function of time t inside a system is:

$$\frac{\partial N(x,y,z,t)}{\partial t} = \Delta \cdot (D\Delta N) - \Delta \cdot (\vec{v}N) + S \tag{1.30}$$

The first term on the right hand side describes particle diffusion, i.e. particle flow due to a difference in density. D is the diffusion coefficient or diffusivity. The second term describes convection for a motion with velocity $\vec{v}$. S describes both the injection and loss of particles due to "sources" or "sinks". In the leaky box model these diffusion and convection terms are replaced with a certain escape probability $1/\tau_{esc}$ that depends on the energy. τ_{esc} is the time that particles spend in the galaxy before they escape, such that the probability to remain in the galaxy after a time t is $\exp^{(-t/\tau_{esc})}$. Furthermore, it is assumed that the density of CRs in the galaxy does not change over time $\left(\frac{\delta N}{\delta t} = 0\right)$. Hence the amount of leakage should equal the amount supplied by the sources and sinks. If this is considered we get:

$$\frac{N_i(E)}{\tau_{esc}(E)} = S_i(E) \tag{1.31}$$

for each particle type i.
The sources and sinks for each particle could be described (in a simplified way) by an insertion from a source, a term describing the loss of nuclei of this type and a term for the generation of these particle with these energies. These could come from the same particle with higher energies through energy loss processes or from spallation by higher mass nuclei. Hence, Eq. 1.31 can be written as:

$$\frac{N_i(E)}{\tau_{esc}(E)} = Q_i(E) - \left(\frac{\beta c\rho}{\lambda_B} + \frac{1}{\gamma\tau_i}\right) N_i(E) + \frac{\beta c\rho}{m_p}\Sigma_{k\geqslant i}\int \frac{d\sigma_{i,k}(E,E')}{dE} N_k(E')dE' \tag{1.32}$$

The first and second part of the second term respectively show the rate at which nuclei interact with the interstellar hydrogen gas and the decay of the particle. The third term describes particle creation from other particles.
With this rather general equation the evolution from a source spectrum $Q_i(E)$ to a measured spectrum $N_i(E)$ after propagation can be described in the leaky box model.

In section 1.3.1 the amount of matter traversed during galactic propagation or matter density ρ_N was used, where it was claimed that it was deduced from the boron to carbon (B/C) ratio. Eq 1.32 now permits us to deduce this relationship. Boron is not produced at the source ($Q_B(E) = 0$), due to the smaller nuclear binding energy per nucleon as compared to helium, but is only created through spallation. If we assume that

the newly created boron does not lose energy, the third term should only include the spallation process. In this case we will only consider carbon and oxygen, and approximate that their measured flux at Earth is equal ($N_C = N_O$). Since boron is stable we can also neglect the loss due to decay. Eq. 1.32 now becomes:

$$\frac{N_B(E)}{\tau_{esc}(E)} \approx -\frac{\beta c \rho_p}{\lambda_B} N_B(E) + \frac{\beta c \rho_p}{m_p} N_C(E)[\sigma_{C\to B} + \sigma_{O\to B}] \tag{1.33}$$

And thus the B/C ratio will behave as:

$$\frac{N_B}{N_C} \approx \frac{\lambda_{esc}}{1 + \lambda_{esc}/\lambda_B} \frac{\sigma_{C\to B} + \sigma_{O\to B}}{m_p} \tag{1.34}$$

where the energy dependent escape length λ_{esc} is used:

$$\lambda_{esc}(E) = \beta c \rho_N \tau_{esc}(E) \tag{1.35}$$

These equations show the relationship between the boron-to-carbon ratio and the matter density ρ_N in the galaxy.
Also the energy dependence of the boron-to-carbon ratio is important. The AMS collaboration recently published their most detailed measurement of the B/C ratio between a rigidity R of 65 GV and 2.6 TV [36]. In their measurement the boron to carbon ratio decreases with $\sim R^{0.333}$. Since the B/C ratio in rigidity and energy are very similar, we could approximate the escape length as:

$$\lambda_{esc}(R) \sim E^{-\delta}, \text{ with } \delta \approx 0.333 \tag{1.36}$$

This can now be used to study how the propagation alters the energy spectrum in this leaky box model. If we neglect fragmentation from higher energy nuclei to protons we can get the proton flux as function of energy from Eq 1.31:

$$N_p(E) = \frac{Q_p(E)\tau_{esc}(E)}{1 + \lambda_{esc}(E)/\lambda_p} \tag{1.37}$$

Since $\lambda_p \approx 55$ g/cm^2 and $\lambda_{esc} < 10$ g/cm^2 for all energies:

$$N_p(E) = Q_p(E) E^{-1/3} \tag{1.38}$$

Thus if the observed spectrum has a power law index of $-2.7(-3)$, only $\sim$ -2.4 (-2.7) is required at the source. This is closer to the predicted spectrum of $\sim E^{-2}$ in Fermi acceleration (Section 1.3.1).

Beyond the leaky box model

The leaky box model obviously oversimplifies the galactic propagation: the galactic magnetic field is ignored, sources are distributed uniformily, the dimensions of the galaxy are not even used. The model provides us with some basic features or rough estimations, but it is clear that more complicated models are needed to explain observations [37]. For example, the leaky box model is not able to explain the observed level of anisotropy in cosmic ray arrival directions (see for example [38]). Due to the uniform distribution of the sources and a uniform diffusion, the leaky box model predicts an isotropic arrival of cosmic rays.
In [39] it is taken into account that the cosmic rays spend a certain fraction of their time in the halo surrounding the galaxy. This naturally introduces some form of diffusion from the sources in the galactic plane to the halo. Therefore this model is called the diffusion model. Furthermore, the average density ρ_{GH} encountered by cosmic rays in this galaxy + halo model is given by:

$$\rho_{GH} = \rho_N \frac{h}{H} \tag{1.39}$$

in which ρ_N is the density of the gas in the galactic disk ($\sim$1 proton/cm^3), h the height of the galaxy ($\sim$200 pc), and H the scale height of the halo. This scale height is estimated to be of the order of 1 kpc.

This would increase the lifetime of cosmic rays in the galaxy (discussion about the power in part 1.3.1), as is actually observed from radioactive isotopes.
In the diffusion model the escape time τ_{esc} is proportional to H^2/D ([39]), with D the diffusion coefficient. The escape length now becomes (Eq. 1.35):

$$\lambda_{esc} = \beta c \rho_{GH} \tau_{esc}(E) = \beta c \rho_N \frac{hH}{D} \tag{1.40}$$

And from Eq. 1.36 the energy dependence of the diffusion coefficient can be obtained: $D(E) \sim E^{\delta}$. This diffusion rate as function of energy has some important consequences. Probably the most important and logical one is the level of anisotropy. The faster the diffusion out of the galactic disk v_D, the larger the level of anisotropy is. Since $v_D = H/t_H \sim D/H$, the anisotropy $A(E)$ as function of energy can be approximated by:

$$A(E) \sim D(E) \sim E^{\delta} \tag{1.41}$$

It shows that the anisotropy grows with energy. If a value of $\delta = 1/3$ is used, an anisotropy of ∼0.4% is expected around 1 TeV and 3-4% around 1 PeV. This behaviour is roughly seen in data: the anisotropy below 100 TeV seems to be almost energy independent, close to 0.1 %, while it rises with energy above 100 TeV. The IceCube Neutrino Observatory observes 0.16 % around 400 TeV and 0.3 % around 2 PeV [38]. These values are best fitted with a $\delta = 1/3$ compared to a $\delta = 0.6$ [40], which predicts an anisotropy way above the measured values. This is, together with the B/C ratio, a second proof that δ seems to be close to 1/3.
Instead of a power law index of -2.7, sources would thus need to produce a spectrum with power law index close to -2.4. Theoretically it is, however, difficult to obtain an index below -2. This difference is one of the main problems in the theoretical understanding of acceleration and propagation of cosmic rays.
It should be noted that the anisotropy is still overestimated with this $\delta = 1/3$. This could be due to the fact that the assumptions in the diffusion model are still oversimplified. For example, we might need to take into account that our solar system is located in between the two spiral arms of our galaxy. There the local anisotropy could be lower due to the lack of sources, while it could be higher in the center of our galaxy. This is further discussed in [40].

1.4.2 Extragalactic propagation: GZK-limit

The intergalactic space outside of galaxies is presumed to be rather empty, without magnetic fields or gas clouds. Extragalactic cosmic rays, probably with energies in the UHECR region ($E > 1$ EeV), are therefore only deflected by about 5 degrees in the magnetic field of the Milky way [3], thus their direction points more or less back to the galaxy where they were created.

Although the interstellar void does not contain much matter, there is an overall faint background glow in the microwave region of the electromagnetic spectrum. This is a relic of the early universe, created shortly after the big bang: the cosmic microwave background or CMB. The CMB has a black body radiation spectrum with a temperature of $T = 2.275$ K, which corresponds to a spectrum that peaks at photon energies of $\sim 2.35 \cdot 10^{-4}$ eV. Soon after the CMB was discovered, Greisen ([41]) and Zatsepin and Kuzmin ([42]) proved that this makes the ISM opaque for cosmic rays with very high energies. If cosmic rays are produced at distant cosmological objects, their flux above $\sim 7 \cdot 10^{19}$ eV would be highly suppressed. At these energies, protons interact with the CMB photons γ_{CMB} via the Δ^+ resonance:

$$p + \gamma_{CMB} \rightarrow \Delta^+ \rightarrow p + \pi^0 \tag{1.42}$$

or

$$p + \gamma_{CMB} \rightarrow \Delta^+ \rightarrow n + \pi^+ \tag{1.43}$$

The pions take away about 20 % of the initial proton energy, and this process continues until the proton energy drops below the particle production threshold. A second process to consider is the electron-positron

pair production from protons interacting with γ_{CMB}. This process turns on at lower energies ($6 \cdot 10^{17}$ eV) but protons only lose ~ 0.1 % of their energy. Hence, this would only produce a dip in the spectrum around the ankle. The photopion production process is the dominant one prohibiting the high-energy protons to travel cosmological distances in the universe.
For heavier nuclei the photopion production process moves to higher energies. For iron this would shift the photopion production threshold way above the observed cosmic ray energies and thus the effect of this process seems to be negligible. However, for nuclei another process kicks in at lower energies: photo-disintegration on CMB photons becomes the dominant interaction process. In addition also interactions with the Extragalactic Background Light (EBL), light in the UV to infrared wavelengths due to star formation processes, become significant. A nucleus with mass A will a certain number (n) of nucleons (N) through the interaction

$$A + \gamma_{CMB,EBL} \rightarrow (A - nN) + nN \tag{1.44}$$

where n is mostly 1 or 2. In [43] the evolution of nuclei with a certain energy and mass number is discussed in detail. In general, this will result in a flux suppression, which occurs for nuclei in the silicon to iron mass range at about the same energy threshold as the GZK limit for protons, by coincidence. All together, the highest energy UHECR will be highly suppressed and should originate from local sources, i.e. sources within a distance of 75-150 Mpc from the Earth. This is sometimes called the GZK horizon.

These processes would influence the composition of the UHECR above the ankle. Composition measurements of these UHECR could reveal which processes are important to consider. It could for example be that the sudden decrease of the spectrum at 50-100 EeV is the real maximal energy produced at cosmic accelerators. In this case the composition would probably increase from light nuclei around the ankle to heavier nuclei close to the cut-off. If a light composition is measured in this entire energy range, the above discussed GZK scenarios are very likely. In that case cosmic accelerators are able to produce even higher energy cosmic rays than the ones observed at Earth.
Aside from composition measurements of these UHECR also neutrinos could answer the question whether the flux suppression is due to the GZK mechanisms. These so-called cosmogenic neutrinos would be produced via the decay of the charged pions produced in Eq. 1.43 and their detection would indicate proton production at energies above the GZK limit.

2

The IceCube Neutrino Observatory

Through endurance we conquer.

Ernest Shackleton

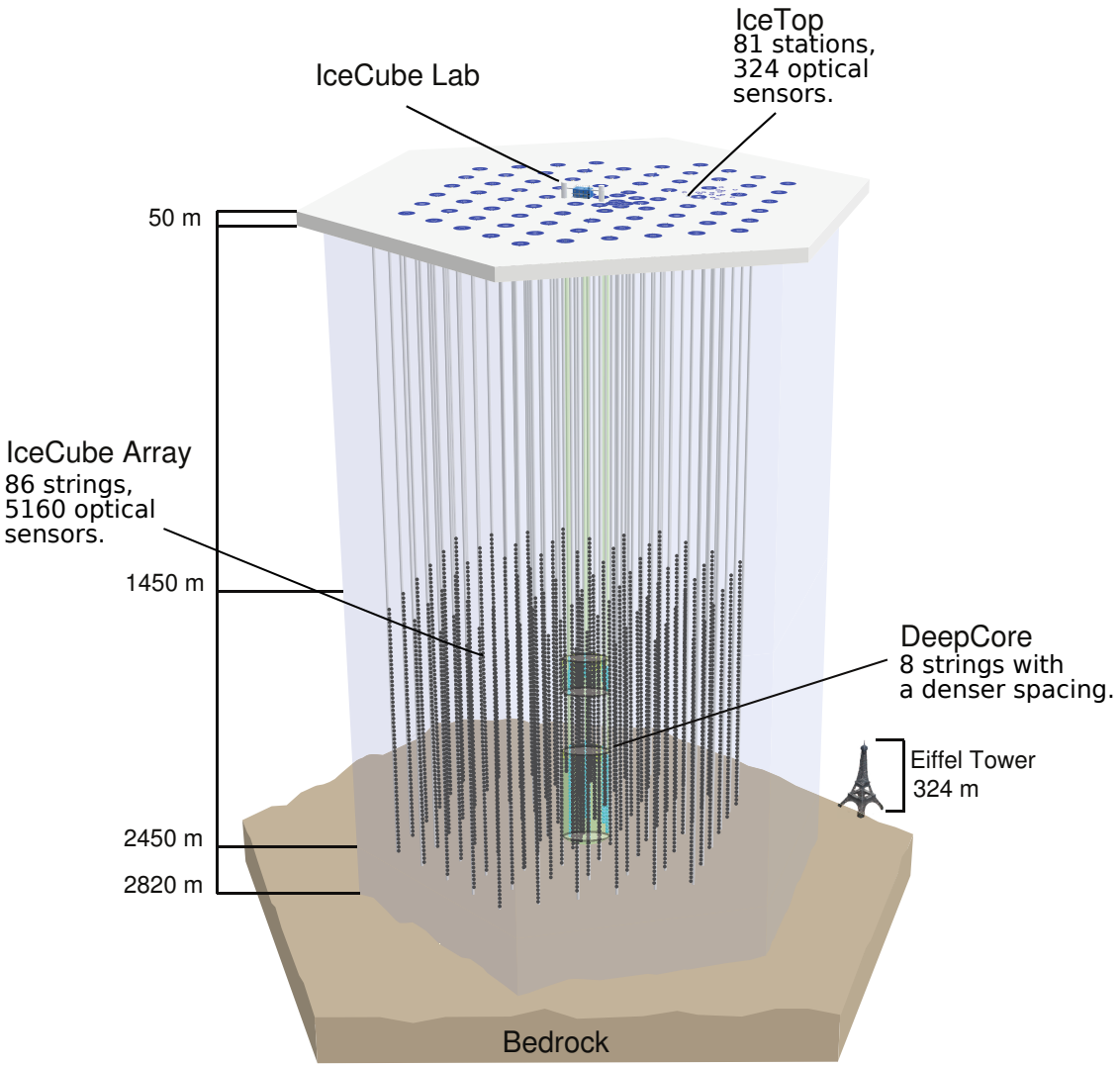

Figure 2.1: A graphical illustration of the IceCube Neutrino Observatory.

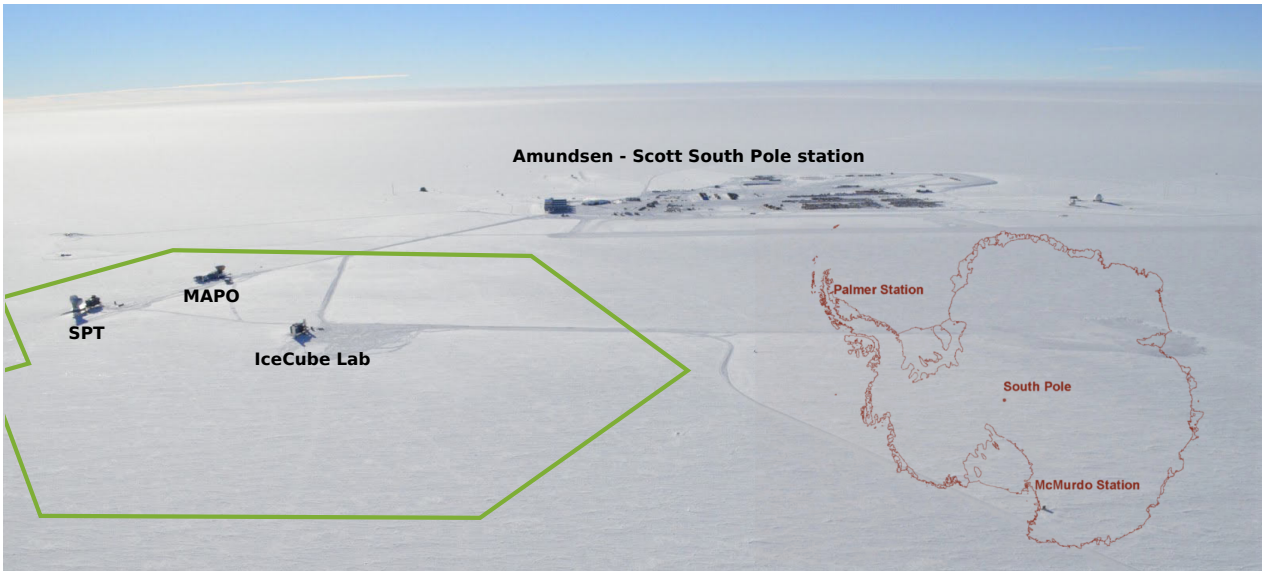

Figure 2.2: The geographical location of the IceCube Neutrino Observatory. The green border indicates the footprint of the IceCube Neutrino Observatory, close to the Amundsen-Scott station. Also the IceCube Lab and the SPT and MAPO telescopes are labeled. The map of Antarctica, with the three United States stations, is shown on the right. The Amundsen-Scott South pole station is located at the Geographic South Pole.

The IceCube Neutrino Observatory ("IceCube") is designed to observe neutrinos from the most extreme sources in the cosmos. While photons and cosmic rays, probably also created at these sources, are respectively stopped by dust and deflected by magnetic fields, neutrinos are ideal messenger particles. They are electrically neutral and interact only very weakly, therefore they are largely unaffected by dust and point back to their production site. Since IceCube is the first detector of its kind, it opened a new window to the universe.

However, neutrino astronomy is extremely challenging. Neutrinos only interact weakly, therefore their interaction probability is very low. And, similar to high-energy cosmic rays, energetic neutrinos from the cosmos are rare. A huge detection volume is thus required. Since it is impossible to fill this volume with active detector material, IceCube uses existing ice as detector medium and detection modules are deployed sparse over the volume (Figure 2.1). Instead of ice, the ANTARES [44] telescope in the Meditteranean sea and future KM3NeT [45] and Baikal-GVD [46] neutrino observatories use water as active detector volume. When a neutrino interacts with a nucleus in the ice (or water), it produces a charged lepton (an electron, a muon or a tau). In addition the neutrino transfers energy to the nucleus, which produces a cascade of (charged and neutral) particles. When a charged particle travels through the ice faster than the speed of light, it emits Cherenkov light (see further in part 2.1.1). Furthermore, particles lose energy, creating more charged particles, which in their turn radiate Cherenkov photons. The Cherenkov photons travel through the ice, where they can hit the detector modules. Based on the arrival time and the amount of light observed by these modules, the direction and energy of the initial neutrino can be reconstructed.

Since a huge volume of ice was required, the IceCube telescope was built deep in the ice sheet of Antarctica. It is located at $\sim$1 km from the Amundsen-Scott South Pole station (Figure 2.2), close to the geographic South Pole. Here, the ice sheet is about 2835 m thick, which is a process of many millions of years of slowly accumulating snow carried by the wind to the center of the South Pole. Due to this slow process and the pressure of the accumulated snow and ice, this results in very clear ice at large depths, where the detector volume of IceCube is located. The -roughly 5000- detector modules are deployed between 1450 m and 2450 m below the Antarctic surface, partially because of the clear ice, but also to reduce the background from (low-energy) cosmic radiation.

As a proof of concept, the Antarctic Muon And Neutrino Detector Array (AMANDA) was built as a precursor of IceCube ([47]). The final AMANDA-II detector housed 677 detectors between 1500 m and 2000 m below the ice surface, on 19 vertical cables. These cables, or "strings", where spread out over a circle with a diameter of 200 m. The AMANDA experiment showed that the deployment of these detectors in the ice is possible. It also showed that the absorption and scattering lengths of Cherenkov light at those depths are large enough such that detectors can be deployed at a large separation. The main goal of this detector, the observation of neutrinos created by EAS in the atmosphere, was already achieved when 10 out of 19 cables were deployed ([48]). Furthermore, reconstructions of (secondary) muon tracks achieved a pointing resolution of a few degrees. This pointing accuracy would allow the reconstruction of individual point sources.

At the surface above IceCube an array of calorimetric tanks is deployed. The tanks contain detector modules, equivalent as the modules deep in the ice, in a closed ice volume. This surface part of the IceCube Neutrino Observatory is called "IceTop". As will be shown in Chapter 5, the combination of IceTop and IceCube makes this telescope also a powerful cosmic ray detector. In Section 2.1 the IceCube Neutrino Observatory with all of its components is described in more detail. The way the data is collected and handled is summarized in Sections 2.2 and 2.3. In Section 2.4 some recent important measurements are highlighted, while Section 2.5 describes the possible upgrade of the detector.

2.1 The detector

In this section the IceCube Neutrino Observatory is explained in detail. We will first describe the detection principle and the detector modules, and then discuss the detector configurations and deployment.

2.1.1 Detection principle

Cherenkov radiation

Around the start of the twentieth century, the study of radioactivity was a very hot topic in physics. During those studies, a pale blue light was observed when a transparent medium was irradiated. First the light was accounted for as a fluorescence emission. However, the observed emission spectrum was continuous, which does not match the expected peaky pattern from fluorescence. The cause of the emission was not found until the late 1930's, when Pavel Cherenkov committed a series of experiments to study this phenomenon in detail [49]. Around the same time Frank and Tamm came with a theoretical explanation [50]. The Nobel Prize in Physics was given to Cherenkov, Frank and Tamm in 1958.
Frank and Tamm found that this blue light is explained by an induction of an electric field caused by a charged particle moving through the medium. When a charged particle moves through a dielectric material, it polarizes the molecules close to the track of the particle. If the particle travels fast enough, a charge asymmetry is created, which results in a dipole field along the axis of the particle [51] (Figure 2.3).
When the particle now traverses the medium at a speed βc faster than the speed of light in that medium, all emitted photon waves are in phase with one another and a resulting wavefront can be seen. This is similar to the triangular wave created when a boat traverses the water faster than the waves, or a sonic boom induced by a jet that crosses the sound barrier. The Cherenkov cone created by a relativistic muon is illustrated in Figure 2.4.

The speed of light in a medium is given by $c/n(\lambda)$, where $n(\lambda)$ is the refractive index of the medium at a certain photon wavelength λ. The angle θ at which the waveforms interfere constructively is defined by:

$$\cos\theta = \frac{c/n(\lambda)}{\beta c} = \frac{1}{\beta n(\lambda)} \tag{2.1}$$

This is known as the Cherenkov relation.
The refractive index of ice is 1.31-1.33 for wavelengths between 300 and 600 nm, which are the wavelengths

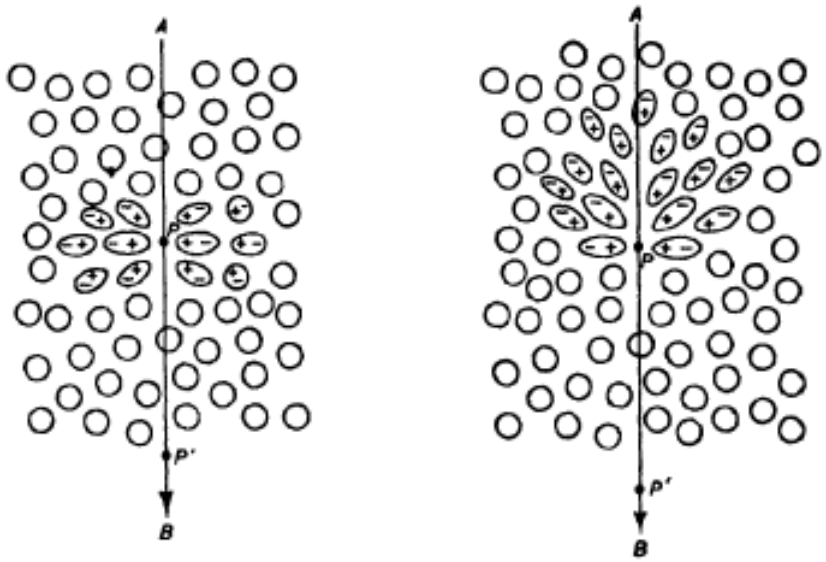

Figure 2.3: The polarization induced by a charged particle in a dielectric material. The two illustrations show the different effect for a slow (left) and fast (right) moving particle. [51]

that can be detected by the IceCube modules (see part 2.1.2). Thus the angle at which the Cherenkov radiation is emitted is $\sim 41^\circ$ in ice (for $\beta \approx 1$), for this wavelength range. The above relation also shows that no radiation is possible if the speed of the particle is below the speed of light in the medium.
Frank and Tamm not only proved the concept of Cherenkov radiation, but also calculated the intensity of the emitted radiation. The number of photons emitted per track segment at a given wavelength is given by:

$$\left(\frac{d^2N}{dxd\lambda}\right) = \frac{2\pi\alpha Z^2}{\lambda^2}\left(1 - \frac{1}{\beta^2 n(\lambda)^2}\right) \tag{2.2}$$

where α is the fine structure constant and Z the charge of the particle. The dependence of the number of created photons on the mass of the primary particle and the velocity is small.

Neutrino signatures

As described before, neutrinos are not detected directly in IceCube but via the products of the reaction between the neutrino and a nucleus in the ice.
The neutrino interacts with a nucleon in the nucleus via the exchange of a charged W or neutral Z boson. When a charged W boson is exchanged, a charged lepton of the same family and opposite charge is created:

$$\begin{aligned} \nu_l + N &\rightarrow l^- + X \\ \bar{\nu_l} + N &\rightarrow l^+ + X \end{aligned} \tag{2.3}$$

where the three lepton families (l = e (electron), μ (muon) or τ (tau)) are considered. X depicts the hadronic residual of the nucleon. This is called a charged current (CC) interaction (see Figure 2.4 for the ν_μ case).
The other possibility is that the neutrino interacts through Z^0 exchange, in which case the neutrino survives, but energy and momentum is transferred from the neutrino to the nucleus, which again creates a hadronic cascade X:

$$\nu_l + N \rightarrow \nu_l + X \tag{2.4}$$

This is a neutral current (NC) reaction. The products of the CC reaction are a lepton and hadronic cascade, while in the NC reaction only a hadronic cascade is created. Both, however, contain charged particles with

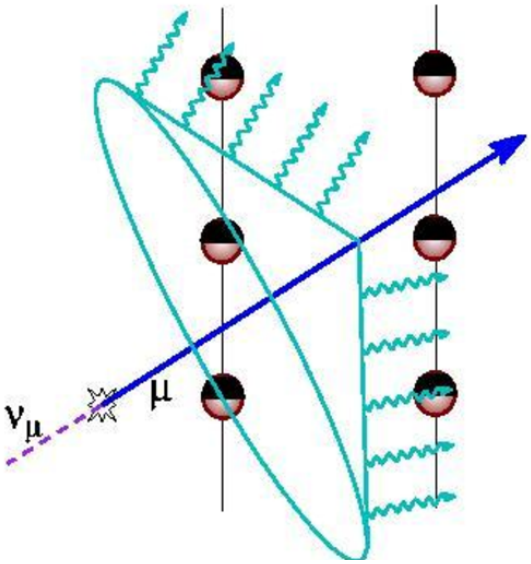

Figure 2.4: The detection principle of a muon neutrino. The Cherenkov cone is shown in pale blue. [52]

high velocities, which will emit Cherenkov light.

It is important to note that when leptons are created in the CC reaction, the observed light in IceCube will mostly not be created by the leptons themselves but by the secondary particles they produce via energy loss. Electrons lose most of their energy very quickly through Bremsstrahlung, thus an electron deposits most of its energy immediately and the signature of an electron neutrino interaction in the detector is a spherical blob of light.
Bremsstrahlung energy loss scales with $1/m^2$ (m is the mass of the particle), thus for more massive particles as the muon- and tau-leptons this energy loss process is slower. In general, muon energy loss can be divided into two categories: a continous part due to ionization, and a discrete part due to radiative effects. These radiative effects include Bremssstrahlung, but also e^+e^- pair production and electromagnetic interactions with nuclei. While the ionization energy loss is almost independent of energy, the total energy loss through radiative processes increases linearly with energy. The average muon energy loss rate can thus approximately be written as [53]:

$$-\frac{dE}{dX} = a + b \cdot E \tag{2.5}$$

with a the ionization energy loss ($\sim$2 MeV cm^2/g) and b the radiative energy loss. The created muons will thus show ”track-like” signatures in the detector, with from time to time large energy losses and correspondingly large deposits of light. In contrast, electrons and the products created in the NC interaction imprint a ”cascade-like” or spherical signature in the detector due to their fast energy loss.

A third possible topology is created by an energetic tau-neutrino (ν_τ). If a ν_τ interacts via the CC interaction, a τ-lepton is created together with the hadronic cascade (Eq. 2.3). The τ has a short lifetime and thus decays quickly, producing another particle cascade. If the ν_τ energy is at least 1 PeV, the initial cascade (when the τ is created), and the second cascade have sufficient separation such that they can be resolved by the IceCube detector. This signature is a ”double bang”. If one of the two cascades is not contained in the detector, such that this typical ν_τ signature is not observed.

2.1.2 Digital optical modules

The main components of the IceCube Neutrino Observatory are the detector modules dedicated to collect the Cherenkov light (the ”eyes” of the telescope). The light is captured with sensitive photomultiplier tubes

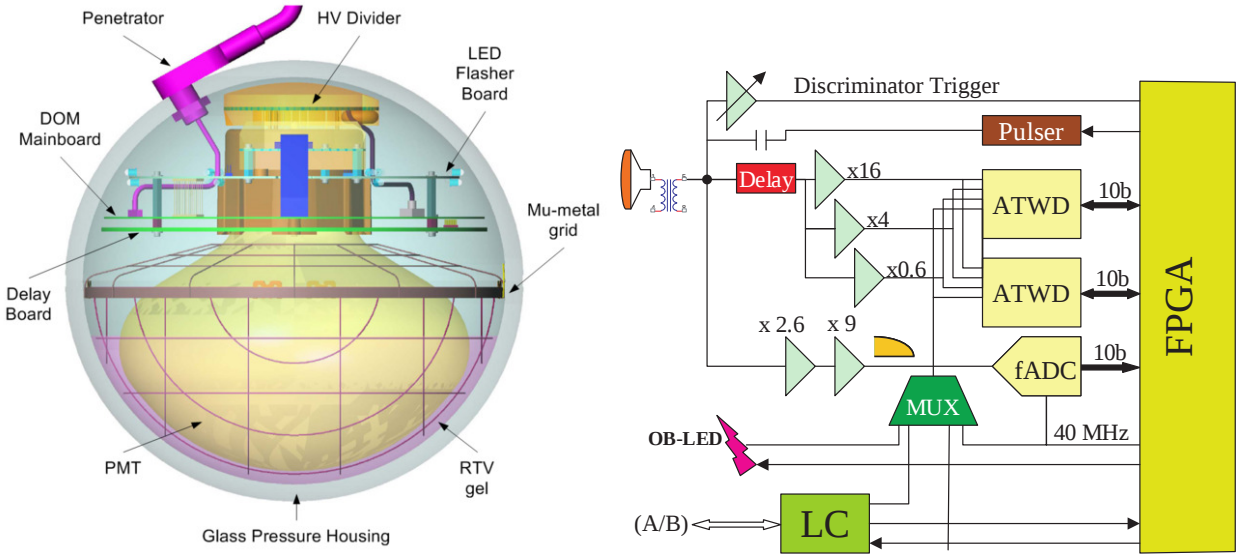

Figure 2.5: Left: An illustration of the components of a digital optical module. Right: A scheme of the main components and connections of the DAQ. [54]

(PMT). Via an on-board digitization system the PMT signal is transformed into a digital signal before it is sent to the surface, hence their name 'Digital Optical Modules' or DOMs (Figure 2.5). Components of the DOM are selected on requirements of long-term reliability, stability and robustness in a cold environment and a precise recording of a large variety of signals. The PMT is housed in a mu-metal grid in order to reduce the influence of the Earth magnetic field. Together with the electronics, it is protected by a 13 inch (35 cm) glass sphere of 0.5 inch thick, separated in two halves and held together with an aluminium waistband. The coupling between the glass sphere and PMT is assured by a silicone gel which also improves optical properties. This glass sphere is opaque for 94 % of 400 nm wavelength light, decreasing to 50 % and 10 % for respectively 340 nm and 315 nm wavelengths.

The 25 cm diameter PMT is described in detail in [55]. All DOMs on standard IceCube strings have a Hamamatsu R7081-02 PMT, while most DOMs in Deepcore (section 2.1.3) use a Hamamatsu R7081MOD PMT, which has a higher quantum efficiency (65 % at a wavelength of 390 mm) compared to the former PMT (25 % at 390 nm). The active surface of the PMT, the photocathode, covers the entire bottom half of the DOM. The photocathode is followed by a series of dynodes that operate at increasing voltages to amplify the signal. When a photon enters the DOM on the bottom half and hits the photocathode, a photoelectron (PE) is created. This electron gets directed towards the first dynode, where more electrons are detached. This signal is directed towards the next dynode, and so on. Hence, a cascade of electrons is created which constitutes the electrical signal on the anode. The 2 kV high voltage (HV) divider for the PMT is located in the upper half of the DOM. Standard IceCube DOMs operate at a HV of $\sim$1.5 kV, which corresponds to a signal gain of $\sim 10^7$. The corresponding PMT waveforms have amplitudes that range from $\sim$ 1 mV for a single photoelectron (SPE) up to $\sim$2 V for the highest signals. The signal widths range from 12 ns to 1500 ns [56]. In the very high signal regions, the PMT is saturated and linear response to the detected charge disappears.

The upper half of the DOM contains the data acquisition system or DAQ (described in detail in [57]), which surrounds the PMT base and HV divider. The central component, the 'DOM Main Board' contains the main building blocks, such as an FPGA (Field Programmable Gate Array), preamplifiers and digitizers. The Main Board also houses a stable 20 MHz oscillator which functions as DOM clock. It serves as input for timestamping the hits within the FPGA and communications. The regular timing calibrations are described in part 2.3.2. The DAQ system further consists of a Delay board, LED Flasher board and penetrator with the

data and power cables.
The scheme on the right in Figure 2.5 shows the main components of the DAQ and the flow of the signal. The signal is decoupled from the PMT through an inductive (toroidal) transformer or toroid, and is then directed towards the delay board, a continuously sampling digitizer (fast Analog to Digital converter (fADC)) and a discriminator trigger.
The DOMs in the deep IceCube detector use two different discriminators: single photoelectron (SPE) and MPE (multi photoelectron). In IceCube the SPE discriminator threshold is set to a voltage which would be caused by 0.25 PE, to be sensitive to single photons. In IceTop the MPE discriminator threshold is used for the high-gain DOMs and the SPE peak for the low-gain DOMs (part 2.1.4). The discriminator is set as a fixed voltage (20 mV and 4 mV for respectively the high- and low-gain).
The delay board introduces a delay of 75 ns. This assures that the part of the waveform before the threshold was crossed can be digitized and provides time to check for a coincident signal in the neighbouring DOMs (part 2.2.2). If the discriminator threshold is crossed, this results in a 'DOMlaunch' or 'hit'. The FPGA then opens one of the two integrated ciruits on the DOM (Analog Transient Waveform Digitizers or ATWDs). Each ATWD chip contains 3 channels with increasing preamplifier gains (0.21, 1.79 and 15.6 on average), in order to cover the entire range of voltages created by the PMT. The ATWD chips sample the analog waveform at a rate of 300 Msps (Mega samples per second), thus every 3.33 ns. They store the analog waveform in a capacitor array of 128 cells, which makes the total recordable time by an ATWD chip 427 ns. The digitization process is done for each cell separately by an ADC (analog to digital converter) and has a 10 bit precision. When the highest gain channel reaches 75 % or 768 counts of its range, the lower channel digitizations are also retained. Hence, the three channels combined have a 16 bit precision. The digitization of each ATWD channel takes about 30 μs, thus about 100 μs in total if all channels need to be digitized. During this time, the chip is busy and cannot record new data. If another DOMlaunch occurs when an ATWD chip is busy, the second ATWD chip on the main board is used to digitize this waveform. Having two ATWD chips on the main board limits the deadtime of the DOM significantly. The fourth input channel of an ATWD chip is connected to a multiplexer which is mostly used for calibration measurements, but is most of the time turned off to save power.
The third data line connects the PMT to the fADC. This fADC digitizes the signal continously using a 40 Msps sampler with a 10 bit precission. 256 samples are stored if the discriminator was passed. This corresponds to a duration of 6.4 μs. Before fADC sampling, an amplification of the signal happens (of a comparable size to the highest ATWD gain channel), as well as a smoothing of the signal in order to limit the effect of the low sampling rate.

The LED board contains 12 LEDs. For most of the DOMs the LEDs are single-coloured at a wavelength of 405 nm. The LEDs are ordered in pairs and evenly distributed along the edge of the flasher board. One of the two LEDs points downward at an angle of 10.7° with respect to the horizontal, the other upward at an angle of 51.6°. After refraction through the glass sphere, they point respectively horizontally and at an angle of 48°, close to the Cherenkov angle in ice. The LEDs can be turned on or off separately or combined. The width and amplitude settings are common for all enabled LEDs. Furthermore, 16 colour-DOMs or cDOMs are deployed which contain LEDs with a variety of wavelengths.

2.1.3 IceCube In-Ice Array

The IceCube Neutrino Observatory (Figure 2.1) consists of 86 cables ("strings") with 60 DOMs each. 78 (standard) strings are arranged on a hexagonal grid separated by 125 m (Figure 2.6). The 60 DOMs per cable are deployed at depths between 1450 and 2450 m below the ice surface, with a separation of 17 m between subsequent DOMs. In total, a volume of $\sim$1 km^3 of ice is thus instrumented with 4680 DOMs.
To detect lower energetic neutrinos a more dense array ("DeepCore") is deployed in the center of IceCube, where 6 extra strings are deployed between the standard strings. The inter-string in DeepCore ranges from 41 m to 105 m. 50 DOMs are deployed at depths between 2100 m and 2450 m, with a vertical inter-DOM

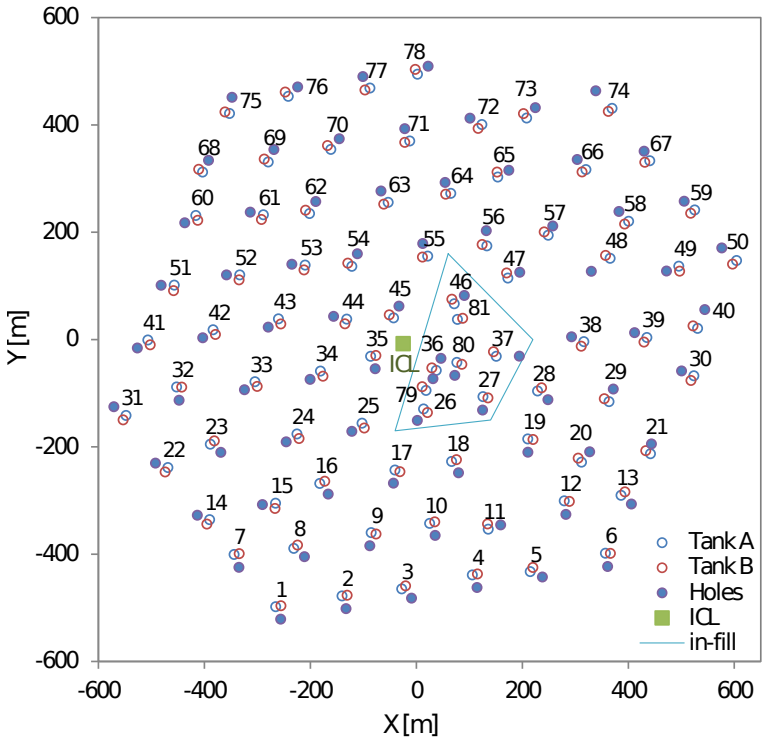

Figure 2.6: A top view of the geometry and horizontal coordinates of the IceCube detector. The positions of the IceCube strings (including Deepcore) are shown as blue dots in the X-Y plane. The open circles show the locations of the IceTop tanks. The blue lines surround the stations that form the in-fill part of IceTop.

spacing of 7 m. 10 more DOMs are mounted on each Deepcore string at depths shallower than 2000 m, with an inter-DOM spacing of 10 m. This volume functions as a veto region to better reject down-going muons from EAS. The reason for the split sub-detector is related to the ice quality in this region, as discussed below.

The relation between the number of created Cherenkov photons and the observed number in the IceCube DOMs highly depends on the properties of the ice. Therefore the photon scattering and absorption lengths in the ice have been, and still are, extensively studied. During the deployment of six IceCube strings an optical laser dust logger has been lowered down in the drill holes [58]. The average of the measurements in the six IceCube holes is shown as the red curve in Figure 2.7. The black line shows the effective scattering coefficient deduced from so-called flasher runs, special calibration runs in IceCube where the LEDs on the LED board of certain DOMs are lit (see also Section 2.3). For the study and development of the South Pole ice (”SPICE”) [59] model used in IceCube, all LEDs on string 63 were lit with the highest possible brightness. The light is collected in the neighbouring DOMs, and from those flasher data the scattering and absorption coefficients are fitted. The SPICE scattering model used in this work is based on Mie scattering, a description of a collision of an electromagnetic plane wave with a homogenous sphere [60] (”SPICE-Mie”).

A good agreement can be observed between the effective scattering coefficient and the dust logger data in Figure 2.7 (at the IceCube depths). The dust logger is sensitive to both air bubbles and dust. The bubbles are only present at depths smaller than 1400 m, thus above the IceCube detector. The dust can be found throughout the entire detector, but the largest peak is seen at depth between 2000 m and 2100 m. Here the amount of dust in the ice increases by about a factor of 10, which is reflected in the scattering coefficient deduced from the flasher data. Also the absorption coefficient increases roughly 10 times at these depths. This ”dust layer” can be related to large climatological changes from $\sim$66.000 yrs ago [61]. The existence of this dust layer eventually explains the split in the DeepCore sub-detector.

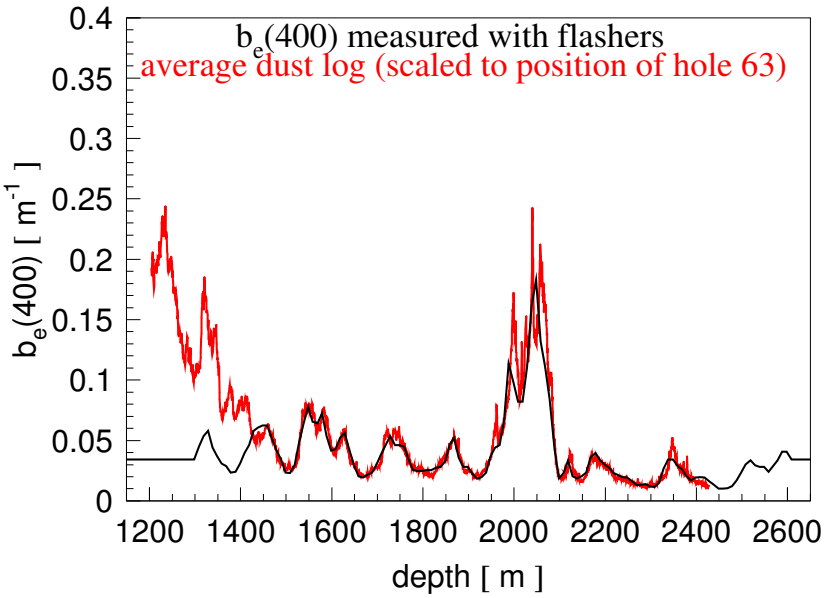

Figure 2.7: The parameter b_e, related to the effective scattering length at a wavelength of 400 nm, as function of the depth in the ice [59]. The red curve describes the average from the dust-log measurements [58], while the black curve shows the effective scattering length deduced from flasher runs where the LEDs on string 63 were lit.

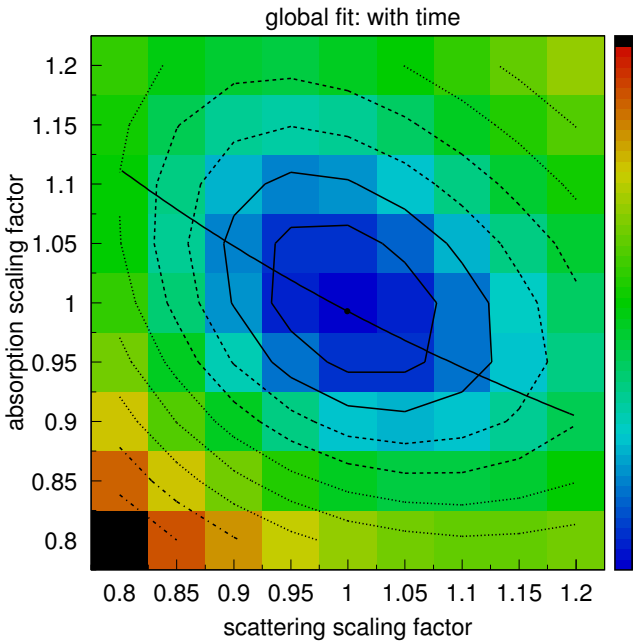

Figure 2.8: The likelihood space in the neighbourhood of the minima for the scattering and absorption factors [59]. The color scale is in log, ranging from $1.05 \cdot 10^5$ to $4.01 \cdot 10^5$.

The scattering and absorption coefficients in this SPICE-Mie model are obtained with a 1σ uncertainty of roughly 10 %, of which 5-7 % statistical uncertainty and 6.5 % systematic uncertainty. The likelihood space is shown in Figure 2.8, which also illustrates the correlation between the absorption and scattering coefficients. This 10 % uncertainty in scattering and absorption can be seen as a 10 % uncertainty in light yield. For analyses which highly rely on an energy measurement from the energy loss and light production, this will be the most important systematic error in the analysis. Further improvements of the model which result in a reduction of the error are currently being implemented. They include a more detailed description of the entire ice volume in IceCube, like the tilt and anisotropy of the ice.

Due to the melting and refreezing after the deployment of the DOMs the ice directly around the DOMs ('Hole ice') has worse optical properties than the main bulk ice. The properties of this Hole ice are less known compared to the bulk ice, but studies are ongoing. During deployment, two cameras (called Swedish Cameras, due to having been developed at Stockholm University) have been installed at the bottom of String 80 [62]. These revealed that, due to the refreezing process, two parts of the hole ice can be distinguished: a very bubbly part in the center of the column, and a rather clear part between that bubbly center and the bulk ice. This can also be expected from a refreezing process from the edge to the center of the column. The effective scattering lenth in the Hole ice is found to be somewhere between 30 and 100 cm for all DOMs [59]. As a baseline a Hole ice scattering length of 50 cm is used in this work, while the extreme 30 and 100 cm are used as systematic error.

2.1.4 The IceTop array

The IceTop array consists of 162 calorimetric tanks spread over 1 km^2. Two detector tanks are deployed on the surface at $\sim$25 m from every IceCube hole. The two tanks (A and B) are separated by 10 m, and are together called a "station". Three more stations are deployed in the center of the array close to three Deepcore strings, which creates an "in-fill" array for IceTop. The location of the IceTop tanks can be seen in Figure 2.6. The terrain has a small slope which makes that the vertical positions of the IceTop tanks range between 1944.54 m (for tank 18A) and 1950.08 m (for tank 74A) above the center of the deep IceCube array.

Figure 2.9 schematically shows an IceTop tank and a real picture of the inside of a tank. The tanks are shown during deployment in Figure 2.10. They are polyethylene cilinders with a diameter of 1.82 m and height of 1.30 m, of which the bottom 90 cm is filled with ice. The 40 cm above the ice is filled with a mixture of air and perlite for thermal insulation and light protection. The tank is closed from above with a wooden lid. Two DOMs are placed with their bottom half, thus with the PMT, in the ice. Their centers are horizontally separated by 58 cm. To be able to capture the entire range of charges induced by cosmic rays the two DOMS in the tank operate at a different PMT gain, respectively 10^5 for the low-gain DOM (HV of 750 V) and $5 \cdot 10^6$ for the high-gain DOM (HV of 1250 V).
On the outside of the tank an extra insulation foam is added to reduce temperature variations inside the tank. To observe a maximal amount of photons the reflectivity of the inside of the tank is increased with the addition of a white liner. For most tanks this liner is zirconium dioxide powder dispersed in high density polyethylene, but 12 tanks have Tyvek bags on the inside of the tank instead. Attached to the tank is a survey pole, since the tanks are soon covered by a snow layer. The location of the center of the DOMs with respect to this survey pole is known to an accuracy of 5 cm. More detailed information is given in [54].

2.1.5 Deployment

The IceCube Neutrino Observatory was deployed over seven seasons or years. This is due to the limited deployment time at South Pole, from about early November to mid-January, because of the cold and darkness during the rest of the year. The number of IceCube strings (including DeepCore) and IceTop stations deployed per season is given is Table 2.1. The fourth column of this table shows the name of the according detector configuration. The data-taking period for a certain configuration is typically from May/June to roughly the same time of the following year.

For the deployment of the IceCube DOMs one first had to drill a hole down to 2450 m deep in the ice. The IceCube DOMs have a diameter of 35 cm while the holes were made with a diameter of 60 cm during drilling to account for the refreezing of the water. The first $\sim$50 m are composed of packed snow (or 'firn'), through which the hole was made using a heated mechanical drill. For the rest of the hole an enhanced hot water drill was used: it pushed water at 90°C under large pressure in the hole to melt the ice. The total time

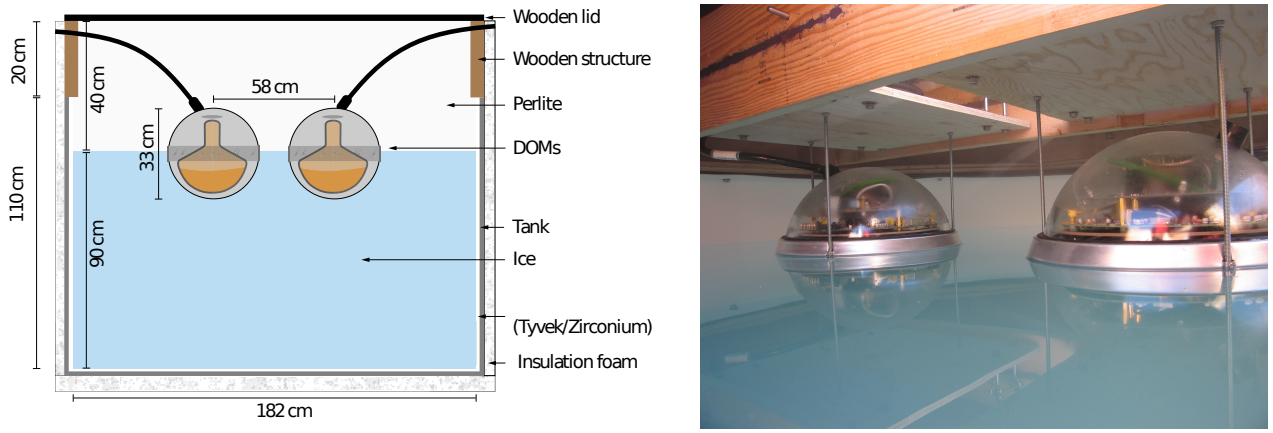

Figure 2.9: Left: an illustration of a cross-section of an IceTop tank. Right: a picture of the inside of an IceTop tank, showing in particular the two DOMs.

Table 2.1: Number of IceCube strings and IceTop stations deployed in each season, together with the configuration.

Season	Number of IceCube strings	Number of IceTop stations	Configuration
2004-2005	1	4	IT4-IC1
2005-2006	8	12	IT16-IC9
2006-2007	13	10	IT26-IC22
2007-2008	18	14	IT40-IC40
2008-2009	19	19	IT59-IC59
2009-2010	20	14	IT73-IC79
2010-2011	7	8	IT81-IC86

to dig an entire hole was $\sim$48 hrs. Then the drill system moved on to a new hole and at the same time the DOMs were deployed on the cable and lowered. The attachment of the DOMs to the cable happened ”on the fly”, thus a DOM was added, the cable was lowered, etc. This process took about 8 hours in total.
Parallel to this, IceTop tanks were installed close to the IceCube holes. As can be seen in Figure 2.10, a trench was dug first such that the two tanks could be placed with their lids even with the snow level. Then the DOMs were mounted in the tank frame and the tank was filled with water. A freeze control unit was added to the tanks. By circulating and degassing the water continuously the ice in the tank was made as clear as possible. The controlled freezing of the water in a tank took roughly 50 days. After that, the freeze control unit is removed and the trench is refilled.

Figure 2.10: An IceTop station during deployment in an open trench (left) and when the trench was refilled with snow (right).

2.2 Data-taking

In this section the IceCube cabling system and the first steps of the data-taking procedure are discussed in detail. These first steps are performed at South Pole before the data is sent via satellite to the North. This includes removal or cleaning of noise and data selection using triggers and filters.

2.2.1 IceCube cabling system

The IceCube cabling system mainly includes the in-ice cable, IceTop cables, the surface junction box (SJB) and the surface cable, as shown schematically in Figure 2.11 (top). Via the penetrator assembly each IceCube DOM is connected to the main cable of the string. Three wire pairs are responsible for a set of two adjacent DOMs. The first wire pair is used for power and bi-directional communication to the surface, while the other two wire pairs are responsible for ”local coincidence” (part 2.2.2) (bottom right scheme of Figure 2.11). Two power and communicaton wire pairs, connecting 4 DOMs, are merged into one four-conductor (”quad”) cable. One in-ice cable with 60 DOMs thus consists of 15 quads responsible for power and communication. Five quads are there for the local coincidence cabling, special instrumentation and a spare quad. Together with the cables of the 4 IceTop DOMs in one station, all these cables are connected inside the surface junction box to the surface cable. Due to their higher signal rate, one power and communication wire pair connects only one IceTop DOM. The surface cables are deployed in a 1 m deep trench below the surface (at the time of deployment) and run into the cable towers to the computing system in the IceCube Lab (ICL).

2.2.2 Local coincidence

The noise rate in the IceCube DOMs is about 560 Hz for standard DOMs and 780 Hz for the high quantum efficiency Deepcore DOMs [56]. The noise mainly emerges from electronic noise or luminescence of the glass sphere. To limit the effect of this dark noise on the data-taking and the amount of data sent to the ICL, a coincident signal between neighbouring DOMs is required. This ”Local coincidence” (LC) check is performed before the waveform is digitized.
In the in-ice array the LC condition on a DOM is fulfilled when one of the nearest or next-to-nearest DOMs on the same string also launches within $\pm 1\mu$s. As described in section 2.2.1, extra local coincidence cables are deployed between neighbouring DOMs to get this information fast (Figure 2.11). If the LC is fulfilled, the ATWD digitizes the entire waveform and the DAQ sends it to the surface. In case of an isolated (non-LC) signal, the digitization procedure is stopped and the ATWD is reset, which reduces the DOM dead time significantly. In this case, only the total charge and a time stamp, gathered from the fADC, is kept. In the

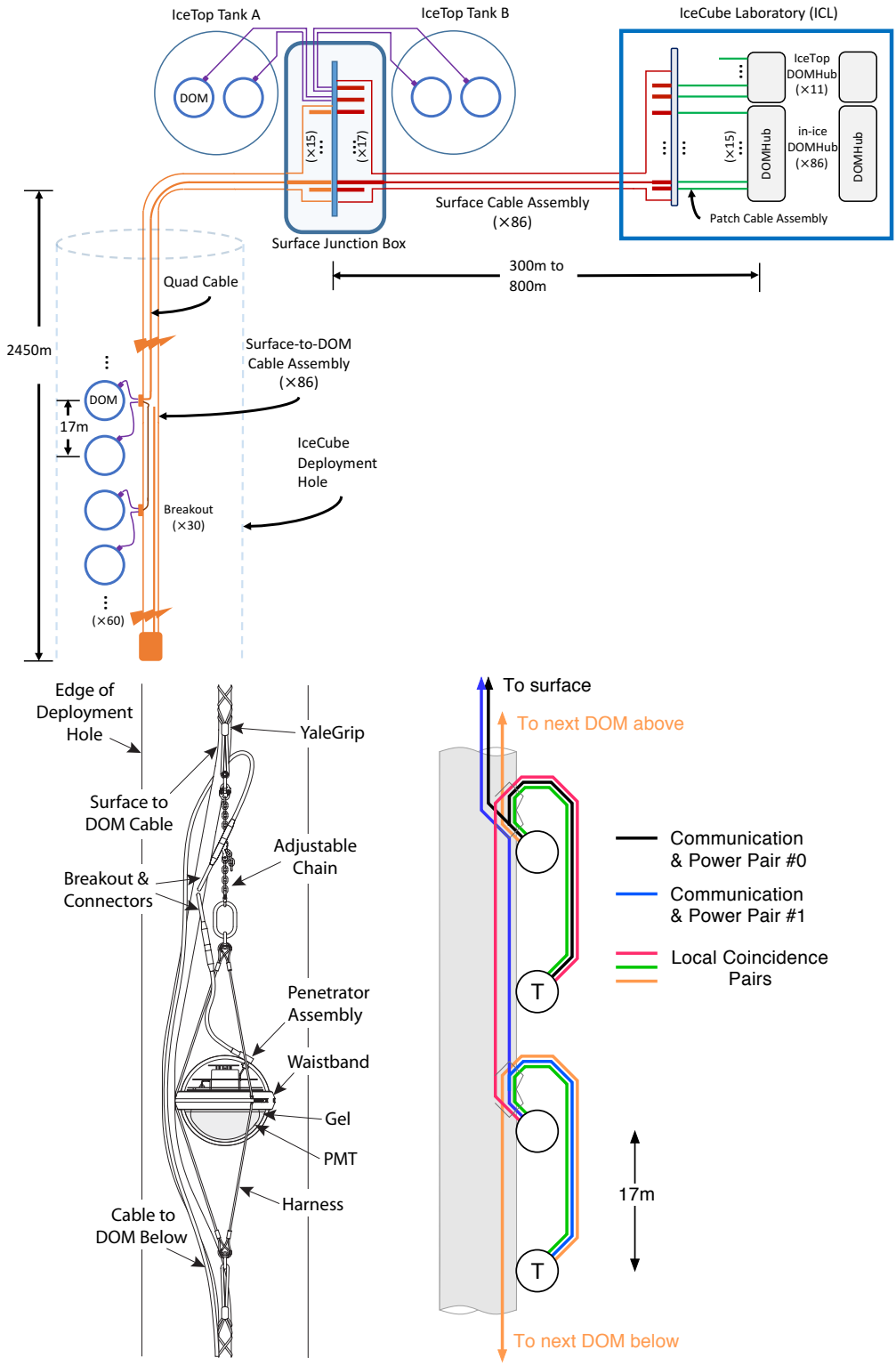

Figure 2.11: Schematic overview of the IceCube cabling system (top), shown for one combination of a station and a string. The bottom plots show the in-ice cabling system and structure for one DOM (left) and a scheme of the power and communication and LC cables for four DOMs (right). [56]

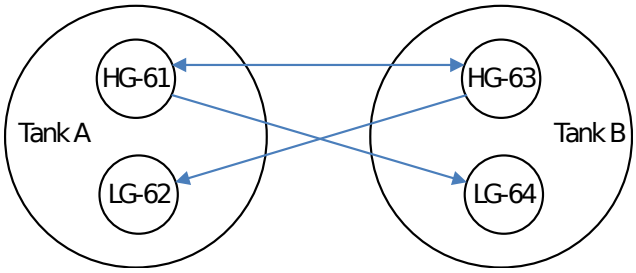

Figure 2.12: Local coincidence cables within one IceTop station. Not drawn is the existing cable between the LG DOMs, which is mostly unused, but could be used if the HG DOM in the tank dies and the LG DOM would become the HG one [54].

following, fully digitized hits are called hard local coincidence (HLC) hits, while isolated hits are soft local coincidence (SLC) hits.

In IceTop local coincidence is determined within one station. If both tanks in a station registered a hit within the coincidence time window of $\pm 1\mu$s, the LC condition is fulfilled and this results in HLC hits in both tanks. In contrast, if only one of the two tanks in the station observes a signal, this gives rise to an SLC hit in this tank. Therefore, either one of the tanks in a station will have an SLC hit, or both will have an HLC hit. For IceTop DOMs the SLC total charge and time stamp are gathered from the ATWD traces. The HLC hits contain the full waveform information.
The main LC cables for IceTop are displayed in Figure 2.12. As shown, this LC coincidence condition is primarily based on the pulses measured by the HG DOMs. This is due to the fact that these HG DOMs are more sensitive than the LG DOMs. Every signal in the LG DOM should also be seen in the HG DOM. However, since HG DOMs have more dead time, additional LC cables exist between the other DOMs. [54]

2.2.3 Data flow

At the ICL, the quads in one surface cable are distributed to computers, called DOMHubs. The 15 data quads of one IceCube string go to a single DOMHub. 11 additional DOMHubs are responsible for the IceTop data collection, where the quads of 8 IceTop stations are gathered in one DOMHub. These DOMHubs contain nine PCI[1] cards, of which eight serve for DOM readout (DOR) and one for GPS timing connection to the IceCube Master Clock. Each DOR card can read out up to eight DOMs. It is also responsible for the power supply to the DOMs, communications and timing.
The collection of the entire 19-rack IceCube computing system at the ICL is called the ”South Pole System” or SPS and includes, next to the DOMHubs, also servers for filtering, communication, etc.

The chain of software running on the DOMHubs and the additional servers is shown in Figure 2.13. The StringHubs, running on the DOMHubs, collect the data and pass it to the main SubTrigger system (discussed below), but also to the ”HitSpool” stream [63]. For the moment, the Hitspool stream saves all data of maximally 16 hours on the DOMHub disk and overwrites it later. This data stream was initially designed for the detection of Galactic supernovae. Many low energy neutrinos would be created in such an explosion, but their individual energy loss in IceCube would be too low to cause a trigger. However, their large abundance could cause a global increase in the hit rate. Such an increase in hit rate would result in a supernova alert which reads out the untriggered Hitspool data during a hundreds of seconds wide time window. Since the development this Hitspool data stream has also proven its use for other analyses. Examples are an online system that grabs 1 second of Hitspool data when a charge of 1500 photo-electons is exceeded, or 1 hour of Hitspool data around the time when the Fermi-LAT experiment measured a significant solar flare [64].

[1] Peripheral Component Interconnect. A PCI card contains a simple integrated circuit and a PCI bus.

Furthermore, this data can also be used to request the full detector readout during, for example, calibration runs of certain DOMs.

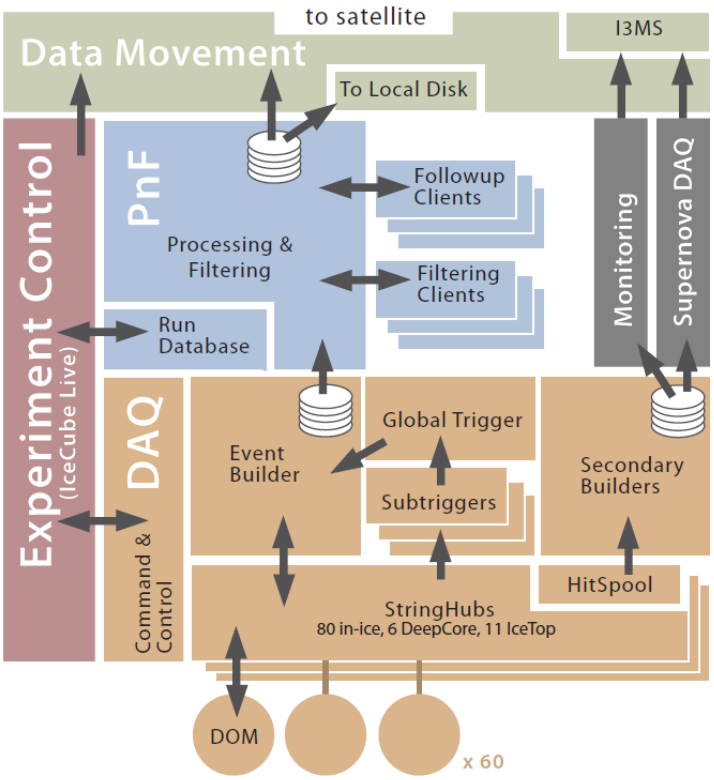

Figure 2.13: A scheme of the IceCube data flow in the computing system at South Pole. [56]

2.2.4 Triggers

The SubTrigger system runs all the IceCube triggers on the data forwarded by the StringHubs. Table 2.2 shows the various triggers defined in IceCube for the main years of data-taking. Also trigger requirements, associated Readout windows and rates are given. Some (unimportant for this work) triggers did not exist in the data-taking years IC79 and IC86.2011 (Table 2.1).
The most important triggers in IceCube are the Simple Multiplicity Triggers (SMT). These are also the triggers relevant for this work. The IceTop SMT trigger requires hits in 6 HLC DOMs, thus 3 stations, in a 6 μs time window. If these hits are found, the IceTop SMT Trigger is passed. The IceCube SMT trigger looks for 8 hit IceCube HLC DOMs in a 5 μs time window. Other existing triggers include the Deepcore SMT trigger, the In-Ice string trigger (looking for 5 DOMs on a string), the IceCube and IceTop volume triggers. From IC86.2012 onwards, a SLOP (Slow Monopole) trigger is included to study very weakly interacting heavy particles. This trigger requires 5 pairs of DOMs to be hit within a large time window, thus this trigger will result in a long readout of the detector. The Fixed Rate Trigger (FRT) reads out the entire detector during 10 ms, but this only happens at a very low rate.

The start of the SMT trigger is defined by the first HLC hit in the triggered subdetector, while the last HLC hit determines the end of the trigger. This decides the trigger length or trigger window. Since the trigger window slides along with the last detected HLC hit trigger lengths longer than 5 μs are possible. If there is no more HLC hit within 5 μs after the previous HLC hit, this previous HLC hit is the last hit and defines the end of the trigger.
The triggered subdetector is then read out not only during the trigger window, but an extra readout is added

Table 2.2: The different triggers used in IceCube, together with their settings. The readout window is given separately for IceTop (IT) and IceCube (IC) DOMs. The relevant triggers for this work are highlighted in bold.

Trigger Name	N HLC DOMs	Trigger Window (μs)	Readout window (μs)	Rate (Hz)
IceTop SMT	6	6	IT: ± 10, IC: ± 10	25
IceCube SMT	8	5	IT: ± 10, IC: $-4, +6$	2100
Deepcore SMT	3	2.5	IT: ± 10, IC: $-4, +6$	250
IceCube string	5	1.5	IT: ± 10, IC: $-4, +6$	2200
IceCube volume	4	1	IT: ± 10, IC: $-4, +6$	3700
IceTop volume	4	0.2	IT ± 10, IC: ± 10	4
IceCube SLOP	N pairs= 5	max 500	IT ± 10, IC: $-4, +6$	12
FRT	-	-	IT+IC: 10000	0.0003

before and after the trigger window (also listed in Table 2.2). The other subdetectors are read out with a time window centered around the start of the trigger. For example, if the IceCube SMT trigger is passed, the IceCube detector is read out starting from 4 μs before the trigger window to 6 μs after the end of the trigger window. IceTop is then read out 10 μs before and after the start of the trigger. If the IceTop SMT trigger is passed, the IceTop detector is read out 10 μs before the trigger window started and 10 μs after it ends, while IceCube is read out for 20 μs centered around the start of the trigger window.

These (sub)triggers are passed to the global trigger system (Figure 2.13). This gathers all the different triggers and merges their time windows into one global trigger readout window. The event builder takes all the data from the StringHubs within this time window and forms one ”DAQ event”. In the more difficult case that multiple physics events arrive close together in time, this global trigger window, or DAQ event, contains the various physics events, and they have to be split afterwards.

A typical triggering scheme for a cosmic ray shower traversing the detector is shown in Figure 2.14. The various passed triggers are shown in the different colours. The light grey band shows the IceCube readout and the darker grey band the IceTop readout. When a cosmic ray shower is detected, it first creates hits in a very short time in IceTop. Hence, the IceTop SMT Trigger window is typically very short. Since the readout window starts 10 μs before the start of the trigger, the first IceTop HLC hits related to a shower are typically around 10 μs after the start of the global trigger window. About 4.5 μs later the muon bundle travelled through 1.5 km of ice and starts to create hits in the ice, resulting in an IceCube SMT trigger. If it is not a very low energy cosmic ray, it is probable that one or more muons travel through the entire detector, which creates HLC hits for at least 3 μs. Due to the propagation of the light in the ice it is probably even longer. This results in a large IceCube SMT trigger window. Again the detectors are read out for some time before and after the trigger window as defined before. The bundle also results in a series of IceCube string and volume triggers, which are not used in this work.

2.2.5 Filters

All data within one global trigger window is sent to the Processing and Filtering (PnF) system. This system selects the events in analysis-focused categories in order to find the most interesting events and to limit the amount of data that needs to be transferred via satellite. Since some filters require more advanced information than the rough charge and hit time, first calibrations and fast reconstructions are applied. The calibration of the DOM hits is described in the next section. Afterwards, some very basic reconstructions are run on the pulses, in order to extract relevant information about the position, direction, energy and goodness-of-fit used by the filters.

About 25 different filters exist within IceCube. These filters are optimized for various analyses and are

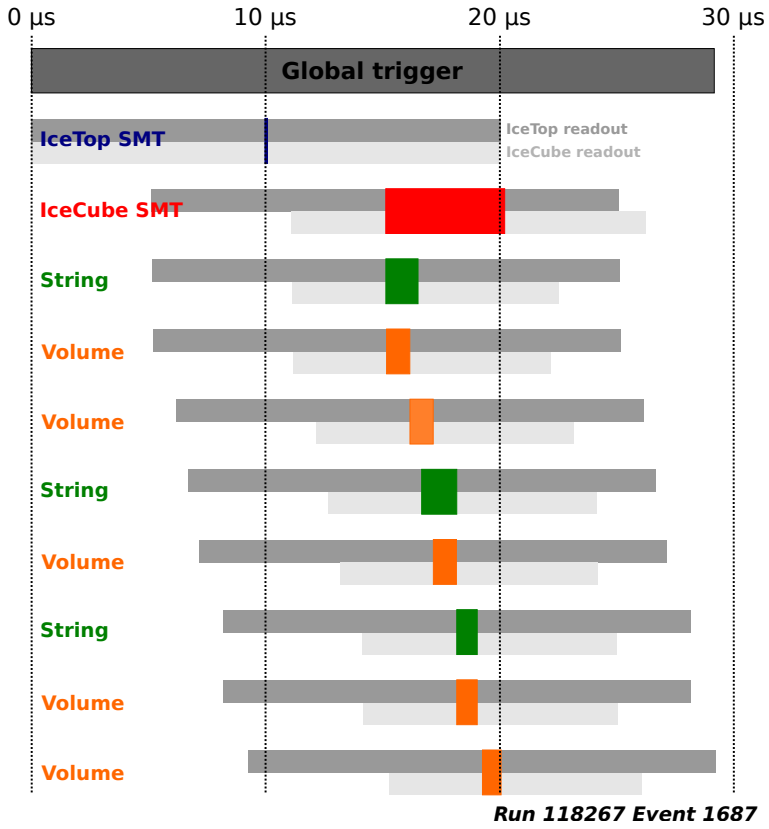

Figure 2.14: Graphical representation of the trigger scheme of a typical (real data) event induced by a cosmic ray air shower. The grey areas represent the readout windows, while the coloured areas show the trigger windows.

updated slightly year by year. The IceTop filters generally look for a certain number of HLC hits in the tanks. Since these are the filters used in this work, they are discussed more in depth in Chapter 5. Typical IceCube filters look for high-quality (muon) track reconstruction, a very high charge deposition, SLOP events, etc. Some triggers, which are for example used to study the detector behaviour or low energetic events, have very high rates. Since these events are less interesting, only a fraction of the events that pass these triggers are sent to the North. This ”extra filter” is called a prescale. A prescale of 10 for a filter means for example that only 1 out of 10 events that pass this filter is sent via satellite.

The bandwidth allowed for satellite transfer is about 100 GB/day, and the amount of triggered data per day is close to 1 TB. Hence, only $\pm 10\%$ of the data can be marked as interesting. This is achieved by a combination of the filter and the prescale. To further reduce the data size, most hits in IceCube are stored in a compressed format: Super Data Storage and Transfer format (SuperDST or sDST). In this format, the waveform is divided in a number of bins in time and the discretized charge in those bins is quantified. SuperDST pulses only take about 9 % of the storage compared to the full waveform. This extra data compressing tool is not used for a small collection of filters. All triggered data is stored locally at the ICL on tapes, and those are shipped to the North during the Antarctic summer season. This data still contains the raw, uncompressed waveforms and can be consulted if required.

2.2.6 Detector uptime and monitoring

In IceCube, one data-taking period, a ”run”, typically lasts for 8 hours. Once a certain run is finished, a new run automatically starts. These run transitions do almost not interrupt the data-taking and thus cause a very limited detector downtime.
All information about a run, like start and end time, data rate, system overflow, etc. is stored and can

be accessed through ”IceCube Live”, a web interface used for the monitoring of IceCube. Normally, runs with problems are flagged automatically, but human checks of all run summaries are required to find small problems that were not caught by automatic flagging. When a run fails by a large extent, human intervention is required, often performed by the IceCube winterovers (who are present at South Pole). This could for example be due to failing computing hardware or power supply in the ICL. Fortunately, major failures do not happen often and the total ”uptime” of the detector is more than 99 %. Often extra checks on the data quality are performed in a more advanced stage of the data processing.

2.3 Calibration

As described in section 2.1.2 the PMT signal is digitized by the on-board DAQ of the DOM and these digital signals are sent to the surface. The goal of the calibration procedure is to re-obtain the initial number of photons that hit the photocathode or created photoelectrons (PEs) at each time from this digitized information. This section summarizes the charge and time calibration procedures briefly, but a full description can be found in [56].

2.3.1 Charge calibration

The charge calibration of the DOM, i.e. the conversion of the recorded digital signal to the number of detected photons, can be separated in the calibration of the PMT and DAQ.
The gain of the PMT and the related high-voltage is calibrated using the ambient ”dark noise”. This noise mostly only releases one electron from the photocathode, thus the charge prior to the amplification of the PMT is known. The total charge in the final waveform then provides the gain of the PMT: it shows up as the single photoelectron (SPE) peak in a charge histogram composed of all the waveforms. The HV is then set such that the gain matches the chosen value (sections 2.1.2 and 2.1.4). The toroidal transformer that connects the PMT and the DAQ also changes the signal slightly. The self-inductance of the toroid mainly introduces a droop in the tails of the waveforms which possibly even undershoots the baseline. This reaction of a voltage drop is modelled as a function of sample time and a rough correction is applied. Since two types of toroids are used in IceCube, the ”droop correction” differs for those types. Furthermore, the droop correction also highly depends on the DOM temperature.
The adjustment procedure of the HV is part of ”DOMCal”, which is run once a year on IceCube DOMs. It is run once a month on IceTop DOMs since these DOMs are subject to larger temperature variations.

The DAQ calibration consists of the determination of the counts at zero input voltage, or pedestal, and gain for each digitizer on the main board. The pedestals need to be subtracted from the waveform to obtain the total charge. They are studied by ”beacon hits”, random hits at a rate of 1 Hz for which it is forced that the entire waveform is read out and sent to the surface. In most cases, no signal has been received from the PMT and these values really give the pedestal values. At this moment, the first 2000 beacon hits of each run are used to determine the pedestals, with some iteration when significant light was observed by the DOM.
The gain of the fADC and each ATWD channel are also calibrated during the special DOMCal runs. An electronic pulser circuit is used which is able to insert SPE-like pulses before the delay board. This gain provides the linear relationship between counts and voltage. The calibration can later be refined with the actual PMT waveforms.

The stability of the PMT gain, digitizer gain and pedestals are constantly monitored during normal data-taking runs using the SPE peak. A typical charge spectrum of an in-ice DOM is shown in Figure 2.15.The SPE peak is fitted with a gaussian on top of an exponential background. Small variations of the gain and baseline are observed, which lead to a shift of maximally 0.05 PE in the SPE peak (except for $\sim$12 unpredictible DOMs). The response of the entire DOM to light in the detector is furthermore constantly monitored by the use of single muons from air showers [65]. On top, special runs can be performed where light is created in the

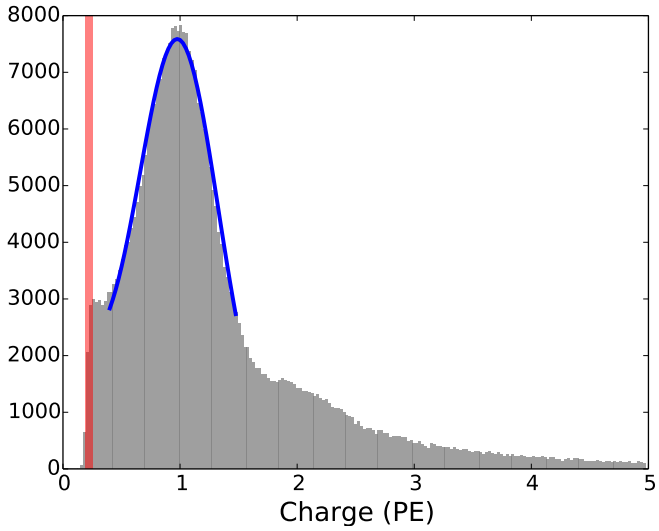

Figure 2.15: The recorded charge distribution of a DOM in IceCube, used to monitor the DOM stability. The threshold is shown in red and the typical single photoelectron peak is fitted with a gaussian on top of an exponential background (blue). [56]

detector by the LED board on the DOMs or by a calibration laser deployed in the ice [66]. Since it is known where and how much light is created, this allows to study the properties of all the neighbouring DOMS. But at least as important, this also allows to study the detector volume, i.e. the scattering and absorption coefficients of light in the ice (section 2.1.3).

2.3.2 Time calibration

Individual DOM clocks are continuously compared with the master clock in the ICL via the RAPCal (Reciprocal Active Pulsing Calibration) procedure [56]. During normal data-taking pulses are sent back and forth from the ICL to each DOM at a rate of about 1 Hz. These pulses are time stamped by the local times of the sender and receiver. For each event the time is determined using the previous and next RAPCal time stamp, and is converted to standard UTC time.
Before the digitization procedure of an event is started (with a DOM time stamp), a delay is introduced between detection of the photons and digitization. This delay is mainly due to the propagation of the electrons inside the PMT and the delay board. The delay board typically introduces a delay of about 75 ns, while the PMT transit takes about 55 ns, mostly dependending on the HV. These transit times can be determined by pulsing the LED on the main-board or LEDs on other DOMs during calibration runs.

2.4 IceCube Neutrino measurements

In this work the IceCube Neutrino Observatory is used to study the cosmic radiation. In all following chapters therefore only the cosmic ray related analysis of the data is discussed. This section highlights some of the other important studies performed with the IceCube Neutrino Observatory.

2.4.1 Astrophysical neutrinos

As discussed in the introduction of this chapter, the primary goal of the IceCube Neutrino Observatory is to study highly energetic phenomena in the Universe using neutrinos as messenger particles. Since neutrinos travel through space mostly unaffected, they point back to the source and thus hopefully reveal them.
However, most of the neutrinos observed by IceCube are not originating from space, but are created by

cosmic ray air showers in the atmosphere (Section 3.2). About 8250 atmospheric neutrinos are detected per month. On top of this IceCube detects about 275 million atmospheric muons per day, each of which might mimick a possible neutrino signal. They create an even larger background for the astrophysical neutrino searches. Since the rate of extraterrestrial neutrinos is very small compared to this background, this is kind of searching for a needle in a haystack.
However, since the energy spectrum of astrophysical neutrinos is expected to be harder than the steeply falling atmospheric neutrino spectrum, one could find the astrophysical neutrinos at the highest energies.

A first analysis that found two neutrinos that were probably astrophysical (with 2.8σ) was looking for very high energy neutrinos [67]. These two neutrinos had a deposited energy of 1.04 ± 0.16 PeV and 1.14 ± 0.17 PeV in the detector and were found in an analysis that had an effective detector livetime of 615.9 days. The first follow-up analysis which was developed was called the HESE (High Energy Starting Events) analysis. In order to look for the highest energies, it required a deposited charge of at least 6000 PE, which corresponds to approximately an energy deposition of $\sim$30 TeV in the detector. Since the main remaining background was atmospheric muons, it used a veto layer existing of the outer DOMs of the IceCube detector (therefore "starting track"). The first light observed for a certain physics event could not originate in this layer. With two years of data, 26 additional events were found in this analysis. Together with the two events found in the previous analysis, this led to a 4σ evidence for Extraterrestrial neutrinos [68]. Another extra year of data added to this analysis resulted in 37 selected neutrino events, which corresponds to a 5.7σ observation [69]. Afterwards the energy threshold was lowered to 1 TeV since an energy dependent veto requirement was applied [70]. While the HESE analysis was sensitive to both track- and cascade-like events (part 2.1.1), specific analyses were developed which focus on one of the two event signatures. These analyses were able to drop the veto condition. The cascade event analysis focused on very short cascades in and around the detector, and found 172 candidate events above 10 TeV [71]. Since muons can travel a long distance through the ice, the effective detector volume could be increased a lot for the analysis looking for track-like events. Due to the atmospheric background, this analysis looked for upgoing muons from muon neutrinos from the Northern Hemisphere [72]. The analyses could be combined to obtain an astrophysical neutrino spectrum (Figure 2.16). For now, no evidence of a break in this spectrum is observed, and the unbroken power law spectrum has a best-fit spectral index of -2.49 ± 0.08.

On top of the energy spectrum of the neutrinos, also the flavor composition of the neutrinos could teach us something about their production mechanism at the sources. Currently the best-fit of the flavor ratio for the combined IceCube measurements gives approximately as many muon neutrinos at Earth as electron neutrinos, and no tau neutrinos [71]. This is shown in Figure 2.17 (left) as the white cross. The square, circle and triangle show the flavor composition at Earth obtained from an assumed flavor ratio at the source.

Since the neutrinos point back to the location of production, one could also look at their arrival distribution and see whether a particular region of the sky produces more neutrinos. This sky-map, in Galactic coordinates, is shown in Figure 2.17 (right) for the events from the three year HESE analysis. No evidence for clustering has been found in this and other astrophysical neutrino searches. Furthermore, diffuse searches looking for accumulation of neutrinos in the atmospheric background have also not found a significant clustering [74].
The detection of a neutrino event on September 22, 2017 provides the first proof of a known blazar as a source of high-energy neutrinos [75]. This neutrino detection fired the realtime system installed by IceCube that notified telescopes around the world for follow-up observations. Soon afterwards, the Fermi Gamma-ray Space Telescope found that this blazar, TXS 0506+056, was in a flaring state at the time. Even higher energetic gamma rays arriving from the direction of this source were observed by the MAGIC telescope. The detection of this $\sim$290 TeV neutrino in coincidence with the gamma ray observation has a significance of 3σ. The IceCube Neutrino Observatory a posteriori also investigated 9.5 years of data to search for an enhanced neutrino emission (at lower energies) from this direction [76]. An excess was observed between September

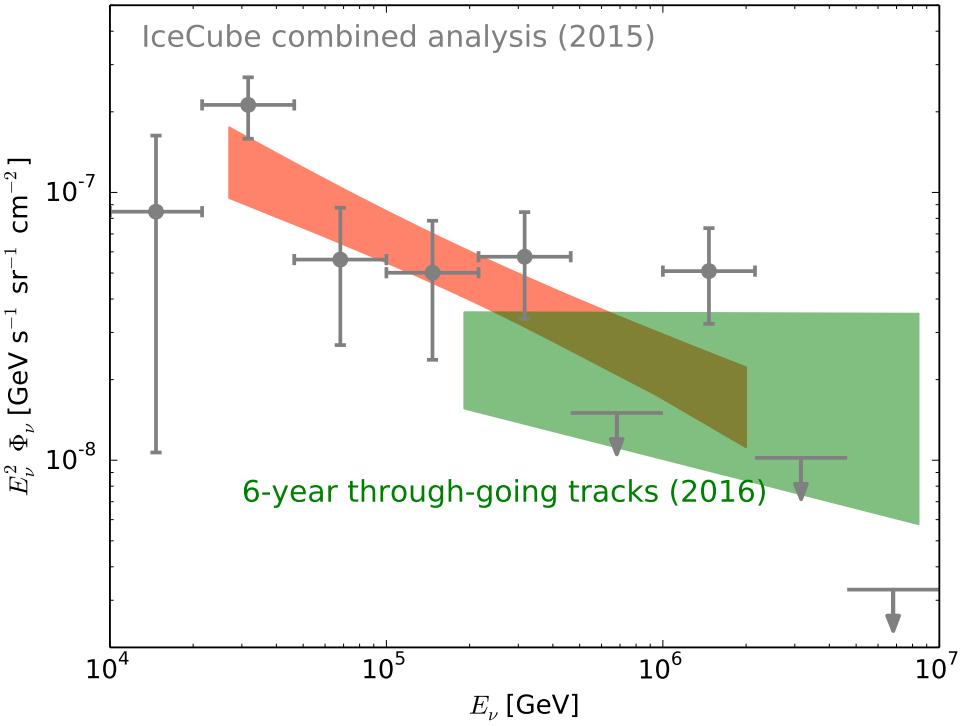

Figure 2.16: Combined fit to the astrophysical neutrino spectrum measured for the various event signatures by IceCube (red). The green band indicates a measurement of muons with energies >200 PeV traversing the detector, using 6 years of data (not included in the red band). [73]

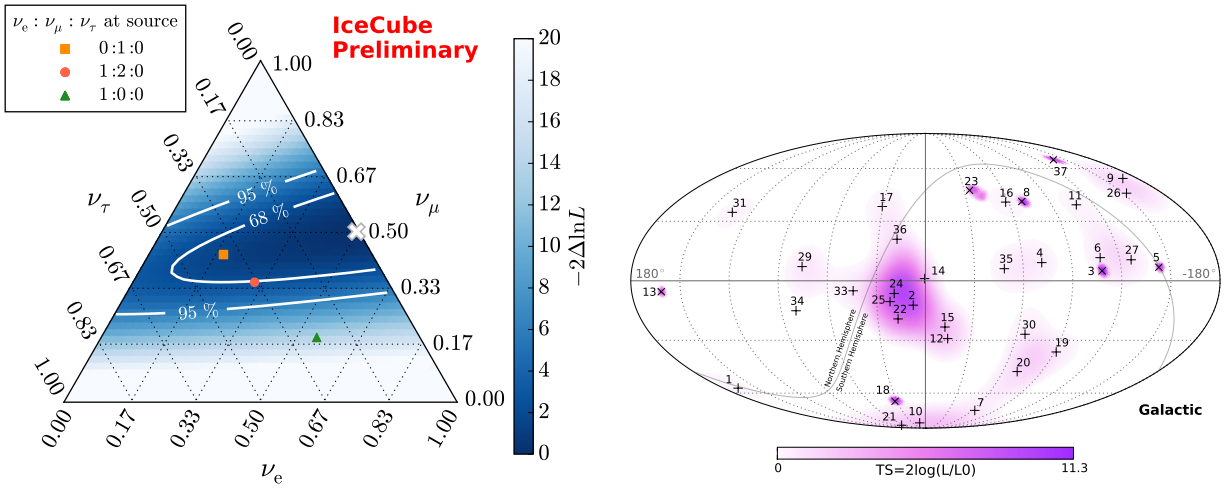

Figure 2.17: (Left) Flavor composition constraints on the astrophysical neutrino flux as measured at Earth by IceCube [71]. The white cross shows the best-fit of the measurement, while the flavor ratios at Earth predicted from three flavor ratios (indicated by the square, circle and triangle) are also shown. (Right) Arrival direction of the astrophysical neutrino candidate events in the 3 year HESE analysis, in Galactic coordinates [69]. The "x" and "+" marks respectively show the track- and cascade-like events. The colors indicate the uncertainty about the position, and thus as well the probability of a point source at this location.

2015 and March 2015, providing $\sim 3.5\sigma$ evidence for neutrino emission from this source.
This strongly suggest that blazars are responsible for at least a part of the acceleration of high-energetic

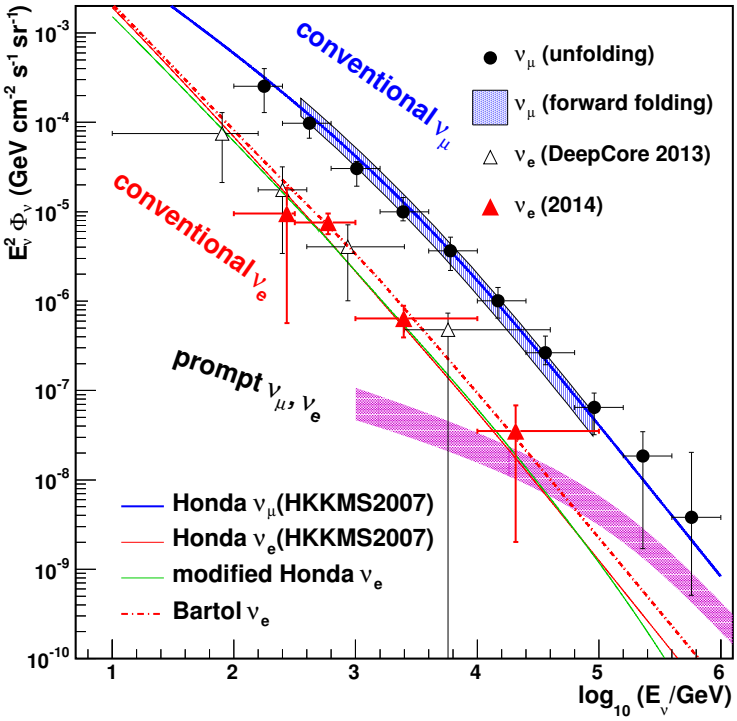

Figure 2.18: Atmospheric electron and muon neutrino fluxes as measured by various IceCube analyses. Also the predictions from the Bartol and Honda models are shown, together with the possible neutrinos from the prompt component. [77].

cosmic rays.

2.4.2 Other analyses

The IceCube Neutrino Observatory could be used as a multi-purpose detector and some of the other analyses are highlighted in this subsection.

Atmospheric neutrino spectrum

One important key to be able to measure the astrophysical neutrino flux is to know the background as detailed as possible. A significant effort in the IceCube collaboration focuses towards the measurement of the neutrino spectrum produced in extensive air showers. These measurements can thus also verify or constrain the models of neutrino production in the atmosphere. Due to their close relation to the production of for example muons in the air showers, these measurements are also a useful input for the study of the hadronic interaction models (section 3.4.4).
Figure 2.18 shows both the atmospheric ν_μ and ν_e spectrum as measured by IceCube, together with the Honda and Bartol model predictions. Also the prediction for the so-called prompt neutrinos, produced from atmospheric mesons that typically contain a charm quark, are shown. Up to now no prompt component has been measured [77]. However, with more data from the following years IceCube might be able to measure or further constrain this prompt component.

Neutrino Oscillations

Atmospheric neutrino oscillations were first discovered by the SuperKamiokande experiment in 1998 [78]. Oscillation measurements from atmospheric neutrinos are mainly sensitive to the disappearance of muon neutrinos, due to the travelled distance from the neutrino production site to the detector and the neutrino

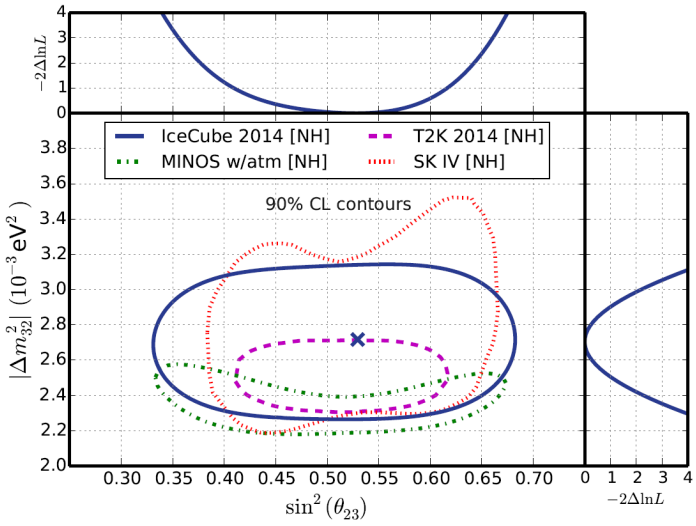

Figure 2.19: IceCube measurements of the neutrino oscillation parameters in the $\sin^2\theta_{23} - |\Delta m^2_{32}|$ plane (90% confidence limits are shown, normal mass hierarchy assumed), in comparison with other measurements [79].

energy. In terms of oscillation parameters this concerns the mixing angle θ_{23} and the squared difference between the mass eigenstates m_2 and m_3 (Δm^2_{23}), i.e. the two heaviest mass eigenstates in the normal mass hierarchy or the heaviest and lightest mass eigenstate in the inverted mass hierarchy.
With the more densely spaced sub-array DeepCore, IceCube is able to measure the ν_μ disappearance from atmospheric ν_μ in the 10 GeV to 100 GeV ν_μ energy region [79]. For this study, the "standard" IceCube array was used as a veto and only upgoing tracks were used, in order to further reduce the contamination from atmospheric muons. The obtained 90 % confidence limit in the $(\sin^2\theta_{23} - |\Delta m^2_{32}|)$ plane is shown in Figure 2.19, together with the results from other experiments. A comparable precision is reached as compared to the dedicated oscillation experiments. The results are also compatible.

Dark matter searches

Dark matter (probably) forms one of the building blocks of our Universe, and is one of the largest open questions in modern physics and astronomy. If these dark matter particles exist, they should not or only very rarely interact with our normal (baryonic) matter. The main candidate for this unknown dark matter is some new kind of elementary particle called a WIMP, or weakly interacting massive particle.
Although their interaction with normal matter is probably very rare, WIMPs could accumulate at places in the Universe where the amount of matter is large. Examples include the center of our Galaxy, dwarf galaxies, or less massive but closer: the center of the Sun and our Earth. This accumulation could then result in self-annihilation of those WIMPs. One of the possible products created in the annihilation reaction could be neutrinos. The neutrinos could then easily escape this dense region.

Since IceCube samples the entire sky, the experiment can look for an excess of neutrinos with energies related to the primary WIMP mass. A non-observation of statistically more neutrinos from those dense regions could thus possibly set a limit on the self-annihilation rate of WIMPs and the nucleon-WIMP cross section, both as function of the WIMP mass. Such study was recently performed for WIMPs in the center of the Earth and Sun [80, 81]. No statistical significant signal is observed in either analysis. The result of the spin-dependent proton-WIMP cross section measurement from the IceCube solar WIMP analysis using 3 years of data is shown in Figure 2.20, where IceCube delivers the best experimental limits above WIMP masses of $\sim$80 GeV. In the spin-independent cross section measurements the Earth WIMP analysis obtains slightly better results

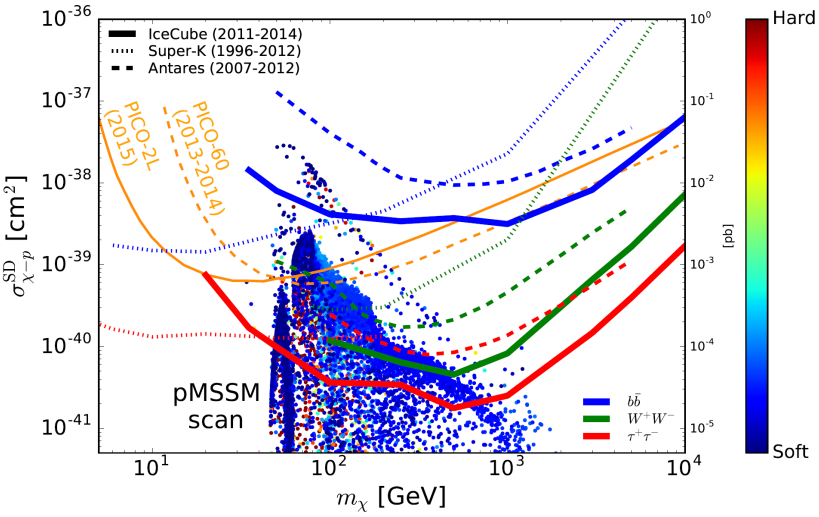

Figure 2.20: Limits on the spin-dependent proton-WIMP cross section $\sigma^{\mathrm{SD}}_{\chi-p}$ derived from the IceCube Sun WIMP analysis, using various decay channels of the WIMP annihilation. The other (thinner) lines show experimental limits from other experiments, while the points show possible WIMP (neutralino) masses from the pMSSM (phenomological minimally super-symmetric model). A 0.3 GeV/cm^3 local dark matter density is assumed. [81]

around 50 GeV, caused by the presence of iron in the core of the Earth. However, significantly better limits for the spin-independent cross section are obtained by specific dark matter experiments.

2.5 IceCube-Gen2

The first years of IceCube data-taking have shown that IceCube is able to perform excellent neutrino physics: astrophysical neutrinos have been discovered, the atmospheric neutrino spectrum has been studied in great detail, dark matter studies have set new limits, etc. However, the small amount of astrophysical neutrinos limits the discovery of their hadronic accelerators, the flavor composition of the astrophysical neutrinos remains unsure and the sensitivity to prompt atmosheric neutrinos is not reached yet. Furthermore, no EeV neutrinos which could be linked to interactions between extragalactic cosmic rays and the microwave background (the ”cosmogenic” neutrinos) are seen yet. Many IceCube data-taking years, beyond IceCube’s lifetime, would be needed to solve these interesting questions in neutrino astronomy.

Therefore, an IceCube extension, called IceCube-Gen2, has been proposed [82]. The deployment and instrumentation of this IceCube-Gen2 detector will use similar technologies as has been used in the IceCube detector and its deployement, and hence will benefit largely from the experience built up during the deployment and running of the IceCube detector. A possible configuration is shown in Figure 2.21. The aim is that this IceCube-Gen2 detector would have an instrumented volume of approximately 10 times the IceCube volume. This could be achieved with only $\sim$120 extra cables with an inter-string spacing of 250-300 m. The doubled inter-string spacing compared to the IceCube detector is possible due to the good optical properties of the ice. This would reduce the sensitivity to $\mathcal{O}$(TeV) neutrinos, but does not affect the measurements of the more energetic astrophysical neutrinos. Furthermore, DOMs could be deployed on the strings 75 m higher and 125 m lower compared to the current DOM placing, since the absorption and scattering lengths of the ice are known to be large, which also increases the geometric area.

Next to an extension of the array, also the deployment of a more densely spaced array in the center of DeepCore is proposed. This would, among other, allow the experiment to set competetive WIMP nucleus spin-dependent cross section limits down to WIMP energies of $\sim$1 GeV.
On the surface an extension of the IceTop array is proposed. The exact detector type and the distribution on

the surface has not been decided yet. This detector array would serve as a veto for the IceCube-Gen2 in-ice array, but the combination of the surface and in-ice Gen2 arrays would be a great tool for cosmic-ray physics as well. The IceCube-Gen2 project would be an important cosmic ray detector in the 10 PeV-EeV region, where the composition of cosmic rays is unclear (part 3.4.3).
Up to now, no decision has been made concerning funding for the IceCube-Gen2 detector. In the current timeline an IceCube Upgrade is planned to be installed in 2022-2023. This upgrade will consist of the deployment of 7 new strings, with about 700 optical modules, in the center of the existing IceTop array. Additionally, also a scintillator and possible radio array is planned to be added on the surface. In December 2017, first prototypes of the scintillators were installed at South Pole [83].

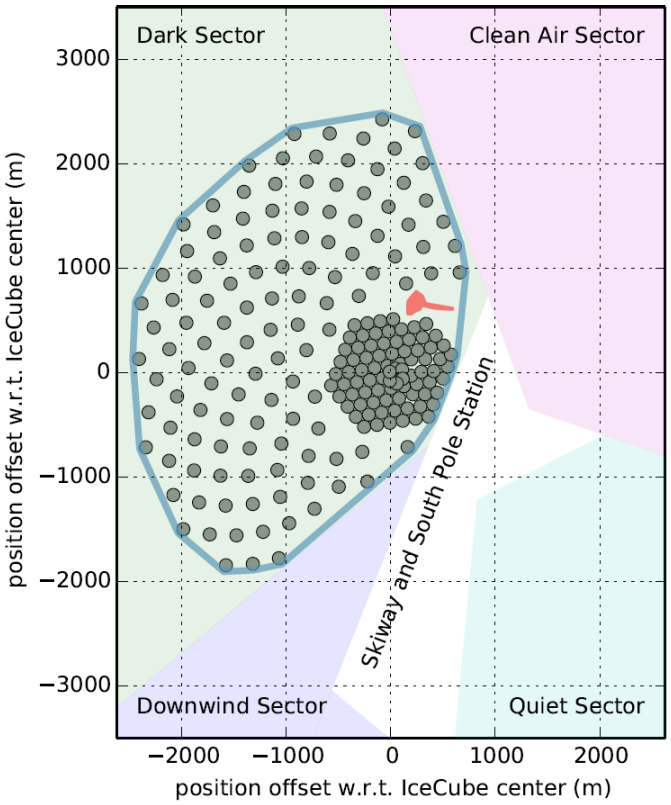

Figure 2.21: Possible configuration of the IceCube-Gen2 detector around the current IceCube detector. This design has a 300 m interstring spacement, but it is far from a final configuration. The grey circles show the string positions, while also the various areas at South Pole are indicated. [82]

3

Extensive air showers

A mighty flame followeth a tiny spark.

The Divine Comedy - Dante Alighieri

Measurement techniques highly improved in the decades after the discovery of cosmic rays. In the 1930's, this resulted in the first coincident measurement of particles by detectors separated in distance (section 1.2.1). Pierre Auger reported on the observation of "Extensive Air Showers" (EAS): giant cascades of secondary particles produced by one primary CR nucleus, which has an energy of at least 10^6 GeV.

The abundance of cosmic rays up to an energy of $10^4 - 10^5$ GeV is sufficient to be analyzed with limited-size balloon or satellite experiments, while the flux of the high energetic cosmic rays (10^{15} eV) is too low for these measurement techniques (section 1.1.1). Large detection areas are required, which have to be built at the surface of the Earth. This however introduces the difficulty that the cosmic rays are not detected directly, but in an indirect manner. Indeed, the interaction length of nuclei with these high energies is smaller than 100 g/cm^2, while the total matter that has to be crossed in the atmosphere before it can be detected is at least 600 g/cm^2 (at a 4 km height) to 1000 g/cm^2 (at sea level). Primary cosmic rays will thus not travel through the entire atmosphere, but first strike an atmospheric nucleus. This happens mostly at heights of tens of kilometers. In such extremely energetic collisions many (secondary) particles are produced. On their turn, these secondary particles interact or decay in the atmosphere and as such a cascade of particles is produced: the extensive air shower. If the primary cosmic ray has sufficient energy, eventually a bunch of secondary particles arrives at the Earth's surface. The number of secondary particles which reach the surface of the Earth could be millions or even more.
These secondary particles from high energy CR constitute a source of natural radiation that we are continuously exposed to, which is about 30 % of the total natural background radiation that we receive. The atmospheric protection to cosmic radiation is a blessing for us and all living organisms on our planet.

The experiments at the surface of the Earth thus observe the secondary products created by the cosmic rays in the atmosphere. From these measurements, the experiments try to reconstruct the cosmic ray energy spectrum and the contribution of each mass group to the spectrum (section 1.3.4). As will be shown, this is not an easy process where many uncertainties are introduced. For example, large shower-to-shower fluctuations arise, the collisions occur at energies that we can not reach in man-made accelerators, etc.
In this chapter the extensive air shower physics are discussed in depth. Section 3.1 describes the medium in which the EAS propagates: the atmosphere of the Earth. The development of the EAS in the atmosphere is discussed in Section 3.2, while in Section 3.3 some particle distributions at one atmospheric depth are described. The most important measurement techniques and some recent experiments and their results are discussed in Section 3.4.

3.1 The atmosphere

Since the EAS develops in the atmosphere, it is important to know the properties of the atmosphere. It is common to divide the atmosphere into separate layers based on the temperature profile. However, the division into separate layers is of less importance for air showers, since particles do not feel the temperature. Instead, their propagation is sensitive to the amount of matter that they encounter, thus the density and integrated density or pressure. Temperature (T) and pressure (P) in the atmosphere can easily be measured. The other important quantity, density, can be deduced from these two variables using the approximation that the atmosphere behaves as an ideal gas:

$$\rho = \frac{P \cdot M_{air}}{R \cdot T} \tag{3.1}$$

where R is the universal gas constant and M_{air} the mean molecular weight of air. The main constituents of the atmosphere are nitrogen (78 %) and oxygen (21 %) [84]. The composition of the atmosphere is stable up to heights of 80-90 km [85]. Since nitrogen has a mean molar mass of 28.0137 g/mol and oxygen of 31.9988 g/mol [86], M_{air} is $\sim$28.97 g/mol.

The integrated density above a certain height h gives the total amount of matter crossed for a particle travelling vertically through the atmosphere. This measure is also called the mass overburden, thickness or atmospheric depth X_v:

$$X_v(h) = \int_h^{H_0} \rho(h')dh' \tag{3.2}$$

where H_0 is the height at which the density is approximately 0, thus the top of the atmosphere. The pressure of the atmosphere is this mass overburden multiplied with the gravitational constant ($P = X_v \cdot g$), where $g \approx 9.83$ m/s^2 at the geographic poles of the Earth. Together with the ideal gas law (Eq. 3.1), this gives:

$$\frac{dX_v(h)}{X_v(h)} = -\frac{g \cdot M_{air}(h)}{R \cdot T(h)}dh \ . \tag{3.3}$$

Now we use the fact that M_{air} is constant in the lowest 80-90 km and, as first approximation, we also assume a constant temperature. Therefore, the atmospheric depth as function of the height is given by:

$$X_v(h) = X_0 \exp\left(-h_0/h\right) \quad \text{with } h_0 = \frac{R \cdot T}{M_{air} \cdot g} \ \text{ the scale height.} \tag{3.4}$$

In an isothermal atmosphere, the atmospheric depth thus decreases exponentially with height. As a consequence also the density profile decreases exponentially. Although this isothermal atmosphere is only a rough approximation, it describes the atmosphere well and deviations are small. This exponential behaviour can be seen in Figure 3.1 where a real atmospheric profile at South Pole is shown up to a height of 50 km. If one looks into more detail, the deviations from this exponential profile would become visible.

If the cosmic ray enters the atmosphere at a certain angle θ with respect to the zenith, it needs to travel further before reaching the surface of the Earth. Hence, the amount of matter it will encounter on its path also increases. If we assume that the Earth is flat, which is satisfactory for $\theta < 65°$, the amount of matter encountered by the CR, or 'slant depth' X, can be related to the atmospheric depth by:

$$X = \frac{X_v}{\cos\theta} \tag{3.5}$$

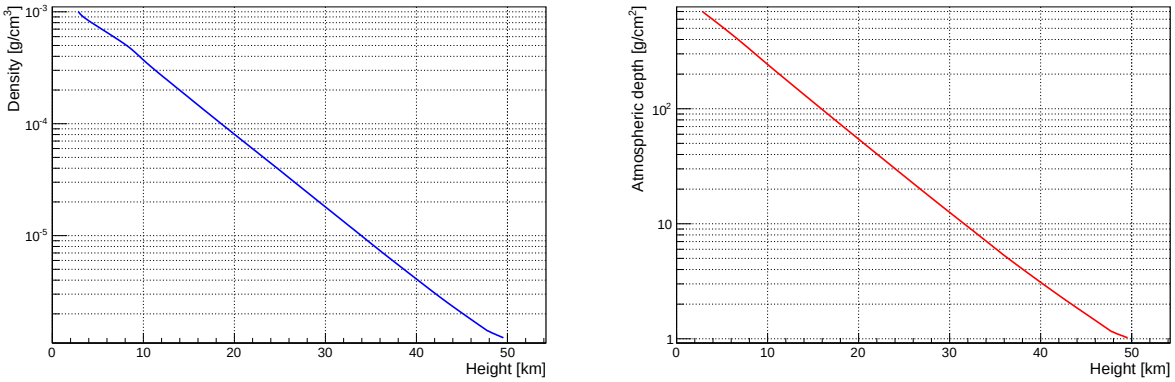

Figure 3.1: Example atmospheric profile showing the density (left) and atmospheric depth (right) as function of the altitude (up to 50 km). This particular atmosphere is the average atmosphere at South Pole during February 2011. The data is obtained from balloon flights from [87] and satellite data from [88], merged by Takao Kuwabara.

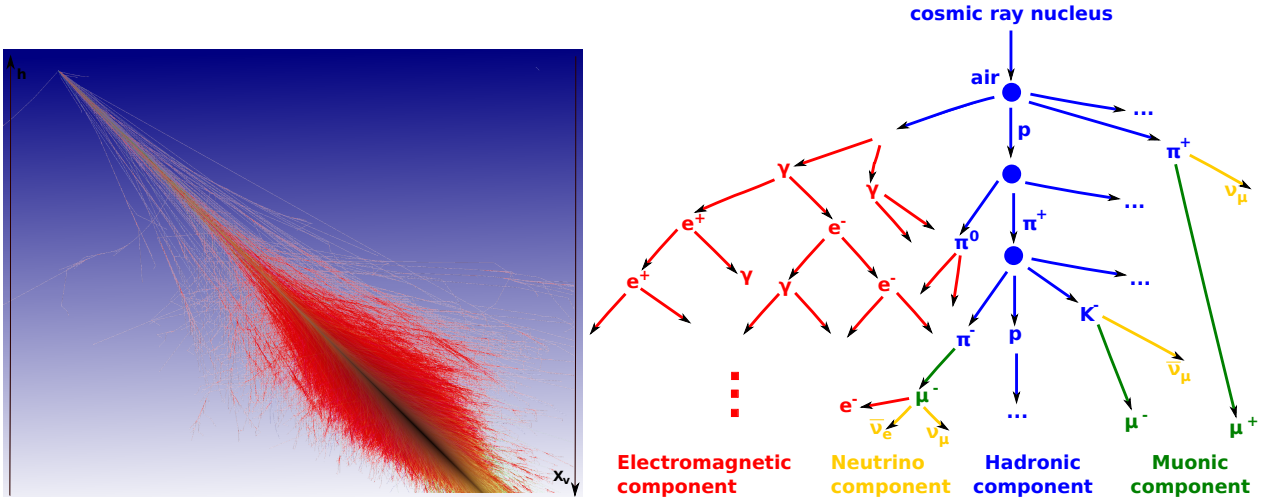

Figure 3.2: Left: A simulated air shower, initiated by a proton primary with an energy of 1 PeV and a zenith angle of $45°$ [89]. Electromagnetic particles are shown in red, muons in green and hadrons in blue. Right: Sketch of the development of an EAS and its splitting into various components.

3.2 Air shower development

When a cosmic ray ion enters our atmosphere, it eventually collides with either a nitrogen or an oxygen nucleus in the air. This collision is extremely energetic and many particles are created. Those will in their turn have a certain chance to interact with an air atom and create even more particles. This process continues for many iterations and a cascade of thousands to millions or even billions of particles is created. This particle cascade travels towards the surface of the Earth. Some of the secondary particles are absorbed in the atmosphere, while others reach the ground and possibly create signals in detectors. The left illustration in Figure 3.2 shows the development of a proton initiated EAS with an energy of 1 PeV and zenith angle of $45°$ in the atmosphere. On the right a very rough sketch of the first interactions in the cascade is shown. This is only the start of the cascade and many more interactions will follow, creating a huge amount of electromagnetic (EM) particles (gamma's, electrons and positrons), together with a smaller number of muons (μ). Also neutrinos (ν) and a small hadronic core of the shower are among the components of an EAS.

The entire process of the air shower development in the atmosphere could be described by a set of coupled transport equations for all the different particle types in the shower. These equations could be derived from the same equation as used for the propagation of cosmic rays in the Galaxy (Eq. 1.30). The evolution of the

flux N_i of particles of type i within a certain energy interval $E_i + dE$ as function of the slant depth can be written as:

$$\frac{dN_i(E_i, X)}{dX} = \sum_j \left(\int_E^\infty \frac{F_{ji}(E_i, E_j)}{E_i} \frac{N_j(E_j)}{\lambda_j} dE_j \right) - \frac{N_i(E_i, X)}{d_i} - \frac{N_i(E_i, X)}{\lambda_i} \tag{3.6}$$

The first term describes the creation of particles with type i, from decay or collisions between a particle j and an air nucleus (integrated over all particle types and energies). The created particle yield per energy E_i from one particle j is given by $F_{i,j}$, while N_j and λ_i respectively indicate the number of particles with type j and energy E_j and their interaction or decay length λ_j. The last two terms describe the particle loss due to interaction (with length λ_i) and decay (with length d_i), both expressed in g/cm^2.
Hence, there is a constant competition between decay and re-interaction of the secondary particles during the propagation. Relativistically the decay length is related to the particle livetime (τ_i) by:

$$d_i = \rho \gamma c \tau_i \tag{3.7}$$

The interaction length or mean free path on the other hand is linked to the nucleus-air cross section σ_i^{air} by:

$$\lambda_i = l_i \rho = \frac{\rho}{n_A \sigma_i^{air}} = \frac{A m_p}{\sigma_i^{air}} \tag{3.8}$$

with l_i the interaction length in cm, n_A is the local number density of air nuclei with average mass A and m_p the mass of the proton. It is important to note that the interaction length in g/cm^2 does not depend on density, while the decay length does. Hence, the ratio between decay and interaction will change throughout the atmosphere.
These transport equations are adequate to describe the EAS in great detail, but they would lead us too far here. The basic but important features of air showers can be illustrated by a few simple approximations, discussed in this section. We start to describe the first interaction, followed by an electromagnetic shower approximation and a generalization to hadronic showers. The resulting particle distributions at a certain observation level are discussed in the following section. In practice, simulations of air showers are used to relate the observed properties to primary particle characteristics. Simulations are further discussed in Chapter 4.

3.2.1 First interaction

The cross section of the nucleus - air collision determines the (slant) depth at which a cosmic ray nucleus will -most probably- interact. For low energies the cross section of these collisions is measured, but for high CR energies this is an unknown factor. They also cannot be calculated within QCD yet, but some approximations could be made using Regge theory or minijet approximation. For center-of-mass energies E_{cm} up to ∼40 GeV, the cross section seems to rise according to $\ln(E_{cm}^2)$. For higher energies the rise of the cross section is approximately related to $\ln^2(E_{cm}^2)$ [3]. In each case, the higher the energy of the shower, the higher the cross section and the earlier it will interact.
This rise in the proton-air cross section is seen in Figure 3.3. The lines represent the values obtained and used in the various codes that model the hadronic interactions in air shower physics. These models all start from a different approximation and therefore different values are obtained. This cross section at high energy could also be measured by air shower experiments, as shown by the black circle in Figure 3.3. Since these analyses need to rely on simulations of and assumptions on the further shower development, they do have large systematic error bars. One could also use these measurements to obtain the proton-proton cross section at this high energy. This obviously extends this cross section measurement to higher energies than reached at accelerators and could possibly restrict the extrapolations performed in models.

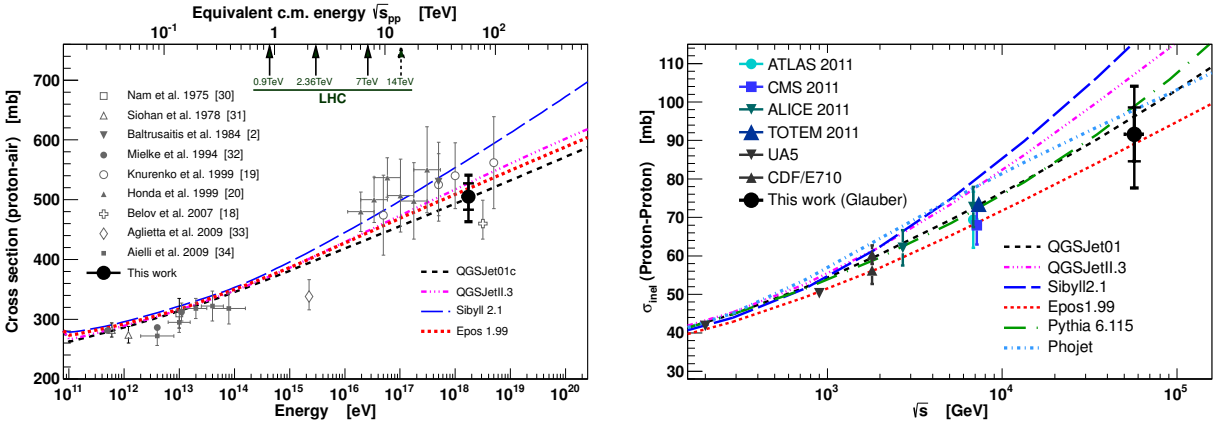

Figure 3.3: Left: The measured proton-air cross section from the Auger experiment (labelled this work) together with other air shower experiments. The cross sections in the hadronic interaction models are shown as the lines. Right: this proton-air cross section converted to an inelastic proton-proton cross section as function of E_{cm} using Glauber theory, where the accelerator data are included. [90]

When the mass of the primary particle rises, so does the cross section of the first interaction. This is quite logical considering the increased nuclear radius. In [91] the nucleus-nucleus cross section is given as:

$$\sigma_{A_1 A_2} = \pi R_0^2 \left(A_1^{1/3} + A_2^{1/3} - \delta \right)^2 \tag{3.9}$$

with $\delta = 1.12$, $R_0 = 1.47 \cdot 10^{-15}$ m and A_1 and A_2 the mass numbers of the two nuclei (the radius R_A of a nucleus scales with $A^{1/3}$). From this it can be deduced that the iron-air cross section is about a factor of 5 higher compared to the proton-air cross section.
The relation between cross section and interaction length is given by Eq. 3.8. If we approximate the proton-air cross section at a lab frame energy of 1 PeV as 400 mb, an interaction length of ~ 60 g/cm^2 is obtained. The mean free path of iron showers of 1 PeV is therefore close to $\sim 10 - 12$ g/cm^2. This means that most proton initiated showers of 1 PeV interact at heights around 20 km above sea level, while this is around 30 km for iron showers (Figure 3.1). Due to the exponential behaviour of the atmospheric density profile, a large tail is present to high altitudes. The extension to lower altitudes is limited: almost all cosmic rays of these energies interact at heights above 15 km.

The actual interaction between two nuclei, for example between a proton and an oxygen nucleus, at these high energies is a complicated process and the knowledge is incomplete. It is not clear how many nucleons are involved in the collision, how much energy is transferred to the secondary particles and how many of these secondary particles are created. In particular the very forward region of the collision, important for air showers, is not covered in the experiments that study the highest human-controlled particle interactions. Therefore data from fixed-target experiments are important to take into account, since they do measure the forward region. However, since these experiments work at even lower energies compared to the main experiments at the Large Hadron Collider, one needs to extrapolate the energy region even further. Rare emulsion measurements during balloon experiments can also provide extra information. Summarized, large uncertainties exist.
It seems that in the fragmentation process of each hadronic interaction generally only a few nucleons are involved, both from the target nucleus and from the projectile. The inelasticity of the collision determines the energy remaining in the leading nucleus, which probably keeps more than 50 % of the initial energy. The number of secondary particles produced in each collision increases with energy, probably reaching $\mathcal{O}(10)$ at an energy of 10^6 GeV. Most of these secondary particles are pions, together with a smaller amount of kaons, charmed particles, nucleons and antinucleons [3, 92]. In the pion component, approximately an equal fraction of π^+, π^- and π^0's are produced.

As shown in Figure 3.2, the charged pions mainly feed the muonic component of the air shower, while neutral pions decay almost immediately to two γ particles, resulting in the EM component of the air shower. The leading particle will continue in the hadronic component of the air shower, which will eventually die out.

3.2.2 Electromagnetic shower approximation

From the above considerations it is clear that the air shower development in the atmosphere is a complicated process. However, with some simplifications the main properties of EAS can be easily deduced. In this section the development of an electromagnetic shower is discussed. The simple Heitler model [93] describes an air shower initiated by an electromagnetic particle: a photon, electron or positron. This allows to deduce the main properties of an electromagnetic shower. The electromagnetic component of a hadronic shower is continuously fed by the hadronic component (and to a lesser extent by the muonic) during various stages of the propagation through the atmosphere. With the consideration that a hadronic shower is a composite of many EM subshowers, together with the hadronic and muonic component, the Heitler model can then be extended to hadronic showers in the following section.

In the Heitler model it is assumed that an EM particle with energy E_0 entering the atmosphere will split into two particles after a certain interaction or splitting length λ_{em} ($\sim$36.7 g/cm^2). Photons produce an e^+e^- pair, while positrons and electrons radiate a photon due to Bremsstrahlung. Both processes are illustrated in Figure 3.2. In this model the radiation length of electrons in air is assumed to be similar to the photon mean free path. Since in reality the photon mean free path in air is 7/9 of the electron radiation length ([94]), this is roughly valid.
Each of the two produced particles obtain half of the energy of the initial particle. After another splitting length, these particles in their turn produce two particles each. This process continues and after n interaction lengths the particle bundle will thus contain $N = 2^n$ particles. Or, since $n = X/\lambda_{em}$ with X the slant depth, $N(X) = 2^{X/\lambda_{em}}$. The particle multiplication slowly stops when the electron or positron energy loss via radiation becomes comparable to the ionisation energy loss. At this critical energy E_c (~ 85 MeV), the EM particles do not produce more particles and get absorbed into the atmosphere. In the Heitler model the energy is equally spread between all particles, and thus the maximal number of particles N in the shower is E_0/E_c. Hence, at a certain slant depth the number of particles is maximal (X_{max}), after which it starts to decrease (Figure 3.4).

The maximal number of particles is thus reached at a slant depth:

$$X_{max} = \frac{\lambda_{em}}{\ln 2} \ln\left(\frac{E_0}{E_c}\right) \tag{3.10}$$

Although this is only a very simple model, it does show some important properties of air showers: the number of particles in an air shower scales linearly with primary energy, and the corresponding depth at which this maximal particle number is reached scales with $\ln(E_0)$.

One of the shortcomings of this simple model concerns the prediction of the e^+, e^- number compared to the amount of photons. The Heitler model results in an equal amount of these EM particles, while in reality the photon number is about 10 times larger compared to the electrons and positrons. Some important processes like the radiation of multiple photons in Bremsstrahlung processes and e^+, e^- absorbation in air are not taken into account in the Heitler model.

3.2.3 Hadronic showers

The Heitler model for electromagnetic EAS was generalized to a simple model for hadron initiated showers by J. Matthews [96]. Consider a proton which collides with an air atom after a certain interaction length

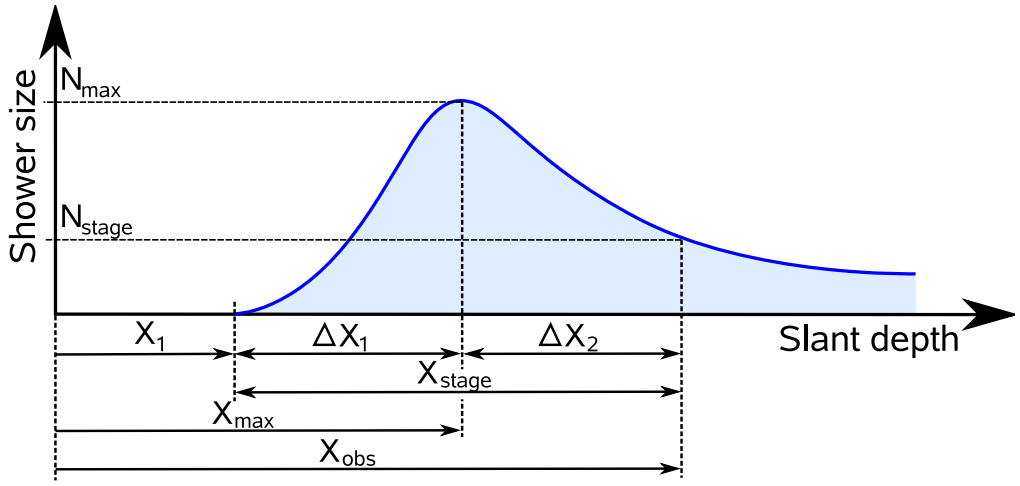

Figure 3.4: Schematic behaviour of the number of particles in an EAS along its path. X_1 is the slant depth of the first interaction, X_{max} the slant depth at which the particle number is maximal, X_{obs} the slant depth at detection and X_{stage} the according stage of the shower development (in g/cm^2) at detection depth. [95]

(section 3.2.1). In this Heitler-Matthews model all the secondary particles produced at this hadronic interaction (N_{sec}) are pions. The ratio between $\pi^+ : \pi^- : \pi^0$ is 1:1:1. The neutral pions feed the electromagnetic component since they decay, almost immediately, to two photons. The charged pions could interact again after a certain interaction length. In the interactions they again produce the same ratio of charged and neutral pions. Hence, after n interaction lengths the total energy remaining in the hadronic part of the shower E_{had} is $\left(\frac{2}{3}\right)^n E_0$, while the energy transferred to the EM component is $E_0 \left(1 - \left(\frac{2}{3}\right)^n\right)$. After many iterations a high fraction of the initial energy is transferred to the electromagnetic component, which eventually dissipates into the atmosphere by ionisation.
In the Heitler-Matthews model this process continues until the energy of the charged pions falls below a certain threshold E_{dec}, where they all decay to muons. The energy threshold, and thus also the number of created muons, depends on the ratio of decay length (Eq. 3.7) and interaction length (Eq. 3.8) of the charged pions. The muon multiplicity is thus defined at the number of interaction lengths where the pion energy equals the decay energy: $N_\mu = N_\pi = (N_{ch})^n$. Here, N_{ch} is the number of charged secondary particles produced in each interaction ($N_{ch} = \frac{2}{3} N_{sec}$). Since the primary energy is equally distributed over all particles, the pion energy (E_π) is given by:

$$E_\pi = E_{dec} = \frac{E_0}{(N_{sec})^n} = \frac{E_0}{\left(\frac{3}{2} N_{ch}\right)^n} \tag{3.11}$$

The elimination of the number of interaction lengths in these equations gives the number of muons in the shower:

$$\begin{aligned} \ln N_\mu = n \cdot \ln(N_{ch}) = \frac{\ln\left(\frac{E_0}{E_{dec}}\right)}{\ln\left(\frac{3}{2} N_{ch}\right)} \cdot \ln(N_{ch}) = \beta \ln\left(\frac{E_0}{E_{dec}}\right) \\ \rightarrow N_\mu = \left(\frac{E_0}{E_{dec}}\right)^\beta \quad \text{with } \beta = \frac{\ln N_{ch}}{\ln \frac{3}{2} N_{ch}} \end{aligned} \tag{3.12}$$

In this simple model the final number of muons is determined by the air density, primary energy, and secondary particle multiplicity created in the hadronic interactions. If the number of charged secondaries $\sim$ 10 a value of $\sim$0.85 is obtained for β. A small but existing dependence on the number of charged secondaries is expected. The uncertainty of β ranges from 0.75 to 0.95. As will be shown in section 3.4, the uncertainty in the final muon number is currently an important topic for indirect measurements.
The fact that the average muon multiplicity grows slower than the primary energy ($\beta < 1$) can be understood by the approximation that the number of charged mesons grows linearly with primary energy, but as the

energy increases they are -on average- produced further down in the atmosphere. There the density is higher and hence the chance of interaction of the mesons increases, reducing the decay rate to muons.
Since muons travel almost at the speed of light and the muon lifetime is $\sim 2.2\ \mu s$, their decay length will be at least several kilometers, and most of them are able to reach the surface of the Earth. Also their energy loss is small compared to EM particles, which means that their energy at detection will be close to the energy that they received from their parent particle and almost all will have an energy higher than the detection threshold.

In hadronic showers the depth of shower maximum is mainly determined by the evolution of the first EM subshowers. These subshowers posses the most energy and thus will dominate the particle number distributions. In the Heitler-Matthews model the depth of shower maximum for hadronic showers is given by:

$$X_{max}^{hadr}(E_0) \approx \lambda_{hadr} + X_{max}^{EM}\left(\frac{E_0}{2N_{sec}}\right) = \lambda_{hadr} + \frac{\lambda_{em}}{\ln 2}\ln\left(\frac{E_0}{2N_{sec}E_c}\right) \tag{3.13}$$

The EM cascades start after a hadronic interaction length λ_{hadr} of the primary nucleus in air, since the created neutral pions decay immediately. The energy within each of these subshowers is $\frac{E_0}{2N_{sec}}$. The factor 1/2 accounts for the splitting of the neutral pions in 2 photons.
This shows that also for hadronic showers X_{max} increases linearly with $\ln(E_0)$. If the secondary particle multilpicity and the hadronic interaction length would be constant as function of energy, the X_{max} increase per decade in energy equals the one in the EM case: $\frac{\lambda_{em}}{\ln 2}\ln 10 \approx 120$ g/cm^2. As described in section 3.2.1, the first interaction length decreases with energy and the secondary particle multiplicity increases. This makes that the X_{max} increase per energy decade, also called elongation rate, is closer to 58 g/cm^2.

These simple approximations neglect some important features of hadronic showers. For example, in reality about 10 % of the secondary particles are estimated to be (the heavier) kaons instead of pions, rare particles like D-mesons are created, and finally also the hadronic core keeps a significant fraction of the primary energy. Nevertheless this Heitler-Matthews model provides an idea of the development and basic properties of hadronic showers.

Longitudinal profile

The number of particles of the main components of the EAS as function of the slant depth, or the longitudinal profile, is shown in Figure 3.5, for an average 1 PeV proton shower. This is obtained from simulations down to an atmospheric depth of 692 g/cm^2 (the average atmospheric depth for the IceTop detector).
The total longitudinal profile of a hadronic shower is usually described using the Gaisser-Hillas function [97]:

$$N_{tot}(X) = N_{max}\left(\frac{X - X_1}{X_{max} - X_1}\right)^{\frac{X_{max}-X_1}{\lambda}} \exp\left(\frac{X_{max} - X}{\lambda}\right) \tag{3.14}$$

where X_{max} and N_{max} are the most important parameters in the fit, respectively the depth of shower maximum and the total number of particles at this depth; λ is the average interaction length ($\lambda \sim 55 - 65$ g/cm^2) and X_1 could be used as point of first interaction (if $X_1 > 1$ is forced).
The stage or depth at which an air shower is observed or sampled can also be described in terms of its "age". A "young" shower is still developping and contains energetic particles. Both the muonic and electromagnetic component are growing. The particles are still located close to the hadronic core. As the shower gets "older", it reaches its shower maximum. At X_{max} the ratio between EM and muonic particles is maximal. The EM component then starts to decrease and the muons become more and more important to eventually dominate. Particles are also more spread out and the shower front is more extended and thicker. The "shower age" is thus an important parameter concerning the particle content and according properties.
Multiple definitions of shower age exist. In this work we will use:

$$s = \frac{X_{obs} - X_{max} - X_1}{\lambda_{em}\cos\theta} \tag{3.15}$$

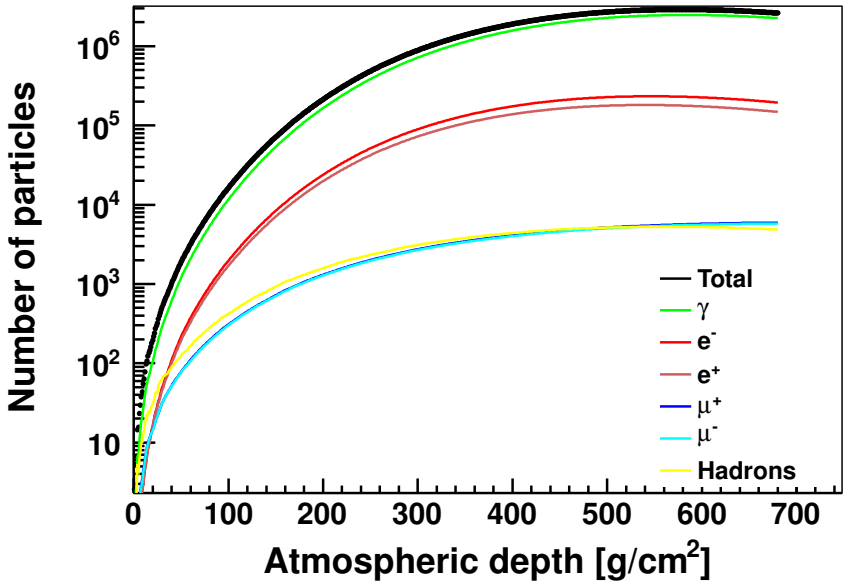

Figure 3.5: Longitudinal evolution of the particle number for various secondary particle types. Here shown is an average of 100 1 PeV vertical proton showers simulated down to an IceTop altitude using an Antarctic winter atmosphere. Simulations are further discussed in chapter 4.

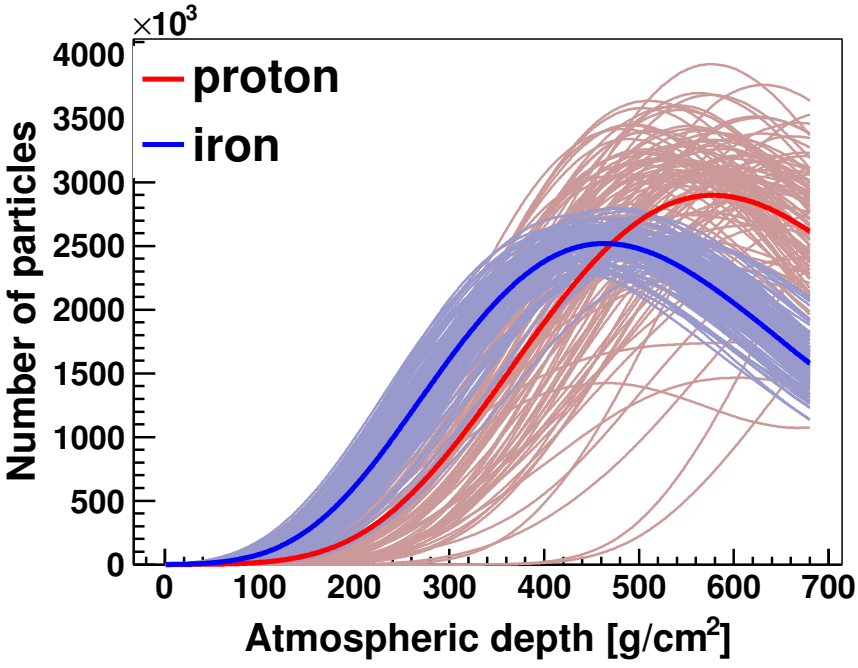

Figure 3.6: Total particle number comparison between 100 1 PeV vertical proton and iron showers. The bright curves show the average particle number. Individual showers are shown by the dim curves, which provide an illustration of the shower-to-shower fluctuations. Simulation specifications are the same as for Figure 3.5.

Both X_{max} and X_1 are expressed in slant depth, while X_{obs} is the atmospheric depth at which the air shower is detected (illustrated in Figure 3.4). Young showers will have a negative shower age, while older showers have a positive shower age. Around X_{max}, the age of the shower will be close to 0 or slightly less.

Higher mass nuclei

The differences in shower observables between primaries of various mass is of great importance to be able to reconstruct the cosmic ray composition.
As described in section 3.2.1, a shower initiated by higher mass nuclei will -on average- have a first interaction higher up in the atmosphere. For the further development one can use the *superposition model* to obtain a rough idea of the differences. In this model a nucleus with mass A and energy E_0 is treated as A independent nucleons, each with energy E_0/A. This is roughly justified since the binding energy between nucleons is $\sim$5 MeV, while the typical energies of the first collisions are significantly higher. Using this, the number of muons becomes (Eq. 3.12):

$$N_\mu^A = A\left(\frac{E_0/A}{E_{dec}}\right)^\beta = A^{1-\beta}\left(\frac{E_0}{E_{dec}}\right)^\beta \ . \tag{3.16}$$

Thus an EAS initiated by a nucleus with a higher mass contains more muons. For example, if $\beta = 0.85$ an iron induced air shower would contain $(56)^{0.15} \approx 1.8$ more muons compared to a proton shower of the same energy.
For the depth of shower maximum (Eq. 3.13) we get:

$$X_{max}^A = X_{max}^p - \frac{\lambda_{em}}{\ln 2}\ln A \ . \tag{3.17}$$

This results in a shower maximum which is $150 - 200$ g/cm^2 higher up in the atmosphere for iron showers compared to proton induced showers, independent of energy. This is only a rough approximation based on the superposition principle. Detailed simulations that take all effects into account show that this difference is closer to 80-100 g/cm^2 and that it decreases with energy.
Hence, the Heitler-Matthews splitting model predicts a clear primary mass dependence of the depth of shower maximum and the muon number. This muon number is anti-correlated with the number of EM particles in the shower, thus heavier showers will on average have less EM particles. Figure 3.6 shows the longitudinal profile compared between proton (red) and iron (blue) initiated showers. As an example vertical showers with a primary energy of 1 PeV are shown. The bright curves show the average profile, while dim curves illustrate individual showers. The deeper X_{max} of proton showers is clearly visible.

Fluctuations

As discussed before, the depth of the first interaction is subject to a large variation since it is a probabilistic process. The cross section defines the atmospheric depth at which 1/e of the primary nuclei interact, but large deviations exist. Also the secondary particle multiplicity, further interactions and thus entire development of the shower are stochastic processes. As a result, each shower will be different and large shower-to-shower fluctuations can occur (Figure 3.6). Typically fluctuations in shower size are proportional to the number of particles at that particular depth, the particle multiplicity is log-normal distributed. Hence, the smallest shower uncertainties are obtained when a shower is detected near the shower maximum. Figure 3.6 also shows that the fluctuations within proton showers are larger compared to the variation within iron showers. This is easily explained within the superposition model, since showers with mass A are a composite of A individual showers.

Due to these fluctuations one is not able to reconstruct the primary mass of one single shower with 100 % confidence, but one needs a large set of air showers in order to obtain reliable results. The shower-to-shower variations are thus causing a significant limitation on the sensitivity of indirect air shower experiments. On the other hand, the fact that the fluctuations depend on the mass can also be used as useful input to composition reconstruction.

3.3 Observation level distributions

The primary detection method for air showers was, and still is, an array of detectors spread over a large area at the surface of the Earth. These sample the EAS at a specific atmospheric depth or observation level. In this section the relations between the distributions at this depth and the specifications of the primary particle are investigated. The total electromagnetic and muonic particle number, the muon energy spectrum, the electromagnetic and muonic lateral distribution of particles and the curvature of the shower front are discussed in detail. These constitute important knowledge when one wants to infer the energy, mass or direction of the primary cosmic ray from the ground level observations.

3.3.1 Particle number

The simplest information that one can get from the air showers is the number of particles in the detector. In combination with the energy of the particles, this determines the total signal observed. In the previous section it was shown that the electromagnetic particle number is linearly correlated with the primary energy, especially at the depth of shower maximum X_{max}. This statement is roughly valid throughout the entire shower development. However, as described before, the EM particle number decreases at depths larger than X_{max}, while the number of muons remains rather stable. Eventually, showers might only consist of muons.

Figure 3.7 shows the electron and muon number extracted at sea level for proton, iron and gamma initiated showers of various energies. Both the increase of the EM and muon particle number with the primary energy are observed. For all of these energies and different primaries, X_{max} is still above sea level. Hence, the electron number already decreased compared to the electron number at X_{max}.
With increasing mass of the primary particle also the muon to electron number ratio increases. This was explained in the previous section. Gamma showers clearly possess less than 10 times as many muons compared to the hadron initiated showers. If experiments have the power to measure both the number of EM particles and the number of muons, they possess sensitivity to the energy and the mass of the primary particle. The separation between proton and iron of the muon/EM ratio decreases with energy, which makes the mass reconstruction (using this information) harder at these high energies.
The curves indicate the one-sigma region caused by shower-to-shower fluctuations. As described above, the shower-to-shower fluctuations are larger for lighter primary particles. It also shows that these fluctuations decrease with energy, as expected due to the increasing particle number. The colours indicate results obtained with various models for the hadronic interactions, which are further discussed in section 3.4.4 and Chapter 4. It should be noted that real detectors do not measure all the particles, but sample the particle distribution at certain positions. Furthermore, the energy threshold of the detectors will clearly influence the measured total particle number.

3.3.2 Muon energy spectrum

The number of muons in air showers is of great importance for the deduction of the mass of the primary cosmic ray. The overall muon number at sea level for primaries of various energy and type was shown in Figure 3.7. In the Heitler-Matthews model (section 3.2.3) the muons are only created once the pion decay length exceeds the interaction length. Thus all muons are created at a single interaction level and have the same energy. This is one of the main shortcomings of this simple model.

In reality, all charged mesons, created at each interaction, have a certain chance to decay to muons. Their re-interaction versus decay probability then depends on the local density of the atmosphere, as discussed in Section 3.2. So muons are even produced from mesons created in the earliest interactions and will thus have a very high energy. Since the energy loss of these muons is small and their decay length exceeds the length to the surface of the Earth, almost all of them will reach the detector level. Hence, this gives rise to a spectrum of muon energies. In the first interactions only a few very energetic muons are produced. As the

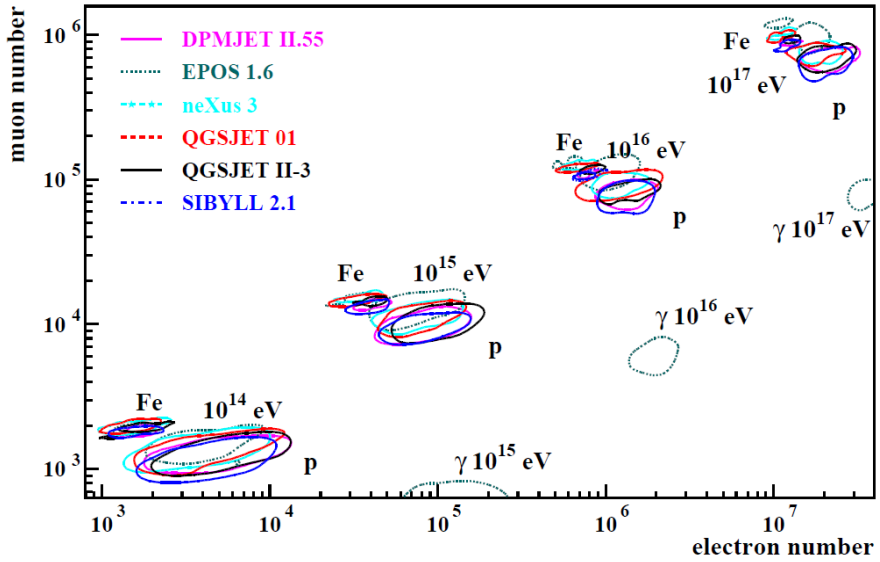

Figure 3.7: Correlation between number of muons and electrons (above a certain cut-off energy) of vertical proton, iron and gamma showers observed at sea level. The curves encircle the one sigma region of the shower fluctuations. They are obtained from shower simulations using CORSIKA ([98]) with various pre-LHC hadronic interaction models. [99]

shower develops, more and more muons are produced with lower and lower energies. This process stops if the meson (or hadron) multiplicity becomes so low that new particle production ceases. On top, these low-energy mesons are produced close to the surface of the Earth where the high atmospheric density causes a significant chance that these low-energy muons re-interact. The produced low-energy muons can furthermore decay to electrons (and neutrinos) or lose all of their energy and be absorbed in the atmosphere. At low muon energies this creates a decrease of the muon multiplicity with decreasing muon energy. This is shown in Figure 3.8, which illustrates the energy spectrum of muons for proton and iron showers of ~ 1 PeV and ~ 100 PeV. The muon spectra are extracted at an atmospheric depth of ~ 700 g/cm^2 and the showers have zenith angles (θ) with $0.8 < \cos\theta < 1$. The bottom plot shows the ratio of the number of muons in iron showers compared to proton showers. This ratio gradually increases as function of the muon energy, up to a certain energy where it starts to decrease and even drops below one. This can easily be explained using the superposition principle (section 3.2.3). Indeed, for proton initiated showers all the primary energy is contained in one nucleon, while this is spread over 56 nucleons in iron. Therefore higher energetic secondary mesons can be created in proton showers, which results in higher energetic muons. This effect becomes less visible at higher energies.
Summarized, it can be concluded that heavier showers contain more muons of all energies, but showers initiated by lighter particles can produce more very high energy muons.

The number of muons above a certain muon energy in a shower was parametrized by Elbert [102], Gaisser and Stanev [103] and others based on Monte Carlo simulations. The Elbert formula for the average number of muons above a certain muon energy E_μ is:

$$N_\mu(> E_\mu) \approx A \frac{0.0145 \text{ TeV}}{E_\mu \cos\theta} \left(\frac{E_0}{A E_\mu}\right)^{0.757} \left(1 - \frac{A E_\mu}{E_0}\right)^{5.25}, \tag{3.18}$$

for a shower initiated by a primary nucleus with mass A, energy E_0 and zenith angle θ. In this formula the superposition approximation is used. The term $\frac{0.0145 \text{ TeV}}{E_\mu \cos\theta}$ accounts for the probability for pion (or kaon) decay at a typical slant depth. The second term treats the muon number increase with primary energy, where β is now 0.757 compared to 0.85 in the Heitler-Matthews model. The decrease in number of muons with energies close to E_0 is described by the last term.

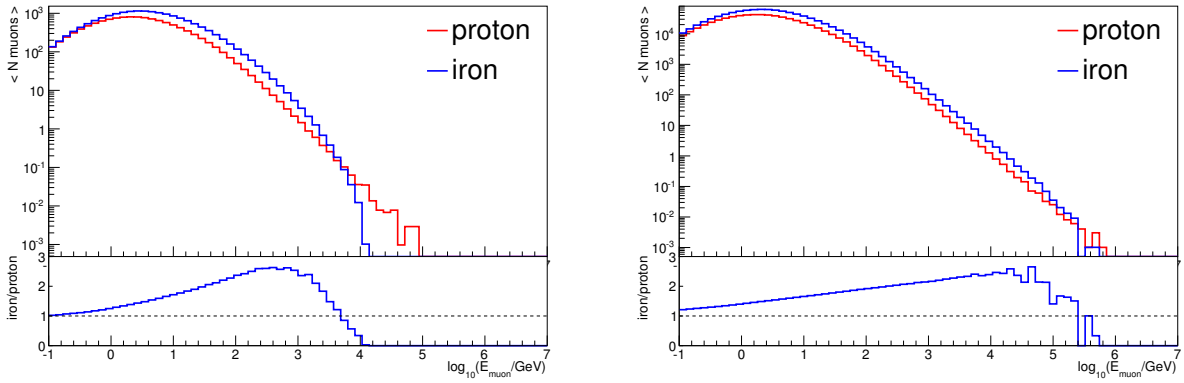

Figure 3.8: Average muon spectra of proton and iron showers with zenith angles $0.8 < \cos\theta < 1$ for energies around 1 PeV (left) and 100 PeV (right). Results are obtained from CORSIKA simulations with Sibyll 2.1 [100] as model for the high-energy hadronic interactions and are extracted at the atmospheric depth of South Pole (~ 700 g/cm^2).

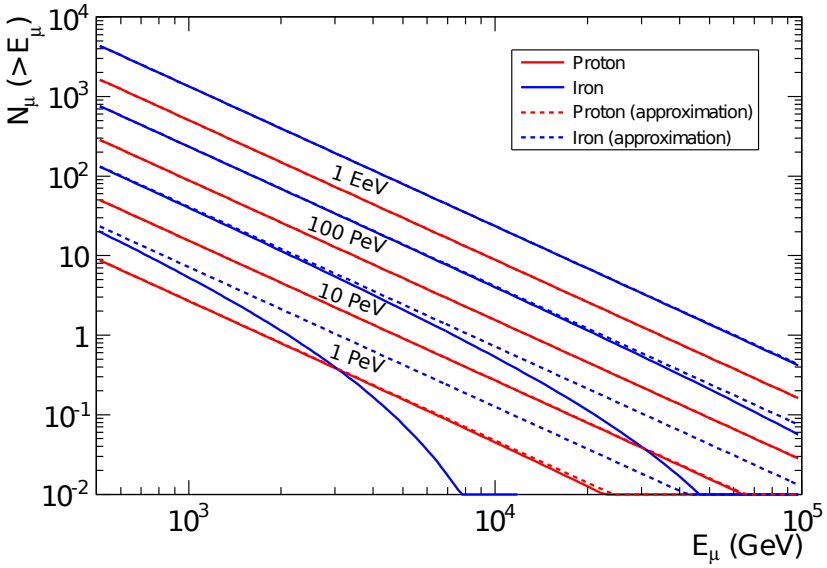

Figure 3.9: Integrated muon spectra for muon energies above 500 GeV for various primary energies and proton and iron showers, as predicted by the Elbert Formula. [101, 102]

The integrated muon spectra for proton and iron initiated showers of various energies, obtained from the Elbert formula, are shown in Figure 3.9. Only muon energies above 500 GeV are considered here. The solid lines show the numbers obtained from the full Elbert formula, while the dotted lines show the numbers obtained excluding the last term.

This high-energy muon spectrum is especially important for deep underground detectors which only measure those high-energy muons. The number of muons in such high-energy muon bundles ranges from $\mathcal{O}(10)$ for PeV showers to $\mathcal{O}(1000)$ for showers with primaries of EeV energies. These high-energy muons are created in the first interactions of the cosmic ray and thus provide a useful sensitivity to those interactions, and a unique probe for a composition reconstruction (and possibly also a primary energy reconstruction).

3.3.3 Lateral distribution

During the propagation of the air shower through the atmosphere the particles extend more and more radially outward. This is due to the transverse momenta of the secondaries of the collisions, the opening angles in Bremsstrahlung and pair production, and multiple Coulomb scattering. Exact solutions require the transfer equations to be solved in great detail. However, an approximate description of the lateral distribution for electromagnetic particles is given by the NKG function (named after Nishimuro, Kamata and Greisen [104, 105]):

$$\rho_{EM}\,(r,s)(\mathrm{m}^{-2}) \sim \frac{N(s)}{R_M^2} r^{s-2}(1+r)^{s-4.5} \tag{3.19}$$

This provides the EM density ρ_{EM} at a certain perpendicular distance to the shower core r, shower age s and total particle number at this age $N(s)$. Instead of Eq. 3.15 an alternate definition of the shower age is used: $s = \dfrac{3}{1+2X_{max}/X}$. R_M is the Molière radius, the radius of a cylinder containing 90% of the deposited energy around showers from Coulomb scattering:

$$R_M = \frac{\lambda_{em}}{\rho} \frac{\sqrt{4\pi/\alpha}\; m_e c^2}{E_c} \tag{3.20}$$

with $\alpha \approx 1/137$ the fine structure constant, ρ the atmospheric density and m_e the electron mass. The electromagnetic splitting length λ_{em} and the critical energy E_c have been defined in section 3.2.2.
The EM particle number is high in the core of the shower, and decreases with increasing distance to the shower axis. If the shower gets older, more energy is distributed to the edge of the shower and more particles are created. This results in a decrease in the slope or steepness of the EM lateral distribution, at all distances from the shower core, with shower age. This is also obtained from Eq. 3.19, which is valid for both electromagnetic and hadronic showers. However, the parameters need to be adapted for hadronic showers, since the hadronic core continuously feeds the electromagnetic component close to the shower. This results in a steeper slope of the EM lateral distribution for hadronic showers.

The lateral distribution of the muonic component in air showers is flatter compared to the electrons. EM particles far from the shower core have a low energy and are therefore easily absorbed in the atmosphere. On the other hand, low-energetic muons, created far from the shower core, can penetrate and propagate to the observation level. The spread of the muonic component is mainly due to the transverse momenta of the secondary particles in the collisions. A muon lateral distribution function (LDF) is given by Greisen [104], which describes the muon density ρ_μ as function of the distance to the shower core r:

$$\rho_\mu(\mathrm{m}^{-2})(r) = \frac{\Gamma(2.5)}{2\pi\Gamma(1.25)\Gamma(1.25)} \left(\frac{1}{320}\right)^{1.25} N_\mu\, r^{-0.75} \left(1+\frac{r}{320}\right)^{-2.5} \tag{3.21}$$

where N_μ is the total number of muons at this observation level. Due to the penetrating power of the muons this muon LDF does not depend on the age of the shower.

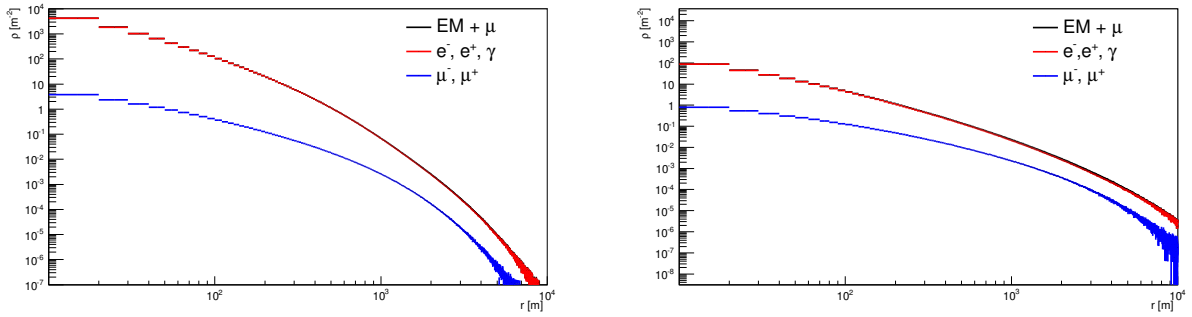

Figure 3.10: Lateral distribution of all particles, and the EM and muonic component separately. As an example (an average of) 10 PeV proton showers are shown with vertical zenith angles ($0.9 < \cos\theta < 1$) on the left and inclined ($0.4 < \cos\theta < 0.5$) on the right. Simulations using CORSIKA are performed using Sibyll 2.1 as hadronic model, extracted at an atmospheric depth of ~ 700 g/cm^2.

Figure 3.10 shows the EM (red) and muonic (blue) lateral distribution for 10 PeV vertical (left) and inclined (right) proton showers, at an atmospheric depth of ~ 700 g/cm^2. The lateral distribution of the sum of these two components (black) nearly overlaps with the EM distribution. In both plots the flatter muon LDF compared to the EM LDF can be observed. The muonic component only affects the total LDF far from the shower core. Close to the shower core, the muonic component is overwhelmed by the large amount of EM particles. This makes it very hard to reconstruct the muon contribution in this region. Therefore experiments often try to count the number of muons far from the shower core. Another option is to deploy a thick shielding above the detectors which stops the EM component.

For proton showers of 10 PeV the depth of shower maximum is smaller than 700 g/cm^2. Hence, for the highly inclined showers the EM component is already greatly reduced, while the muonic component remains stable. The muon to EM ratio thus increases for higher inclined showers of these primary energies.

A reliable reconstruction of the LDF is an important tool for indirect air shower experiments with an array of particle counters. The location where the particle density (and thus the total LDF) peaks indicates where the core of the shower hits the surface. But more important, the LDF can be used to obtain an indication of the energy and mass of the primary particle. Indeed, while the energy estimate using the number of detected particles (section 3.3.1) highly depends on the nearest distance between the core of the shower and one of the detectors, the LDF fits the entire distribution and thus provides a more stable energy measurement.
The LDF slope at a certain distance from the shower core provides an estimate of the mass of the primary particle, since EAS initiated by higher mass nuclei contain more muons (section 3.2.3) and these muons dominate the signal at the edge of the shower. Furthermore, as discussed before, the steepness of this total LDF is sensitive to the age of the shower.
If the experiment is able to reconstruct a separate muon and EM LDF, a more detailed measurement of the muon contribution can be performed. This thus increases the sensitivity to the primary composition.

3.3.4 Shower front

The arrival times of the particles in the detectors depend on the lateral distance of the detectors from the core of the shower. This is especially true for inclined air showers, as illustrated by Figure 3.11. The part of the shower closer to the array (here on the right) will first arrive at the detectors. This is the ”early” side, while the opposite side is the ”late” side. A detailed measurement (of the order of nanoseconds) of the particle arrival times can thus be used to reconstruct the direction of the air shower.

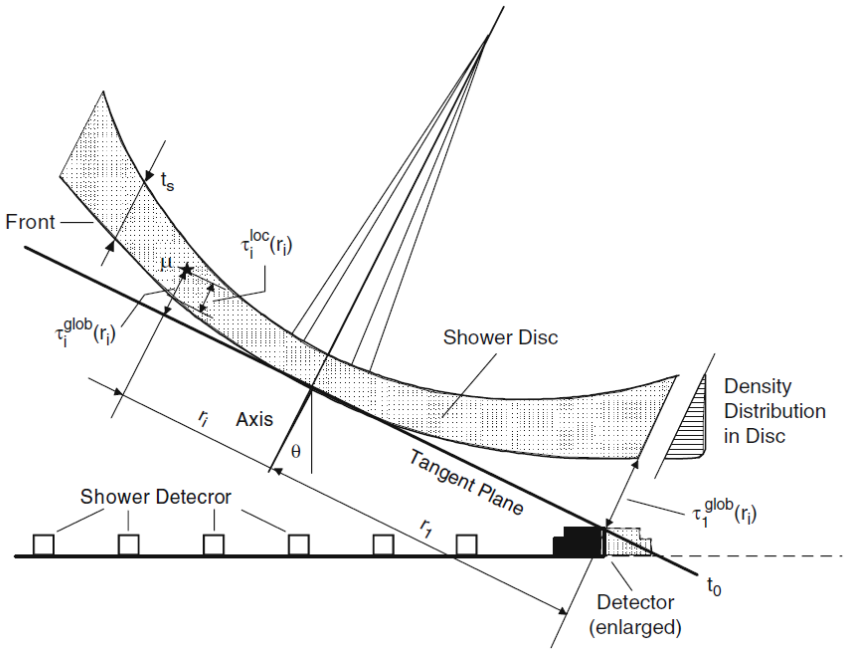

Figure 3.11: Illustration of the curvature and thickness of the shower front, from [92]. The density distribution of the particles inside the shower front is also shown. θ is the zenith angle of the shower, t_i the arrival time of particle i at a perpendicular distance r_i from the shower axis and τ indicates the delay of the curved shower front with respect to a plane wave.

A primary (”first guess”) reconstruction of the shower direction can be obtained with the approximation that the shower front moves in one plane (indicated as Tangent Plane in the figure). In reality the shower front is, however, not flat, but it shows a certain curvature. This spherical shell is centered around the shower axis. A better direction reconstruction is obtained when the time delay of the curved shower front with respect to the plane approximation is included. This time delay also increases with increasing age of the shower, and thus could possibly be used as extra parameter in energy and/or composition reconstructions. Another feature for an inclined shower is that a part of the shower still needs to travel some distance while the other part has already hit the detector array. This causes that in this further part the EM component already decreased, which creates some assymmetry in the signal. A proper reconstruction needs to take this into account.

3.4 Indirect Measurements: techniques, experiments and recent results

In this chapter the development of cosmic ray air showers and observation level distributions has been discussed in depth. This knowledge could only be gathered by the accumulated work of all experiments in the past. However, as shown in Chapter 1, a detailed and completely final answer on the sources of cosmic rays has not yet been achieved. The exact energy spectrum and composition above the knee of the spectrum remain uncertain. This is due to the indirect detection method in this energy range. As shown in Section 3.2 the number of interactions during the EAS propagation is large, the interactions are taking place at energies we cannot reach at Earth, it is a complex process where simulations with approximations are needed, etc. All these factors limit the reconstruction of the properties of the primary particle from the indirect measurements using the secondary particles.

Therefore, the research field of indirect cosmic-ray measurements is still very active. It is the hope to, at one point in the future, also identify the nature and sources of the highest energetic cosmic rays. This section starts with an overview on the current measurement techniques (section 3.4.1) and the main experiments

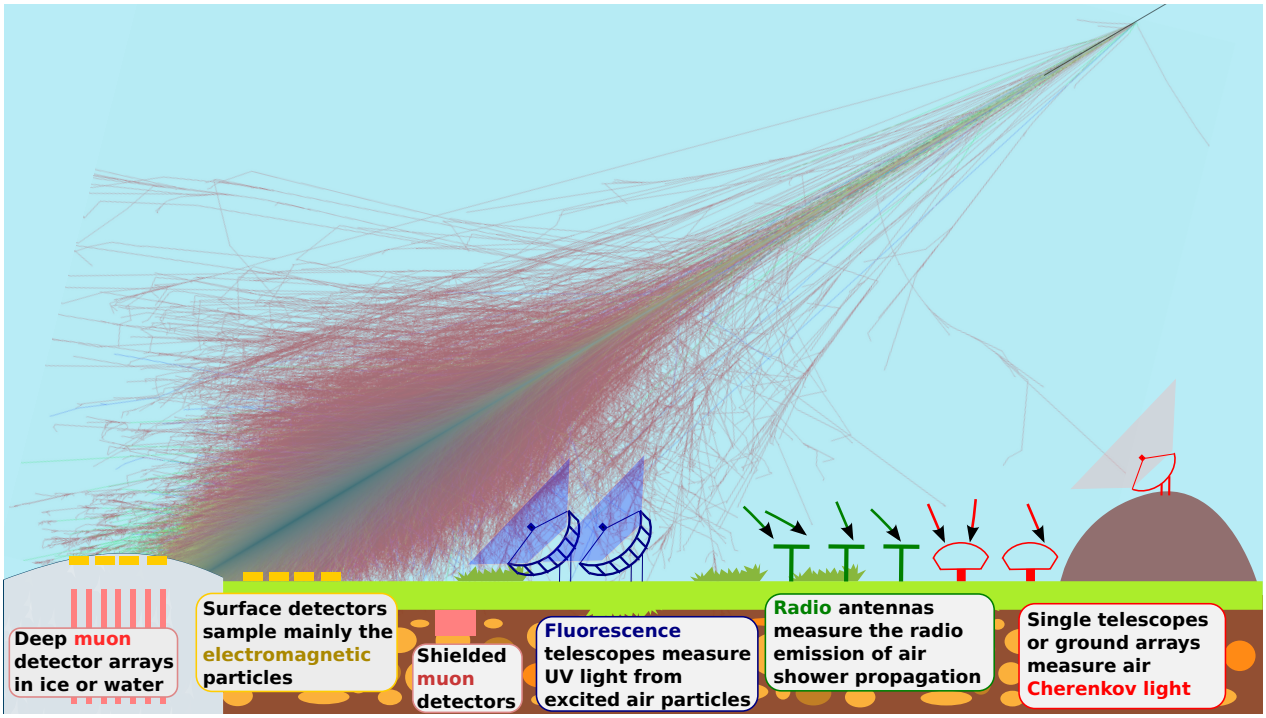

Figure 3.12: Sketch of the main indirect cosmic ray measurement techniques. The simulation of the air shower is obtained from [89].

(section 3.4.2). In section 3.4.3 the current status of the energy spectrum and composition are discussed, together with the main remaining questions or disambiguities. At the end, in section 3.4.4, a short discussion is provided on the hadronic interaction models. These models currently seem to cause the major uncertainty in the composition reconstruction.

3.4.1 Measurement techniques

Many new measurement techniques were developed during the last decades, in order to improve sensitivity and probe various parts of the extensive air showers. Figure 3.12 provides a schematic picture of most detection techniques, while a broad overview and history is given in [106]. We elaborate more on a few detection techniques here.

Surface detector arrays

When Pierre Auger coined the term ”extensive air showers”, his experiment consisted of a number of Geiger counters spread over a certain area. This detection method is still widely used, although the Geiger counters are now replaced by large scintillator counters, tracking detectors or calorimeters. Most calorimeters make use of water or ice as material, and measure the Cherenkov light emitted when a particle (or group of particles) traverses the calorimetric tank. The arrays of detectors sample the air shower at one atmospheric depth with typically at least 100 detector stations arranged in a regular pattern. The larger the distance between subsequent detectors, the higher the low-energy threshold for air showers. The highest energy that can be reached is determined by the total (effective) area spanned by the detector array. Due to the steeply falling cosmic ray energy spectrum, the flux of very energetic showers eventually becomes too low to obtain enough statistics if the detector is too small.
The relation between the measurements of this technique and the primary particle has extensively been discussed in the previous section. Using a surface detector array, the primary energy can be obtained from the measured lateral distribution of the particles (section 3.3.3). Often the reconstructed signal at one typical

distance, where fluctuations are minimal, is used to establish the conversion to the primary energy. The direction of the EAS is deduced using the timing between the hits in the separate detectors (section 3.3.4).
If the number of muons can be measured separately from the dominant electromagnetic part, a primary mass reconstruction could be performed. In order to do so, one could shield the detectors to get rid of the EM component, look for muons at the edge of the shower, or fit the signal distribution with a combination of an EM + muonic lateral distribution function. Alternative mass sensitive parameters could be the slope of the (EM) lateral distribution function or the curvature of the shower front, since both vary with the age of the shower.

The experiments that use these detector arrays are based at ground level. Many interactions have occured before the shower is detected, causing large shower-to-shower fluctuations (section 3.2.3). These experiments thus need a large dataset to obtain a reliable reconstruction of the primary energy spectrum and composition. Another disadvantage of surface arrays is that they heavily rely on simulations to relate the measurements to the properties of the primary cosmic ray. Since the assumptions within those simulations concerning hadronic interactions are uncertain, the reconstructed primary energy or mass are also subject to large uncertainties.
An advantage of such ground detector arrays is that they can operate continuously and have a very large opening angle.

Underground detectors

Instead of deploying detector units at the surface on the Earth, one could also bury them. These underground detectors only measure the muonic component of air showers, since the EM component is absorbed by the shielding material or the Earth. The deeper in the Earth a detector is deployed, the higher the energy of the muons should be to reach it. With $\sim$2 MeV cm^2/g energy loss for minimum ionizing muons one can easily calculate the lower energy threshold. If we consider water as example (with a density $\rho \approx 1$ g/cm^3) a muon needs to have at least an energy of $\sim$10 GeV to propagate to a detector below 50 m of water, while it requires $\sim$100 GeV to propagate down to 500 m.
Experiments which only consist of an underground detector could reconstruct the primary energy and mass of cosmic rays very roughly through the number of muons or muon multiplicity. However, disentangling the mass and energy of the cosmic ray is very hard. Therefore, the combination of an underground detector with a surface detector would provide a sensitivity to the energy with the surface detector and a good mass probe using the high-energy muon multiplicity measured in the deep detector.

Fluorescence telescopes

When an EAS propagates through the atmosphere the EM particles ionize the surrounding atoms. In particular the nitrogen atoms are excited and in the de-excitation process UV light is produced. If the primary energy exceeds 10^{17} eV, sufficient light can be collected by telescopes on the ground to reconstruct properties of the air shower [107]. The fluorescence telescopes have many pixels and are often operated in "stereo mode" with multiple telescopes, which creates a full view of the air shower. A major disadvantage of the fluorescence telescopes is that they can only be operated during dark and clear nights. Their duty cycle is thus only 10-20 %. Therefore they are often used in coincidence with a surface detector array.
By a measure of the created fluoresence light in small slant depth bins along the shower axis it is possible to reconstruct the longitudinal development of the air shower. Commonly a Gaisser-Hillas profile (Eq. 3.14)is used to perform this fit. The amount of fluorescent light corresponds to the energy deposited in the atmosphere, thus the calorimetric energy. To allow a reconstruction of the full (primary) energy of the shower, the shower profile is extrapolated to account for the part below ground and the invisible energy carried away by muons and neutrinos is estimated. This missing energy is deduced from simulations or from the number of muons measured by the ground array [108]. The primary composition can be inferred from the reconstructed depth of shower maximum (section 3.2.3) when a certain hadronic interaction model is assumed.

Air Cherenkov detectors

If the refractive index of a medium is larger than 1, which is almost always the case, highly energetic particles can travel faster then the speed of light in the medium. In the 1930's P. A. Cherenkov found that if these particles are charged, they radiate photons which mainly have wavelengths in the UV part of the electromagnetic spectrum [49]. Cherenkov radiation was explained in more detail in section 2.1.1. The refractive index of air is slightly above 1, moderately depending on the air density and thus the altitude. Since the abundant EM particles possess enough energy to exceed the light speed in air, an EAS can also be seen with sensitive Cherenkov light collectors. Large imaging air Cherenkov telescopes (IACTs) are sensitive to air showers between $\sim$30 GeV and $\sim$100 TeV. Smaller non-imaging air Cherenkov telescopes could be spread over a large area similarly as ground detector arrays and thus also reach very high cosmic ray energies. Since most of the Cherenkov photons have wavelengths in the UV part of the spectrum, the fluorescence telescopes are also sensitive to this Cherenkov light. These observatories can thus use Cherenkov light to detect air showers with energies $< 10^{17}$ eV, where the amount the fluorescent light is too small. Similar to fluorescence telescopes, these Cherenkov detectors also need cloudless nights and thus have a duty cycle of 10-20 %.
Since the amount of Cherenkov light roughly scales with the number of EM particles, the measured Cherenkov light density could be related to the primary particle energy. The slope of the lateral distribution of the Cherenkov light can be related to the depth of shower maximum and thus to the primary composition [109].

Radio signal measurements

Probably the most difficult but promising method to measure EAS is via the radio emission. This emission was discovered in the 1950's. Yet only during the past two decades one started to undestand the radio signal of EAS. This is due to the currently used combination of the radio detection method with better understood particle arrays [110]. The main signal in the radio range of the spectrum arises from the electric field induced by the spread between the positrons and electrons in the air shower. This geosynchrotron radiation is caused by the magnetic field of the Earth. A second effect, which accounts for 10-15 % of the radio signal, is due to the larger fraction of electrons compared to positrons in air showers. These electrons are ripped of of atmospheric atoms while the EAS traverses the atmosphere. For frequencies $<$100 MHz the EAS radio emission is coherent in the direction of the shower propagation. Similar to all previous detection methods, the total signal roughly corresponds to the primary energy, and the slope of the lateral distribution relates to the primary composition. Furthermore, the time structure of the radio signal, which can be measured in detail, adds more information. This detection method is not yet that powerfull compared to other methods, but is at this moment often used as an addition to existing detector arrays. It is expected that, due to the low cost and improved understanding, this detection method might gain importance.

3.4.2 Overview of recent experiments

In this part recent and important cosmic ray experiments are covered. Figure 3.13 indicates the sensitive energy range of some main experiments.

Below the knee

The cosmic ray flux is sufficient up to $\sim$100 TeV to allow a direct detection of the primary cosmic ray. For energies below 1 TeV, mostly satellite experiments or experiments mounted on space stations are used to measure the spectra of the light elements. The most detailed elemental spectra over a broad energy range are provided by the AMS-02 experiment, for all elements up to oxygen [111, 112, 113].
With increasing energy also the sensitive detector area needs to grow, and up to now these large and heavy detectors were not brought to space. Instead large balloons can be used to carry them up to the upper atmosphere. The CREAM experiment performed multiple balloon flights above Antarctica, where it benefits

from the circumpolar winds to allow long balloon flights. Over several years they accumulated ∼161 days of exposure. Five balloon flights were used to report a measurement of the elemental spectra of eight mass groups between proton and iron from ∼1 TeV to ∼100 TeV in 2010 [114]. In order to improve statistics and increase their high energy limit, in August 2017 the adapted CREAM payload was sent to the ISS space station, and is now called ISS-CREAM [115]. Other direct measurement experiments include [116] PAMELA [117], ACE [118] and ATIC [119].
The energy region between ∼100 TeV and ∼1 PeV is the transition region between direct and indirect measurements. Investigations in this energy region are particularly challenging since satellite or balloon payloads have a too small detector area, while air showers induced by cosmic rays of these energies only create a small or even no signal at the surface of the Earth. At this moment the available data in this energy region is limited. In any case, ground experiments that want to be sensitive in this energy region need to be located at large elevations. One such experiment is located in Tibet, at an altitude of 4300 m above sea level (a.s.l). The ARGO-YBJ experiment consists of a 6700 m^2 area fully covered with Resistive Plate Chambers (RPCs) which can measure the particle density in great detail. They reported on the measurement of the all-particle and proton + helium spectrum in this transition region [120]. Many experiments which perform high-energy gamma astronomy are also sensitive to cosmic rays in this energy region and thus cosmic ray measurements are a significant part of their program. Such experiments with ground detectors are HAWC [121] at 4100 m a.s.l. in Mexico, LHAASO [122] at 4410 m a.s.l. in China or GRAPES-3 [123] at 2200 m a.s.l. in India. Also IACTs can be sensitive to cosmic rays in the ∼10 TeV to ∼100 TeV energy region. Such experiments include the H.E.S.S. [124] and MAGIC [125] telescopes. [126]

Between the knee and the ankle

The IceCube Neutrino Observatory, the experiment used in this work and extensively discussed in the previous chapter, is sensitive to cosmic rays in the energy region between ∼1 and ∼1000 PeV. With its unique combination of a surface component and a deep detector the electromagnetic and muonic component can be measured on the surface, combined with the high-energy muon information in the deep detector. The details on the cosmic ray measurement method with the IceCube Neutrino Observatory are the subject of Chapter 5.
However, the first important results on the cosmic ray composition and detailed energy spectrum from ∼1 to ∼100 PeV were published by the KASCADE (Karlsruhe Shower Core and Array Detector) experiment in 2005 [127]. The experiment was located at the Karlsruhe Institute of Technology (Germany) at a height of 110 m a.s.l.. In this experiment a combination of unshielded and shielded detectors allowed a separate measurement of the electromagnetic and muonic component. Furthermore, in the center of the array a hadron calorimeter, a muon tracking detector with muon threshold of 0.8 MeV and muon chambers with threshold 2.4 GeV were placed to increase the sensitivity to the hadronic core and the muons. 252 detector stations were separated by 13 m and thus spread over an area of 200 x 200 m^2 was reached. In 2003, 37 scintillators were added next to the KASCADE array with a 137 m separation between the detectors, resulting in a 0.5 km^2 effective area (called KASCADE-Grande). KASCADE-Grande finished data taking in 2009 but the array was, until 2013, still used to study the EAS detection with a radio array (LOPES) [128].
More experiments active in this energy range are located in the Tunka Valley in Siberia, in Tibet and Yakutsk. The Tunka-133 experiment, inaugurated in 2009, uses clusters of non-imaging air Cherenkov telescopes spread over roughly an area of 3 km^2 [129]. Hence, their sensitive energy range ranges from a few to 1000 PeV. The atmospheric overburden in the Tunka valley, located at a height of 675 m a.s.l., is on average 938 g/cm^2. In the following years, more detection methods are added to study the different shower components. The wider focus of the array is reflected in its new name TAIGA (Tunka Advanced Instrument for cosmic ray physics and Gamma Astronomy). In 2012 and 2013 25 radio antennas have been included in the Tunka array, forming Tunka-Rex (Tunka Radio extension) [130]. The Tibet III Air Shower array (4300 m a.s.l.) combines fast timing detectors using photomultiplier tubes (PMTs) with detectors where scintillators and PMTs are combined. These are roughly spread over an area of 36.900 m^2 and therefore

the array is sensitive to cosmic ray energies between ∼1 and ∼200 PeV [131]. The Yakutsk Array combines buried muon detectors with surface scintillation counters and Air Cherenkov telescopes. This array is already in operation since 1974, with various configurations. In the current configuration the various detectors are spread over ∼10 km^2 with various separations. Therefore, this array is mainly sensitive at slightly higher energies, from roughly 30 PeV to about 10 EeV [132].

The two currently active experiments that study the ultra-high energy cosmic rays above the ankle, discussed in more detail below, also implemented more dense infill-arrays to lower their energy threshold. The Pierre Auger Observatory (PAO) included several extensions to their existing array [133]. The AMIGA project adds buried muon detectors and an array of 61 surface Cherenkov tanks with an inter-tank distance of 750 m spread over an area of 23.5 km^2. This array is overlooked by the HEAT (High Elevation Auger Telescopes) fluorescence telescopes, which cover an elevation from 30° to 58°, higher than the standard PAO fluorescence telescopes. Furthermore, a radio array AERA (Auger Engineering Radio Array) is being installed in between the AMIGA detector stations. Also the Telescope Array (TA) experiment added a low-energy extension: TALE (Telescope Array Low Energy Extension). Here, 45 scintillation counters with 400 m spacing and 31 counters with 600 m spacing are used as a ground array, accompanied by fluorescence telescopes with high elevation. These fluorescence telescopes now measure the Cherenkov light produced in the atmosphere. Promising first results even lower the energy limit to as low as 4 PeV [134].
Also radio arrays start to be sensitive in this energy range. The LOFAR experiment (Low Frequency Array) showed that a good X_{max} determination is possible in the energy range around 10^{17} eV [135]. Based on these results, future experiments like the Square Kilometre Array (SKA) have a great potential to study cosmic rays in this important energy range [136].

Ultra-high-energy cosmic rays above the ankle

Huge detection areas are required to detect sufficient cosmic rays with primary energies above the ankle of the CR spectrum ($> 10^{18}$ eV). These cosmic rays are often called ultra-high-energy cosmic rays or UHECR. The world's largest observatory is the Pierre Auger Observatory (PAO) in Argentina, covering ∼3000 km^2 [133]. The PAO is a hybrid experiment, i.e. it uses both a ground array of Cherenkov tanks combined with fluorescence detectors. The 1660 ground detectors are equally spread over the area in a configuration with ∼1500 m spacing (aside from the denser AMIGA array). A station with 6 fluorescence telescopes is located at each of the four main sides of the array. Each telescope covers a field of view of 30° in elevation and 30° in azimuth. The combination of the surface array and the fluorescence telescopes provides an excellent primary energy and mass sensitivity. The PAO measures various parts of the EAS are measured, which allows cross-calibration between the different detectors. Also an examination of the hadronic interaction models is possible. Since the Cherenkov tanks of the PAO are large, the contribution of muons to their signal is significant. Due to the difficult separation of the muonic and the EM signal, the PAO is in the process of installing extra scintillation pannels on top of the tanks. The updated PAO will be called AugerPrime [137].
The Telescope Array (TA) uses a combination of a ground array and fluorescence telescopes. Compared to the PAO the ground array of the TA experiment is smaller: it consists of 507 detectors spread over 700 km^2. The detector stations here are scintillator panels, as compared to Cherenkov tanks for PAO. Furthermore, 3 fluorescence stations surround the ground array, containing in total 38 fluorescence telescopes [138]. Since PAO is located in the Southern hemisphere while TA is in Utah, United States, both detectors are complementary in their field of view. This is important with regard to anisotropy studies of the ultra-high-energy cosmic rays. On top of the TALE array that was added, the TA experiment is currently also deploying extra detector stations and telescopes to make their array four times larger than it is now (TAx4).

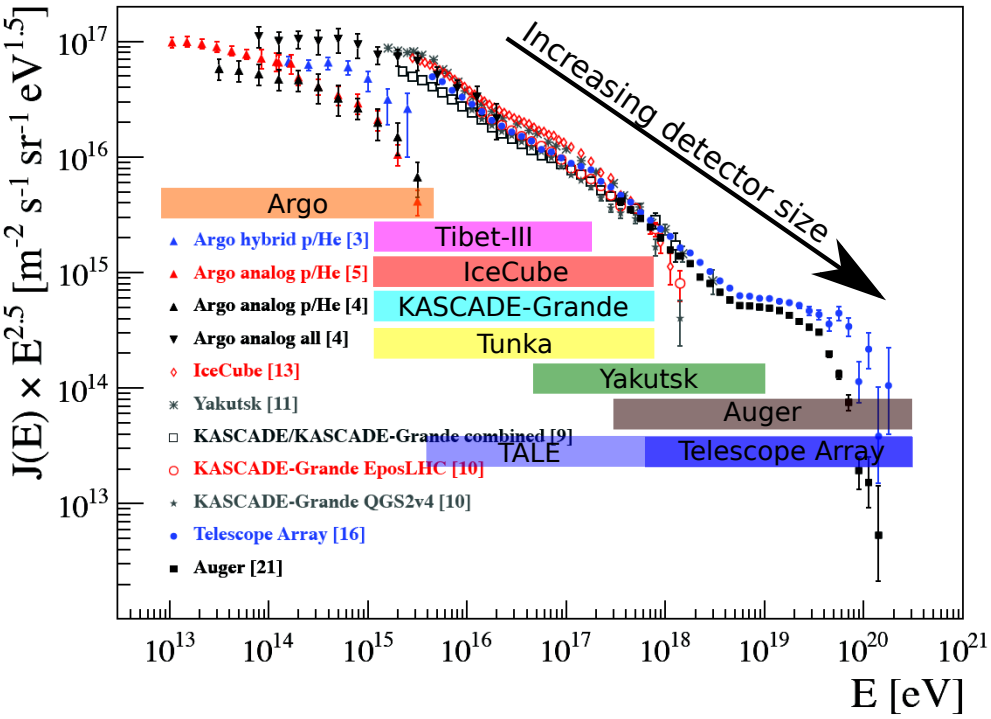

Figure 3.13: Compilation of the main indirect measurements of the cosmic ray energy spectrum as presented at the International Cosmic Ray Conference in 2015. The flux has been reweighted with $E^{2.5}$ to illustrate the details in the spectrum. Also the sensitive energy ranges of the main experiments are shown. Figure adapted from [126].

3.4.3 Recent results

Energy spectrum

The main properties of the cosmic ray energy spectrum have shortly been discussed in section 1.1.1. In the region where direct experiments are sensitive the all-particle energy spectrum is well known. The transition region between direct and indirect measurements (∼10 TeV to ∼1 PeV) is, however, still subject to uncertainties since only a few experiments are active in this energy region.
Since the 21st century experiments are constructed that are sensitive in the energy region above the knee. As a result the details in the higher end of the cosmic ray spectrum now become visible. Figure 3.13 shows a summary of all indirect energy spectrum measurements presented at the International Cosmic Ray Conference in 2015 [126]. Overall, the combination of all experiments provides a clear shape of this energy spectrum. Differences in the measured flux between experiments reach about 20 % at most and mostly bagree within their systematic error band (which is not shown).
The presence of the hardening of the spectrum around 3-4 PeV (the 'knee') is now seen by various experiments. The IceCube experiment published the most detailed measurement in the energy range between 1 and 100 PeV [139]. The observation of a '2nd knee' around 100 PeV by KASCADE(-Grande) [140] is confirmed by the IceCube, Yakutsk and TALE experiments. At higher energies the 'ankle' feature is clearly seen by the PAO and TA experiments. The sharp drop in the flux around $10^{19.5}$ eV, possibly caused by the GZK mechanism (section 1.4.2) or the maximum energy that can be reached by accelerators, is seen by both the TA and the PAO experiments. This flux decrease seems to occur at slightly lower energy in the PAO observations compared to TA. This disagreement remains even when the systematic uncertainties are taken into account, which is thus not understood yet.

Mass composition

To deduce which accelerators in the universe could be the main source of cosmic rays of a certain energy the knowledge of the composition at these energies is also important. The presence of a Peters cycle (section 1.3.4), i.e. a rigidity determined increase of the mean mass followed by a steep decrease, could hint towards a cosmic accelerator reaching its maximal energy and another source taking over. This source type should then be less abundant and more powerful.

Figure 3.14 shows the main composition measurements in the primary energy range between the knee and the ankle. These plots primarily show the average mass or $< \ln \mathrm{A} >$ as function of the energy. The upper left plot displays the result of the Yakutsk Cherenkov Array (without systematic errors) [141]. For IceCube the $< \ln \mathrm{A} >$ result is shown (upper right) with the various systematic errors [142, 143]. In this measurement also the individual energy spectra of four mass groups (proton, helium, oxygen and iron) are determined. An update of this measurement is in the pipeline [144]. The lower left figure shows the KASCADE-Grande composition result [140], where their total sample has been divided in an electron-poor (heavy) and electron-rich (light) sample. The bottom right plot summarizes $< \ln \mathrm{A} >$ results of the CASA-BLANCA, Tunka-133 and Yakutsk experiments in this energy range, and Auger, TA and HiRes at higher energies, from [145]. Lines to guide the eye are added to this figure. The hadronic interaction model used in this last plot is QGSJet01, while it is QGSJet-II.03 for the KG result and the Yakutsk result shown in the upper left panel. IceCube used Sibyll 2.1 as a model for this result, while QGSJet-II.03 was used as alternative model to determine the systematic uncertainty due to the hadronic interactions. These hadronic interactions are discussed further on in section 3.4.4.
It can be observed that all experiments measure an increasingly heavy composition from the knee up to $\sim$100 PeV. Whether the knee in the spectrum is due to a proton or helium cut-off is still an open question. Above $\sim$100 PeV both KG and the Yakutsk array measure a decrease of the average mass. In this case, the 2nd knee could be explained by a cut-off of the heavy elements, in particular iron. Since the charge of an iron nucleus is 26, this would agree with a Peters cycle if the knee (around 3-4 PeV) is caused by a proton cut-off ($26 \cdot 4$ PeV ≈ 100 PeV). The composition measurement of the IceCube Neutrino Observatory on the other hand does not show this average mass decrease above 100 PeV. Instead, the average mass seems to remain more or less constant and heavy. This measurement was also confirmed by the measurement of the muon multiplicity spectrum by the IceCube Neutrino Observatory. In that analysis only the in-ice component of the IceCube Neutrino Observatory was used. The measured muon multiplicity between 100 PeV and 1 EeV seems to agree with a multiplicity spectrum caused by heavy primaries [146].

Figure 3.15 shows recent UHECR measurements of the depth of shower maximum by the PAO [147] and TA [148] experiments. To obtain these results both experiments combined the ground array information with the fluorescence light yield measurement. To interpret the measurements in terms of the cosmic ray composition, the average X_{max} values obtained from simulations with certain interaction models and primary elements are added (seen as the lines in the figures). Next to the average X_{max} measurement as function of the energy, the PAO also provides the elemental fractions or elemental spectra for four mass groups (proton, helium, nitrogen, iron) [149].
Between $\sim$100 PeV and $\sim$1 EeV the PAO measures a decreasing average mass, similar to the Yakutsk and KG composition measurement. A very light ankle is observed. For energies above the ankle the PAO measures a rising average mass. This increase in mass is obtained with each of the hadronic interaction models. Important differences between the hadronic interaction models arise in the more detailed reconstruction of the elemental fractions. For example, at the highest energies the nitrogen contribution is dominant when Sibyll 2.3 or EPOS-LHC are used as hadronic interaction model, while with QGSJet-II.04 helium is the dominant element. The TA result has fewer energy bins and thus a less detailed structure. This is due to their smaller size and thus limited statistics compared to the PAO. Contrary to the PAO they seem to observe a light composition along the entire energy range. In a joined working group it was however sorted out that when the systematic errors are taken correctly into account, both experiments agree in their mass determination [150].

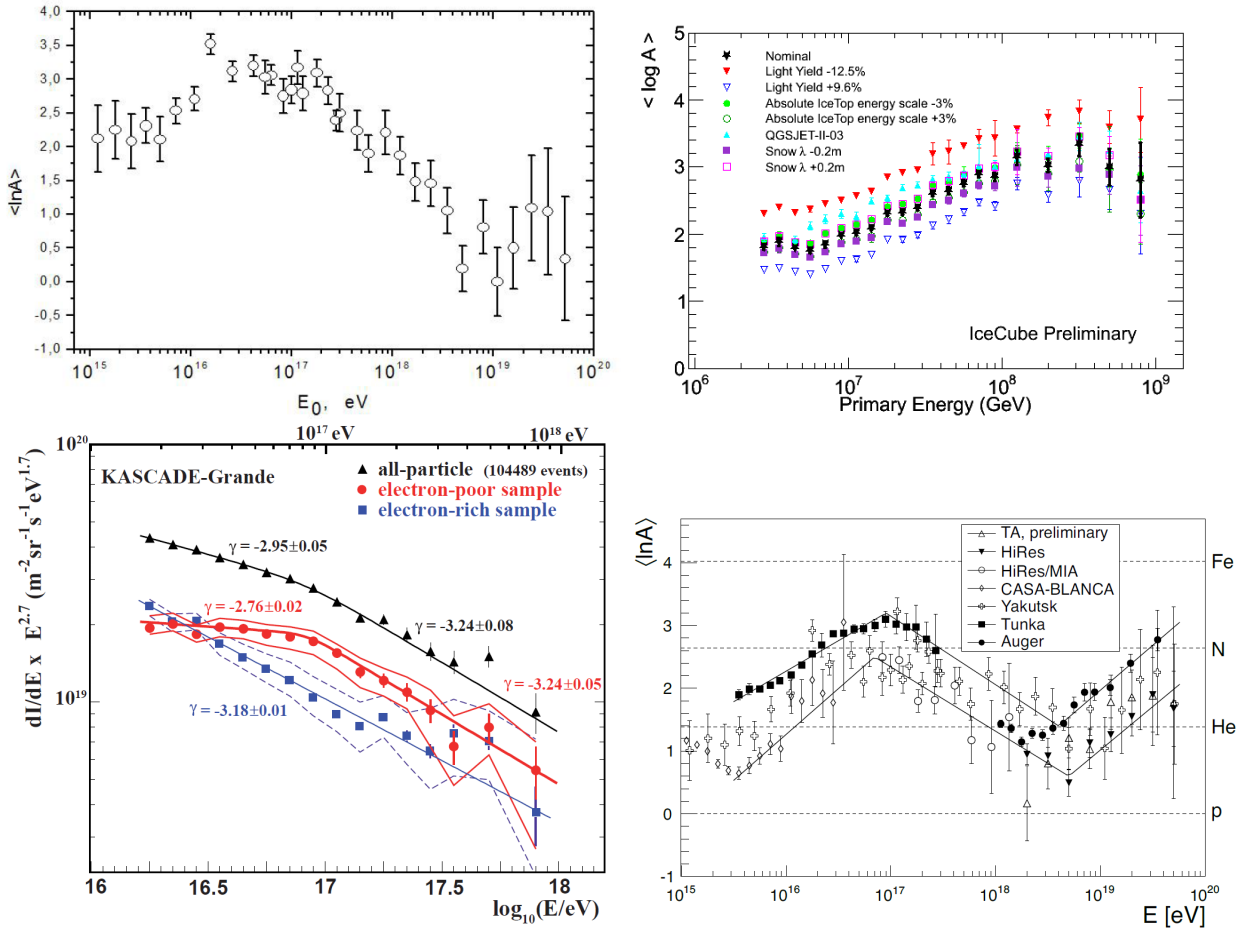

Figure 3.14: Selection of composition measurements in the energy region from the knee to ankle. Top: $< \ln A >$ measurements of the Yakutsk Array [141] (left) and IceCube [143] (right). Bottom left: KASCADE-Grande energy spectra of an electron-rich (light) and electron-poor (heavy) sample [140]. Bottom right: Compilation of some indirect $< \ln A >$ measurements with lines to guide the eye. [145]

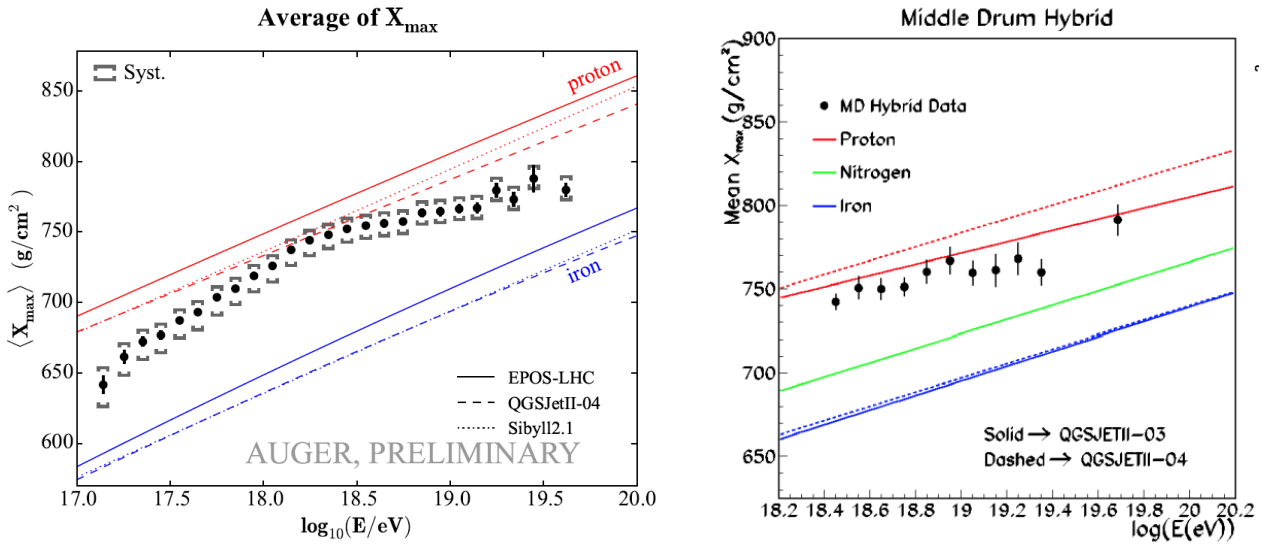

Figure 3.15: Average X_{max} measurements of the Pierre Auger Observatory (left) [147] and the Telescope Array (right) [148] as presented at the ICRC 2015.

Conclusions and remaining questions

The development of the measurement techniques during the last decades and the new generation of experiments now result in a more detailed knowledge of the cosmic ray energy spectrum, from the lowest energies to the highest. Some discrepancies exist within experiments, but the general picture is clear: the simple, uninteresting, power-law behaviour of the energy spectrum has disappeared. The knee and the ankle have been observed by multiple experiments, and more features like the 2nd knee appeared. With even more and better measurements more details may become visible, although shower-to-shower fluctuations inherently cause a smearing of the energy spectrum.

The main challenge for the indirect air shower measurements now becomes the measurement of the average mass as function of the energy. Or even better, the reconstruction of the energy spectra of separate mass groups. At this moment the light knee is confirmed by most experiments, although the ARGO-YBJ result, where the proton + helium spectrum (Figure 3.13) shows an early drop before the knee, causes some tension. This is not understood and more experiments in this energy region are needed. The HAWC Observatory could possibly clarify this situation [151]. The average mass increase from the knee to $\sim$100 PeV is also established, although variations between experiments exist. Above this energy the results of the various experiments show larger uncertainties and variations.
The KASCADE-Grande, Yakutsk and PAO experiments all measure a decreasing average mass from 100 PeV and 1 EeV. With regard to those experiments, IceCube measures a heavier composition in this energy region. A seemingly stable composition is observed, although the error bars are large and therefore it is difficult to draw a final conclusion. Nevertheless, the discrepancy between IceCube and the other experiments is clear. It will be important to clarify what the reason is for this discrepancy as soon as possible. The composition uncertainty in this energy range has the consequence that the exact energy at which the galactic to extragalactic transition occurs is still unknown. Aside from the composition measurement, an answer to this question could also come from the measurement of the cosmic-ray anisotropy, as discussed in [152].
The evolution of the average mass above the ankle has important implications for the interpretation of the sudden flux decrease at $\sim 10^{19.5}$ eV [153]. If the composition remains light, a GZK cut-off explanation seems plausible. An increasingly heavy composition on the other hand could point towards the maximum energy that can be reached by the cosmic accelerators. This last scenario seems favoured by the PAO measurements. However, no final conclusion is reached yet and thus the upgrades to the UHECR obervatories are crucial.

Due to the uncertainty of each measurement and the variations between the experiments, one currently combines results of the composition and energy spectrum from all experiments to deduce possible populations or sources of cosmic rays. It should be noted that the energy spectra deduced by most experiments need to be scaled slightly $\mathcal{O}(10\%)$ to agree with eachother. One example of such a fit is the Gaisser-Stanev-Tilav (GST) global fit [4], which was shown and discussed in section 1.1.1. Another example is the Global Spline Fit (GSF), which uses most measurements and -important- also includes their error bars [154]. These efforts are important to obtain a global and reliable view of the full cosmic ray energy spectrum and composition.

3.4.4 Hadronic interactions

Due to new detection materials and the increase of the computing power, the experiments have reached a good sensitivity during the last decades. The composition measurements from the indirect air shower experiments themselves are not very detailed yet, but one can have confidence in the overall behaviour.
As discussed above, a disagreement in the composition between various experiments is observed, especially at energies above $\sim$100 PeV. It might not be a coincidence that this is the maximal energy obtained at human-controlled facilities, especially the Large Hadron Collider (LHC). Since the measurement techniques seem solid, it is now assumed that the discordance could be due to the fact that the experiments use different observables to reconstruct the composition. At this moment it is accepted that a mass reconstruction using X_{max} does not need to agree with one using muons on the surface or in underground detectors. It seems that

the simulations, i.e. the modelling of the hadronic interactions, currently limit us to obtain a matching picture of the mass from different experiments. Since the details of the EAS depend on these hadronic models, and the models are known not to be perfect, this should come to no surprise. Up to roughly 100 PeV, the hadronic models are tuned to the LHC and other data. Above this energy the uncertainties within the hadronic models grow, which makes it difficult to infer the correct mass of the primary particle from observations of secondary particles produced after many interactions. It is clear that the hadronic interaction models currently play a very important role in indirect air shower measurements. It seems required that more time and work is invested in the study of these hadronic interactions and improvements of the models.

Recently, the hadronic interaction models have undergone an update to include the latest measurements from the LHC and fixed-target experiments, and to accomodate anomalies seen by air shower experiments (discussed further on in section 4.2). These show some improved measurements and a better understanding, but large uncertainties also remain within these post-LHC models. For example, the description of the pion-air interactions still remains a large source of uncertainty [155]. Therefore, alternative hadronic models are always used as systematic uncertainty on the measurement, or various results are published with the various hadronic models (for example [149, 156]).

If experiments measure multiple variables of the EAS, they could check the internal consistency of the hadronic interaction models and thus provide valuable feedback. This is for example performed by PAO, where it was found that the number of muons at the surface is too small in simulations compared to the predictions using their composition measurements with X_{max} [157, 158]. Also the muon production depths would indicate a heavier composition compared to the X_{max} measurement, even heavier than iron for a certain hadronic interaction model [159].
The KASCADE-Grande experiment reported on a consistent muon density measurement between data and simulations in their energy range, but observed a too small muon attenuation length in simulations [160].

In the analysis performed in this thesis work we will compare a measurement of the energy deposition in the deep in-ice detector with the slope of the lateral distribution function (at 125 m from the shower core) reconstructed with IceTop. While the signal measured in the in-ice component of the detector is sensitive to the number of high-energy muons in the shower, the slope of the lateral distribution is related to the number of low-energy muons and the age of the air shower. Also this allows an internal check of the hadronic interaction models. Furthermore, it might explain the IceCube discprepancy with the other experiments concerning the composition measurement.

4

Air shower simulations for IceCube

”O Deep Thought computer,” he said, ”the task we have designed you to perform is this. We want you to tell us....” he paused, ”The Answer.”

The Hitchhikers guide to the galaxy - Douglas Adams

While a direct detection of cosmic rays allows the immediate determination of the energy and type of the primary cosmic ray (CR), indirect measurements need to relate observations of the secondary particles to the properties of the primary CR. During the air shower development millions of particles are created, a fraction of the energy dissipates into the atmosphere, some particle types are not observed, etc. Therefore, Monte-Carlo (MC) simulations are required to interpret the measurements. They are an essential part of the indirect cosmic ray studies.

This chapter describes cosmic ray simulations, especially for the extensive air showers (EAS) studies performed with the IceCube Neutrino Observatory. Section 4.1 treats the simulation of the air shower propagation in the atmosphere. Since the modelling of the energetic collisions of the hadrons is an essential part of the simulations and is important for this work, the models are discussed in more detail in Section 4.2. In Section 4.3 the detector simulation is shortly summarized. Some details of the specific simulation datasets are described in Section 4.4.

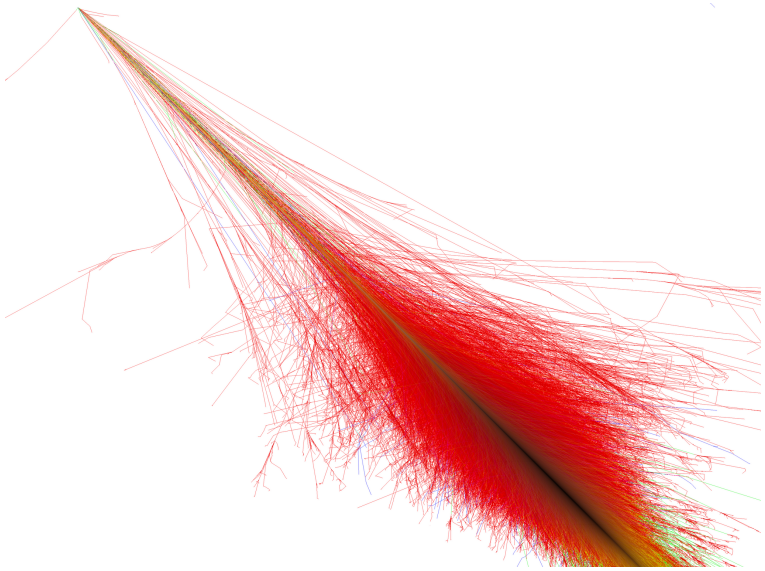

Figure 4.1: EAS simulation with CORSIKA. The primary particle was a 1 PeV proton with a zenith angle of 45°. The red lines indicate the electromagnetic particles, while the green lines show the muons. [89]

4.1 Air shower simulation: CORSIKA

The development of an air shower in the atmosphere is simulated using CORSIKA (COsmic Ray SImulation for KAscade) [98]. This code was developed for the KASCADE experiment but is now used by all indirect air shower experiments. This FORTRAN code injects particles at the top of the atmosphere, simulates the interactions and tracks the particles during the EAS propagation through the atmosphere (Figure 4.1). The particle distributions are then read out at a certain altitude.

CORSIKA allows a large variety of input settings. The primary particle type can be set, together with an energy, zenith and azimuth range in which the values are randomly chosen. The energy spectrum produced in simulations for IceTop is chosen to follow an E^{-1} spectrum, to produce sufficient low- and high-energy events.
The particle interactions are described using external models. Also these have to be specified as input parameters. For IceTop simulations the description of the electromagnetic component is performed with the EGS4 model [161]. The hadronic interactions at energies below 80 GeV are modelled with FLUKA [162, 163]. Since the energies involved in the higher energetic hadronic interactions could exceed the energy obtained in accelerating facilities at Earth, these are more difficult to model. Therefore extrapolations and assumptions need to be performed, which naturally introduce uncertainties. Multiple models exist that try to describe these energetic interactions. Since this work aims, among other goals, to study these high-energy hadronic interaction models, they are discussed in more detail in Section 4.2.
The energy threshold below which muons and hadrons are not further tracked was chosen to be 0.05 GeV in IceTop. Electrons and positrons are not tracked when their energy drops below 0.01 GeV and this threshold is 0.002 GeV for gammas. Below these thresholds particles are not able to create a detectable signal in the IceTop tanks. The shower propagation is simulated down to a user-specified altitude. In the first IceTop simulations this was set as 2834 m above sea level (a.s.l.). However, due to the increasing snow heights on top of the tanks with the years, this became too low and this observation level was raised to 2837 m a.s.l. Additional parameters include atmosphere (section 4.1.1) and thinning (section 4.1.2) settings, seeds for random number generators and logging outputs.

4.1.1 Atmosphere

Since the atmosphere is the medium through which the air shower develops, it is of great importance that the simulated atmosphere describes the real atmosphere as accurately as possible. In CORSIKA the composition of the atmosphere is uniform and always 78.1 % N_2, 21.0 % O_2 and 0.9 % Ar. This agrees well with the realistic values (Section 3.1).
The local density highly influences the decay (Eq. 3.7) versus interaction probability (Eq. 3.8) of a particle. Therefore it is important to take the detailed density variations into account. In Section 3.1 it has been deduced that for an isothermal atmosphere both the density and atmospheric depth X (or "thickness") increase exponentially with decreasing altitude. For a more realistic atmosphere this isothermal condition is not valid and the density profile deviates from this exponential behaviour. This should be taken into account, especially at South Pole, where the atmosphere is very specific due to the presence of the large Antarctic ice sheet and the di-annual alternation between polar day and polar night.

Multiple atmospheric depth profiles are implemented and can be selected in CORSIKA. In these CORSIKA atmospheres the atmospheric depth as function of the altitude is described in 5 layers, of which the lower four are exponential:

$$\mathrm{X}(h) = a_i + b_i e^{-h/c_i} \quad i = 1, ..., 4 \; . \tag{4.1}$$

In the fifth layer a linear decrease of the atmospheric depth with height h is used:

$$\mathrm{X}(h) = a_5 - b_5 \frac{h}{c_5} \; . \tag{4.2}$$

Table 4.1: The 6 South Pole atmospheres included in CORSIKA, selected with the ATMOD option.

ATMOD	Description
11	March 31, 1997 South Pole atmosphere (MSIS-90-E)
12	July 01, 1997 South Pole atmosphere (MSIS-90-E)
13	Oct. 01, 1997 South Pole atmosphere (MSIS-90-E)
14	Dec. 31, 1997 South Pole atmosphere (MSIS-90-E)
15	South Pole atmosphere for January after Lipari
16	South Pole atmosphere for August after Lipari

The parameters a_i, b_i and c_i are determined such that X(h) is continuous and can be differentiated continuously. The density ρ can be calculated using $\rho(h) = -\frac{\mathrm{dX}(h)}{\mathrm{d}h}$. The derivative of the density profile does not need to be continuous.

For the South Pole six atmospheres can be selected, given in Table 4.1. In the simulations used for the IT73-IC79 detector configuration (Table 2.1) of IceCube and IceTop the July 01, 1997 South Pole atmosphere (ATMOD 12) was used.
These atmospheres describe the South Pole atmosphere rather well, although not perfectly. The July 1, 1997 atmosphere (ATMOD 12) has an average density profile close to the average of July. The surface pressure of this atmosphere in the simulations is, however, closer to the average of an entire year instead of to the average July surface pressure. This disagreement is not desired if one wants to compare the data and simulations. Furthermore, the layer close to the Antarctic surface (the 'inversion layer', section 5.5.2) is badly modelled.

To reduce the effect of a (slightly) wrong atmosphere on analyses, a more realistic atmosphere model was developed during this thesis work. The five-layered structure (Equations 4.1 and 4.2) needs to be respected within CORSIKA, but both the boundary heights between the layers and the parameters a_i, b_i and c_i can be chosen by the user. This allows to construct a specific profile and to perform simulations with user-specified monthly atmospheres, which would benefit e.g. studies of seasonal variations.
Atmospheric data to construct these profiles was obtained by balloon flights from the Antarctic Meteorological Research Center (AMRC) [87] and satellite data from the Atmospheric Infrared Sounder (AIRS) [88]. Daily pressure and temperature measurements are available up to an altitude of ∼45 km, depending on the season. These measurements have been converted to thickness and density, and merged into altitude bins of 50 m. Subsequently, the data of each month was merged into an average monthly profile. Five years of atmospheric data were used, from 2007 up to and including 2011.

To obtain the parameters typical for a certain month, the atmospheric depth profiles of this month of each of the five years are fitted with the fixed shapes (Eq. 4.1 and 4.2). The density profile is fitted simultaneously, where the relationship with the atmospheric depth is taken into account. Above the highest available data (∼45 km) the fourth layer is extrapolated up to 100 km. For the profile above 100 km the parameters of the fifth layer of one of the 4 MSIS South Pole atmospheres are used. The output of the fit consists of the parameters (a_i, b_i and c_i) of each of the 4 layers, the boundary heights between the layers and the parameters of the fifth layer of the selected MSIS South Pole atmosphere.

The fitting procedure consists of two iterations. In the first step the first, second and third boundary height are varied by respectively 500 m, 1000 m and 2000 m. The smaller step size for smaller heights is introduced due to the greater importance of these low altitudes in the air shower development. The boundary heights between the three layers can vary respectively between 2850 m and 8000 m, 8000 m and 23000 m and from 12000 m to 42000 m. The third boundary layer should be at least 1000 m below the maximum height of

Table 4.2: Atmospheric parameters of the fit to the average April atmospheres of 2007-2011. Layer 5 equals the upper layer of the March 31, 1997 South Pole atmosphere implemented in CORSIKA (Table 4.1). These parameters are used for the simulation production of air showers for cosmic ray studies with IceTop and IceCube.

Layer i	Height (km)	a_i (g/cm^2)	b_i (g/cm^2)	c_i (km)
1	2.835-7.600	-69.7259	1111.7	7.66099
2	7.600- 22.000	-2.79781	1128.64	6.41716
3	22.000- 40.400	0.262692	1413.98	5.88082
4	40.400-100.000	$-8.41695 \cdot 10^{-5}$	587.688	6.93300
5	100.000- 112.800	0.00207722	1	$5.4303203 \cdot 10^{4}$

the measurements. Furthermore, at a height of 100 km the atmospheric depth is forced to agree with one of the MSIS South Pole atmospheres. This atmosphere is then used above 100 km. For each combination of possible boundary heights the total sum of the quadratic distance between the measurements and fits (the total $\chi 2$) to the five density and thickness profiles was minimized.
In the second iteration a more detailed variation of the boundary layers around the optimal values obtained in the first step is performed, to further improve the results. This detailed variation was not performed in the first step to limit the required computing time. The step size is now decreased to 100 m for all boundary heights. Again the atmospheric depth and density profiles of the five average monthly atmospheres are fitted. The combination of parameters and layer boundaries that results in the smallest $\chi 2$ can then used as input to CORSIKA.
The resulting parameters for all months are given in Appendix A.

Instead of using one of the atmospheres implemented in CORSIKA, for the bulk simulations of the IT81-IC86 configuration (given further on in Table 4.6) it was chosen to use one of these realistic monthly profiles. Preferably, the atmospheric density and thickness profile represents the average of an entire year, and also the atmospheric depth at the surface approaches the yearly average ($\sim$692 g/cm^2). As such, seasonal variations only smear the data but do not result in a systematic error. Hence, one monthly atmospheric profile is chosen to perform the bulk simulations, and the data of this particular month can then be used for the data-MC studies.
Figure 4.2 shows the average monthly atmospheric depth and density profiles of all months relative to the average of an entire year. This was obtained from the available atmospheric data at the time of the analysis, thus using 5 years of data. From this figure it can be seen that November and April seem to approach the average yearly profile best. It was chosen to use the April atmosphere, and the parameters obtained for the average April atmosphere are given in table 4.2.

Figure 4.3 shows the real average atmospheric depth (left) and density (right) as function of the altitude for July 2010, February 2011 and April 2011 (solid lines). On top of this the profiles from the April fit and the CORSIKA South Pole July 1, 1997 atmosphere are shown (dashed lines). This shows that the April fit agrees with the April 2011 atmosphere. The monthly variation and the agreement between the CORSIKA July atmosphere and the real July atmosphere are also observed.
A more detailed look at the fit is given in Figure 4.4. This figure illustrates the difference in atmospheric depth (left) and density (right) as function of the altitude between the 5-year average April and the fit (black), but also the year-to-year variations and the difference with the CORSIKA July 1, 1997 atmosphere.
This shows that the atmospheric depth of the April fit is continuous and within the variation between the different April atmospheres. It approaches the average atmospheric depth at the surface: a deviation of ~ -3 g/cm^2 is observed. In total the thickness at ground level is thus ~ 5 g/cm^2 higher compared to the yearly average. Also the density of the 5-layered fit describes the realistic average profile reasonably well. Close to the surface the deviation increases due to the inversion layer. This inversion layer is still not

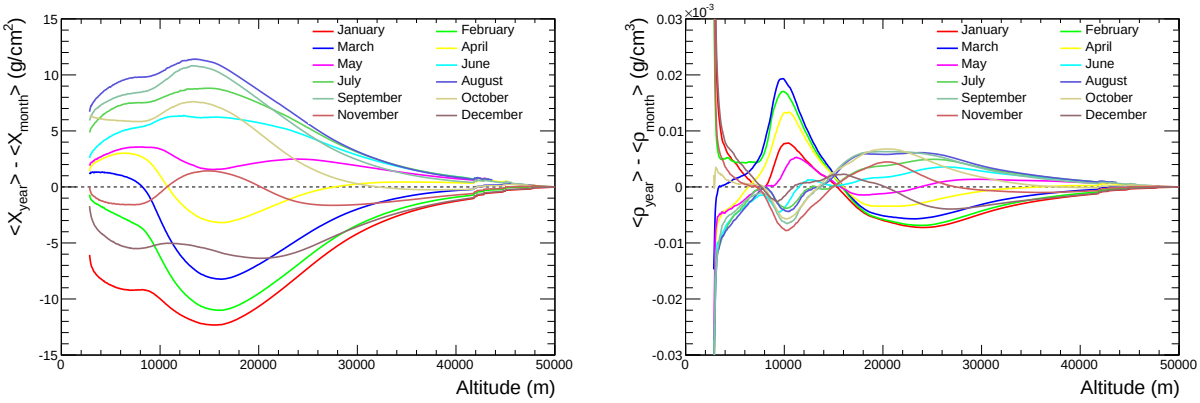

Figure 4.2: Average atmospheric depth $< X >$ (left) and density $< \rho >$ (right) per month, obtained with 5 years of data (2007 - 2011), as function of the altitude, compared to the average 5-year atmosphere.

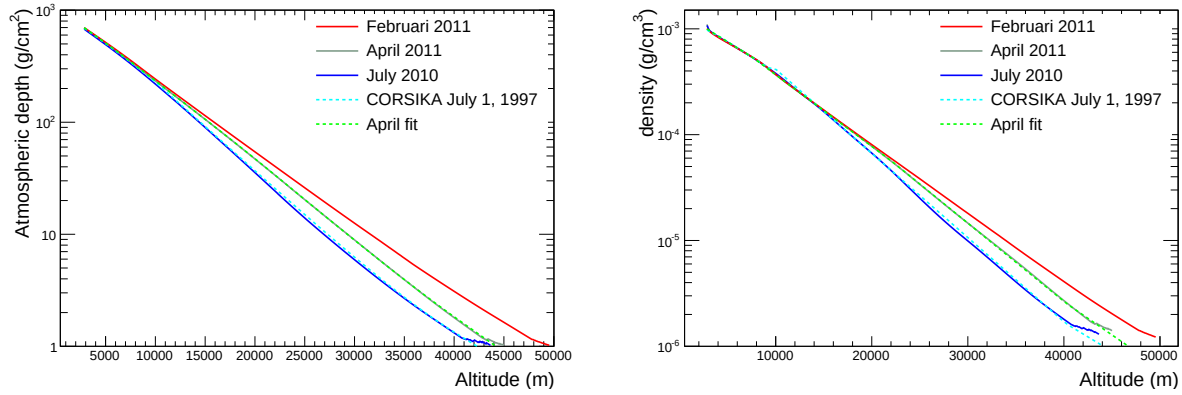

Figure 4.3: Atmospheric depth (left) and density (right) profile as function of the altitude. The average from the data measurements for the months July 2010, February 2011 and April 2011 are shown, together with the profiles of the South Pole July 1, 1997 implemented in CORSIKA and the used profile based on the average of April 2007-2011.

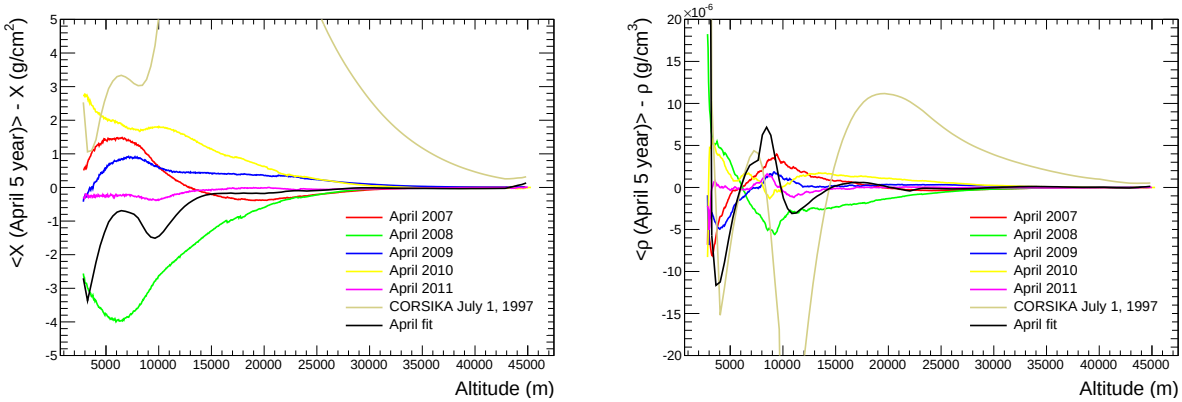

Figure 4.4: Atmospheric depth X (left) and density ρ (right) profile variations between the average of 5 years of April atmospheres (baseline) and the fit to this 5 year average (black), the CORSIKA July 1 atmosphere (light brown) and the April months of the five individual years.

described perfectly by the fit, which seems extremely difficult because the fit is forced to obey this five layered structure. Overall, this new profile shows to be reliable and satisfactory for the current needs. However, it also seems possible to further improve these studies and models if required.

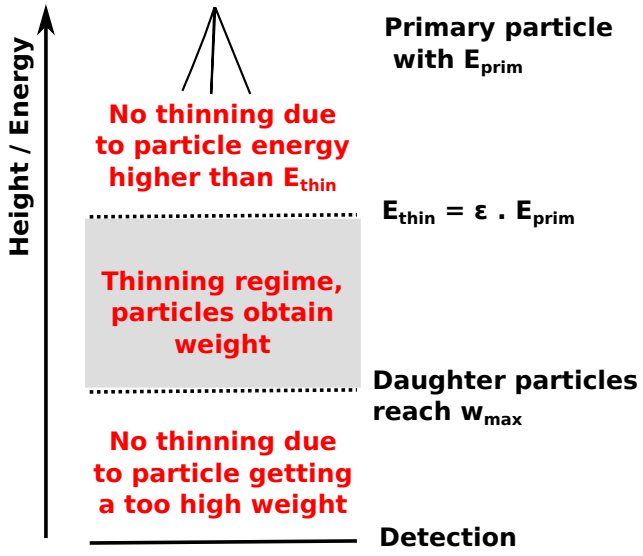

Figure 4.5: Sketch of the development of the thinning procedure.

4.1.2 Thinning

As the energy of the primary particle E_{prim} increases the number of secondary particles grows rapidly. If the approximate linear increase in EM particle number with primary energy (Figure 3.7) is used, roughly 10^8 electrons are expected at sea level for a 10^9 GeV primary particle, while the number of photons is even a factor of 10 larger (Figure 3.5). When all these particles need to be tracked and saved on disk, this becomes extremely time and memory consuming. A single simulation of a 10^9 GeV air shower for example would take a few days on a standard computer and occupy almost 100 GB of disk space. Since a large set of simulated air showers is required for a cosmic ray analysis, this full shower simulation is impossible at high energies.

To solve this problem a statistical thin sampling (or ”thinning”) method can be applied during the air shower propagation [164]. The thinning algorithm only keeps a limited number of secondary particles for further propagation, while other particles are discarded. The kept particles gain a weight according to the number of omitted particles. With this thinning method, 10^9 GeV air showers are simulated in hours as compared to days without thinning, and the file size is limited to about 1 GB.
At detection level the remaining particles then need to be ”dethinned” to restore the original shower as accurately as possible. The more particles are removed from the shower the faster the simulation and the smaller the final output file will be. However, this results in a loss of information and thus introduces larger uncertainties. If too many particles are removed it is impossible to restore the orginal shower reliably and artificial fluctuations are introduced. The thinning settings need to be well chosen such that these introduced fluctuations are smaller then the shower-to-shower fluctuations and no extra unphysical behaviour is created.

The settings that can be chosen in CORSIKA are the thinning level ϵ_{thin} and the maximal particle weight w_{max}. The thinning level defines the thinning energy $E_{thin} = \epsilon_{thin} \cdot E_{prim}$. Particles can be thinned (i.e. removed) as soon as their energy is below E_{thin}. Hence, E_{thin} rises linearly with E_{prim} if the thinning level is the same for all primary energies. As such, the total number of particles in the shower remains roughly constant for all energies and the computing time and storage are close to constant.
This thinning procedure is illustrated in Figure 4.5. In the first particle generations the particles still posses an energy higher than E_{thin}. After a certain number of interactions thinning starts, where some particles are removed and the others gain weight. These particles could then possibly reach their maximal weight w_{max} where the further thinning of the daughter particles is stopped.

Hence, in more detail, as soon as the energy E_d of one of the secondary (or daughter) particles produced in an interaction is below E_{thin}, the thinning procedure is started. Depending on whether the sum of the energy of all daughter particles is below E_{thin} or not, a different thinning procedure is used.
If $\sum_d E_d < E_{thin}$, only one of the daughter particles is kept with a probability p_d related to the particle energy:

$$p_d = \frac{E_d}{\sum_i E_i} \tag{4.3}$$

where i runs over all daughter particles.
This particle, the only one which is kept, obtains a weight $w_d = 1/p_d$. If the mother particle already has a weight itself (w_m), the weight of the daughter particle becomes $w_d = w_m/p_d$, i.e. the weights are multiplied.
In case that the sum of all daughter energies exceeds E_{thin}, all daughter particles with an energy higher than E_{thin} are kept, while the other particles are kept with a probability :

$$p_d = \frac{E_d}{E_{thin}} \tag{4.4}$$

and the weight is again $w_d = 1/p_d$. This thinning method ensures a smooth thinning at various energy levels and makes sure particle densities representing the original particle density are fine at detection level.
If one of the daughter particles reaches or exceed the maximal weight w_{max}, all secondary particles produced in this interaction are not further thinned. This limits "overthinning" that could cause artificial fluctuations to arise.
In CORSIKA one can choose a separate thinning level and maximal weight for the hadronic + muonic part and the electromagnetic part of the shower. This allows to keep the less abundant and (often) more important muons and hadrons, while the EM particles are thinned.

In simulations for IceTop, thinning is applied for air shower simulations with energies above 10 PeV. Normal (not thinned) simulations are performed up to 100 PeV. The region from 10 to 100 PeV is an overlap region between the two procedures and can thus be used to check the validity of the thinnning procedure. The electromagnetic thinning level is chosen to be $\epsilon_{thin}^{EM} = 10^{-6}$ up to a primary energy of $10^{8.4}$ GeV. This seems to be a good compromise between computing time and accuracy [165]. While the thinning energy rises with primary energy up to $E_{prim} = 10^{2.4}$ PeV, above this energy it is kept stable at $10^{2.4}$ GeV ≈ 273 GeV. This is done to avoid thinning of muons which can travel down to the in-ice detector: since the thinning energy E_{thin} is at least 273 GeV, particles with higher energies are never thinned. As such, no dethinning of those muons is required. Hence, a thinning level of $\epsilon_{thin}^{EM} = 273/E_{prim}$ is chosen for primary energies above $10^{2.4}$ PeV. The maximal weight for electromagnetic particles is chosen to be $w_{max} = E_{prim}\epsilon_{thin}$, and thus rises from 10 at $E_{prim} = 10$ PeV to 273 at $E_{prim} = 273$ PeV above which it remains 273. Muons and hadrons are chosen to not be thinned at all in air shower simulations for IceTop. Most muons thus have a weight of one, some low-energy muons might have very small weight due to re-interaction of the EM particles.
The dethinning procedure used in IceTop, aiming to retrieve the full particle distributions, is described in section 4.3.3.

4.2 Hadronic interaction models

The high-energy hadronic interactions constitute the starting point of the extensive air shower. An accurate modelling of these hadronic interactions is therefore of crucial importance. In section 3.4.4 the uncertainty induced by these models on the interpretation of the indirect measurements has been discussed. In the current situation it seems that when different EAS observables are used to reconstruct the original particle type, different results on the composition are obtained. Hence, a possible conclusion can be that the details in the air shower simulation are (slightly) off.

Most probably this is due to the description of the high-energetic hadronic collisions, since these interactions occur at energies that cannot be studied in man-made collider facilities. At the Large Hadron Colider (LHC), for example the accelerated protons currently (run II) have an energy of[1] 6.5 TeV. The total energy in the center-of-mass system is thus 13 TeV. The center-of-mass energy E_{cm} reached at the Tevatron was 1.8 TeV. In collisions that occur when a cosmic ray enters the atmosphere the cosmic ray possesses a huge energy, while the atmospheric nucleus is at rest (fixed-target collision). The relation between the center-of-mass energy and fixed-target energy is given by:

$$E_{cm} = \sqrt{s} \approx \sqrt{2 E_p m_t} \tag{4.5}$$

where s is the Mandelstam variable, E_p is the energy of the projectile and m_t is the mass of the (fixed) target. If the target is a proton, a center-of-mass energy of 1.8 TeV agrees roughly with a fixed-target energy of 1.7 PeV. The center-of-mass energy reached at LHC roughly corresponds to 90 PeV fixed-target energy. These energies are within the IceTop sensitive energy range but do not yet reach the highest energies of cosmic rays measured by IceTop ($\sim 10^3$ PeV). The ultra-high-energy cosmic rays (UHECRs), studied by the Pierre Auger and Telescope Array experiments, possess energies way beyond the energies achieved at the LHC. Furthermore, the very forward region in the collision is important for cosmic ray physics, but cannot be studied by the ATLAS [166] and CMS [167] experiments at LHC since their detectors do not cover this region. The smaller LHCf [168] and TOTEM [169] experiments focus on forward particles close to the beamline. In general, the accelerator experiments mainly detect reaction products with a large momentum transfer (”hard” interactions), while cosmic-ray experiments detect particles from ”soft ” interactions with a low momentum transfer. At last, at LHC mainly protons are accelerated and studied. Only from time to time heavier nuclei are injected in the accelerator, and they are studied to a lesser extent. In cosmic rays, on the other hand, the air nuclei are mostly oxygen and nitrogen, and the projectiles can be heavier nuclei, but also for example secondary pions.

The models that describe the hadronic interactions thus need to rely on a theoretically-founded principle to scale the measured parameters from accelerator to cosmic-ray energies. The three leading models that are commonly used to describe the hadronic interactions with $E_{cm} > 80$ GeV are Sibyll [170], QGSJet [171] and EPOS [172].
The general picture to describe the interactions used by all models relies on quantum chromodynamics (QCD). In the interaction between the projectile and the target nucleus multiple ”parton ladders” (quark + gluon) are created, which emerge from colour exchange between the contributing partons of both nuclei followed by a hadronization process [173, 174]. While the evolution of the hard (high-p_t) partons can be described by perturbative QCD, the soft (low-p_t) parton evolution is approximated with Gribov-Regge field theory [175, 176]. The detailed treatments of the energy sharing and the further evolution of the partons differ between the models and lead to varying extrapolations. QGSJet and Sibyll have a minimal set of parameters and are focussed towards the description of air showers. QGSJet is based on multipomeron exchange, a quasi-particle with quantum numbers equal to the vacuum quantum numbers. Sibyll on the other hand is based on the dual parton model, Lund string fragmentation and the minijet approximation. Furthermore, it uses the semisuperposition model to describe nucleus-nucleus interactions [100]. EPOS also uses the multipomeron

[1] 1 TeV = 10^3 GeV

Table 4.3: Overview of the leading hadronic interaction models with their pre- and post-LHC versions.

pre-LHC model	post-LHC model
Sibyll 2.1	Sibyll 2.3
QGSJet-II.03	QGSJet-II.04
EPOS	EPOS-LHC

exchange approximation [177]. As opposed to QGSJet, EPOS focusses on the tuning to and description of accelerator data, mainly from heavy ion interactions. Therefore it has a detailed implementation with many tuneable parameters.

All of these models were recently updated to include the results from the Large Hadron Collider, i.e. mainly ATLAS, CMS, TOTEM and LHCf and fixed-target experiments like NA61/SHINE [178]. The pre-LHC models are respectively Sibyll 2.1 [100], QGSJet-II.03 [179, 180, 181] and EPOS 1.99 [182, 183], while the updated post-LHC versions are Sibyll 2.3 [184], QGSJet-II.04 [171] and EPOS-LHC (v3400) [172]. Further improvements to Sibyll 2.3 have lead to a Sibyll 2.3c version [170]. The difference between this version and Sibyll 2.3 is, however, small regarding air showers. Larger effects are present for lepton fluxes and neutrinos. The current simulations for cosmic ray analyses with IceTop and IceCube use Sibyll 2.3 as post-LHC version of the Sibyll hadronic model, not Sibyll 2.3c. A short overview of the pre- and post-LHC versions of the models is given in Table 4.3

As discussed above, the models all start from roughly the same base approximation, but differ significantly in further theoretical approach and extrapolations to higher energies. This has important consequences for the final EAS observables. Mainly the interaction cross section, secondary particle multiplicity and number of charged versus neutral particles are the most important variables that influence the final distributions. Furthermore, also the angular distribution of the secondaries, the energy fraction and type of the leading particle etc. are important. In [185] the pre- and post-LHC versions of QGSJet and EPOS are discussed. The changes within Sibyll are highlighted in [184] and [170].

In the following we describe the influence of the models on two important composition-sensitive variables: the depth of shower maximum (X_{max}) and the muon multiplicity N_μ.
The evolution of the cross section with energy was shown before in Figure 3.3, which also indicates the values in the various pre-LHC hadronic models. New data from the LHC was added to these measurements, which put stringent constraints on the models. This results in a much better agreement in the cross section or mean free path between the various models, where the variation between QGSJet and EPOS decreased by about a factor of 5 [185]. Sibyll 2.1 had the largest cross section of all pre-LHC models, and this is decreased in Sibyll 2.3 [186], agreeing more with the data and with EPOS and QGSJet. From Eq. 3.13 it can be seen that this change in cross section is important for the position of the depth of shower maximum (X_{max}). Consequently, this also has an influence on the number of electromagnetic particles observed at the surface, since the age of the shower changes. The same equation furthermore shows that the number of produced secondary particles (N_{sec}) has an influence on the position of shower maximum, but that the dependence is weaker (log). The differences between the models on the other hand concerning the particle multiplicity are larger as than for the cross section. While for pre-LHC models the variation in secondary particle number could reach a factor of 10 at the highest energies, this variation is reduced to a factor of $\sim$2 for the post-LHC models. The elasticity of the collision (the energy fraction carried away by the leading particle), also, among other effects, influences the position of X_{max}. Probably related to the somewhat lower secondary particle multiplicity in Sibyll 2.3, this model shows the highest elasticity [174].
The tuning of the models to LHC data thus resulted in a converged and more trustworthy result for these parameters. This is reflected in the current X_{max} prediction by the models. While the X_{max} prediction for a certain primary particle type at 10^{11} GeV varied by 70 g/cm^2 between the pre-LHC models, this is reduced

to 40 g/cm^2 for the post-LHC models. Sibyll 2.3 predicts the largest X_{max} and QGSJet-II.04 the smallest. This seems directly related to the fact that Sibyll has the lowest secondary multiplicity. In general, all post-LHC models predict a slightly deeper depth of shower maximum compared to the pre-LHC models. The comparison of the data to these updated curves thus results in an increase of the average reconstructed mass compared to the pre-LHC models. The elongation rate, the increase of X_{max} with primary energy, seems now consistent between Sibyll, EPOS and QGSJet. The current post-LHC X_{max} predictions are shown in Figure 4.6 (left), together with recent data. Figure 4.7 (left) indicates the shift in X_{max} of the post-LHC models as compared to the pre-LHC Sibyll 2.1.

A second important change in the pre- versus post-LHC versions of the models involves their prediction of the produced muon multiplicity at detection level. Since more than 10 years it is known that the number of muons produced in simulations (using pre-LHC models) does not agree with the muon number observed in data. For example, in [187] it was stated that "*the derived muon density would correspond to a primary cosmic ray composition heavier than iron*", which does not agree with the composition measurements using X_{max} (part 3.4.3) and also does not seem probable. Moreover, the prediction of the muon number varied enormously according to the chosen interaction model. For example, the prediction of the number of muons in iron produced showers for QGSJet II.03 was as much as the predicted muon multiplicity for proton induced showers of the same energy when EPOS 1.99 was used as hadronic interaction model.
In the post-LHC versions of QGSJet and Sibyll the muon number is significantly increased, which is -very roughly stated- related to the number of charged versus neutral particles. There are two mechanisms leading to an increased muon number [188]. The first is the increased rate of the production of baryon-antibaryon pairs during the string fragmentation process, instead of mesons. These baryons undergo further interactions which create more low-energy muons. A second mechanism is the fact that ρ^0 mesons could be created instead of leading π^0 mesons. ρ^0 mesons have spin-1, as opposed the spin-0 π^0, and they decay roughly 100% to $\pi^+\pi^-$. Hence, the energy is kept in the hadronic part of the shower and not diverted to the electromagnetic component. Also this results in more muons. This ρ^0 creation is indeed verified at fixed-target experiments. The ρ^0 creation was already implemented in the pre-LHC EPOS 1.99, but not in Sibyll and QGSJet. Hence, the number of muons in EPOS 1.99 and EPOS-LHC remains roughly similar. QGSJet and Sibyll, on the other hand, both show an increased muon number in the post-LHC models compared to the pre-LHC models. In Sibyll even a relative muon number increase of more than 20 % is observed [184]. As opposed to the pre-LHC versions of the models, the various models now seem to roughly agree in the average muon number, with a maximal difference of $\sim$20 %. The absolute muon multiplicity in the different models is shown in Figure 4.6 (right), while the increase as compared to Sibyll 2.1 is shown in Figure 4.7 (right).

It can be concluded that the models have undergone important updates and a more coherent picture is obtained. However, still some caution is required and significant uncertainties remain. Indeed, for example the Pierre Auger Observatory still measures roughly 30 % (2σ) more muons in data as compared to simulations [157] for vertical showers. Furthermore, while the number of muons roughly agrees within the models, significant differences still arise in the muon energy spectra. It seems therefore still possible that a measurement of high-energy muons results in a different composition as compared to when lower energetic muons are used to deduce the primary particle type. On top, also the distance from the shower core at which the muons are sampled might influence the reconstructed composition, since the slope of the muon lateral distribution function is subject to significant uncertainties.
Hence, the cosmic ray experiments themselves can and should provide further useful input to the models, which is one of the aims of this work.

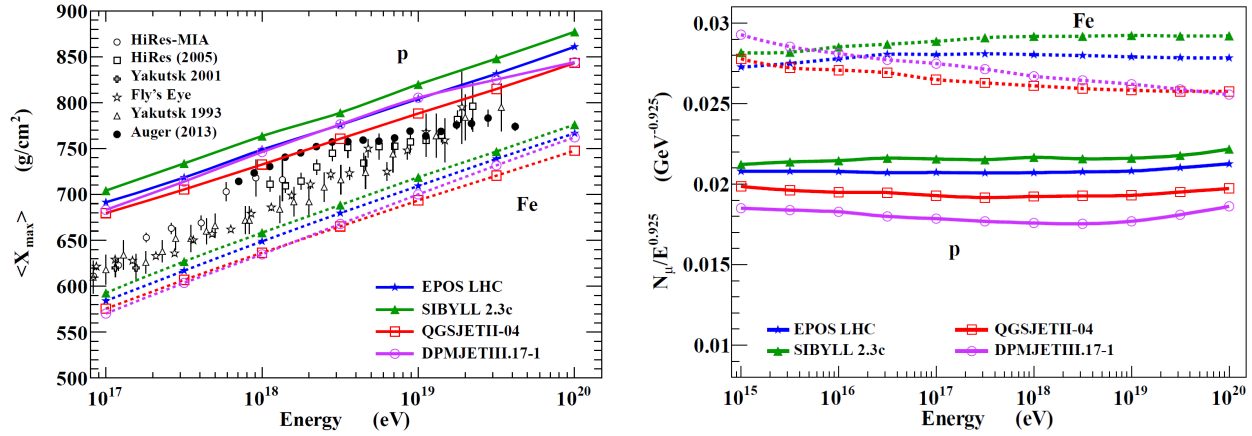

Figure 4.6: Average depth of shower maximum X_{max} (left) and number of muons N_μ (right - weighted with $E^{-0.925}$). The averages obtained with the various hadronic interaction models are shown in the various colours (proton: solid ; iron: dashed). For X_{max} also the data is added. [174]

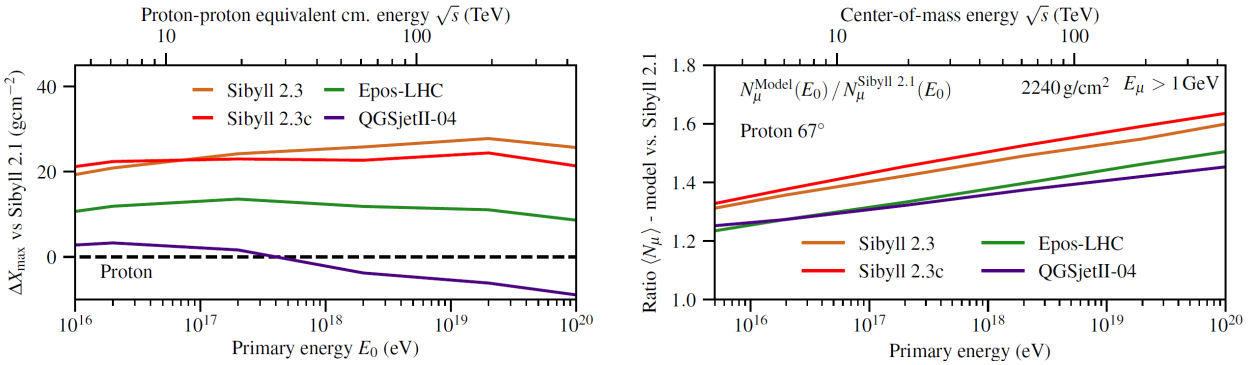

Figure 4.7: Change in depth of shower maximum X_{max} (left) and muon multiplicity N_μ with $E_\mu > 1$ GeV (right) of the post-LHC models with regard to Sibyll 2.1. [170]

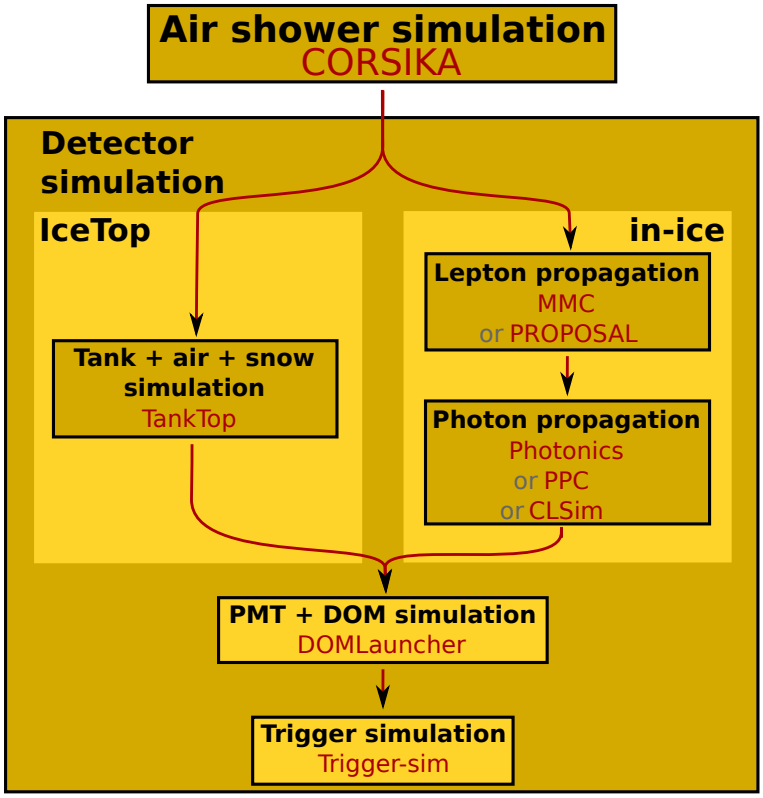

Figure 4.8: Rough flow chart of the main steps in the simulation chain.

4.3 Detector simulation

To be able to compare the data to the simulations also the full response of the detector to the air shower needs to be simulated. All secondary particles at the observation level chosen in CORSIKA (2837 m a.s.l.) are read out and propagated through the detector. The main steps in the simulation procedure are illustrated in Figure 4.8 and further explained below. Firstly, the shower is thrown at a random position in the vicinity of the array. Then the response of IceTop to all particles is simulated, and only the muons with an energy $E_\mu > 273$ GeV are propagated to the deep IceCube detector. The simulation of the PMT response and the signal processing by the DAQ is common for IceTop and IceCube DOMs. Finally, also the trigger is simulated, since for the data this is part of the data-taking process. As such, the same reconstruction can be applied to both data and simulation.

4.3.1 Resampling

Since the CORSIKA simulation of high-energetic showers takes a long time and a huge amount of statistics is required for high-level analyses, the air shower is first resampled several times. Effectively, this means that every simulated air shower is copied and thrown at a random position in and around the IceTop array. As such, the air shower has various unique footprints on the IceTop array.
Each air shower is resampled 100 times and randomly distributed in a circle around the center of the IceTop array. The radius of this circle should be at least the distance up to which a shower of a certain energy can still create a trigger in the IceTop array. Since the lateral size of an EAS increases with primary energy, also the resampling radius should increase with the primary energy. The resampling radii used in the simulations for various primary energy bins are given in Table 4.4.

Figure 4.9 displays the distribution of the number of used resamples per simulated shower, as function of the primary energy (for primary energies from 100 TeV to 100 PeV). On top, the distribution is shown for all

Table 4.4: Resample radius for the various primary energy bins.

$\log_{10}(E_{\mathrm{prim}}/\mathrm{GeV})$	Resampling radius (m)
5.0-6.0	800
6.0-7.0	1100
7.0-8.0	1700
8.0-9.0	2600
9.0-9.5	2900

events which pass the IceTop SMT trigger (section 2.2.4) and a cosmic ray filter (section 5.2.3). The black line indicates the average number of resamples used for an air shower which passes the trigger and fitler with at least one of its resamples. With increasing energy, the average number of used resamples increases, until another decade in energy is reached and the resample radius increases (Table 4.4). In the middle panel the same distribution is shown, but only the resamples which show a good event quality in IceTop (section 5.3.6), i.e. with a reliable reconstruction, are used. This thus shows the number of resamples used in an analysis that uses only the IceTop detector. In the energy region between 1 and 10 PeV this can reach up to 30 resamples per shower, with an average of $\approx$15. In the bottom figure only the resamples that have a reliable reconstruction in both the IceTop and IceCube detector (section 5.4.4) are shown. For a coincident analysis, on average around 5 resamples seem to be used per simulated shower, if one of the resamples passes the IceTop and IceCube event selection.

4.3.2 IceTop simulation

When the location of the shower core is randomly chosen within the resampling area, the EAS footprint on the IceTop array is calculated. Since an air shower can consist of millions of particles it is more efficient to treat the particles one by one: each particle is read out separately from the CORSIKA file and forwarded to the detector simulation, where its signal deposition is simulated. As a first step it is examined whether the particle could intersect with one of the tanks, where a safety margin of a 30 cm around the tank is used. If no tank is found within 30 cm of the particle track, the particle is omitted. A kept particle is checked for a possible weight obtained during the thinning procedure (section 4.1.2). For particles with a weight exceeding 1 the ”dethinning” algorithm (section 4.3.3) is applied.

Before the particle hits the tank it first needs to propagate through a certain amount of air and snow. The particle interaction with material is simulated using the common Geant4 package [189]. The snow, discussed in depth in section 5.5.1, was modeled as pure H_2O with a density of 0.38 g/cm^3. The used snow height on top of the tanks for simulations of a certain data-taking season are based on the first in-situ measurements of the according Antarctic summer season, in October or November. These months are somewhere in the middle of the data-taking period of one season, which often starts in May. Thus, they -very roughly- correspond to the average snow level of that season. For example, simulations of the IC86.2012 data-taking year (from May 2012 to May 2013) use the snow heights measured in October 2012.

The signal deposition of a particle in the IceTop tank is computed using the standalone ”TankTop” code [54, 190], which is also based on Geant4. Instead of performing the entire chain of particle propagation, energy loss, Cherenkov light generation and light propagation in the tank a parametrization of the light yield is used [191]. First, the track length of the particle through the tank is computed. The number of emitted photons along the track is then drawn from a Poisson distribution with the expected number given by the Frank-Tamm Formula (Eq. 2.2). TankTop provides the parametrization of the linear relationship between number of produced photons and photons at the photocathode. The conversion parameters used in TankTop, varying on a tank-by-tank base due to different optical properties, are determined from special calibration measurements in data. As such, the signal of a vertical muon is the same in data and simulation. This

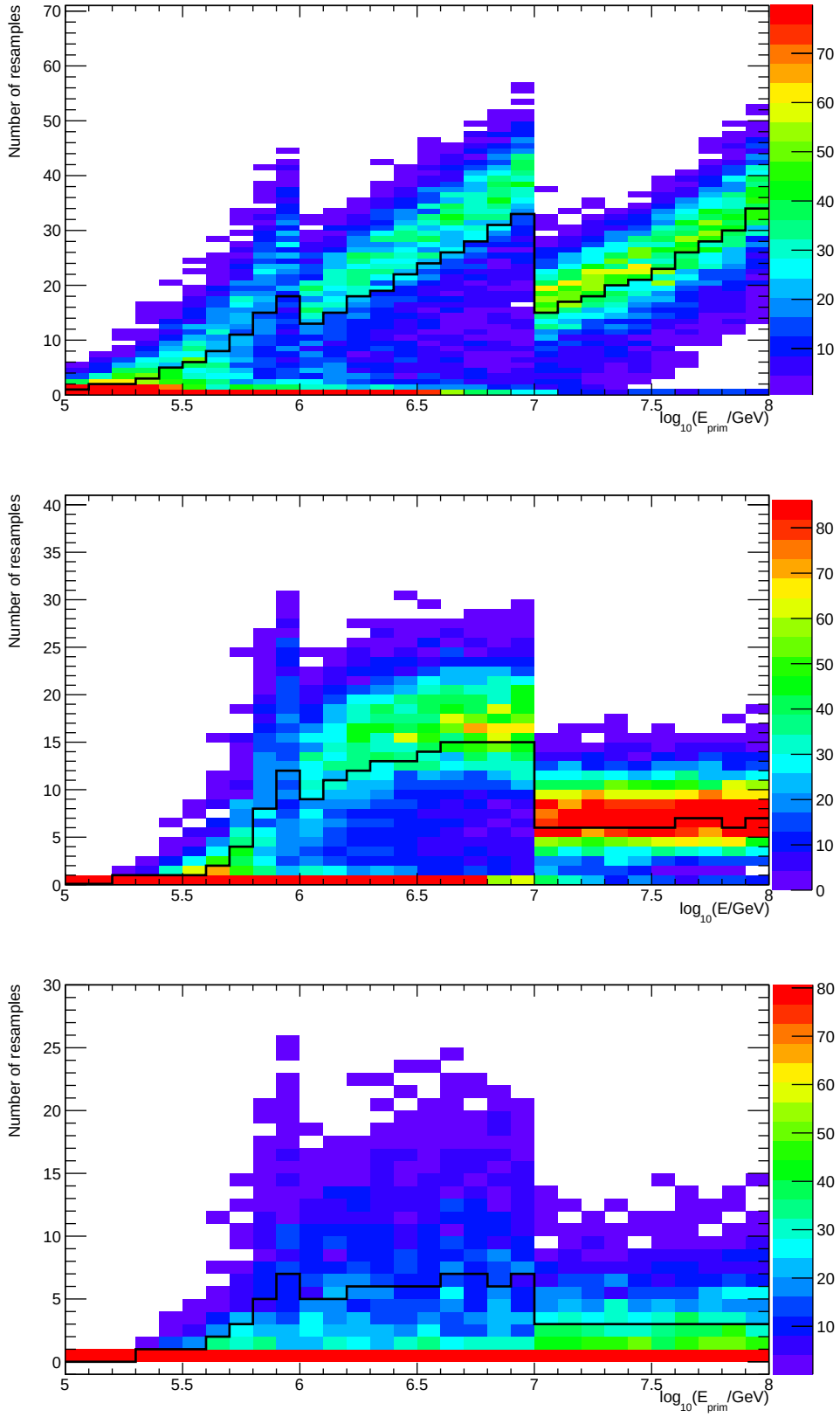

Figure 4.9: Distribution of the number of used resamples of simulated CORSIKA air showers, as a function of the primary energy. The black line indicates the average. Top: distribution after cosmic ray trigger and filter, center: only using events that survived the IceTop event selection (section 5.3.6). Bottom: events surviving the IceTop and IceCube event selection (section 5.4.4).

calibration, using vertical muons, is described in detail in part 5.2.2. It is also studied in more detail using simulations of low-energetic showers and a full simulation of the tank, including the PMT and DOM electronics [192]. In the end the peak of the simulated charge distribution differs by a factor 1.02 between simulations and data. This is used as correction factor but also defines the charge uncertainty and will thus be used as systematic error.

The arrival times of the created Cherenkov photons follow an exponential profile after their creation. The time constants depend on the reflectivity of the tank and is thus different for the tanks with the Zirconium compared to the Tyvek liners. In the main simulation the information about which initial particle causes each photoelectron is not kept to limit the computing time and file size. However, this is an option in the simulations which can be useful for certain analyses, like the time structure of the waveforms.

After the deduction of the number of photoelectrons per DOM and their time structure the response of the PMT and DOM electronics is simulated. This is performed similar to the in-ice DOMs [193] and aims to mimic the real PMT and DAQ behaviour as accurately as possible. In the simulation of the photomultiplier tube the initial photoelectron pulses are amplified with the gain and smeared according to the PMT charge response function [55]. Also the arrival times at the anodes are smeared. Furthermore, the creation of pre- and afterpulses needs to be simulated. Finally the simulation also includes the saturation of the PMT. The output of the PMT simulator is used as input for the simulation of the DAQ system [57], i.e. mainly the processing occuring on the DOM mainboard (part 2.1.2). The discriminator is modelled where the single photoelectron waveforms deduced from calibration runs in real data are used to determine the discriminator threshold for each DOM. As a next step the local coincidence conditions are checked and a possible dead time is taken into account. Finally, also the digitization procedure by the ATWD channels and FADC chip is simulated. This DAQ simulation also includes the beacon launches and electronic noise simulation. As such, the simulation resambles the data as closely as possible.

At the end also the trigger system is simulated, which includes both the IceTop and IceCube part (described in section 4.3.4). It should be noted that multiple showers occuring in the same trigger window are not simulated. Furthermore, also other than electronic noise is not simulated. The cleaning algorithms described in Chapter 5 should, however, take care of this. The same analysis scripts including cleaning and reconstruction can thus be applied to both data and simulation.

4.3.3 Dethinning

If, for high-energy air showers, the thinning algorithm was applied (part 4.1.2), one needs to account for this during the detector simulation. The goal of this dethinning (or ”unthinning”) procedure is to restore the shower that would have been obtained without thinning as accurately as possible. This can be done by taking the weights w_p gathered by the particles into account, since these represent the number of missing particles of similar energies and properties.

One method to do this is to only take the particles which intersect with the thank, as for normal showers, and inject them w_p times in the tank. This, however, causes the use of the same particle multiple times which could introduce artificial fluctuations.
An alternative approach is to enlarge the area around the tank in which particles are accepted and inject them all in the tank. For particles with weight w_p the area should then be increased by a factor of w_p, such that hopefully w_p similar particles are sampled. However, with this area increase caution is required since the local particle density and properties need to be preserved. Indeed, if a too large resampling region is chosen, possible biases can be created due to the steepness of the lateral distribution function. Since the lateral distribution function is steeper close to the core of the air shower the resampling region is in general smaller close to the core compared to further. Despite the possible bias, this introduction of a sampling region

is better than the generation of w_p clones of the same particle and is often used for dethinning algorithms. It was first described in detail in [194] by P. Billoir. In general, a fixed sampling region is defined around each tank (A_{samp}). In this paper these regions are ring segments, with an opening angle of 40° as seen from the shower core. The radius of the ring segment increases with the distance to the shower core, and should not exceed 10 % of this distance. Due to the increased area to accept particles all particles in this area obtain a reduced weight:

$$w_{pr} = w_p \frac{A_{dp}}{A_{samp}} \tag{4.6}$$

where A_{dp} is the area of the tank (with radius R and height H) seen by a particle with zenith angle θ_p:

$$A_{dp} = \pi R^2 + 2RH \tan\theta_p \tag{4.7}$$

If the sampling region remains too small to account for a certain weight of a particle, $w_{pr} > 1$ and this particle nevertheless has to be cloned w_{pr} times. If, on the other hand, the reduced weight of the particle is smaller than 1, the particle is inserted in the tank with a probability w_{pr}. The arrival time of the particle is corrected according to the shower front and a time smearing is introduced.

The dethinning algorithm used in the current cosmic ray simulations for IceTop also uses the increasing sampling area. It is described in detail in [165]. However, instead of using a predefined sampling area it tries to deduce the optimal area on the fly. To get the best resampling area two requirements need to be met:

1. The average reduced weight (Eq. 4.6) of all the particles in the resampling area should approach one, which would avoid cloning particles many times. This translates in the following minimization:

$$|\frac{\sum_p w_p A_{dp}}{A_{samp}} - n_{samp}| = min \tag{4.8}$$

   where n_{samp} is the number of particles inside the sampling area.

2. The average particle density in the tank should be reproduced in the entire area. Instead of using the limited tank area for the estimation of the local particle density, a slightly larger area (A_{ext}) is used. In [165] this is chosen to be a circle with a radius of 10 m. Hence, the following equation needs to be minimized.

$$|n_{samp}\frac{A_{ext}}{A_{samp}} - n_{ext}| = min \tag{4.9}$$

   with n_{ext} the number of particles in A_{ext}.

A further requirement is $n_{samp}/n_{ext} > 0.05$ to exclude very small optimal sampling radii. To obtain the optimal resample radius an iteration over possible resampling radii from 1 m to 25 m is performed.

An example of obtained resampling radii as function of the distance between the tank and the shower core is shown in Figure 4.10, for a proton initiated shower with an energy of 1 EeV. Hence, the maximal weight in these simulations is 273 (section 4.1.2). As can be seen, the found optimal resampling radii decrease with the distance to the shower core. This is partially due to the fact that muons, which in general have weight 1 (secttion 4.1.2) and become more important far from the shower core, are taken into account in this minimization. Furthermore, also the choice of A_{ext} can cause this decrease of the resampling radius with distance of the tank to the shower core. Although this minimization technique seems a smart procedure to find an optimal dethinning area, it contradicts one of the main requirements posted by Billoir: that the radius of the dethinning area should decrease with distance to the shower core to guard the local particle density at the tank. Indeed, as the radius of this circular resampling area increases, this would result in an increasing bias towards a higher energy deposit due to the steep LDF. At the moment, the influence of the existing unthinning method on the simulations is being investigated. No evidence of an effect in the simulations is

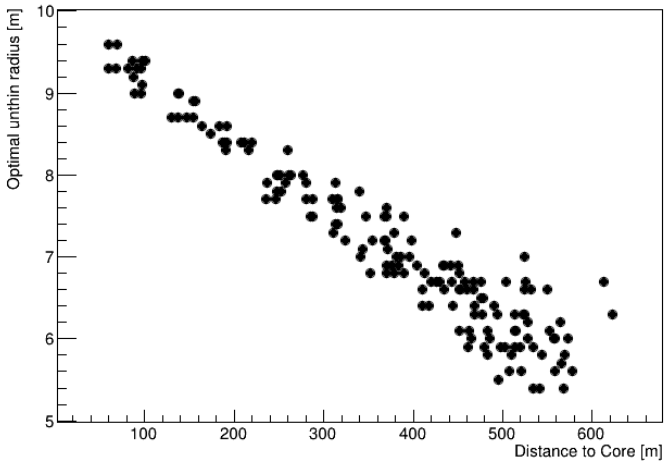

Figure 4.10: Obtained unthinning radius as function of the distance to the shower core for a 1 EeV proton initiated shower in the IceTop dethinning procedure. Each dot represents an IceTop tank.

found yet.
Nevertheless, a possible bias would be less with the ring segment as proposed in the paper by Billoir [194]. Therefore, an unthinning procedure close to the one proposed by Billoir is now being implemented in the IceTop simulation [195]. Further studies already compared the two unthinners in their behaviour and quality [196]. Although no clear sign of an error in the previous unthinner is observed, some suspision remains.

4.3.4 IceCube simulation

At the moment when the particles are read out from the CORSIKA files, relocated and injected in the IceTop tanks, a separate list of muons with energies exceeding 273 GeV is constructed. These muons can propagate down to the IceCube detector. They create secondary particles through energy loss processes and, altogether, generate a huge amount of Cherenkov photons. Their entire path from the surface to the detector is simulated, although they can also be stopped at smaller depths or completely miss the detector. The energy loss processes and secondary particles are saved if they take place within a volume with height 1700 m and radius 1200 m around the center of the IceCube array.

The initial code used for the muon propagation and the energy loss simulation in IceCube was MMC (Muon Monte Carlo) [197]. Since this was written in Java it became more and more difficult to support its integration with the main simulation project, which is mainly C++ based. Therefore the successor code of MMC, PROPOSAL (Propagator with Optimal Precision and Optimized Speed for All Leptons) [198] was written in C++. Aside from the better performance with regard to processing speed, it also provides an improved precision. However, the results obtained with MMC and PROPOSAL are very similar. The cosmic ray simulations for the IC79 configuration used MMC for the muon propagation and energy loss processes, while simulations from IC86.2011 onwards use PROPOSAL.
In the next step of the simulation chain the Cherenkov photons are generated, propagated through the ice and saved if they hit one of the DOMs. Since many Cherenkov photons are produced, this is a time consuming step in the simulations. The main package used to perform cosmic-ray simulations for the IC79 configuration is Photonics [199]. Photonics uses dedicated simulations to produce look-up tables containing the final photon flux in spacetime for many photon emission points. The photon emission angle and the incident photon angle on the DOM are furthermore taken into account, thus in total the tables are binned in 6 dimensions. The actual simulation datasets then use an interpolation of these tables to describe the photon

propagation process. Furthermore, also the ice properties need to be taken into account (section 2.1.3). This is done using the SpiceMie ice model [59], with the measured parameters for scattering and absorption as a baseline. Alternative tables need to be produced for simulation datasets used to cover the ice systematic uncertainties.
However, this interpolation method using tables suffers from various problems. At first, for every small change in, for example, the ice model new tables need to be generated, which is very time consuming. Furthermore, also the interpolation can be a problem and loading the tables requires large memory. With the rise of GPU (Graphical Processing Unit) computing two new photon propagation packages were developed. These can perform direct photon tracking due to the large parallellization ability of GPUs. CLSim [200] uses the openCL (open Computing Language) API to perform the parallel computing on the GPUs. PPC (Photon Propagation Code) [201] uses CUDA, software developed by the NVIDIA computer hardware company to perform general-purpose computing on their NVIDIA GPUs. CLSim on the other hand can be used on many architectures. CLSim decouples the photon production, propagation and storage. Only the propagation part is performed using GPUs. The photon production can make use of a full Geant4 simulation or a parametrization by for example PPC. The cosmic-ray simulations for the IC86.2011 configuration and following partially use CLSim. Since a muon bundle consists of many muons, which each produce large stochastic energy losses with according Cherenkov photons, this direct propagation method is still too time consuming. Instead, a hybrid simulation method is used: the direct photon propagation is only performed for the Cherenkov photons created by the muons themselves, while the Cherenkov photons from the cascades still use an interpolation of tables. The tables could be obtained from Photonics or defined inside CLSim and use an improved interpolation method using splines [202].

Afterwards, noise is added to the simulations, including thermal and nonthermal noise due to radioactive decay in the PMT and glass sphere [203]. The simulation of the PMT and DOM electronics is performed exactly the same as for the IceTop DOMs (described in section 4.3.2). Afterwards, the trigger is simulated, which was also discussed in section 4.3.2.

4.4 Framework and dataset specifics

4.4.1 IceTray and IceProd

The sequence of the various parts of the software and analyses within IceCube are linked via one main framework, called ”IceTray” [204]. Within this framework, separate software modules act on the data on an event-by-event base. The separate modules largely decouple the various analysis parts and allow an easy plug-in of new parts, while via the event-by-event analysis many events can be split over several computing nodes to speed up the process.
In order to accommodate the huge computing requirements for a large experiment such as IceCube, an efficient computing system needs to be adopted. In the IceCube collaboration a software package called ’IceProd’ was developed [205, 206]. This package distributes the various computing jobs over participating computing facilities around the world. It also collects information about whether or not the job succeeded, how many jobs still remain, decides on the priorities of certain jobs, etc. Official collections of data (’datasets’) are then used by many collaborators within the IceCube collaboration. As such, resources are shared and also errors occur less frequently.

4.4.2 Datasets used

In the work described in the following chapters both the datasets produced for the IC79 and IC86.2012 configuration (Table 2.1) of the detector are used. A list of all these datasets is provided in Tables 4.5 and 4.6, for respectively IC79 and IC86.2012 simulations. The dataset numbers, given for reference, refer to the Level 2 name of the datasets. The tables list the most important dataset properties: primary particle

Table 4.5: Specifications of the datasets produced for the IC79 configurations.

Primary	Int. model	Zen. (°)	Atm.	Thinned	$\log_{10}$(E/GeV)	N showers	Dataset
H	Sibyll 2.1	0-40	July 1, 1997	No	5-8	2000	7006
He	Sibyll 2.1	0-40	July 1, 1997	No	5-8	2000	7241,7263
O	Sibyll 2.1	0-40	July 1, 1997	No	5-8	2000	7242,7262
Fe	Sibyll 2.1	0-40	July 1, 1997	No	5-8	2000	7007
H	Sibyll 2.1	0-40	July 1, 1997	Yes	7-9.5	2000	7579
He	Sibyll 2.1	0-40	July 1, 1997	Yes	7-9.5	2000	7791
O	Sibyll 2.1	0-40	July 1, 1997	Yes	7-9.5	2000	7851
Fe	Sibyll 2.1	0-40	July 1, 1997	Yes	7-9.5	2000	7784

Table 4.6: Specifications of the IC86.2012 datasets used in the analysis presented in this thesis.

Primary	Int. model	Zen. (°)	Atm.	Thinned	$\log_{10}$(E/GeV)	N showers	Dataset
H	Sibyll 2.1	0-65	April	No	5-8	2000/3	12360
Fe	Sibyll 2.1	0-65	April	No	5-8	2000/3	12362
H	Sibyll 2.3	0-65	April	No	5-8	200	12632
Fe	Sibyll 2.3	0-65	April	No	5-8	200	12633
H	EPOS-LHC	0-65	April	No	5-8	200	12634
Fe	EPOS-LHC	0-65	April	No	5-8	200	12635
H	QGSJET II-04	0-65	April	No	5-8	200	12636
Fe	QGSJET II-04	0-65	April	No	5-8	200	12637

type, hadronic interaction model, zenith angle range (in °), atmospheric profile, whether the showers where thinned, the energy range (in $\log_{10}$(E/GeV)) and the number of showers present in each energy bin of 0.1 in $\log_{10}$(E).
As can be seen, the IC79 simulations range from a primary energy of 10^5 to $10^{9.5}$ GeV. The used IC86.2012 simulations only range up to 10^8 GeV (100 PeV), since the thinned simulations have not yet been finished at the time of this analysis. The IC86.2012 simulations, on the other hand, focus on the various post-LHC hadronic interaction models, although the base datasets were still produced with Sibyll 2.1.

The different properties of the simulation sets for the two configurations translate into their application further on in this work. The IC79 simulations, covering the full energy range investigated by IceTop, are mainly used in the development of the analysis chain of cosmic rays with the IceCube Neutrino Observatory (Chapter 5). The IC86.2012 simulations on the other hand are used in the study of the hadronic interaction models in a specific energy range, i.e. for the analysis described in this work (Chapters 6 and 7).

4.4.3 Weighting

As described in Tables 4.5 and 4.6, the produced simulation datasets include a fixed number of events per energy bin of 0.1 in $\log_{10}$(E/GeV). On top of this each shower has been resampled 100 times over a certain area around the core of the IceTop array (section 4.3.1). Furthermore the produced energy spectrum in simulation follows an E^{-1} spectrum (section 4.1), which does not at all resemble the real distribution in data (section 1.1.1).
To compare the distributions of all variables between simulation and data, the simulation needs to be reweighted to -roughly- agree with the data distributions. This includes several steps where one has to take the number of produced events, the width of the energy bin, the produced energy spectrum, the zenith angle and the resample area into account.
As approximation for the data a certain flux model $\Phi_{model}(E)$ is assumed. This could be a simple power law spectrum for all masses, or a more complicated model like the H4a model [207]. The flux in simulation $\Phi_{sim}(E)$ should thus be reweighted to this model:

$$w(E) \cdot \Phi_{sim}(E) = \Phi_{model}(E) \tag{4.10}$$

where a certain weight w depending on the energy is introduced.
This weight can thus be computed from the model and the simulated flux:

$$w(E) = \frac{\Phi_{model}(E)}{\Phi_{sim}(E)} = \frac{\Phi_{model}(E)}{\phi_{sim}(E) \cdot E^{-1}} \tag{4.11}$$

where the total simulated flux is already split into two components. The E^{-1} factor accounts for the fact that the simulations produce an E^{-1} spectrum. $\phi_{sim}(E)$ on the other hand should include all other factors contributing to the number of produced events in one $\log_{10}(E)$ bin.
This is given by:

$$\phi_{sim}(E) = \frac{\log_{10}(e) \cdot 100 \cdot N_{ev}(E)}{0.1 \cdot A_{res}(E) \cdot \Omega_{sim}} \tag{4.12}$$

$N_{ev}(E)$ is the number of simulated events in this energy bin, and the factor 100 accounts for the resampling. The resample area $A_{res} = \pi \cdot r_{res}^2$ depends on the energy, as shown in Table 4.4. The factor $\frac{\log_{10}(e)}{0.1}$ arises from the binwidth.
Since the total flux is always given per steradian, also the simulated solid angle Ω_{sim} should be taken into account. This is given by:

$$\Omega_{sim} = \pi \cdot \sin^2 \theta_{max} \tag{4.13}$$

where θ_{max} is the maximum simulated zenith angle.

The reweighting procedure of the simulations to a realistic data flux is illustrated in Figure 4.11. Here the proton datasets for the IC79 configuration are used (Table 4.5). The top plot shows the number of air showers as function of the primary energy that survive the IceTop event selections (described further on in section 5.3.6). At the lowest energies one observes the detection threshold. At higher energies one clearly observes the cascaded decrease of the event number, caused by the stepwise increasing resample area (Table 4.4). This has been taken care of in the central figure, by applying a weight as given in Eq 4.12. This figure also illustrates the stable number of successfully reconstructed events within the IceTop area. Finally, this is reweighted to a realistic energy spectrum (Eq. 4.11): the flux at 1 PeV is used as determined by the H4a model, while the energy spectrum decreases following $E^{-2.7}$ below and E^{-3} above 1 PeV.

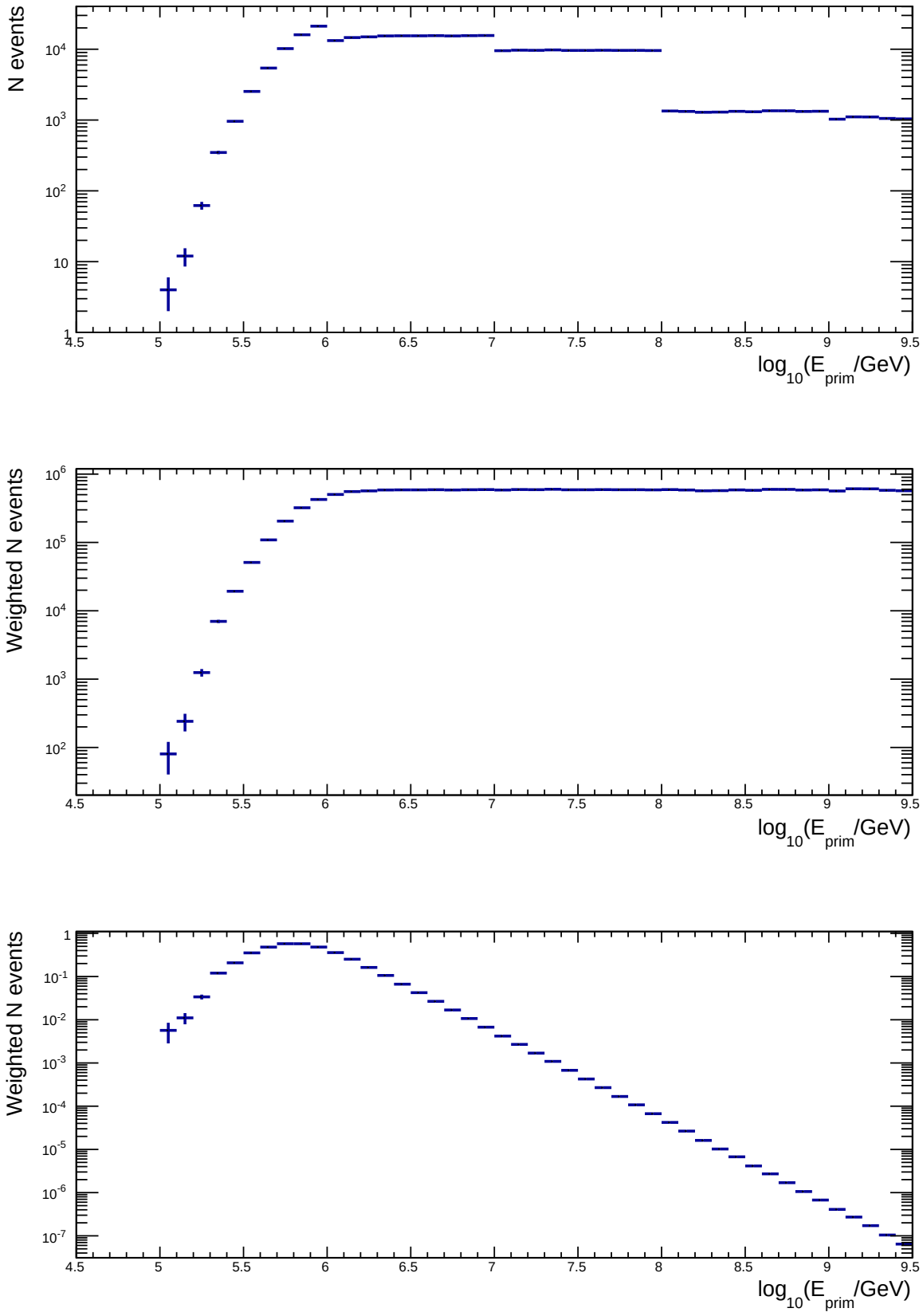

Figure 4.11: Illustration of the simulation reweighting, using the proton IC79 simulation datasets (Table 4.5). Top: number of events as function of primary energy after IceTop quality cuts (section 5.3.6). Central: the events obtained a weight related to the resampling area. Bottom: reweighted to a flux model.

5

Cosmic ray physics with IceCube

Study nature, love nature, stay close to nature. It will never fail you.

Frank Lloyd Wright

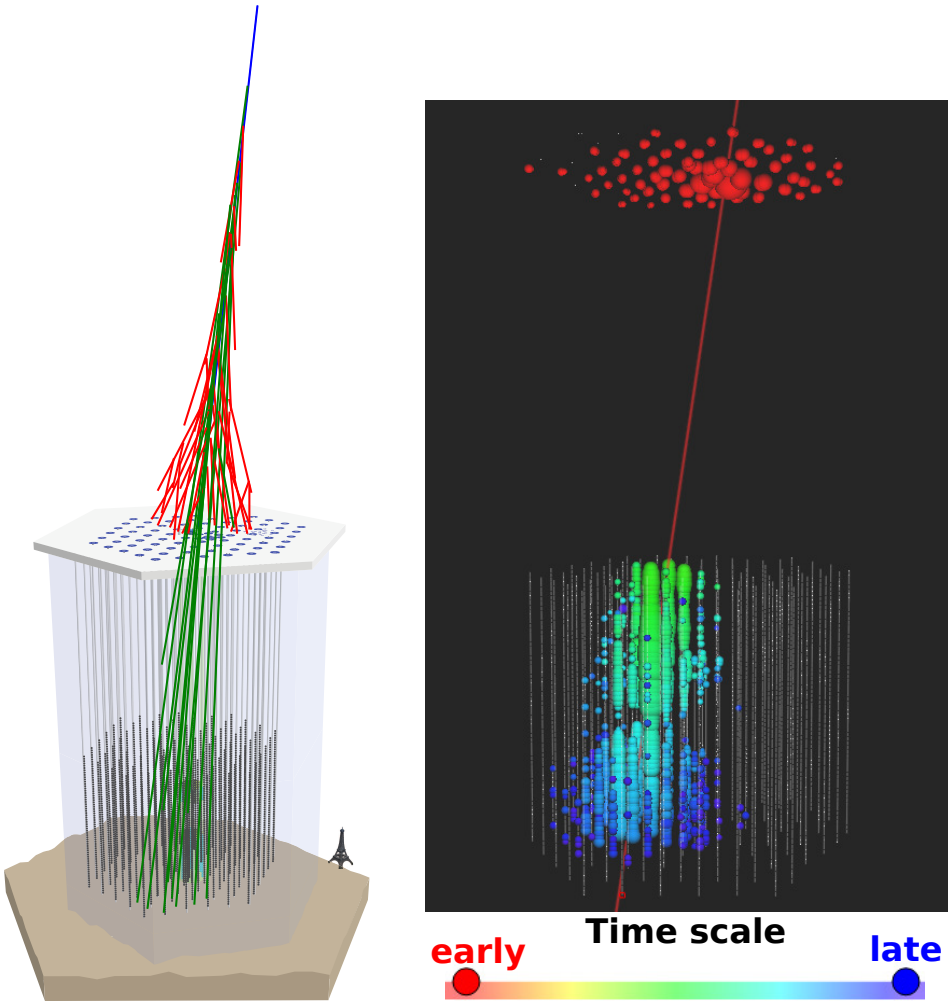

Figure 5.1: Left: Graphical illustration of a cosmic ray air shower traversing IceTop and IceCube. The blue line shows the primary particle, while the red lines represent the electromagnetic component and the green lines the high-energy muons. The number of particles is highly suppressed compared to reality. Right: real data event detection with IceTop and IceCube. The color scale shows the time evolution of the signals.

The IceCube Neutrino Observatory is a very useful detector to study cosmic rays, besides its main purpose of neutrino astronomy. The main cosmic ray detection methods have been described in section 3.4, where IceCube was treated very briefly. A detailed description of the IceCube Neutrino Observatory was given in Chapter 2. In this chapter the EAS detection with IceTop and IceCube is explained in detail.
Section 5.1 starts with an overview of the cosmic ray detection method with the IceCube Neutrino Observatory. The first processing of the data was explained in section 2.2, but the part specifically for cosmic rays is treated in more depth in section 5.2, together with the preliminary data processing at the computing centers in the North. The more advanced analysis of cosmic ray data is described in sections 5.3 and 5.4 for respectively the IceTop and IceCube array. The performance and evaluation of this event processing is discussed in section 5.6. Section 5.5 finally discusses the main environmental effects that need to be taken into account for cosmic ray analyses with the IceCube Neutrino Observatory.

5.1 Cosmic rays in IceTop and IceCube

The combination of a surface array and deep in-ice detector makes the IceCube Neutrino Observatory unique in its cosmic ray detection method. If an extensive air shower (EAS) traverses both the IceTop and IceTop array, the IceTop array samples the abundant electromagnetic (EM) component ($\gamma, e^{\pm}$) and the low-energy muons ($\mu^{\pm}$), while the high-energy muon bundle propagates down to the IceCube detector (Figure 5.1).

5.1.1 Cosmic rays at IceTop

As discussed in section 3.4.1, the density and size of a ground array determine the energy range in which the experiment is sensitive to cosmic rays. The low-energy boundary of the energy range is determined by the distance between the nearest detectors, while the high-energy limit is set by the area over which the detectors are spread. Since the IceTop tanks are distributed over 1 km^2 (section 2.1.4), this results in sufficient cosmic ray detections up to roughly 1000 PeV.
The two tanks that build a station are separated by 10 m, but this one station only does not provide sufficient information to reconstruct the air shower properly. The main IceTop trigger (section 2.2.4) is only passed with six ”hard local coincidence” (HLC) DOMs (section 2.2.2), or three hit stations, in a time window of 6 μs. Standard IceTop stations are about $\sim$125 m separated from each other, thus an EAS only passes the trigger if particles with enough energy are spread over a lateral range of roughly this distance. This can be fulfilled for air showers starting from a few 100 TeV in primary energy, although not all showers of these energies which fall into the IceTop array are detected. The standard IceTop array only becomes fully efficient for air showers with primary energies above a few PeV. Instead, the InFill array, the more dense array in the center of IceTop, should be able to lower the energy threshold to 100 TeV [208]. Furthermore, since 2016 a trigger is in use and a reconstruction is being developed for air showers that only hit 2 stations (or 4 tanks) in order to further reduce the detection threshold. This InFill array and two-station trigger can provide an overlap with the direct cosmic ray measurements.

The Antarctic plateau is located at a height of $\sim$2835 m above sea level (a.s.l.), which corresponds to an average pressure of 680 hPa or an atmospheric depth/overburden of 692 g/cm^2 (section 3.1). In the energy range between 1 and 1000 PeV this is closer to the depth X_{max} at which the air shower reaches its maximal number of particles compared to detector arrays at lower altitudes. This is seen in Figure **??**, which indicates the average depth of shower maximum for proton, iron and gamma showers as function of the energy, obtained with pre-LHC hadronic interaction models (section 4.2). This figure also shows the IceTop/IceCube sensitive energy range and the average atmospheric depth (blue line) and its variation (blue band). This pressure variation is mostly due to daily atmospheric weather variation. The depth of the shower maximum for 1 PeV showers is $\sim$450 (iron) to 550 $\sim$g/cm^2 (proton), which corresponds to a height of around 5 km above the IceTop array. With higher energies, the shower maximum approaches the surface more and more. Around 100 PeV, proton showers reach their shower maximum on average at the IceTop depth. Iron showers

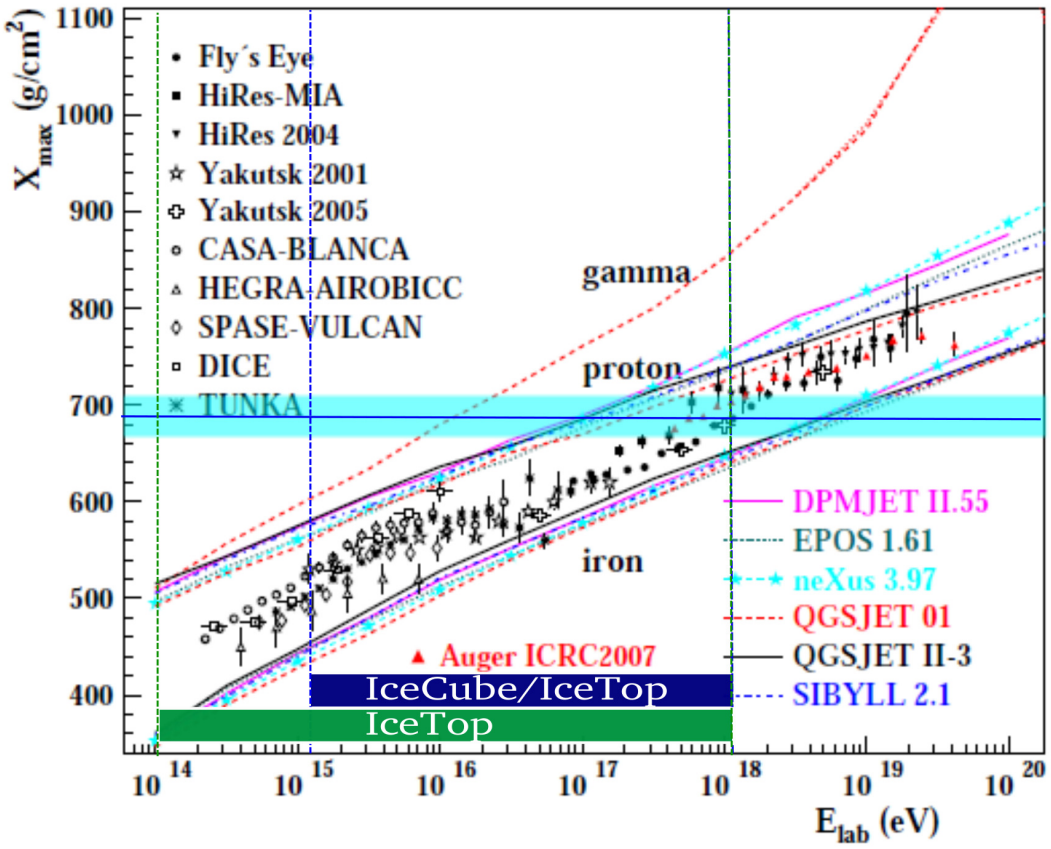

Figure 5.2: Depth of the shower maximum X_{max} as function of the shower energy, for simulations of gamma, proton and iron showers with various pre-LHC hadronic interaction models. Data measurements from some experiments are also shown. The sensitive energy range of IceTop (including InFill) and the coincident IceTop/IceCube detector are indicated, together with the average atmospheric depth at the IceTop height (blue line). The pale blue band shows the atmospheric depth variation. Adapted from [99].

of those energies have their shower maximum on average still slightly above the surface. The detection of an air shower close to its X_{max} results in a high particle number and thus statistical fluctuations decrease significantly. This helps IceTop to measure the cosmic ray energy spectrum in great detail.

The IceTop tanks act as calorimetric tanks, using the Cherenkov emission of charged particles that deposit (part of) their energy in the IceTop tank. Hence, as opposed to arrays with dedicated buried or shielded muon detectors, IceTop measures the combined signal deposited by electromagnetic particles and muons (plus a small number of hadrons). While the EM component is highly abundant close to the shower core, the muons are mainly visible at the edge of the shower where they deposit their typical VEM (vertical equivalent muon) signal (section 5.2.2). As described in section 3.3, a ground array (like IceTop) primarily uses the EM component to reconstruct the primary energy of the shower. The signal distribution is fitted with a lateral distribution function (LDF) to obtain a reliable energy estimate. The fitted signal at a certain distance, or shower size, is an excellent parameter to reconstruct the primary energy. The steepness of this LDF, evaluated at a certain distance to the shower core, can indicate the age of the shower (section 3.2.3) and is influenced by the number of muons at the edge of the shower. At large distances, where the muonic signal is visible above the EM signal, the muon density can be reconstructed, which provides another indication of the composition of the cosmic ray.

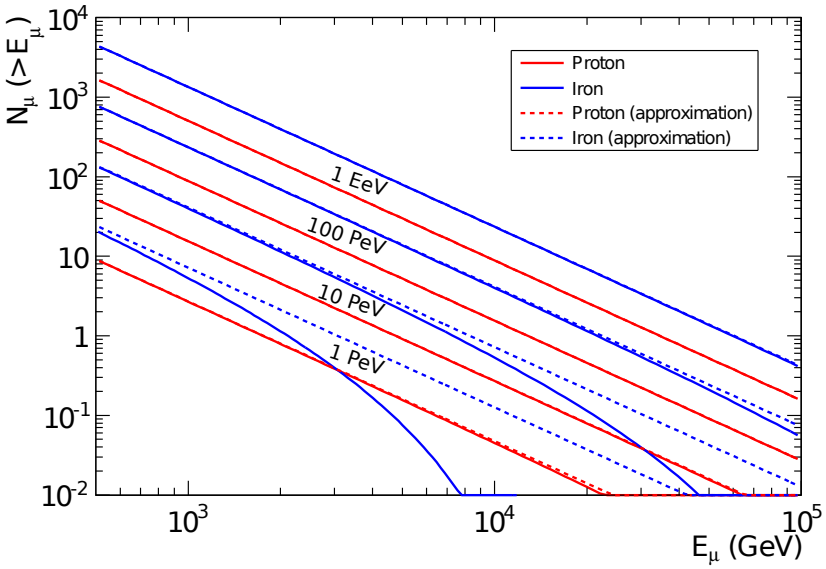

Figure 5.3: Integrated muon spectra for muon energies above 500 GeV for various primary energies and proton and iron showers, as predicted by the Elbert Formula. [101]

5.1.2 Muon bundle propagation to IceCube

While other cosmic ray experiments mainly detect EAS with ground-based arrays or telescopes that observe the propagation through the atmosphere (section 3.4.1), IceCube can combine the ground array measurement with the detection of the high-energy (HE) muons using the deep in-ice detector (Figure 5.1). In a rough back-of-the-envelope calculation one could assume that a muon only loses energy through ionization, which is ∼2 MeV/cm. Hence, in order to travel down to a depth of 1450 m in ice (even more for inclined showers), muons would require at least an energy ∼275 GeV. In reality muons also lose energy stochastically and ∼400 GeV is required to create a significant signal at a depth of 1500 m. These muons provide a very unique insight to the cosmic ray, since they are created in the first few interactions in the atmosphere. Therefore, they are an excellent tool to reconstruct the composition.
The composition sensitivity of these high-energy muons was illustrated in Figure 3.9, which is reshown in Figure 5.3 since it is crucial for the measurement method. This figure shows the number of muons above a certain muon energy, induced by proton and iron showers and for various primary energies, as deduced from the Elbert Formula (Eq. 3.18). Muon bundles initiated by iron showers thus contain ∼2.5 times more HE muons compared to proton initiated showers. If one is at least able to measure the energy of the primary cosmic ray reliably and provide a good reconstruction of the muon bundle energy loss, this provides a unique way to reconstruct the primary composition.
From this figure we can also deduce that the number of HE muons that can travel down to the IceCube detector is around 10-20 for a 1 PeV air shower, while it is $\mathcal{O}(1000)$ for a 10^3 PeV shower. This HE muon bundle is highly collimated due to the high forward momentum of the first collisions in the EAS development where the muons are created. The radius of the muon bundle is slightly larger for iron showers compared to proton showers, but is for both ∼50 m, increasing with primary energy.

For a coincident EAS detection -air showers going through both IceTop and IceCube- the rate is slightly lower compared to an IceTop-alone analysis due to the limited angular detection range. This results in a similar low-energy threshold of a few PeV and a slightly lower maximal energy limit, but still close to 1000 PeV. Hence, the IceCube Neutrino Observatory is sensitive to cosmic ray energies between the ”knee” and the ”ankle” of the energy spectrum. This is a very interesting range since the transition from galactic to extragalactic cosmic rays probably occurs in this energy range.

5.2 Online and Offline standard data processing

In the following sections the entire processing chain specific to cosmic ray analyses in IceCube is discussed. The first part of the data processing is run at South Pole (called 'Online' or 'Level 1 (L1)') on all data present in a global trigger window (section 2.2.4). On this data the filters are run. All data that passed the filters (and prescales) is then sent via satellite to the North, where a further data processing happens ('Offline' or 'Level2 (L2)' processing). The data obtained after L2 processing is often the starting point for analyzers. However, during this work, we developed a further standard processing for cosmic ray analyses with IceTop and possibly also IceCube. This is called cosmic ray 'Level3 (L3)' processing and includes the latest pulse cleanings, reconstructions and topological description parts used in the current cosmic ray analyses. The L1 and L2 processing are described in this section, while the more advanced L3 processing chain is treated in Sections 5.3 and 5.4. The analysis described in this work, outlined in the following chapters, uses this L3 data without further applied data processing.

5.2.1 Online processing (L1)

All the data contained in one global trigger window is sent to the PnF (Processing and Filtering) system (Figure 2.13). This PnF system performs a first processing of the data, splits the data into interesting physics events and runs the filters on these splitted events. In this work we call all the data within one global trigger window a 'DAQ (Data Acquisition) event', while an 'event' is used for pulses which are split into interesting physics events. One DAQ event, the collection of all pulses within one global trigger window, can thus contain multiple (physics) events. For example, one of these events can be caused by an upgoing muon from created by a neutrino, while another event is caused by a downgoing air shower. If they are close in time, the pulses created by these events are merged into one DAQ event and they are split by the PnF system.

A schematic overview of the L1 processing performed by the PnF scripts is given in Figure 5.4. As a first step the pulses recorded by DOMs that are known not to be reliable are cleaned out. These DOMs are kept in a "container" and are excluded from further reconstructions. The remaining launches are then calibrated using the procedure described in section 2.3. The raw counts are first converted to milliVolts, and by using the signal (in mV) of single photoelectron (SPE) pulses the number of PEs can be reconstructed. This procedure is, however, slightly different for HLC (hard local coincidence) and SLC (soft local coincidence) pulses, since the HLC pulses contain the full waveform information, while for the SLCs only a charge and time stamp are transferred to the surface.
For the HLC hits the proper baseline substraction can be performed. The HLC waveforms are then fit with a distribution in time of SPE signals, to obtain the signal in number of photoelectrons (PE). The HLC pulses in IceTop are further converted from PE units to VEM (vertical equivalent muons), using the calibration described in the following section 5.2.2.
For the SLCs on the other hand the conversion from counts to mV by a gain and baseline correction was performed on the DOM itself. These gain and baseline values are averages which might differ slightly from the true values. This total charge in mV is divided by the SPE peak charge to get the charge in number of PE. Due to the possible errors introduced by this rough procedure, the IceTop SLCs are recalibrated in the further L3 processing (section 5.3.2). If the calibration procedure failed for some reason, the DOM is discarded and kept in another container with DOMs that should not be used further on ('CalibrationErrata').
The pulse time saved for an SLC hit was obtained from the time of the first hit in this pulse. For the HLCs on the other hand the time of the first hit is based on the rise time of the first peak in the pulse pattern. The leading edge is fitted between a charge of 10 % and 90 % of the first peak and this fit is extrapolated down to the baseline to define the start time of the HLC hit. The trailing edge of the pulse is defined as the time when the charge drops below 10 % of the first peak. These two together then also define the pulsewidth. This time offset between SLC and HLC hits is treated in the L3 processing (section 5.3.2).

Up to this stage, the low-gain (LG) and high-gain (HG) DOM in a tank were treated separately. When

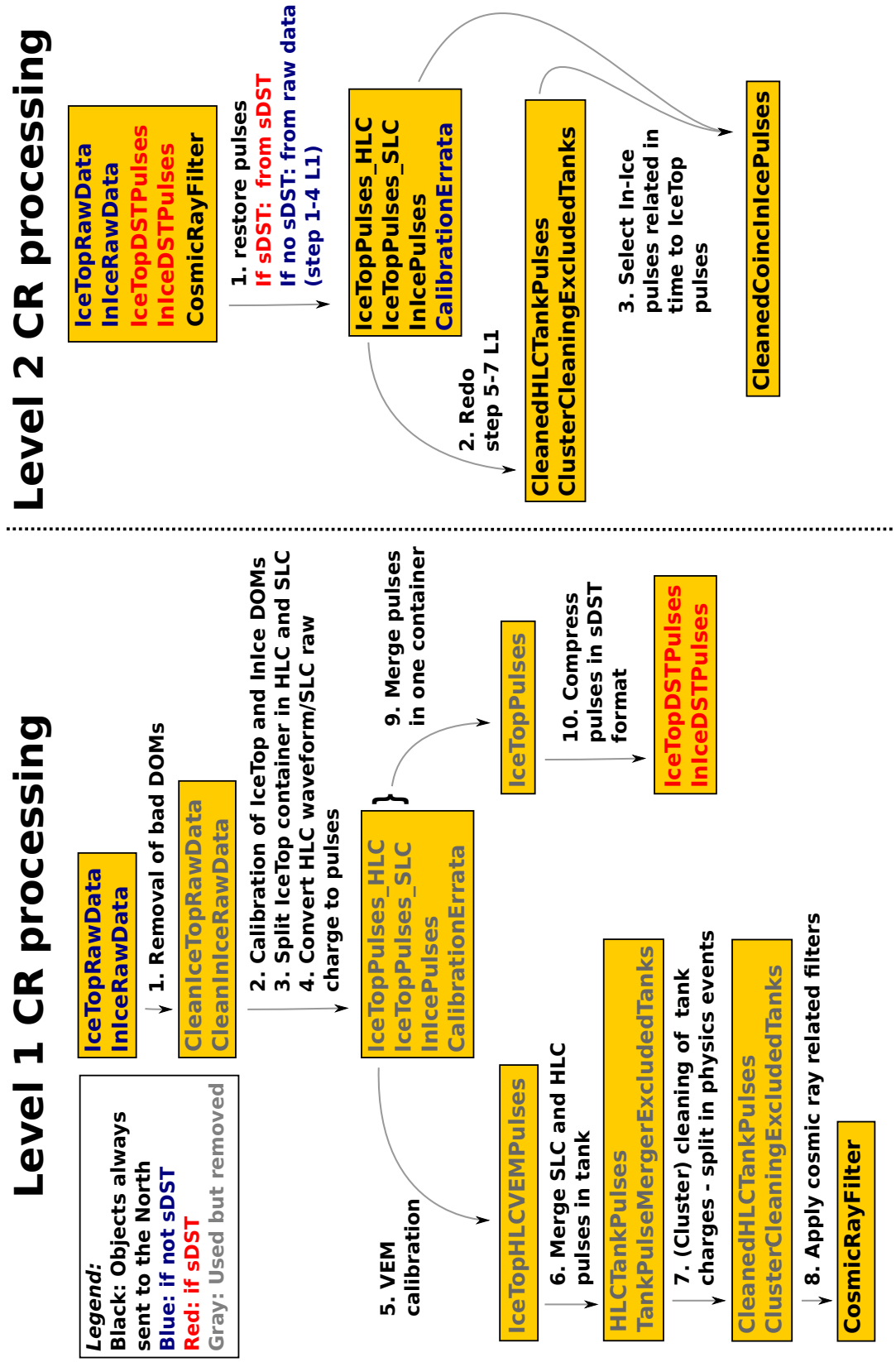

Figure 5.4: Flowchart of the main parts of the Level 1 and Level 2 processing for cosmic ray (CR) analyses with IceTop and IceCube.

both the LG and HG DOMs were hit, this information is combined into one global tank charge. Since the HG DOM provides the most detailed information, the HG DOM is used by default to represent the tank charge. If the PMT of the HG DOM was saturated, i.e. the charge exceeds a certain saturation threshold, the best-matching LG pulse in time is used as tank charge. The time difference with the HG DOM time should not exceed 40 ns. If no corresponding pulse in the LG DOM is found also this tank is omitted and kept in a separate list. The tank is furthermore omitted if the HG DOM was not responding during the trigger window, for example due to the dead time of the DOM. Since the HG signal is more detailed than the LG signal, the time of the HG pulse is always used as pulse time in the tank charge.

Cosmic ray analyses use the IceTop HLC tank pulses to split the pulses into interesting physics events. This uses a simple pulse cleaning algorithm, which looks for a possible correlation between the hits. The hits are ordered in time, and the difference between subsequent hits in this list should not exceed $\Delta t < |\Delta \mathbf{x}|/c + t_{tol}$. Here $\Delta \mathbf{x}$ is the distance between the two tanks where the hits where recorded and t_{tol} is the tolerated extra deviation, which is set to 200 ns. Up to the IC86.2011 configuration (Table 2.1) this was performed based on stations, where the average time and position of the tanks was used. Afterwards this procedure was converted to be based on the individual tanks. Next to the assembly of pulses into events, the algorithm also removes a large fraction of noise or background. Finally the pulses related to separate physics events are gathered in containers.

For IceTop, the filters, described in section 5.2.3, are ran on these splitted pulses. The pulse selection procedure is illustrated with a real data example in Figure 5.5. In this particular case the global trigger window was extended due to a long SLOP trigger (section 2.2.4). On the top left both the HLC and SLC IceTop hits in this trigger window are shown. The top right plot only shows the HLC hits. These clearly show 3 clusters of hits in both time and space. The cleaning and splitting procedure was able to separate the three clusters into three separate physics events. However, only the two events in the bottom plots passed the filter conditions (section 5.2.3).

The pulses of the deep detector are calibrated as described above. This concerns all the In-Ice pulses in one global trigger window. At this point no splitting of these pulses is performed. Instead, this is treated in the Level3 processing (section 5.4.1).

In the first years of data taking, up to IC86.2011, the HLC waveforms of the events that passed the filters were fully sent to the North, together with some basic reconstructions. At the start of the IC86.2012 data taking year the super Data Storage and Transfer (sDST) compressing tool (section 2.2.5, [56]) was introduced. Pulses compressed to the sDST format only take $\sim$9 % of the bandwidth compared to the original pulses. Depending on which filter the event passed (section 5.2.3), either the sDST pulses or original waveforms are sent to the North. Most of the other information about the event is removed to reduce the file sizes that need to be sent over satellite. Next to the raw waveforms or sDST pulses, only the filter and trigger information is kept. All filtered events in one run (section 2.2.6), which typically lasts 8 hours, are sent together with geometry, calibration and detectorstatus (GCD) information of this run. In all further data processing these special 'GCD-files' are used when the data of this particular run is being analyzed.

5.2.2 VEM Charge

Since each IceTop tank has slightly different properties the response of a DOM to the same deposited energy differs from tank to tank. This is especially true for tanks with Zirconium liners versus Tyvek liners. In order to obtain a uniform charge unit over all tanks, such that the tank response to a certain particle is similar among the tanks, the tank charges are normalized to the charge deposited by a vertical muon ('Vertical Equivalent Muon' or VEM).

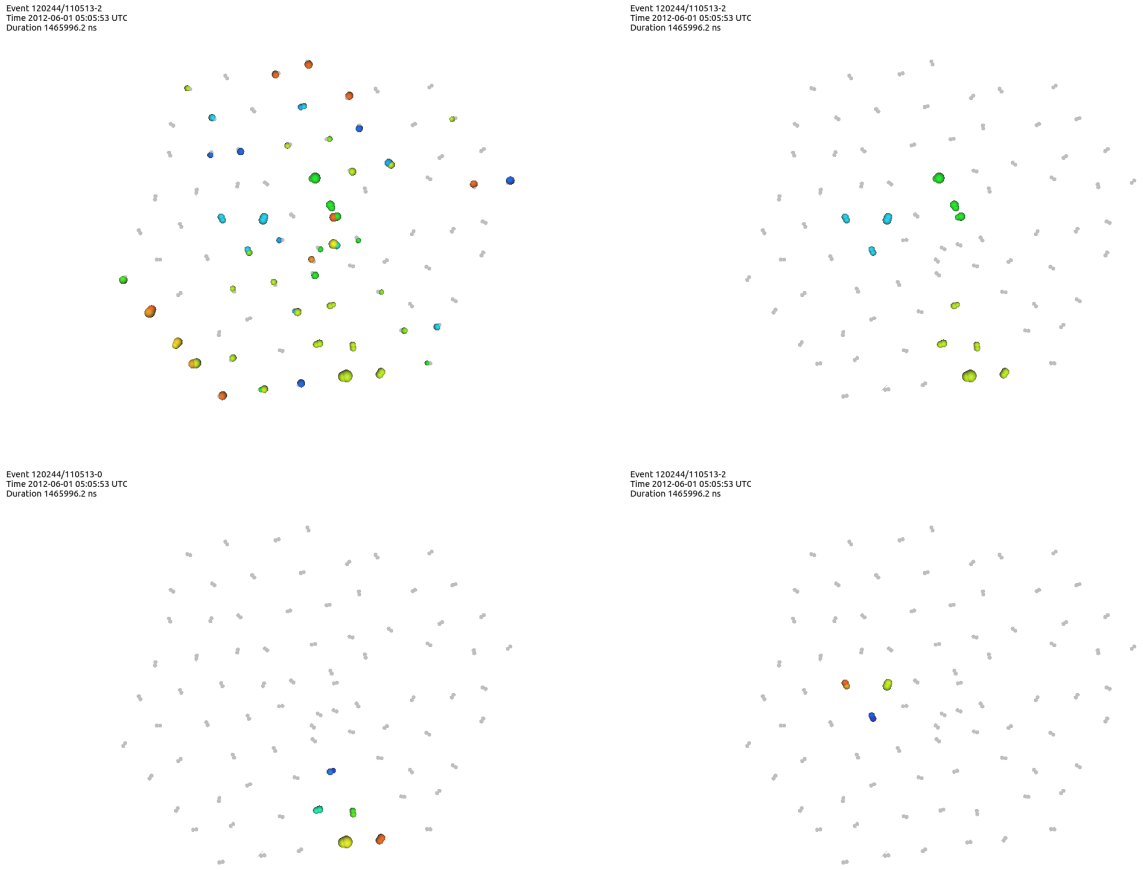

Figure 5.5: Real data example of the Level 1 pulse selection and filtering. Colours indicate timing , from early (red) to late (blue), while the circle sizes denote the measured charge. Top left: all IceTop pulses in the global trigger window. Top right: HLC pulses only during this trigger window. Bottom: the two events kept after the event splitting algorithm described in section 5.2.1 and selection by the filters (section 2.2.5).

This VEM charge is determined using the background of atmospheric muons from low-energy showers, and is continuously monitored during normal data taking: every 8192nd crossing of the discriminator threshold of the HG DOM in a tank a readout of the DOM is forced. If for this hit the local coincidence condition with the other tank was fulfilled, the next DOM launch is used. This results in a rate of 0.2 Hz for these special VEMCal (VEM calibration) launches [54].
The energy of these single atmospheric muons traversing the IceTop tanks is roughly 2 GeV. Muons of this energy are ”mimimum ionizing” and therefore always lose about the same energy along their track through the tank. Since the Cherenkov light emitted by the secondary particles also only varies slightly the DOM response curve to a vertical muon is rather narrow and this can be used for calibration purposes. This can be seen in the left plot of Figure 5.6, which shows an example charge spectrum of the HG DOM of tank 61A, obtained from VEMCal launches on April 15, 2012. The distribution is fitted with an EM contribution (red) and a muon contribution existing of through-going muons and edge-clippers (muons traversing part of the tank). The function is given in [54]. The 1 VEM unit (black arrow) is defined as 95 % of the muon peak (green arrrow). The 5 % shift of the muon peak to lower values is obtained from a study that performed in-situ measurements with muon taggers [209], which really only use almost perfectly vertical muons. As a result, on average 1 VEM corresponds to $\sim$125 PE for the Zirconium liner tanks. For the tanks with a Tyvek liner roughly 200 PEs are produced for 1 VEM. This PE per VEM spectrum obtained in data can also be reproduced in simulations, up to a 2-3 % level [192]. This provides confidence in the used simulations and also defines the charge uncertainty which needs to be taken into account.

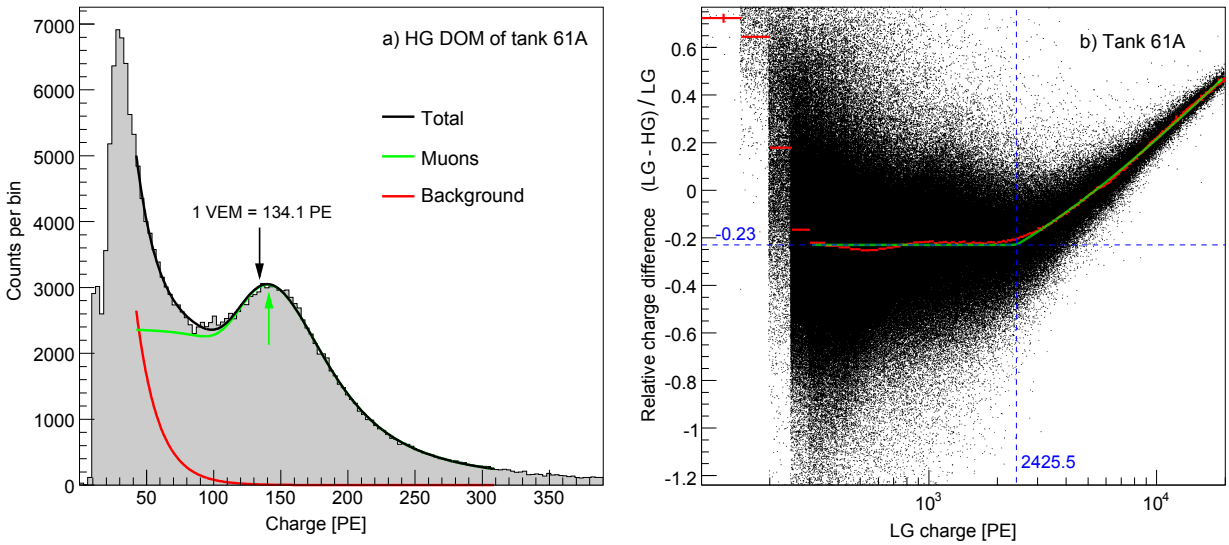

Figure 5.6: Left: charge spectrum from special VEMCal launches for the HG DOM of tank 61A taken on April 15, 2012. The muon (green) and EM component (red) are fitted separately. Right: the relative charge difference between the LG and HG DOM of tank 61A as function of the LG charge. [54]

The right plot of Figure 5.6 shows the relation between the LG and HG DOM charge measured simultaneously with the same tank (during normal data taking). One would assume that the LG and HG DOM on average measure the same charge. However, this figure shows that the LG DOM measures roughly 20 % less charge. This is independent of the LG DOM charge up to the saturation region of the HG DOM. This is not understood, but taken into account by a fit (green) to the average relative charge difference (red). The VEM unit for LG DOMS agrees roughly with 105 PE for the tanks with Zirconium liner and $\sim 0.8 * 200 = 160$ PE for the few tanks with the Tyvek liners. This figure also allows to determine the charge at which the HG DOM starts to saturate. This HG-LG cross-over point is at an LG charge of roughly 2425 PE for tank 61A.

As described above, the VEMCal launches are gathered during normal data taking. Therefore, the stability of the VEM value can be monitored continuously. The VEMCal distributions of two weeks are combined, from which the VEM value is determined. The maximal variations between two consecutive calibrations are roughly $\pm 10\%$, with an RMS of 3%. Up to the IC79 data taking year these VEMCal variations were immediately entered in the data processing chain and thus the data was corrected for these variations. Later on, a stable value is used throughout the entire year since some undesired behaviour was observed. Now it was decided to insert these values, after verification, during the Level 3 processing (section 5.3.2).

5.2.3 Cosmic ray Filters

In total roughly 25 different filters exist in IceCube which serve various purposes (section 2.2.5). The cosmic ray related filters with their prescale values and rates are listed in Table 5.1. They are listed for the data taking configurations from IC79 to IC86.2015, which is the data targeted in this work and currently implemented in the Level3 processing.

During IC79 and IC86.2011 data taking (June 2010 - May 2012), the IceTop filters used were the IceTopSTA3 and IceTopSTA8 filters. This means that either 3 or 8 HLC stations needed to be present in the cleaned and split pulses. They were respectively prescaled with a factor 3 and 1. Hence, an event which triggers between 3 and 8 stations will obtain this prescale of 3, if 8 or more stations are hit the event is always kept (prescale of 1). Next to the filters concerning only IceTop, specific filters for the coincident IceTop-IceCube analyses

Table 5.1: All cosmic ray related filters implemented in IceCube, for the IC79 to IC86.2015 configurations. Also their prescale values and rough rates (without prescale) are given.

Configuration	IceTop filters	Prescale	Rate	sDST filters	Prescale
IC79	IceTopSTA3	3	24.8		
	IceTopSTA8	1	1.5		
	IceTopSTA3_InIceSMT	2	8.1		
	IceTopSTA8_InIceSMT	1	0.5		
	InIceSMT_IceTopCoinc	100	100		
IC86.2011	IceTopSTA3	3	23.2		
	IceTopSTA8	1	1.5		
	IceTopSTA3_InIceSMT	2	7.2		
	IceTopSTA8_InIceSMT	1	0.5		
	IceTop_InFill_STA3	1	3.7		
	InIceSMT_IceTopCoinc	100	100		
IC86.2012	IceTopSTA3	10	22.3	SDST_IceTopSTA3	1
IC86.2013	IceTopSTA5	1	6.1	SDST_IceTopSTA5	1
IC86.2014	IceTop_InFill_STA3	1	3.7	SDST_IceTop_InFill_STA3	1
IC86.2015	InIceSMT_IceTopCoinc	100	100	SDST_MuonCalibration	1

were used during those years: the IceTopSTA3_InIceSMT and IceTopSTA8_InIceSMT filters. Aside from the 3 and 8 IceTop station filter to be passed, they also require an InIce SMT trigger (section 2.2.4). The prescale of the IceTopSTA3_InIceSMT filter is 2, while the IceTopSTA8_InIceSMT filter keeps all events. Although those filters were specifically developed for the coincident analysis, they are not used in this work in order to keep consistency between the various years.
In IC86.2011 the full array was completed, including the InFill array in the center of IceTop. In order to keep homogenous filter rates of the standard filters over the array, the 3 extra InFill stations (79, 80, 81) are not included in the standard IceTop filters. Instead, a specific filter was developed which is passed if at least three stations in the InFill area (defined in section 2.1.4) were hit, called IceTop_InFill_STA3. If at least three out of five standard stations in the InFill area are hit, both the standard IceTop filter and the InFill filter are passed. All events which pass the special InFill filter are sendt North (prescale of 1).

Significant changes to the filters were introduced at the start of the IC86.2012 data taking year. For the following seasons, these IC86.2012 settings remained unchanged. Since most of the standard IceTop reconstructions (section 5.3.4) need at least 10 tanks to be hit, the IceTopSTA8 filter was replaced by the IceTopSTA5 filter, keeping the prescale of 1. Furthermore, the IceTop-IceCube coincident filters were dropped. The main change from IC86.2012 onwards was, however, the introduction of sDST (section 5.2.1) in the data processing at South Pole. Each filter got an equivalent sDST filter, which has a prescale of 1 since the compressed sDST format allows for more events to be transferred via satellite. The IceTopSTA3 prescale was moved to 10. If the standard filters (and prescales) are passed the raw waveform information is sent over satellite, while for sDST events the sDST pulses are sent in sDST format.

The rates of the various filters remain rather constant over time, although it can be observed that the rates of the STA3 filters slightly decrease. This is due to the accumulation of snow on top of the tanks (section 5.5.1), which results in less low-energy showers triggering sufficient stations. The effect on the STA8 filters is smaller.

The two (physics) events displayed at the bottom of Figure 5.5 passed the filtering conditions. The data used was from IC86.2012, and the event on the bottom left passed the IceTopSTA5 filter, while the one on the right passed the IceTopSTA3 filter. The third cluster of HLC pulses seen on the top right plot did not pass

any of the IceTopSTA3, IceTopSTA5 or IceTop_InFill_STA3 filters, since two standard stations outside the InFill area were hit, together with one purely InFill station (station 81).

5.2.4 Offline standard processing (L2)

The Level2 processing mainly regains the information which was obtained in the L1 processing but was deleted to save bandwidth for the data transfer from South Pole to the North. This is summarized in Figure 5.4.
First, the raw waveforms are recalibrated to PE for standard filters. If on the other hand only the sDST pulses were sent, these pulses are uncompressed and separated in an HLC and SLC pulse container. Afterwards, the IceTop charges are combined again into tank charges, the pulses in number of PEs are converted to VEM charges and the cluster cleaning and event splitting is redone. This is similar to the L1 processing. On top, also a first selection of the in-ice pulses that can be related in time to the IceTop pulses due to an EAS is performed. All this processing occurs in the days after the data arrival in the North. This allows fast monitoring of the data, such that for example calibration or code problems can be observed and solved as quickly as possible.

5.3 Level3 processing: IceTop

While a qualitative event processing is the aim of the L2 processing, this is not always possible. This is especially true for the IceTop data, since the conditions on the surface can change rapidly and are not continuously monitored. These changes need to be measured and verified before they are used, which is impossible when the data is processed soon after it arrived in the North. Therefore these correct values are not included in the Level 2 processing. The main effect is the variation of the snow height on top of the tanks. Furthermore, also the temperature on the surface can influence the DOM temperature and thus calibration constants.
To remedy these problems, the cosmic ray working group decided to develop a further processing of the data, called '(cosmic ray) Level 3' processing [210]. This Level 3 processing also includes further cleanings, reconstructions and event descriptions. As a first step, the scripts were based on the IceTop-alone and coincident analyses of the IC79 data [101, 139], and their update to three years of data [143].
This Level 3 processed data should serve as a reliable starting point for analyzers. The IceTop part of the Level 3 processing is extensively discussed in this section, and a schematic overview is given in Figure 5.7. The IceTop Level 3 processing starts with a clean-up and unification of the Level 2 files, followed by recalibrations of the tank signals. Subsequently a more detailed noise cleaning algorithm is used before the reconstructions are done. Finally, this reconstruction is used to introduce an even more advanced event cleaning. Event description parameters are introduced, which could for example be used for event selection. The IceCube part of the L3 processing is described in the following section, the description of environmental effects in section 5.5 and the L3 verification in section 5.6.

5.3.1 Clean-up, unification and GCD modification

To reduce the processing time and the file sizes, the first step of the L3 processing exists of removal of the unnecessary information from the Level 2 files. This includes almost all in-ice information with exception of the pulses and excluded DOM lists, reconstructions, etc. As a second step, the names of the objects in the files are unified over the years. The names in Level 2 changed slightly over the years, which was remedied at the start of the Level 3 processing. Furthermore, the cosmic ray filters are re-run. For all data taking years the IC86.2012 (and later) filters are used (IceTopSTA3, IceTopSTA5 and IceTop_InFill_STA3), to obtain a unified processing for all configurations. If the event did not pass any of these filters the entire event is omitted. Furthermore, if only 3 or 4 stations were hit extra checks are performed to see whether these stations are located next to each other. If not, this event is also removed. From IC86.2012 onwards the data

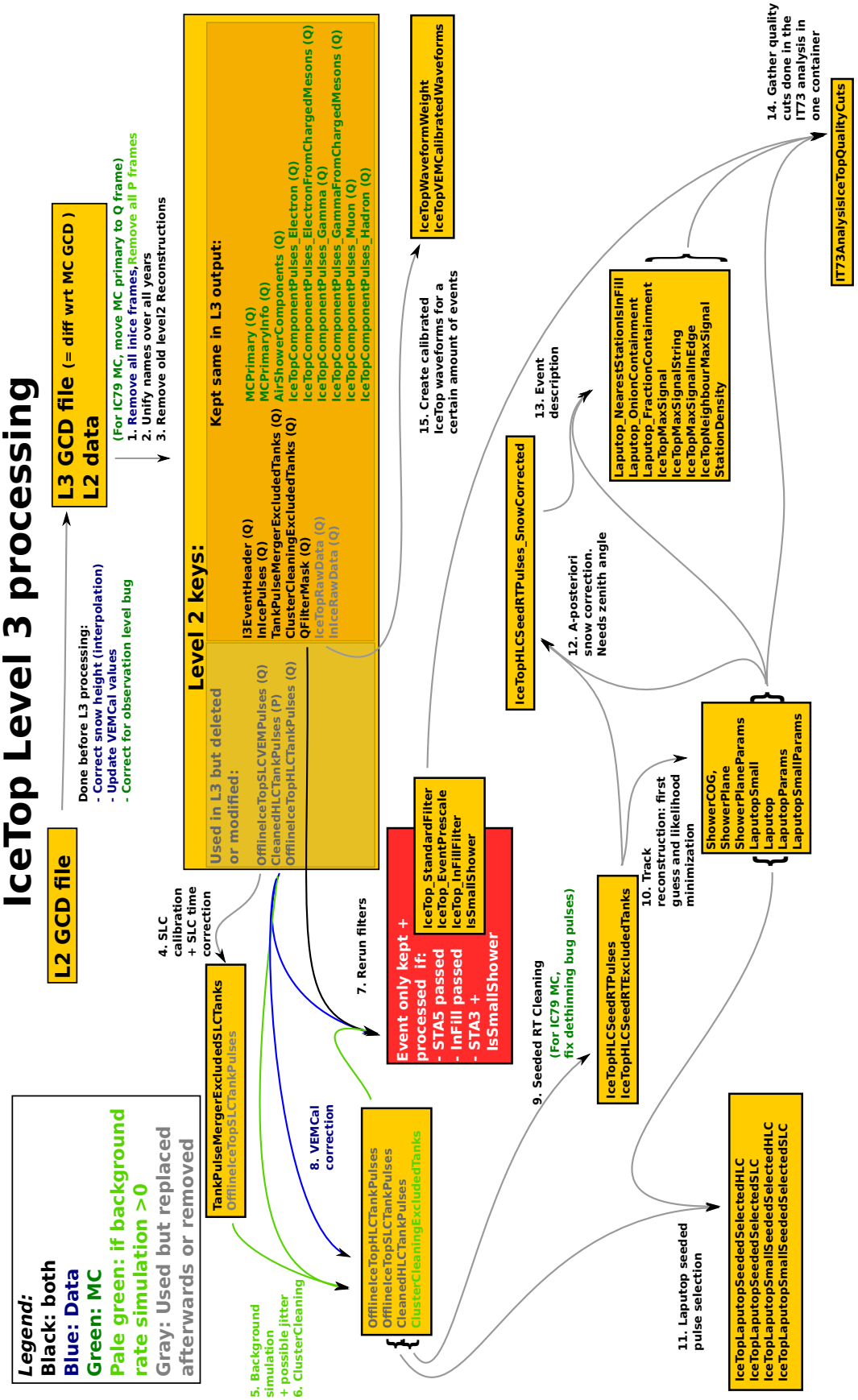

Figure 5.7: Flowchart showing the IceTop part of the Cosmic Ray Level3 processing.

processing and pulse cleanings are tank-based instead of station-based. In this stage of the L3 processing the older years were also converted to tank-based.
Furthermore the snow heights (section 5.5.1) and verified VEMCal values are obtained from the database and replaced in the GCD file of the run.

5.3.2 Calibration

SLC Calibration and time correction

As discussed in section 5.2.1, for SLC pulses only the total charge stamp and its launch time is kept. The number of PEs is obtained by dividing the charge stamp in mV by the charge of one PE. If the event passed one of the non-sDST filters also the information about which ATWD chip and channel is used are saved. Since the gain and baseline correction occur by the firmware on the DOM with a fixed baseline and gain, the seasonal variations induced by the temperature changes are not taken into account. Therefore the SLC charge could be slightly wrong compared to the charge obtained from an HLC pulse, which is fully calibrated using recent DOMCal values.

This is corrected during the L3 processing. SLC calibration constants are determined by processing HLC hits as SLCs and comparing the charges [211]. The relationship between the two is then saved per ATWD chip and channel, for each run. This relationship is then used to correct the SLC charges in Level 3. For the events which only passed a sDST filter the information about which chip and channel was used has been lost. Thus for SLC hits in these events a correction using the average over both chips and the three channels is used.

A similar procedure is applied to correct the time of the SLC pulse. While the time of an HLC pulse is deduced from the leading edge of the calibrated waveform, the SLC time is the launch time of the DOM. Therefore, an offset is expected between the two, which is undesirable if both HLC and SLC hits are used in an analysis. In contrast to the study of the charge discrepancy, the time correction constants are now obtained by converting HLCs to SLCs [212]. The obtained difference between the HLC leading edge time and the SLC launch time is shown in Figure 5.8, where real data was used. On average it seems that this difference is around 10-18 ns, slightly depending on the measured charge. The spread of the distribution is mostly of the same order of magnitude. In Level 3 processing the SLC times are shifted such that they match the HLC times, using the deduced correlations as shown in Figure 5.8. No time dependence is observed, so that the correction is constant over time.

VEMCal correction

As described in section 5.2.2, the absolute calibration of a tank is performed using the charge deposited by vertical (equivalent) muons. The position of the VEM peak determines the conversion from the charge in PE to the VEM charge. The VEMCal values, i.e. the position of the VEM peak and the LG charge at which the HG DOM starts to saturate (HG-LG crossover), are monitored using a special VEMCal trigger that runs parallel to standard data taking. Two weeks of data are used to fit the distributions and obtain the VEMCal values. The monitoring of the HG DOM in tank 20A in 2012 is shown in Figure 5.9, as an example. The top two plots indicate the VEMCal values. The third panel gives the ratio of the muonic (S) to electromagnetic (B) part of the signal, deduced from the fits to the charge distribution (Figure 5.6 - left) . The bottom three panels show the MPE rate, high voltage and DOM temperature.

These VEMCal values were insterted in the Level2 processing up to the IC79 data taking season. It was, however, observed that not all values were reliable, and from the IC86.2011 season onwards the L2 values were kept constant over time. After a verification procedure [214], these bi-weekly values are now inserted in Level 3. The final tank charge is corrected by the ratio between the (uncorrected) L2 VEM peak charge with the charge of the VEM peak inserted in Level 3.

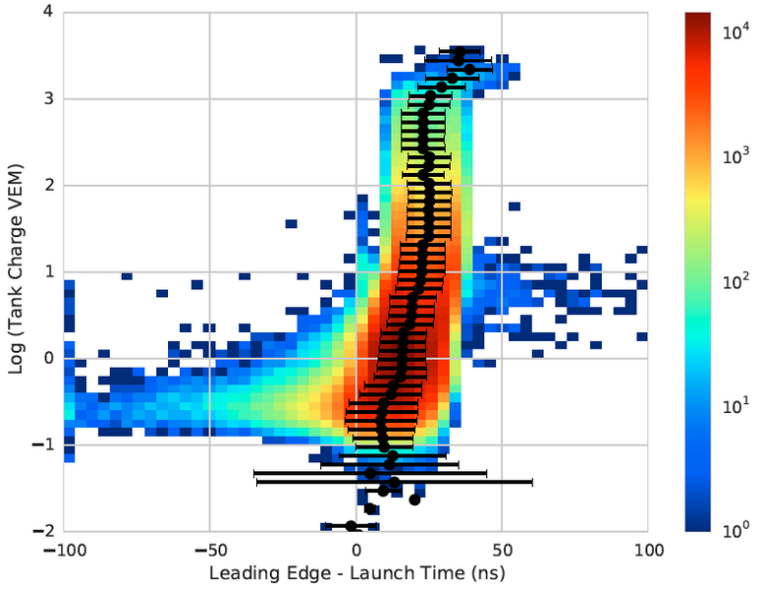

Figure 5.8: Charge of the (converted) HLC pulses as function of the difference between the leading edge time (as used by for HLC pulses) and the launch time (used for SLC pulses), . The median value is shown in black, together with the sigma of the distribution. [212]

The left plot of Figure 5.10 shows the uncorrected average charge in VEM per run, for the HG (top) and LG (bottom) DOM of tank 20A, as function of the run number. 3 years of data are shown in this figure, from IC79 to IC86.2011. The right plot shows the same charge after the correction using the verified bi-weekly averaged VEM values. Also the HG-LG cross-over point is corrected with average bi-weekly values. Since the VEMCal values were already inserted in L1 and L2 for IC79 data there is no change visible from L2 to L3 average charge up to run 118174 (the last run of IC79 data taking). The average charge of the HG DOM after Level2 processing shows significant variations. These peaks and dips are most probably due to the seasonal variation of the DOM temperature. Apparently, these effects are not completely taken into account by the DOMCal, but if the VEMCal calibration is performed correctly, the effects largely disappear, as seen in the average charges obtained after L3 processing. The remaining increase of the average charge is due to snow accumulation (section 5.5.1), which causes the abundant low charges to not trigger the DOMs and as a consequence the average charge increases. The LG DOM shows smaller seasonal variations in its average charge and a better VEM stability. The run-to-run variations are larger due to the smaller statistics per run (smaller energy depositions).
This correction seem to work reasonable well, although still some uncertainties remain. With better and better understanding of the data, these last issues will be hopefully resolved as well.

Simulation of background and jitter

While the VEM correction is only applied to data, for simulations a possible background generation and charge jitter simulation is implemented in L3. Simulations do not include the simultaneous detection of multiple air showers, other background noise or charge smearing (section 4.3.2). This might result in a data-simulation discrepancy which is of course undesired. Especially for analyses sensitive to the detailed signals, for example using the SLC hits at the edge of the shower, this could be important.

In Level3 this background and charge jitter simulation is implemented. A background rate of 1470 Hz is inserted using a certain charge distribution, both extracted from real data [215]. Effects like charge merging, dead time and SLC to HLC conversion are taken into account.

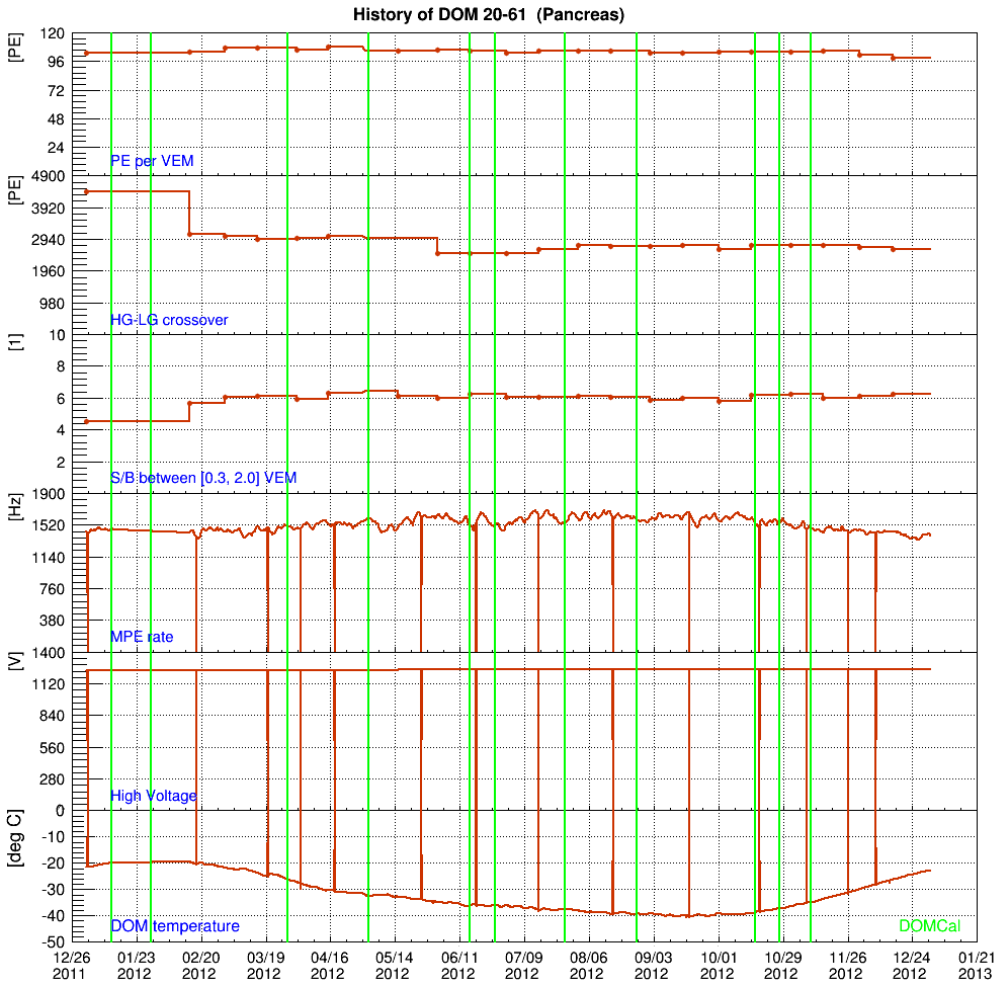

Figure 5.9: Calibration monitoring plots for the HG DOM of tank 20A, for one year (2012). From top to bottom: the position of the VEM peak in number of PE, HG-LG crossover point, muonic (S) vs electromagnetic (B) fraction between 0.3 and 2 VEM, the MPE rate, high voltage and DOM temperature. [213]

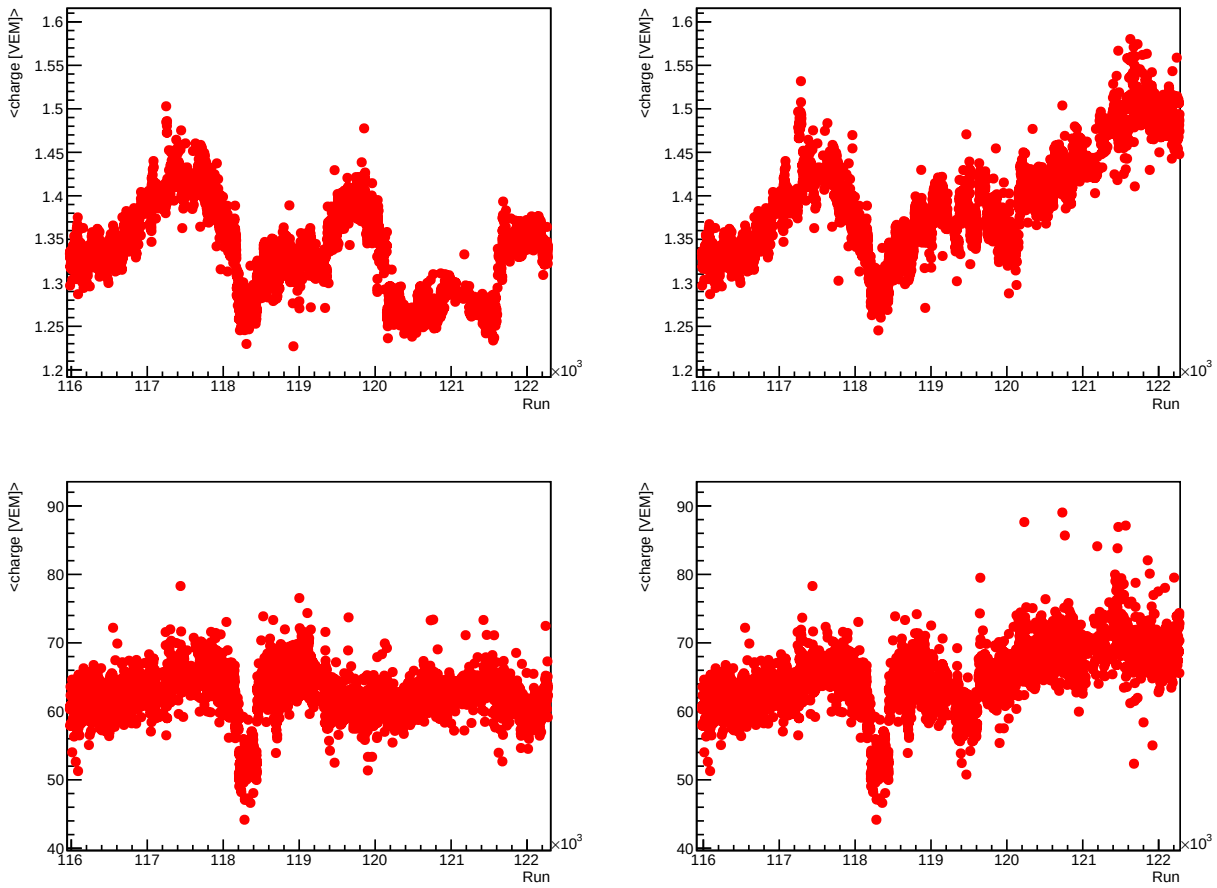

Figure 5.10: Left: average charge measured in the HG (top) and LG (bottom) DOM of tank 20A, obtained from cleaned Level2 data. Every red dot represents one (good) run. 3 years of data are used, from IC79 to IC86.2012. Right: The same charges after the VEMCal correction as applied in Level3 processing.

The deduction of the HLC and SLC charge are perfect in simulation: what is put in the simulation, comes out. In data ,however, the VEM charge might drift even in between the bi-weekly VEM calibration and, apart from the SLC charge offset treated above, the rough SLC charge determination also introduces some charge uncertainty. In Level 3 an extra smearing of the simulated charges can be inserted [216]. From the comparison of the width of the muon (VEM) peak in data and simulation it was deduced that an extra smearing (σ) of 5 % and 10 % is required for respectively the HLC and SLC pulses. The smeared charge (Q_s) is thus obtained from the unsmeared charge (Q_{us}) by:

$$Q_s = Q_{us}\,(1 + \sigma z) \tag{5.1}$$

where z is a random number from a normal distribution with mean 0 and standard deviation 1.

Most of the background simulation is afterwards again removed by the noise cleaning algorithms. It is however found that this a posteriori addition of noise introduces some unphysical behaviour [217]. Both the charge and jitter simulation are therefore only optional features in the Level3 processing turned off by default at this moment. Further studies are ongoing.

5.3.3 Pulse selection

The simple splitting and noise cleaning algorithm performed on the IceTop HLC pulses in the L1 and L2 processing performs quite well. However, the criterium is rather loose. If a noise hit is located 240 m away

from the last real physics hit, it is still allowed to be at most 1 μs later. Some PMT afterpulses, which come generally $\sim 1\mu$s after the real hit, are thus also kept. To obtain a solid and good reconstruction of the shower core, direction and lateral distribution these still need to be removed.

In L3 a second cleaning algorithm is implemented which removes almost all of these bad hits [101]. This algorithm is currently only run on HLC pulses, since these are the pulses used in the current reconstruction procedure (section 5.3.4). It uses the cleaned pulses produced by the cluster cleaning in L2 as an input. The algorithm first looks for a cluster of 3 HLC hits within a certain radius and time, and then selects HLC hits in a radius R of 180 m within a time T of 450 ns around these hits. Therefore, this cleaning algorithm is called "Seeded RT" cleaning. Two more iterations of adding tanks in a circle around the selected tanks are performed. This removes most of the noise hits and keeps the hits related to the real physics event. If a tank has both a noise hit and a hit related to the air shower the noise hit is removed and the other hit is kept. If the tank only has a hit which is rejected by the cleaning, the tank is entirely omitted from the reconstruction. This could be further improved by only removing the tanks that had a noise hit before the actual physics event, but is currently not implemented. These early hits possibly cause dead time of the DOM, while later noise hits are not able to affect the data-taking at the time of the event.
The gain of this cleaning procedure is illustrated in Figure 5.11. The top left figure shows all the recorded pulses, only excluding the possible tanks marked as bad by the detector monitoring. The upper right figure shows the remaining pulses after the simple cleaning performed in the L1 and L2 processing. The pulses in stations 46 and 81 (in blue in the upper left plot) seem to belong to a separate small event which only hits 2 stations close to each other. The pulse times in these tanks are about 28 μs after the hits related to the larger event. The two HLC hits in station 72 (in blue in the upper right plot) arrive approximately 1 μs after the real physics event. Therefore they are not cleaned by the simple cleaning algorithm. The Seeded RT algorithm however excludes these (probable) noise hits. The properly cleaned event can be seen in the bottom plot of Figure 5.11.

5.3.4 Air shower reconstruction

The set of properly calibrated and cleaned HLC pulses is now used as input for the reconstruction procedure. This reconstruction of an air shower with a ground array aims to obtain the core position, direction and parameters sensitive to its primary energy and mass as accurately as possible. The core position and direction are rather easily measured if the core position is contained in the IceTop array. The energy and mass on the other hand are inferred from the entire (lateral) distribution of the particles. As described in section 3.3 the shower size can be related to the primary energy, while the mass could possibly be inferred from the slope of the lateral distribution, due to the relation to the age of the shower and the flatter lateral distribution of the muon component. A loglikelihood minimization procedure tries to find the proper core position, direction, shower time, and lateral distribution function. Since a likelihood space with many parameters could easily converge to a wrong local minimum, a proper seed for the minimization procedure is important. This seed is obtained with a rough first guess procedure of the core and direction.

First guess core and direction

It is highly probable that the core of the shower is located close to the tanks which observed the highest deposited charges (Q), or "loudest" tanks. Therefore the first guess of the core position uses the charge-weighted position of the 7 loudest tanks:

$$\mathbf{r}_{COG} = \frac{\Sigma_{i=1}^{7} \mathbf{r}_i \sqrt{Q_i}}{\Sigma_{i=1}^{7} \sqrt{Q_i}} \tag{5.2}$$

This position $\mathbf{r}_{COG}$ is the center-of-gravity (COG) of the EAS. The number of participating tanks (7) and used weight (0.5) was determined in [101]. This shower COG method performs rather well if the real core of the shower is inside the array. However, this method is never able to reconstruct the shower core outside

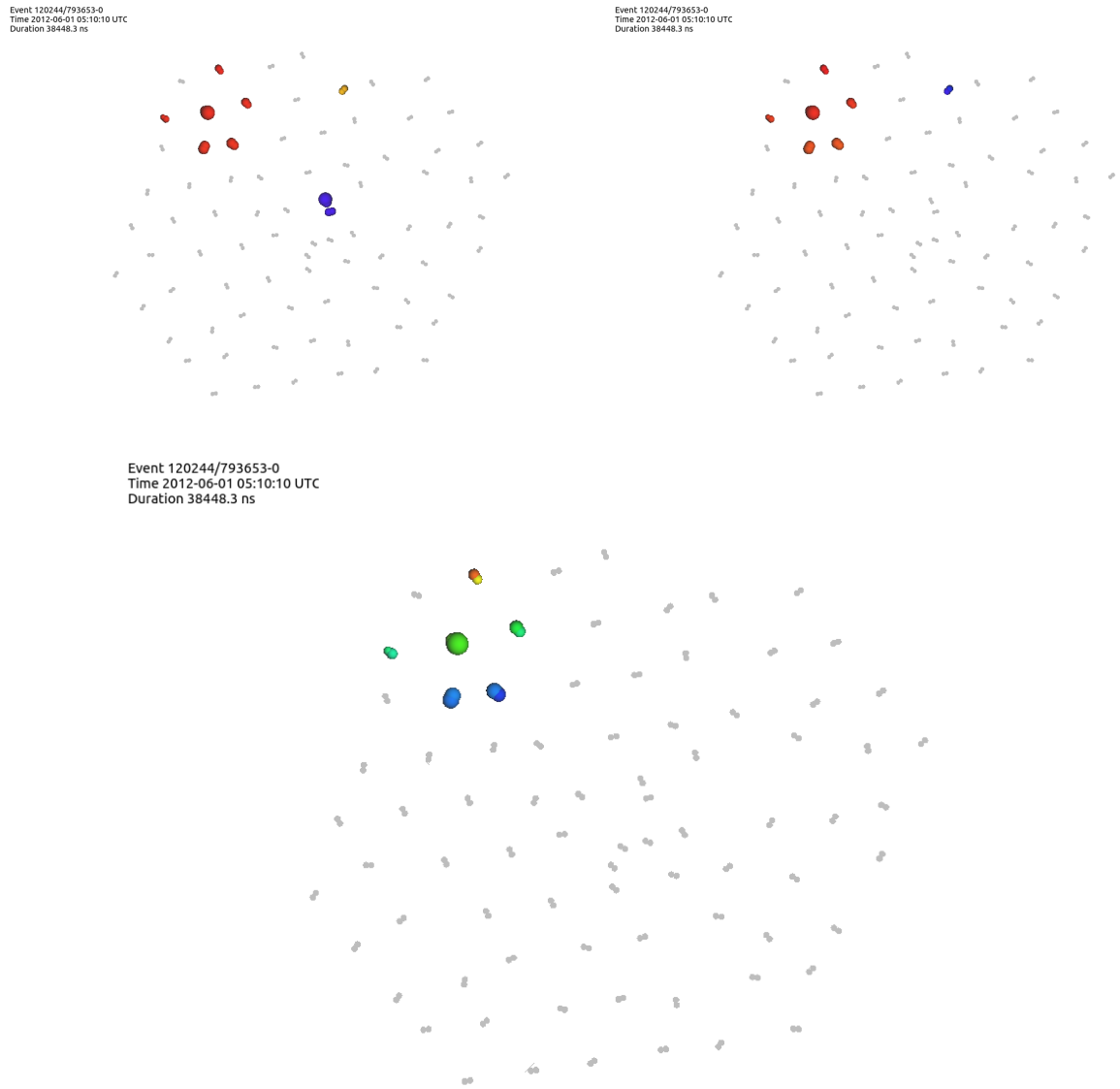

Figure 5.11: Real data event illustrating the Seeded RT IceTop HLC pulse cleaning procedure implemented in Level 3 processing. The colours indicate the pulse time evolution (from the first hit in red to the last hit in blue), while the circle size shows the total charge measured in the tank. Top left: HLC tank charges without event cleaning, only ”bad” tanks are excluded. Top right: Kept HLC pulses after the first cleaning as explained in section 5.2.1. Bottom: HLC pulses after the Seeded RT cleaning algorithm, described in section 5.3.3.

of the array, which is often the case.

As a first rough approximation to obtain the direction of the EAS, the shower front can be approximated by a plane wave. In reality, the shower front is curved, as illustrated in Figure 3.11.
The direction reconstruction minimizes the time difference between the measured hit times (t_i^{meas}) and the expected times (t_i^{plane}) from the plane wave using a chi-squared (χ^2) minimization:

$$\chi^2 = \Sigma_i \left(\frac{t_i^{meas} - t_i^{plane}}{\sigma} \right)^2 \tag{5.3}$$

where the summation now takes all HLC hits into account. In this first guess approximation 5 ns is used for all fluctuations (σ). The expected time of a hit in a certain tank i with position (x_i, y_i, z_i) is given by:

$$t_i^{plane} = T_0 - \frac{ux_i + vy_i}{c} \tag{5.4}$$

T_0 is the arrival time of the center of the shower at the surface, u and v describe the direction **n** of the shower:

$$\mathbf{n} = \left(u, v, -\sqrt{1-u^2-v^2}\right) \tag{5.5}$$

In a second iteration also the z position of the tank is taken into account. A rather good first guess of the direction is obtained using this plane fit approximation.

Advanced fitting: lateral distribution and curvature

The advanced minimization technique tries to reconstruct the core position and direction even better using a full likelihood scan of a 7-parameter space: three parameters describe the position, two the shower direction and two more parameters the lateral distribution function (LDF).
The full likelihood takes the probability for a certain charge (L_Q) at a certain time (L_t) into account, but also the probability that the tank is saturated (L_{sat}) and a no-hit probability (L_{no-hit}):

$$L_{tot} = L_Q + L_t + L_{sat} + L_{no-hit} \tag{5.6}$$

The charge likelihood is given by [54]:

$$L_Q = -\Sigma_i \frac{\left(log_{10}\left(S_i\right) - log_{10}\left(S_i^{exp}\right)\right)^2}{2\sigma^2_{\log_{10} S}\left(S_i^{exp}\right)} - \Sigma_i \ln\left(\sigma_{\log_{10} S}\left(S_i^{exp}\right)\right) \tag{5.7}$$

where the summation runs over all hit tanks, except tanks at distances closer than 5 m to the shower core, due to the unphysical behaviour of the used parametrization (Eq. 5.8). The fluctuations of the tank charge ($\sigma_{\log_{10} S}$) are described below. This equation thus tries to minimize the difference between the measured tank charge and the expected charge (S_i^{exp}) at a certain distance R_i from the shower axis.
Since IceTop measures an energy deposition instead of a particle density, the NKG function (Eq.3.19) does not describe the measured charges properly. Instead, an empirical formula was developed from simulations to fit the combined electromagnetic and muonic charge deposition [218]. This is a double logarithmic parabola (DLP):

$$S^{exp}(R) = S_{ref}\left(\frac{R}{R_{ref}}\right)^{-\beta-\kappa\log_{10}\left(\frac{R}{R_{ref}}\right)} \tag{5.8}$$

where β and κ are respectively the slope and curvature of the LDF at the reference distance (R_{ref}). S_{ref}, the signal at the reference distance, and β are free parameters of the fit, while κ is fixed at 0.303. The reference distance is chosen such that the reconstructed charge at this distance is an accurate primary energy estimator. It is thus required that the shower size at this distance fluctuates as little as possible (for showers with the same primary energy). If this parameter is furthermore as independent as possible of the primary mass, the reconstruction of the primary energy will have rather small uncertainties. The steepness and shower size at this distance are then also minimally correlated. In the standard IceTop analysis where at least 5 stations are used this distance is found to be 125 m [219]. Thus S_{125} is the parameter used to reconstruct the energy. The analysis which reconstructs the energy spectrum using the InFill array uses 80 m since the lateral spread of the lower energetic showers is smaller [208]. During this LDF fitting procedure, the charge in a tank is also corrected for the snow on top of this tank, which attenuates the signal. This is discussed further on in section 5.5.1.
An example of an LDF fit to the measured charge distribution as function of the shower core distance is shown on the top right of Figure 5.12. The figure on the left indicates the footprint of the shower on the

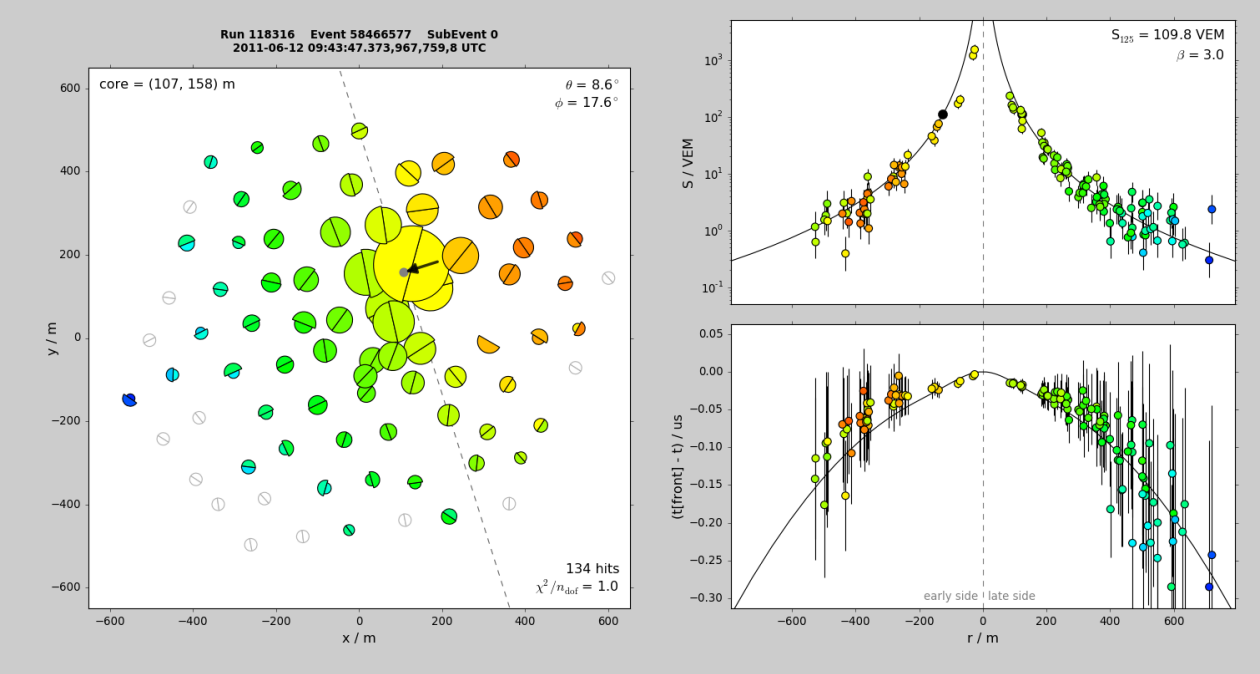

Figure 5.12: Position, direction, lateral charge and curvature reconstruction of a real data event. The colours indicate the timing, from red (early) to blue (late). Left: footprint of the air shower on the IceTop array. Each half circle indicates a tank, of which the size indicates the deposited signal. The arrow and line illustrate the direction of the incoming shower front. Upper right: measured charge as function of the distance to the shower core, together with the fit. Bottom right: deviation of the measured time from the shower plane approximation, as function of the distance to the shower core. Also the curved fit to these deviations is shown.

IceTop array. The colours again indicate the timing of the hits, while the (half) circle sizes show the total charge measured in a tank. The bottom right figure displays the fit to the curved shower front, as discussed below.

This LDF is able to describe the charge lateral distribution rather well. However, the muons far from the shower core are often exceeding the expected signal from this DLP. Work is ongoing where the electromagnetic and muonic LDF are fitted separately [220]. Furthermore, if a shower is inclined, the charge distribution is not symmetric around the shower, since part of the shower is detected at an earlier stage compared to the other part. This is currently not taken into account, but this work is under study.

The time deviation Δt from the plane wave approximation (Eq. 5.3) as function of distance R to the shower core is approximated and fitted with [221]:

$$\Delta t(R) = aR^2 + b\left(1 - \exp\left(-\frac{R^2}{2\sigma^2}\right)\right) \tag{5.9}$$

with $a = 4.823 \cdot 10^{-4}$ ns/m^2, $b = 19.41$ ns, σ=83.5 m. The function is a sum of a parabola and gaussian function around the shower axis. The time likelihood L_t minimizes the difference between the measured times and the expected times, which is the sum of the plane wave approximation (Eq. 5.3) and the deviation from this plane wave (Eq. 5.9):

$$L_t = -\Sigma_i \frac{(t_i - t_i^{exp})^2}{2\sigma_t^2\,(R_i)} - \Sigma_i \ln\left(\sigma_t(R_i)\right) \quad \text{with } t_i^{exp} = t_i^{plane}(R) + \Delta t(R) \tag{5.10}$$

The time fluctuations σ_t are described below. If the time difference between two pulses in a station differ by more than 80 ns these pulse times are omitted as well from the fit. This curvature function has been optimized

when the IceTop detector had only 26 stations completed. Therefore it does not describe the high-energy EAS perfectly, which can for example be seen in the deviation of the points from the fitted line in the bottom right plot of Figure 5.12. Studies are ongoing to improve this curvature fit [222].

Tanks can be saturated if the deposited energy is high, which could happen close to the shower core due to the large abundance of particles (Figure 3.10), especially for very energetic air showers. The PMT response starts to behave non-linear and the output reaches an upper threshold. While this occurs for the HG DOM around 2500 PE (Figure 5.6), the LG DOM saturates around 90000 PE. The fact that a tank is probably saturated if its charge reaches this saturation threshold (S_{sat}) needs to be taken into account. The proper (expected) charge S_i can then be any value above this saturation threshold. Thus the saturation term in the log-likelihood is:

$$L_{sat} = \Pi_i \int_{S_{sat}}^{+\inf} \frac{1}{\sqrt{2\pi}\sigma_{log_{10}S(S_i^{exp})}} \exp\left(-\frac{(\log_{10} S_i - \log_{10} S_i^{exp})^2}{2\sigma^2_{log_{10}S(S_i^{exp})}}\right) d\log_{10} S_i \tag{5.11}$$

where the multiplication runs over all the tanks with a charge exceeding 90000 PE.

Also the fact that a tank is not hit is important information, and needs to be considered in the log-likelihood. The probability that a tank is not hit (P_{no-hit}) is 1 minus the probability that the tank is hit (P_{hit}), thus:

$$L_{no-hit} = \Sigma_i \ln\left(1(-P_{hit})^2\right) \tag{5.12}$$

where i now runs over all tanks that did not trigger. The probability that a tank is hit depends on the expected charge S^{exp}. It is given by integrating the gaussian probability distribution of possible signals around this S^{exp}, from the detection threshold S^{thres} to infinity:

$$P_{hit,i} = \int_{S^{thres}}^{+\infty} \frac{1}{\sqrt{2\pi}\sigma_{log_{10}S(S_i^{exp})}} \exp\left(-\frac{(\log_{10} S_i - \log_{10} S_i^{exp})^2}{2\sigma^2_{log_{10}S(S_i^{exp})}}\right) d\log_{10} S_i \tag{5.13}$$

The multiple photoelectron detection (MPE) threshold, used in IceTop, is roughly 20 PE.

The full minimization procedure is performed in several steps in order to obtain a stable fit. As a seed the above described first guess for the core and direction are used, a β of 2.6 is assumed and S_{125} is approximated based on the observed pulses close to 125 m from the first guess shower axis. For physics events where at least 5 HLC stations contain pulses after the event cleaning algorithms (section 5.3.3) the reconstruction is split into three steps. In the first the direction is fixed while the charge LDF and the core position are fitted. In this iteration β is only allowed to have a rather average slope (between 2.9 and 3.1), such that mainly the core position can be optimized. The core position is moved around in a box with 400 m sides around the initial core, with a stepsize of 10 m. In the second iteration also the shower direction is fitted using the curvature function (Eq. 5.9), while the core can only vary within a box of 15 m sides around the core reconstructed in the first step (2 m stepsize). β should also have a realistic value between 2 and 4. During third and last step of the minimization procedure the direction is fixed once more, while the core should be contained within a box with 45 m sides (1 m stepsize). The slope of the LDF (β) is almost free (boundary parameters 0 and 10). In each step the S_{125} should not exceed 10^8 VEM. These values were optimized for showers with their core inside or close to the IceTop array and zenith angles up to 40°. [101]

In the case that only 3 to 5 HLC stations had pulses related to the physical event a limited shower reconstruction is performed, since a minimization of a 7-parameter space is impossible with less than 8 hits. In this limited reconstruction (called ”smallshower”) only the first step of the standard reconstruction is performed. The track direction reconstructed by the plane wave fit is kept as final direction. β is allowed to vary between 1.5 and 5, while the core is varied in a box with 200 m sides (20 m stepsize).

Shower fluctuations

When a distribution of data points is fit, as is performed in the fit of the lateral distribution and curvature, the assumed errors can highly influence the fit results. Therefore, the estimated fluctuations of the measured signal ($\sigma_{\log_{10} S}$ in Equations 5.7, 5.11 and 5.13) and time (σ_t in Eq. 5.10) need to be estimated as accurately as possible. These fluctuations are naturally induced by the air shower propagation.

The currently implemented functions that describe the fluctuations were deduced in [223, 224]. In this study the standard deviation $\sigma_{\log_{10} S}$ of the (log-normal) signal distribution around a signal $\log_{10}(S)$ is quantified in both simulations (IT16 configuration) and experimental data (IT26 configuration). This is obtained by a comparison of the charge in two tanks in one station, which are roughly at the same distance from the shower core. They should thus observe a similar signal with only a variation induced by the signal fluctuations in the shower. In the real detector configuration the tanks are, however, almost never located at the exact same distance from the shower core, due to their 10 m separation. This induces a slightly different charge in the two tanks, which influences the shower fluctuations. Therefore also a special "ring simulation" is developed where multiple tanks are placed at the same distance from the shower core and only vertical showers are simulated. The obtained fluctuations as function of the charge are shown for both simulation studies and data in Figure 5.13 (right). The left plot of Figure 5.13 shows the comparison of the charge in two tanks in one station. The mean of the gaussian function fitted to the difference in charge between the two tanks, indicated by the slanted lines (a and b), roughly results in one point on the right figure. While for the right figure showers with all primary energies are used, the left figure only used events with a $\log_{10}(S_{125}/VEM)$ between 1.3 and 1.4. This latter study tried to look into more detail in a possible signal fluctuation dependence on the primary energy [196].

Using the left figure, the three distinct regions ($\log_{10}(S/\mathrm{VEM}) < 0.4$; $0.4 < \log_{10}(S/\mathrm{VEM}) < 1.5$; $\log_{10}(S/\mathrm{VEM}) > 1.5$) on the right figure can be better understood. In the first region, describing the fluctuations of the lowest signals, no large variations are possible due to the threshold of roughly 20 PE ($\log_{10}(S/\mathrm{VEM})\approx$-1). All deposited signals are close to this threshold and no large fluctuations are allowed. These fluctuations then increase moderately up to $\log_{10}(S/\mathrm{VEM})\approx 0.4$. This is due to the presence of the typical signals induced by muons (1 VEM) around these signals. If one of the tanks was hit by a muon and the other not, a significant difference in charge is observed. This double-peaked signal variation spectrum due to the muons can be seen in the intersection a, as compared to intersection b. At higher signals (the 2nd region) the expected decrease of the fluctuations roughly proportional to the square root of the signal is observed (Figure 5.13-right). The charge fluctuations seem to rise again for high charges, at least in the real data sample. These are , however, not fluctuations, but are due to the steep rise of the LDF in this high charge reason, which causes a larger and larger charge difference between the two tanks. This can also be seen on the left plot, where the distribution broadens again for $\log_{10}(S/VEM) > 1.5$.

The final function of the charge fluctuations is obtained from the ring simulation [225], since in this study the tanks are located at the exact same distance from the shower core:

$$\log_{10}(\sigma_{\log_{10}(S)}) = \begin{cases} -0.548 - 0.078\log_{10}(S) & \log_{10}(S) < 0.340 \\ -0.373 - 0.658\log_{10}(S) + 0.158\log_{10}^2(S) & 0.340 \leq \log_{10}(S) < 2.077 \\ -1.058 & 2.077 \leq \log_{10}(S) \end{cases} \quad (5.14)$$

where the signal S is expressed in VEM. Studies are ongoing which improve these analyses with the full, completed detector array.

The fluctuations of the arrival times are also deduced from data of IT26 configuration. It only depends on the radius from the tank to the shower axis [223]:

$$\sigma_t(R_i) = 2.92\ \mathrm{ns} + 2.77 \cdot 10^{-4} \cdot (R_i)^2 \quad (5.15)$$

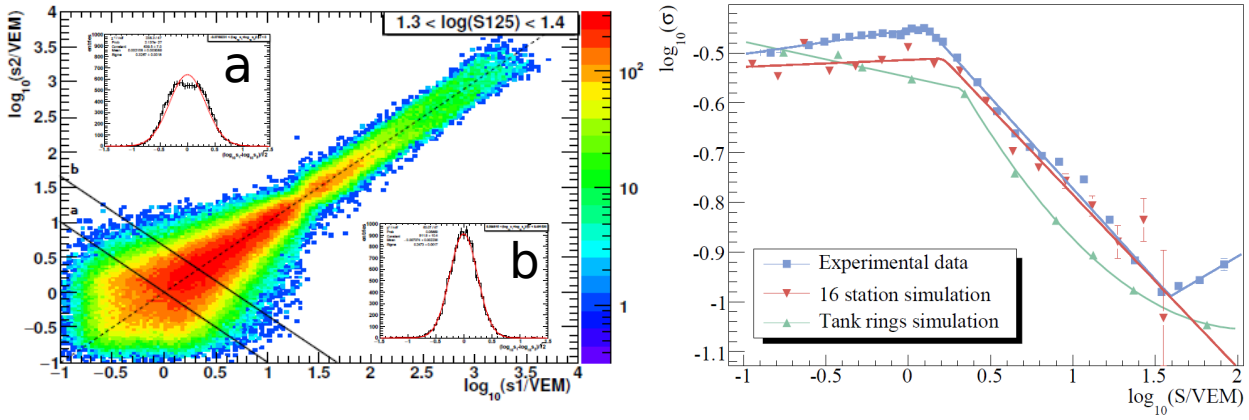

Figure 5.13: Left: charge correlation of Tank A vs Tank B in a station, from experimental data in a $\log_{10}(S_{125}/\mathrm{VEM})$ bin between 1.3 and 1.4 [196]. Right: log of the standard deviation of the charge distribution as function of the (log of the) charge. Results are obtained from experimental data when the detector consisted of 26 stations, together with simulation studies. A simulation of the detector when 16 stations were deployed (2005-2006 season) and a special ring simulation are shown [223].

with the radius expressed in m. No energy dependence of the uncertainties in the arrival time is observed (up to now) and included. A new study with the full detector aims at improving these fluctuations together with an update of the curvature function (Eq. 5.9), with a main focus on the energy dependence [222].
Both the charge and time uncertainties are also shown in Figure 5.12. In this figure it can be seen that at large distances the arrival time fluctuations are probably overestimated.

Relation between S_{125} and primary energy

As discussed above, the obtained shower size at a reference distance of 125 m (S_{125}), is an excellent parameter to relate to the primary energy of the shower. This is shown in Figure 5.14. The left figure illustrates the correlation between the primary energy and S_{125}, with again restriction to the standard zenith angle range $\cos\theta > 0.8$. This illustrates the linear correlation between $\log_{10}(S_{125}$ and $\log_{10}(E_{prim}/GeV)$, as expected from the equivalent increase in the number of secondary particles (Figure 3.7). The deviation from the linear correlation is small for most events, which will translate into a good energy resolution. Some showers with rather high energies are reconstructed with a too low value of S_{125}. These (rare) events do survive all the quality cuts, but are in fact misreconstructed events that have their core position far outside the array (section 5.6.1). The $\log_{10}(S_{125})$ distribution per energy bin is fitted with a gaussian function and the obtained averages are shown as the red curve in the right figure. The blue curve shows the same distribution for showers initiated by iron primaries. A small composition dependence of the S_{125} to primary energy relation can be observed. This is small enough to consider S_{125} rather independent of the primary particle type, but needs to be taken into account for advanced analyses of for example the energy spectrum.

5.3.5 Pulse selection based on track

In the Level3 processing of the cosmic ray related events a third pulse cleaning algorithm is implemented [226]. This cleaning algorithm can now benefit from the reconstructed track to perform a more advanced noise cleaning with the track as a seed. The primary uncleaned tank pulses are used as input and are selected based on whether their arrival time is in accordance with the track reconstruction using a plane wave approximation. Hits are allowed within a window of -200 ns to +800 ns around this plane wave approximation.
The advantage of this pulse selection procedure over the ”SeededRT” algorithm is that also pulses far from the HLC core can be selected, even if these hits are far from its neighbours. For muons far from the shower core these hits can be physically related to the actual extensive air shower. Therefore this pulse selection is

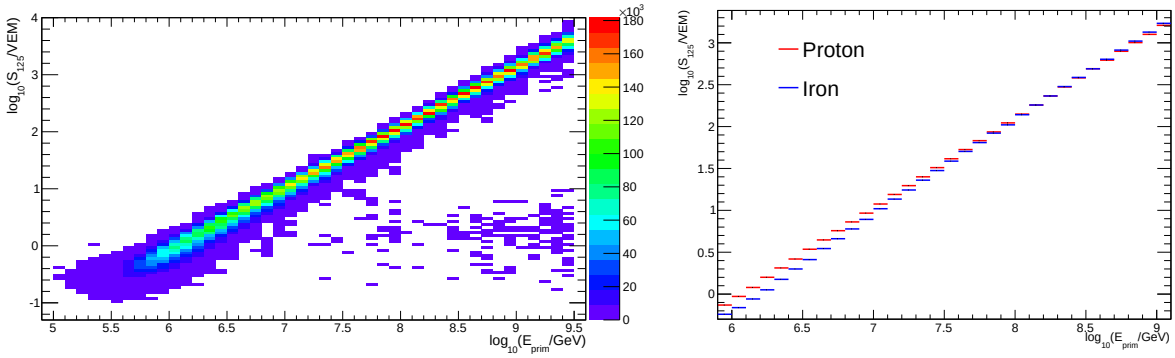

Figure 5.14: 2D distribution (left) of the reconstructed $\log_{10}(S_{125}/VEM)$ as function of the decadic logarithm of the primary energy in GeV for proton showers with zenith angle θ restriction $\cos\theta > 0.8$. The cuts described in section 5.3.6 are applied, no reweighting to a realistic spectrum occured to highlight the behaviour well for all energies. The red curve in the right figure indicates the mean of the gaussian function fitted (per energy bin) to the left figure. The blue curve shows the equivalent curve for iron initiated showers. Both are shown in the interesting and reliable energy range and are obtained after reweighting to a realistic energy spectrum.

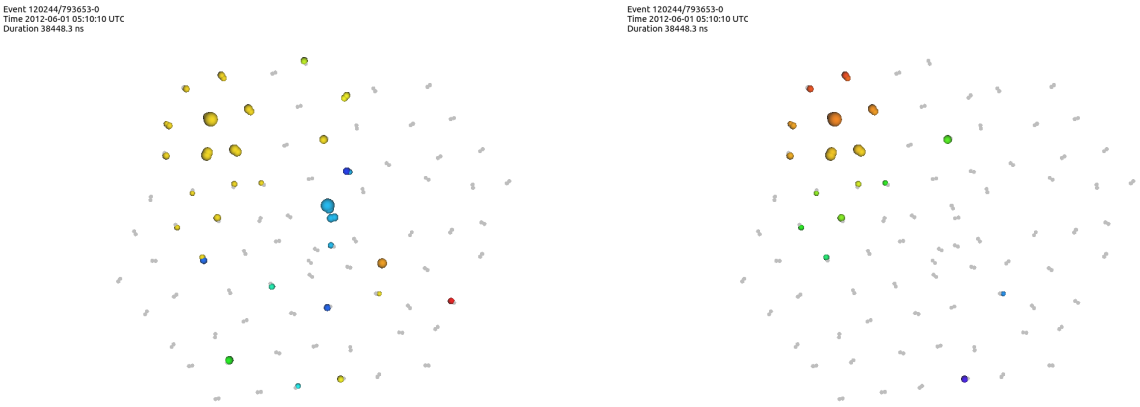

Figure 5.15: Left: uncleaned HLC and SLC tank pulses. Right: HLC and SLC tank pulses after the cleaning seeded with the reconstructed track, as explained in section 5.3.5.

a further improvement with regard to the ”SeededRT” algorithm. This is especially true for the SLC pulses, which are subject to more noise and can also be effectively cleaned with this procedure.

This (SLC) pulse cleaning can be seen in Figure 5.15. On the left the uncleaned HLC and SLC tank pulses are shown, while the effectiveness of this cleaning algorithm is shown on the right. Most of the noise SLC pulses are removed, while the good SLC hits obviously add important information to the event. For analyses that add the SLC information these cleaned pulses can serve as input for an additional reconstruction procedure or to obtain the charge as function of distance to the shower axis with the inclusion of SLC hits. The reconstruction of the muon density far from the shower core uses these cleaned pulses [227].

5.3.6 Event quality description and cuts

As a last part of the IceTop component of the Level 3 processing for cosmic rays, extra variables are created which describe the reconstructed event topology. Together with simple requirements like the fact that the filter is passed and the convergence of the reconstruction fits (section 5.3.4), these can assure a set of properly described events that can be used in advanced analyses. Most current cosmic ray analyses in IceCube focus

on air showers where the primary energy is at least ∼1 PeV, the zenith angle should be roughly $< 40^{\circ}$ and it should land inside the IceTop array. All these variables aim to assure that these requirements are fulfilled.

To ensure that the actual shower core was inside the array, and not outside the array and misreconstructed inside, it is first required that the tank with the highest charge is not on the edge of the array. This mainly removes events where the electromagnetic particle density at the edge of the array is still sufficient, so if the actual shower core is not too far outside the array.
If the core is even further, the signal in the array is dominated by muons due to their flatter LDF compared to the EM LDF (section 3.3.3). Hence, these muons can cause the highest signal in a tank to be not on the edge of the array. In order to remove these badly reconstructed events, an extra cut is introduced which requires that the highest signal in a tank is at least 6 VEM. As an extra, also the other tank in this station needs to have observed a signal of at least 4 VEM. These values are corrected for snow on top of the tanks. This ensures that the signal is not governed by muons far from the shower core, but that the electromagnetic shower core is actually contained inside the array. These highest signal requirements furthermore also effectively remove low-energetic events and inclined events, which are not targeted in the standard Level 3 processing.
Unfortunately, some events with their reconstructed core outside the IceTop array -although rare- still survive the above cuts. To remediate this a final cut occurs on the position of the reconstructed core, wich is required to lie within the IceTop array. A polygon is drawn between the outer tanks of the array (Figure 2.6) and the intersection of the line conneting the reconstructed shower core and the center of the IceTop array with this polygen is computed. The length of the line between the shower core and IceTop center D_{it} is then compared to the line between the center and this intersection point d_{it}:

$$\text{IT containment fraction} = \frac{\mathrm{D}_{it}}{\mathrm{d}_{it}} \tag{5.16}$$

This is also illustrated in Figure 5.39. As is visible on this figure, a similar requirement will be demanded for the track through the deep IceCube array.
A containment factor larger than 1 thus means that the shower core is not contained in the array (an ”uncontained” event), while events with their core inside the IceTop array have a containment factor <1. Furthermore, it is also checked whether the event falls inside the infill area.
The combination of all these cuts avoid migration of events from outside of the array to inside, which would influence the final measured event rate.

During further quality checks it was found that some events with weird topologies still have a very poor reconstruction. This type of events has hits very sparsely distributed over the IceTop array. The reconstruction procedure still converged, but the results are mostly not reliable. It is for example very difficult to indicate a core position with a good accuracy. This event topology is probably caused by very inclined air showers where only the muons survive, which then create hits distributed over the array. To remove these events, two more quality cuts are used. A first way to achieve this is by the construction of a quantity called ”station density”. To compute this first a circle with the shower COG (Eq 5.2) as center and edge at the furthest hit station is constructed. Then the ratio between the number of hit tanks and the total number of tanks is taken. When the hits are sparsely distributed over the array, this thus results in a low tank density.
Furthermore, since these hits all have roughly the same low charge, the reconstructed lateral distribution function is very flat. Events which have a β lower than 1.4 are therefore removed.
These two cuts also remove multiple air showers which hit the IceTop array at roughly the same time, but were not caught by the splitting and cleaning algorithms.

All quality cuts performed in the standard analyses with regard to the IceTop part are given in Table 5.2. These are also the event requirements used further on in this work. The first two cuts are inevitable required to reconstruct an air shower. The following four thus mainly assure containment in the IceTop array, while the last two remove the events with weird event topologies.

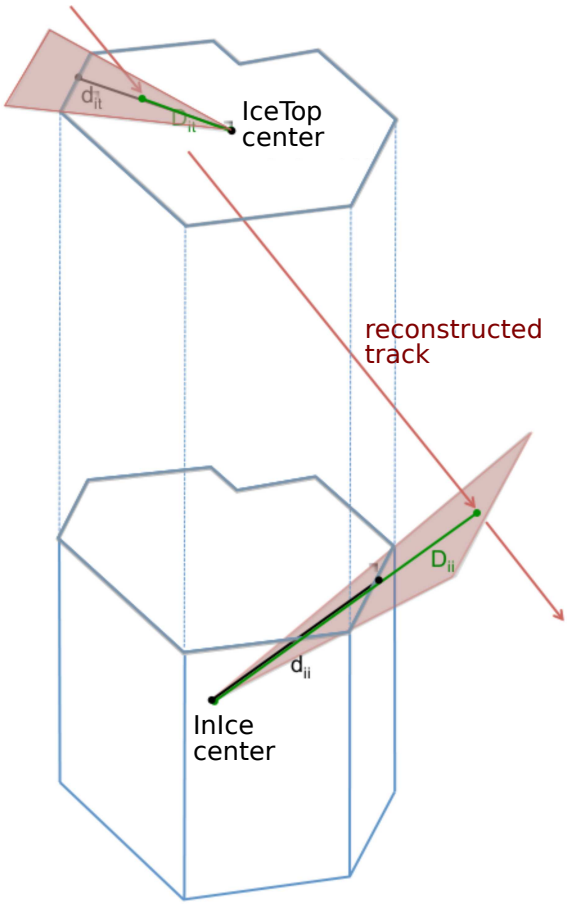

Figure 5.16: Illustration of the containment requirements in IceTop and IceCube. The red arrow represents the reconstructed track, D_{it} and d_{it} respectively indicate the distance between the center of IceTop and shower core and edge of the array. The closest approach of the track to the center of the IceCube array is given by the line D_{ii}, while the distance between center the border of the IceCube volume following this line is indicated with d_{ii}.

Table 5.2: Set of IceTop quality cuts to obtain well-described events, suited for standard analyses.

Quality cut	value
Filter passed	true
Reconstruction succeeded	true
Loudest station not on edge	true
Highest charge	> 6 VEM
Charge in neighbouring tank of highest charge tank	> 4 VEM
IceTop containment factor	$<$0.97
Station density factor	> 0.2
Slope at 125 m from shower core (β)	> 1.4

5.4 Level 3 processing: IceCube

Muons with an energy exceeding 300 to 400 GeV can penetrate through the 1.5 km thick ice layer and create a series of hits in the deep detector. In air showers, these high-energy (HE) muons come in bundles containing up to thousands of muons. The main purpose of the reconstruction procedure is to obtain an estimate of the number of HE muons, which is an excellent parameter to identify the primary particle type (section 3.3.2). The series of steps in the reconstruction procedure is schematically shown in Figure 5.17. The first step

treats the selection of the in-ice hits that are causally connected in time to the hits in IceTop (section 5.4.1). Hereafter the IceCube Level 3 processing is split in two distinct branches, mostly suited for different types of analyses. A coincident analysis that aims to study air showers that have their core inside the IceTop array uses the track reconstructed with the surface array to perform the in-ice pulse selection and energy loss reconstruction (section 5.4.2). If the core of the EAS lies outside IceTop, the determination of the track with IceTop is unreliable and the track is reconstructed based on the energy loss deposition in the IceCube detector (section 5.4.3). Further quality cuts are defined for the muon bundle analysis based on the track reconstruction with IceTop (section 5.4.4), to provide a set of well-described events.

5.4.1 Pulse selection

When an air shower causes an IceTop SMT trigger, the deep IceCube detector is read out for ± 10 μs centered around the start of the trigger (Table 2.2). This time window suffices to record all pulses related to the HE muon bundle. The muon bundle then also fires one or more IceCube triggers.
All IceCube SLC and HLC pulses were calibrated in Level 1 and Level 2 (section 5.2), and the hits in the known bad DOMs were removed. Furthermore also waveforms with calibration problems are removed and kept in a separate list. At last, an extra correction is included ("Pass 2") before the actual pulse selection, due to an inconsistency in the determination of the peak position in the charge spectrum of single photo-electrons. No such correction will be required in the future, since all the files created after the Level 2 processing are reprocessed with this Pass 2 correction.
For (most) cosmic ray analyses all the data within one global trigger window is split into interesting physics events based on the hits in the IceTop tanks. This procedure was described in section 5.2.1. The IceCube data remained untouched and the pulses related to the air shower need to be selected at this point in the analysis. Background noise or hits caused by other events shortly before or after the muon bundle need to be removed.

Coincident time window cleaning

The first step is to find an InIce SMT trigger which could be causally connected to the IceTop trigger by the propagation of a muon bundle. Sometimes only one trigger is present in one global trigger window, but in many cases multiple InIce SMT triggers are present and the according SMT trigger needs to be selected. This is especially true when also a trigger with a long readout window was passed, for example a SLOP or fixed rate trigger (Table 2.2).
Figures 5.18 and 5.19 provide an example event to illustrate this first pulse selection procedure. The global readout window was in this case extended due to the presence of a SLOP trigger. In the event view (Figure 5.18) the hit time is given by the colour scale, here chosen from grey to yellow to red to highlight the important physics events. In this colour scheme all early noise hits appear in grey, while two track-like events are displayed in yellow and red. The size of the spheres illustrates the amount of Cherenkov light detected in a DOM. Figure 5.19 shows the total charge deposition as function of the global trigger time of this DAQ event. The two track-like events are clearly visible in the charge deposition of the IceCube pulses (around 820 and 845 μs). These energy depositions also fired the InIce SMT triggers.
The causal relation with the IceTop pulses (at $\sim$840 μs) reveals that the second (larger) energy deposition is the true muon bundle related to the IceTop event (seen in red in Figure 5.18). Indeed, using the speed of light as approximation, the signal of the muon bundle should appear roughly 5 μs later as compared to the IceTop hits.

The IceCube pulses are thus expected in a certain time window after the IceTop hits, which can be used to remove all hits outside this time window. This coincident time window cleaning ("coinc-twc") procedure first looks for an InIce SMT trigger in a window ranging from 2 μs to 7 μs after the IceTop trigger. For muon bundles that would be contained in both IceTop and IceCube, it would suffice that the window starts at $\sim$ 5 μs (for vertical showers) and ranges up to 7 μs (for showers with zenith angle $\sim$40 °). The extension of the lower boundary of the time window to 2 μs is done to include inclined air showers that traverse the

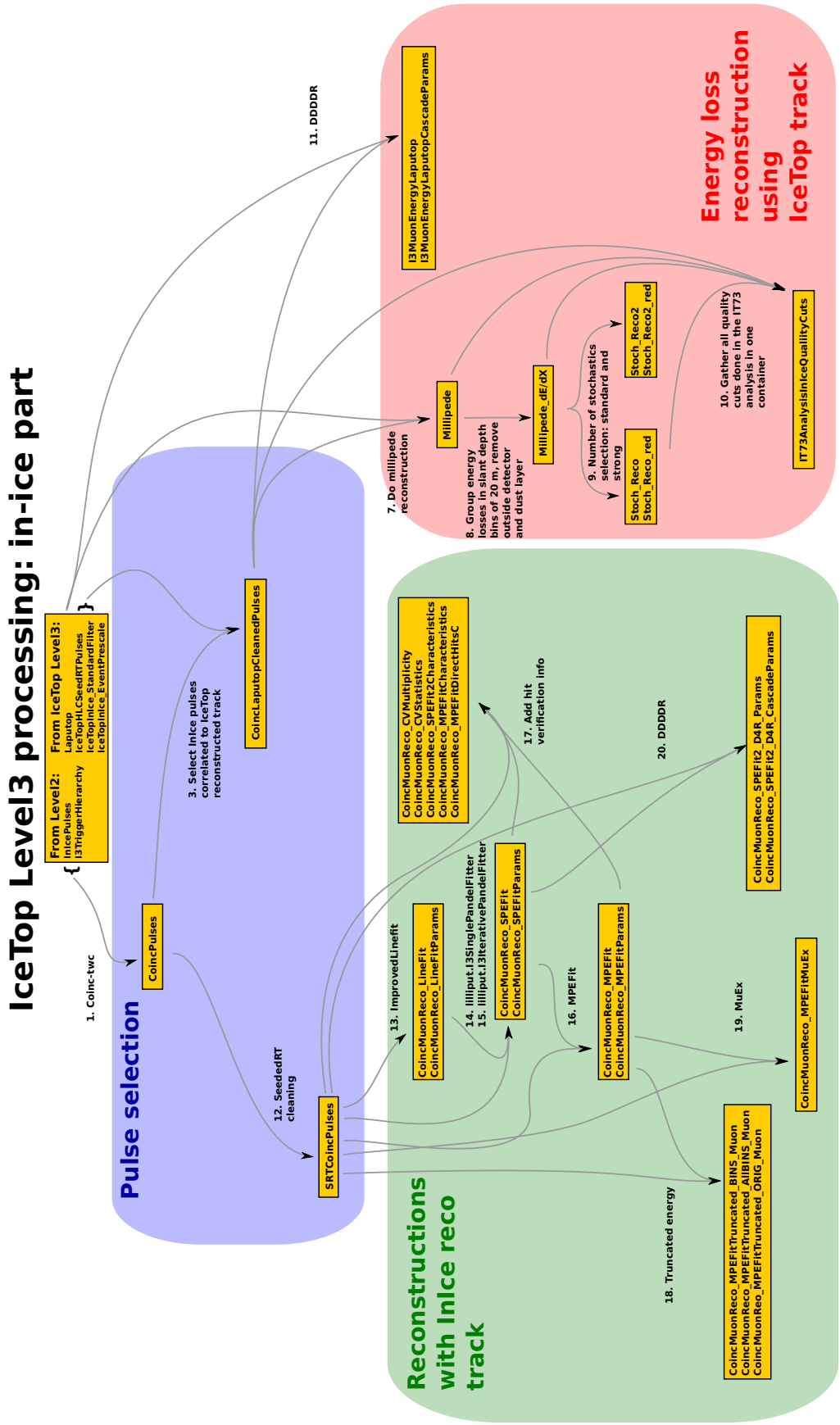

Figure 5.17: Flowchart showing the IceCube part of the cosmic ray Level 3 processing.

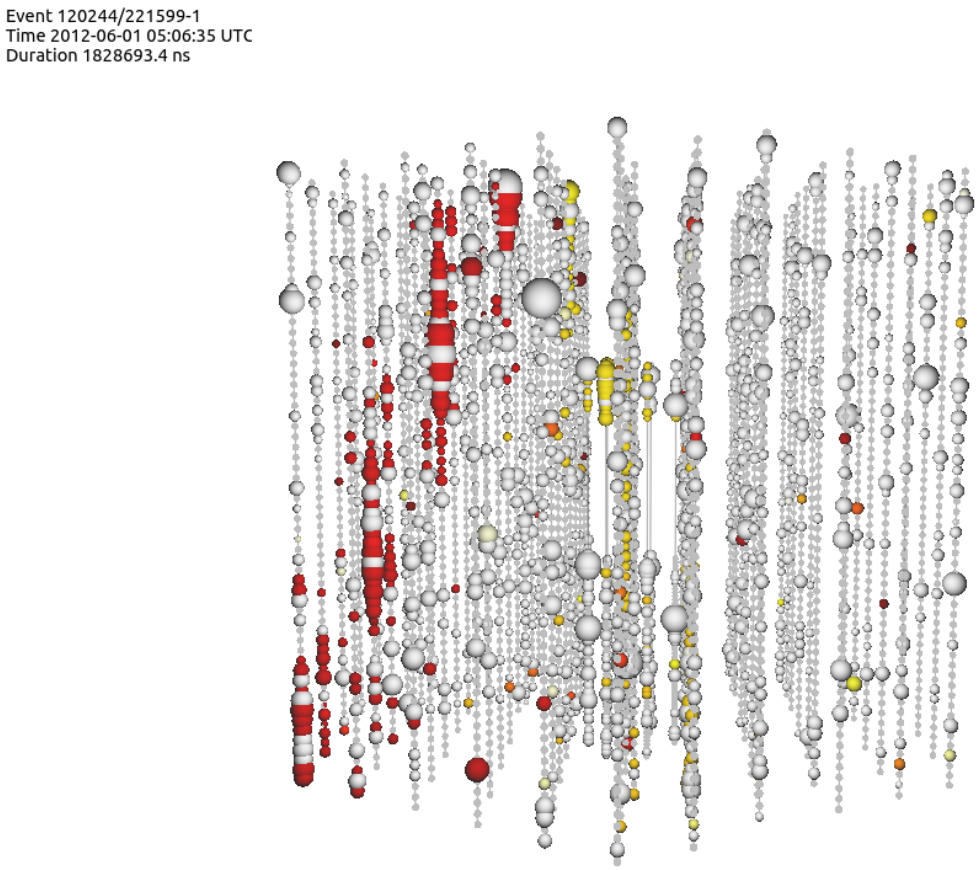

Figure 5.18: Charge deposition in the IceCube array during a long global readout window for (real data event). Each sphere represents one DOM and the size of the sphere illustrates the amount of Cherenkov light collected by the DOM. The colour scale ranges from grey to yellow to red. The signals corresponding to the muon bundle related to hits in IceTop are seen in red. Another track-like signal, arriving before the actual muon bundle, is seen in yellow. The charge deposition as function of time of this event is shown in Figure 5.19.

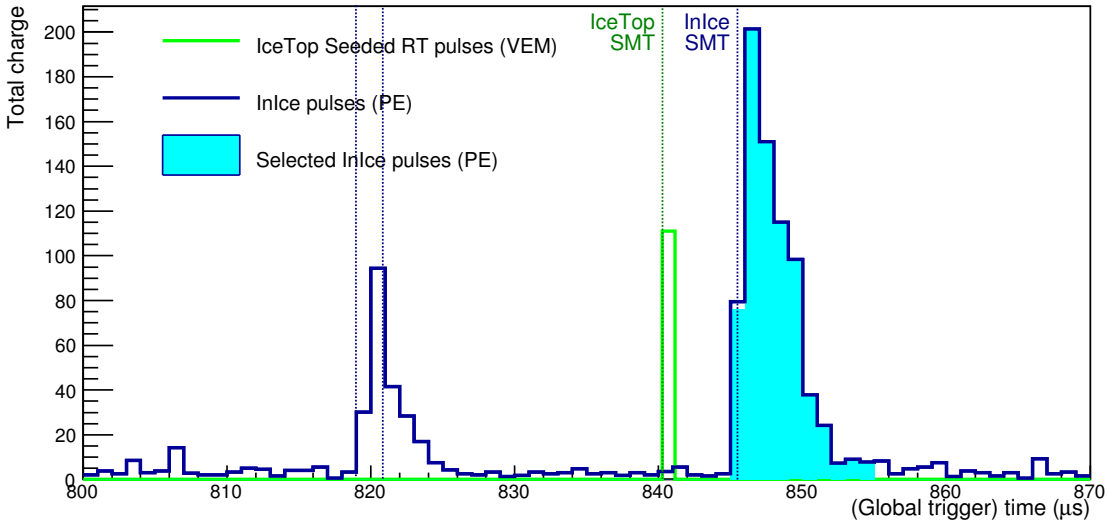

Figure 5.19: Measured charge as function of the time of an example (real data) event, illustrating the selection (filled area) of the IceCube pulses (blue) related to the IceTop pulses (green). The event can be seen in Figure 5.18. The time is given with respect to the start of the global trigger. The unit of the total charge observed in a time bin is VEM for the IceTop pulses and number of PEs for the IceCube pulses. The dotted lines indicate the IceTop (green) and InIce (blue) SMT trigger times.

IceCube detector but have their core outside the IceTop array (but still create an IceTop trigger). 2 μs is chosen such that air showers with inclinations up to 65 $^\circ$ are included.
When the correct InIce SMT trigger is found, the pulses are selected from 0.3 μs before the start of the trigger until 0.4 μs after the end of the trigger, while the other pulses are removed. The length of the cleaning window is restricted to 6.5 μs. Longer lengths could be caused by for example PMT afterpulses extending the trigger window, but are not physical. If multiple InIce SMT triggers are present within the coincident time window, they are all selected and the cleaning window is extended. This then has to be taken care of by further cleanings.

The selected pulses for the event in Figure 5.19 are indicated with the pale blue area. Figure 5.20 (top) provides an event view of the selected pulses, where the colour scheme used is now from red (early) via yellow and green to blue (late).

Pulse selection based on IceTop track

The ideal air shower signature is obtained when the shower axis is contained within both IceTop and IceCube. In this case an optimal reconstruction can be performed with both detectors. The existing analysis aiming to reconstruct the energy spectrum and composition, as well as the analysis described in this work, only uses those ”ideal” events.
For these events, the reconstruction of the core and direction of the air shower using the tank signals in IceTop (section 5.3.4) provides a better resolution than a possible track reconstruction with the deep IceCube detector. The obtained resolutions are shown at the end of this chapter in Figures 5.47 and 5.48. While the IceTop detector units are small containers where the Cherenkov photons are detected very fast after the charged particles entered the tanks, in the deep IceCube detector the created Cherenkov photons often have to travel a further distance. This results in a better timing resolution with IceTop and thus an according better angular resolution.

The track reconstructed using IceTop can now be used for a further pulse selection, since the hits in the

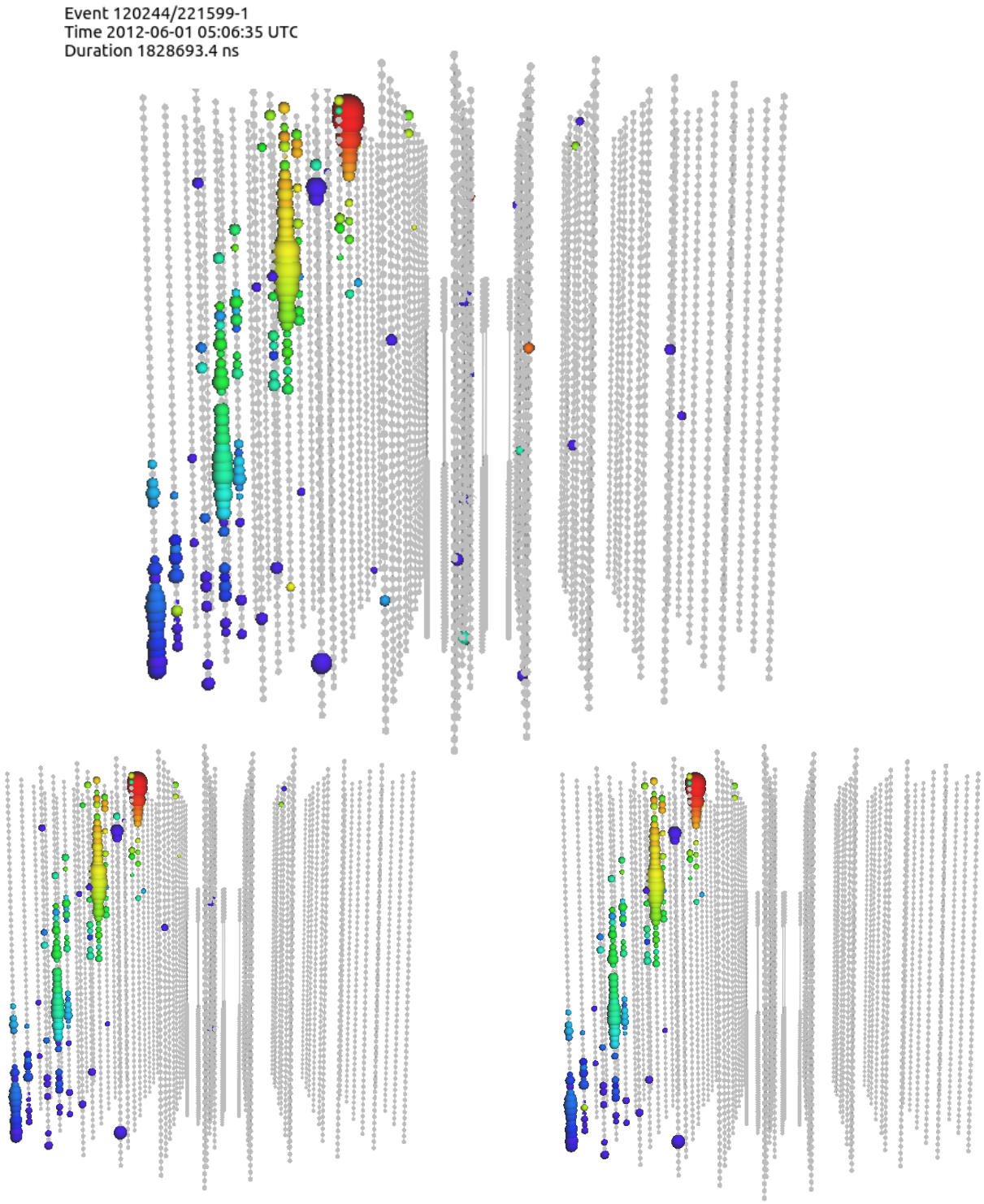

Figure 5.20: Illustration of the IceCube pulse cleaning methods for cosmic rays. Colour scale: red (early) to blue (late). The original uncleaned IceCube pulses of this data event can be seen in Figure 5.18. Top: Pulses selected with the coincident time window cleaning algorithm. Bottom left: Further cleaning using the track reconstructed with IceTop. Bottom right: Seeded RT cleaning of the coinc-twc selected pulses.

deep detector should be related to this track. Hits earlier than the arrival of the muon bundle cannot be correlated to the event seen in IceTop and are therefore removed. This is performed by calculating the time residual of the hit with regard to the propagation of the bundle through the ice. This time residual should not be under -400 ns. Furthermore, hits outside a cilinder with a radius of 500 m centered around the track are also removed. These are most probably noise hits. The bottom left panel of Figure 5.20 illustrates the selected pulses for the event used to illustrate the coinc-twc cleaning, after the cleaning around the track.
Next to the fact that the background removal results in a more reliable energy loss reconstruction, this procedure is also extremely useful to remove random coincidences between independent events detected in the surface and deep array. This is illustrated with a different real data event in Figure 5.21, where the track reconstructed using the hits in IceTop is given by the red line. The muon bundle related to the IceTop hits does not intersect with the IceCube array, while another event (a muon bundle or single muon) arrived shortly before the expected energy deposition of the muon bundle. The hits caused by this energy deposition are accepted by the coincident time window cleaning, but are now correctly removed by the requirement that the hits should be within the cilinder around the track reconstructed by IceTop.

Seeded RT cleaning

The addition of more data on top of the ideal event signatures would be beneficial for many analyses, especially at high primary energies. This gain in detection efficiency could be achieved with the inclusion of air showers that have their core outside the IceTop array, but a muon bundle trajectory that intersects with the deep array. A large air shower created by an energetic primary particle would still create a useful footprint on the IceTop array to estimate the primary energy. These showers are not used in the analysis described in the following chapters, but a separate branch of the IceCube part of the cosmic-ray Level 3 processing is created for these kind of events. The study of this type of events is ongoing.

Since the algorithms that try to reconstruct the core and direction with IceTop are not able to obtain a satisfactory resolution, the IceCube signals are used to perform a directional reconstruction. However, before the reconstruction can be performed reliably, a more accurate hit selection needs to be done. Otherwise the algorithms would be too much influenced by these noise hits. Similar to the IceTop cleaning described in section 5.3.3, this 2nd noise removal procedure is based on the causal distance - time (RT) relation between hits. The seeds, of which there can be many, consist of 2 HLC DOMs next to eachother with hits close in time. Starting from the seeds hits in the neighbouring DOMs are iteratively added, i.e. with a maximum distance of 150 m and time difference of 1 μs. This is performed for two more iterations, making a total of 3 iterations. The hits that were not selected in this ”Seeded RT” procedure are omitted.
The seeded RT cleaned pulses of the event in Figure 5.20 are shown on the bottom right event view. The noise hits far from the real muon bundle track are removed, while all hits that seem to be related to the bundle are kept. This should allow for a reliable track reconstruction. It can be seen that the difference between this pulse cleaning algorithm and the pulse selection based on the track reconstructed using IceTop is small for this event. This is true for the ”ideal” events with a track going through both IceTop and IceCube.
However, a further optimization of the pulse cleaning algorithms in preparation for the track reconstruction in the ice might be desired for future analyses.

5.4.2 Energy loss reconstruction based on track from IceTop

All muons in the HE muon bundle lose energy via a combination of constant ionization processes and large radiative processes. The energy loss along the track is thus a superposition of many particle cascades, as illustrated in Figure 5.23 (left). This is a simulated event, where the separate muons are shown as the red lines and the various energy losses as coloured spheres. The colour of the sphere indicates the time of the energy loss, while its size depicts the amount of energy that was deposited. The created Cherenkov light, emitted by the muons themselves or by the secondary particles created in the energy loss processes, travels through the ice and part of the light is captured by the DOMs. The signal detection is not shown in Figure 5.23, but

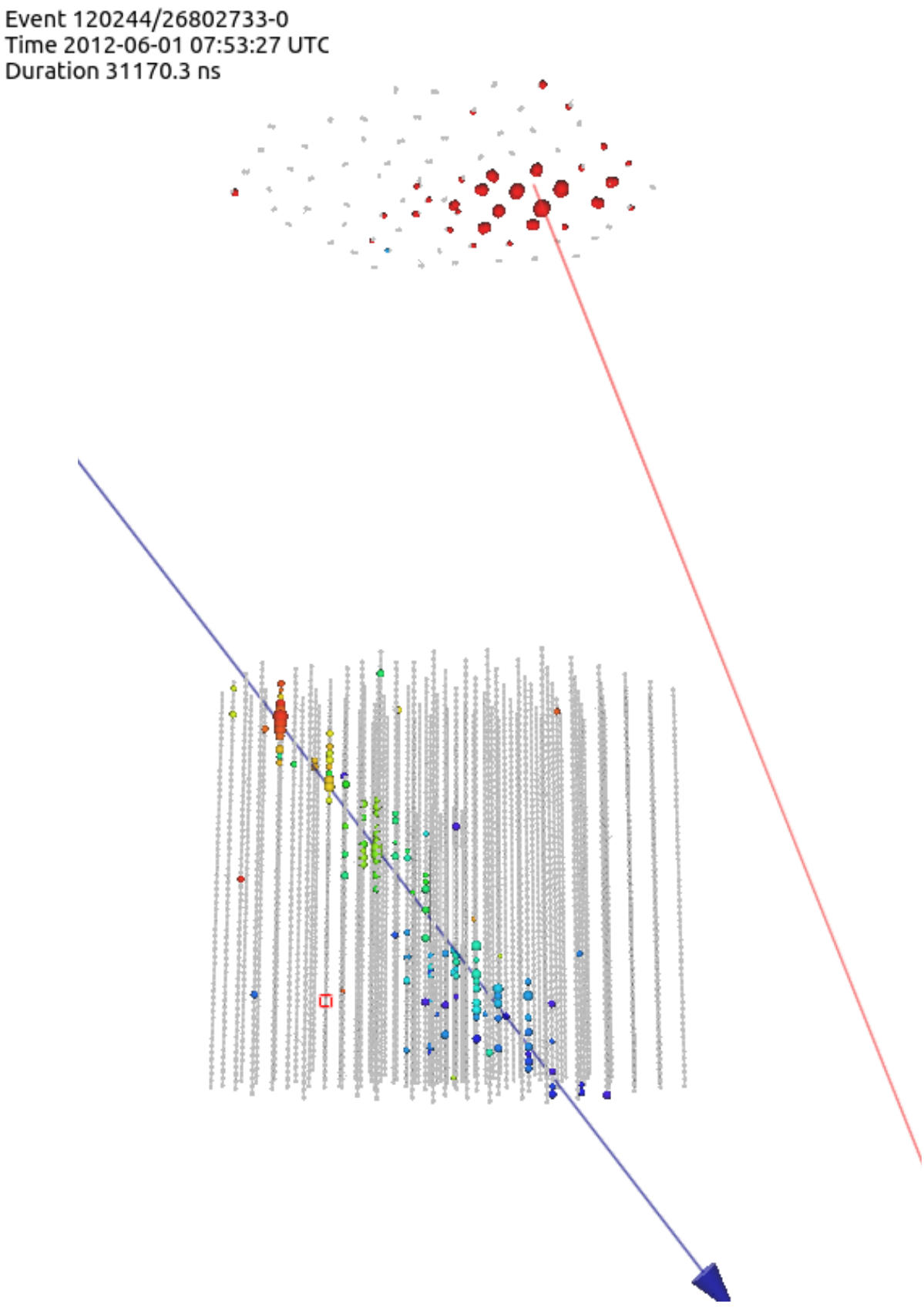

Figure 5.21: Example event illustrating the removal of coincident detections, by the IceCube cleaning procedure around the track reconstructed by IceTop. The IceCube pulses shown are selected by the coincident time window cleaning algorithm. As shown by the track reconstructions using IceTop (red) and IceCube (blue) these are two uncorrelated events, and the cleaning of the pulses around the IceTop track will remove these IceCube pulses.

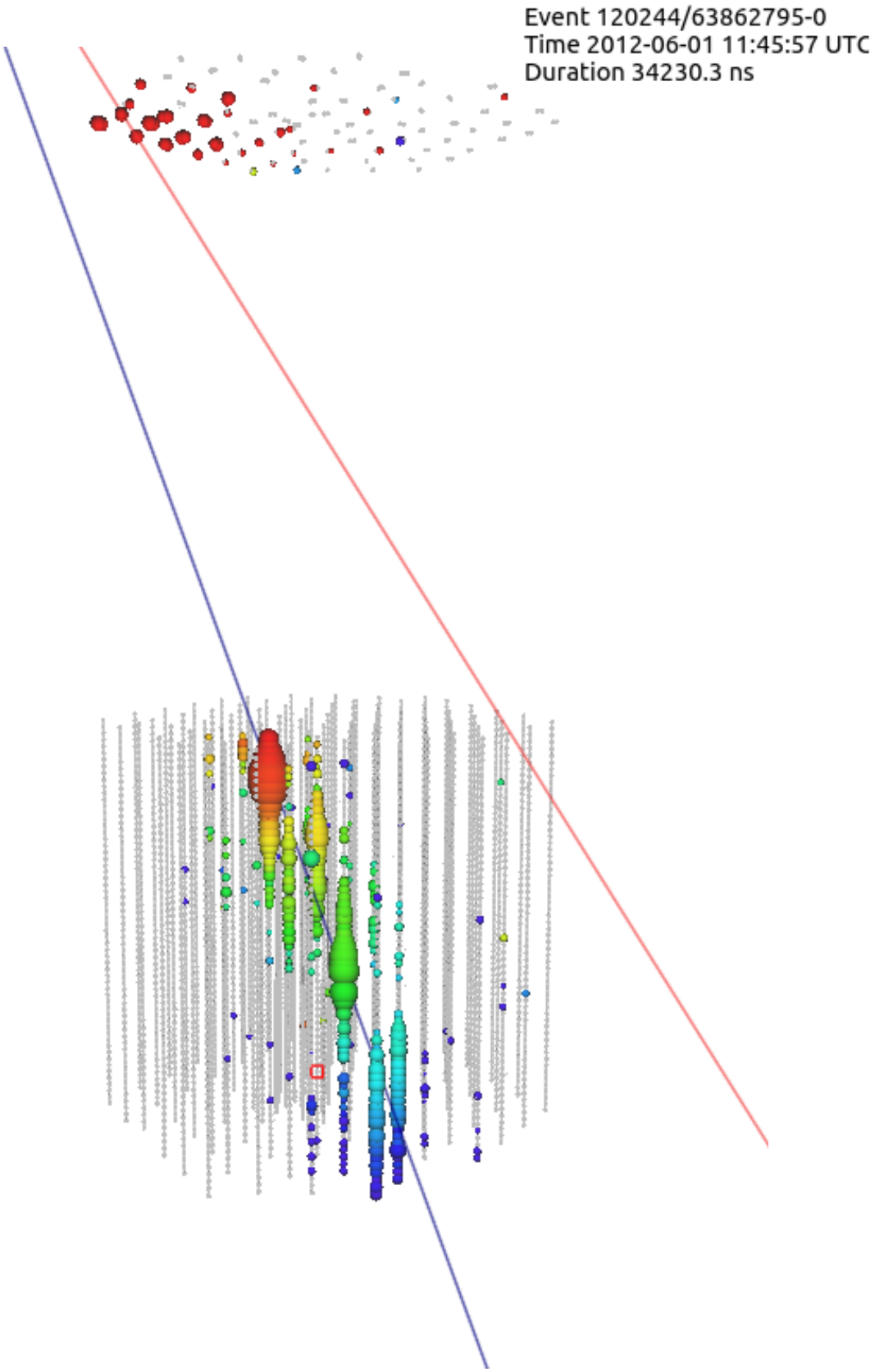

Figure 5.22: Example event view where the core and direction are wrongly reconstructed using the IceTop array (red line), since the core of the shower is located outside IceTop. The IceCube track reconstruction (blue line) obviously performs better.

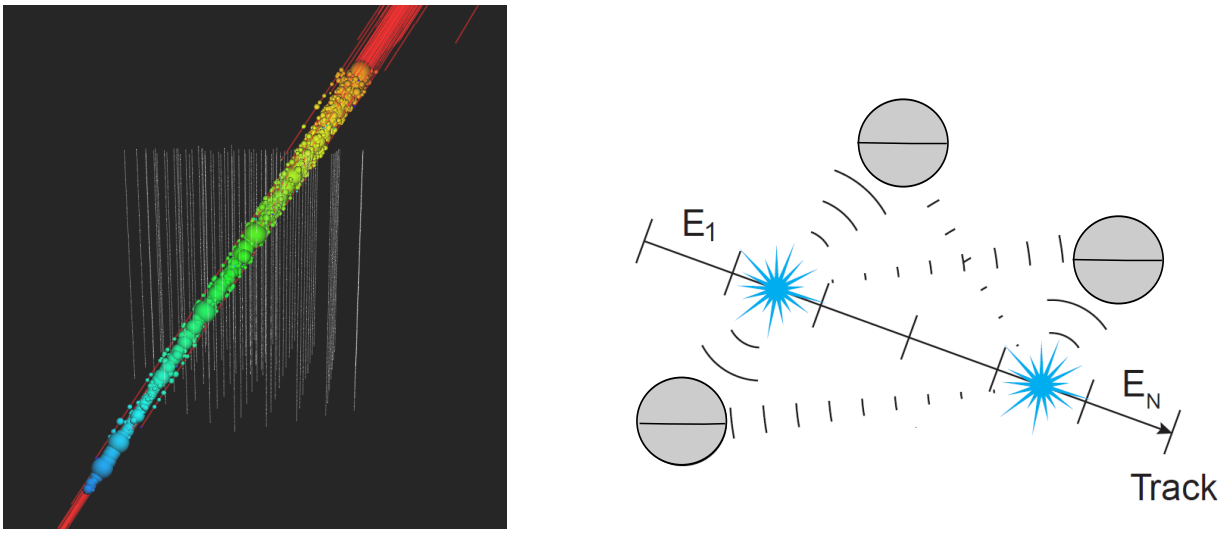

Figure 5.23: Left: simulation of a muon bundle going through the IceCube detector. For this particular event, an iron shower with a primary energy of about 100 PeV was simulated with Sibyll 2.1 and the July 1, 1997 atmosphere. Each red line represents a muon, while the spheres show the energy losses of the muons. The size of the sphere represents the amount of energy loss, while the color scales with the time (thus position), going from red to blue. The signal detections by the DOMs are not shown. Right: sketch of the series of energy losses along the particle track, followed by the radiation of Cherenkov photons detected by multiple DOMs. Figure adapted from [228].

can be seen in the figure on the front page of this chapter (Figure 5.1). These pulses are now used to reobtain the original properties of the muon bundle, i.e mainly the number of high-energy muons. This provides the sensitivity to the mass of the primary particle, although the shower-to-shower fluctuations are large. It should be noted that the amount of energy that a muon loses is also proportional to its energy. Hence, a degeneracy between the number of muons and the muon energy is present and the reconstructed energy loss and muon multiplicity are far from perfectly correlated.

For the events which have a reliable reconstruction of the track with IceTop, the energy loss reconstruction is based on this track. The pulses in the IceCube DOMs were selected on their proximity in time and space to a muon bundle passing through the ice in the direction and location determined by IceTop. In the Level 3 processing for cosmic rays two methods to reconstruct the energy losses along the IceTop track are implemented, which are shortly described below. The first of the two methods is used in this work (following chapter). Further cuts that are implemented and used are also based on the former method.

Waveform unfolding and bundle energy loss profile

Many energy loss processes of the large number of muons create a huge amount of Cherenkov photons along the track of the muon bundle. The Cherenkov light travels in all directions through the ice to the DOMs, affected by the dust particles or air bubbles through scattering and absorption processes. The light created at one location is hence often seen by several DOMs. These DOMs are located close and far from the track and detect direct and scattered photons. The waveform in a DOM is thus often a superposition of many Cherenkov photons. These could have been created from the same particle cascade and all travelled to the DOM via a different path, thus arriving at a slightly different time, or they could have been generated from various energy deposits at different positions along the muon bundle. This is illustrated in the right panel of Figure 5.23 and can be translated to the linear algrebra expression:

$$\vec{Y} = \mathbf{P}\vec{E} + \vec{N} \tag{5.17}$$

where $\vec{Y}$ are the measured charges in PE per DOM, $\vec{E}$ is the vector of energy losses along the track and $\vec{N}$ is the charge from the noise in the DOMs. $\mathbf{P}$ is the matrix that models the transmission of the light through

the ice. The goal of the reconstruction procedure is to unfold the waveforms $\vec{Y}$ in all DOMs and reconstruct the energy deposits $\vec{E}$ in track segments along the muon bundle trajectory. This is not an easy process, and is performed with a reconstruction called "millipede", described in detail in [65]. The transmission matrix **P**, or "photon table", is created from particle simulations in all directions and various primary energies, which are subsequently spline-fitted. Different tables are produced for every different assumption of the scattering and absorption coëfficients (section 2.1.3). Furthermore, also a certain DOM efficiency (section 2.1.2) needs to be assumed. Both of these effects, ice properties and DOM efficiency, are roughly linearly proportional to the reconstructed energy loss. Since the uncertainty on these values is large, they are an important source of systematic error. Millipede then uses a likelihood minimization where poissonian fluctuations are considered and the vector of energy losses is retrieved as an output.

For the muon bundle energy loss reconstruction the track is divided into segments with a length of 20 m. This seems a good trade-off between the accuracy of the locations of the energy losses on one hand and computing time and statistical variations on the other hand. The energy depositions are computed at slant depths ranging from 1300 m to 2600 m. In reality the muon bundle is spread out over $\mathcal{O}$(10 m), but in this procedure the approximation is made that they are all travelling along the bundle axis. Their arrival time is smeared with a gaussian with a width of 30 ns. The energy loss reconstruction using millipede could be further optimized for muon bundles.

The millipede output is shown for an example event in Figure 5.24. The black histogram indicates the individual reconstructed energy losses in every bin along the muon bundle track. The energy losses in the dust layer and outside the detector are removed. This obtained energy loss in bins along the bundle trajctory is subsequently fit with a function to obtain useable parameters (solid red curve). The function was derived in [101]:

$$\left(\frac{dE_{\text{bundle}}}{dX}\right)(X) = \left(\frac{\kappa A}{\cos\theta}\right) \cdot e^{-bX} \cdot \gamma_\mu \cdot \left(\frac{E_0}{A}\right)^{\gamma_\mu - 1} \cdot \left[\left(-\frac{E_0}{A}\right)^{-\gamma_\mu} \left(\frac{a}{\gamma_\mu} - \frac{b}{1-\gamma_\mu} \cdot \frac{E_0}{A}\right) + \left(\frac{a}{b}(e^{bX} - 1)\right)^{-\gamma_\mu} \left(\frac{a}{\gamma_\mu} - \frac{a}{1-\gamma_\mu}(e^{bX} - 1)\right)\right] \tag{5.18}$$

where a=0.23881 GeV/m and b=$3.2852 \cdot 10^{-4}$ m^{-1} are respectively the ionisation energy loss and the radiative energy loss constant from the average energy loss of muons. κ=14.5 GeV and γ_μ=1.757 are parameters from the Elbert formula (Eq. 3.18). The mass parameter A is kept fixed at 16 and the only parameter that is fitted is E_0. This does not represent the primary energy since A is kept fixed. Instead, the energy loss at a 1500 m slant depth ($\frac{dE}{dX}$(X=1500 m)) as read from the fit is used as the main parameter sensitive to the mass of the primary particle.
The relation with the number of muons with an energy above 400 GeV is shown in Figure 5.25. In the left panel the 2D distribution is shown, for proton showers with a primary energy between 1 and 1000 PeV. Only the more vertical showers with a zenith angle θ with $\cos\theta > 0.8$ are used. The right panel gives the means of a gaussian fit to each vertical bin (of the number of muons), for both proton and iron showers. These plots show the (approximate) linear relation in log-log space between the two variables. Since showers induced by heavier primaries possess more muons, this parameter provides a clear composition sensitivity. As discussed before, also a large spread is seen in the reconstructed energy loss for a certain number of HE muons. Hence, many showers are required to perform a successful estimate of the composition of cosmic rays (in a certain primary energy bin). This variable ($\frac{dE}{dX}$(X=1500 m)) is used in the analysis described in the following chapters and its proton-iron separation is discussed and shown there.

In the analysis of the energy spectrum and composition of cosmic rays with IceTop and IceCube, two more variables are used. While showers initiated by heavier primaries contain more HE muons, the average

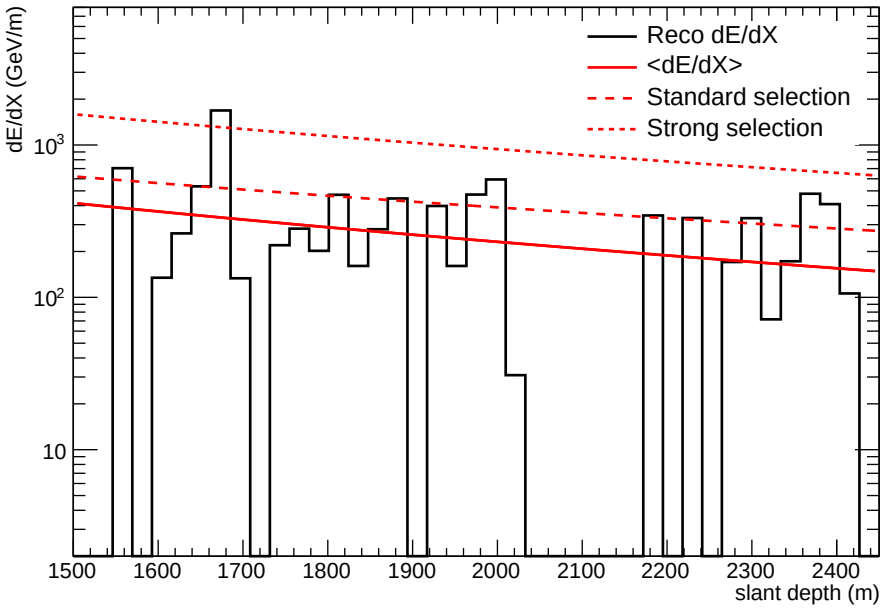

Figure 5.24: "Millipede" reconstruction of the energy loss (in GeV/m) as function of the slant depth along the track (in m) for one example event (black histogram). The solid red curve shows the average energy loss, from a fit to the binned energy losses (Eq. 5.18). The dotted curves give the levels above which the number of stochastic losses are counted.

muon energy is higher for lighter nuclei. This is seen in Figure 3.8 and can be easily understood with the superposition principle. For lighter nuclei more energy is available per nucleon in the first collisions, which result in higher energetic secondaries and thus more energetic muons. Since the stochastic energy loss processes increase with increasing muon energies, one could also expect a difference in the extreme energy losses measured in the ice. Therefore, two thresholds are chosen above which the number of stochastic losses are counted. These limits are shown in Figure 5.24 with the dotted red lines. The standard selection uses the criterium

$$\frac{dE}{dX}(X_i) > 5 \cdot \left(\frac{dE_{\text{bundle}}}{dX}\right)^{0.8} , \tag{5.19}$$

while for the strong selection

$$\frac{dE}{dX}(X_i) > 7 \cdot \left(\frac{dE_{\text{bundle}}}{dX}\right)^{0.9} \tag{5.20}$$

is used.

Data-Derived Deterministic Differential Deposition Reconstruction (DDDDR)

Next to the above described waveform unfolding algorithm, another reconstruction method of the energy loss profile is implemented in the Level 3 processing: Data-Derived Deterministic Differential Deposition Reconstruction ("DDDDR"). This method has been used and described in the measurement of the muon multiplicity with the deep IceCube detector [146]. The IceTop component was not used and the directional information was obtained as described in the following section. In this study the light quantity as function of the distance to the muon (bundle) track has been studied in real data events. The light attenuation for the DOMs with increasing lateral distance to the shower axis was found to behave as shown in Figure 5.26 (left). At small lateral distances (up to d_0) the light density can be approximated as constant with increasing distance to the track, while it decreases exponentially at larger distances. The exponential decrease is caused by the absorption and scattering of the light in the ice. For each horizontal layer in the ice such a curve is

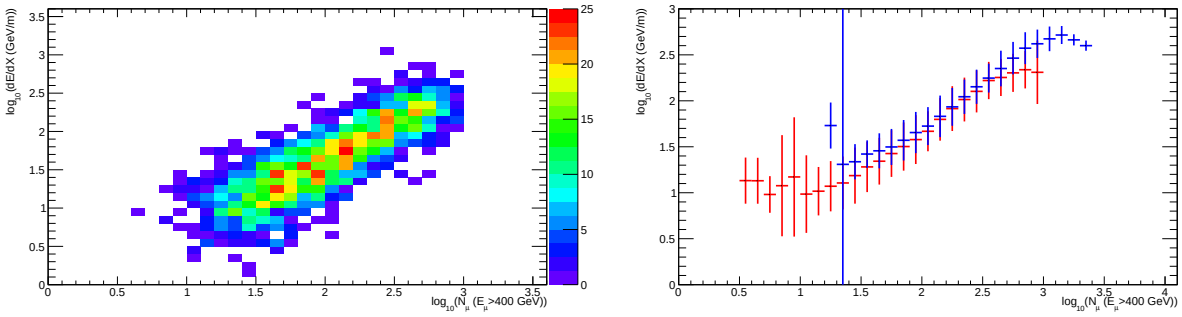

Figure 5.25: The reconstructed average energy loss at a slant depth of 1500 m in relation to the number of muons, obtained from simulated air showers for the IC86.2012 configuration (Table 4.6). The muon energy is at least 400 GeV, while only air showers with a primary energy between 1 and 1000 PeV are used. The zenith angle θ is restricted to $\cos\theta > 0.8$. Left: 2D distribution for proton initiated showers. Right: mean and sigma of a gaussian fit to each vertical bin in this distribution, for proton (red) and iron (blue) showers.

produced and fitted (black curve). The derived number of photons that are created can further be related to an actual energy loss using simulations. As such, the total conversion from measured DOM charge q_{dom} to a reconstructed muon (bundle) energy loss $\frac{dE_\mu}{dX}$ for each DOM is given by:

$$\frac{dE_\mu}{dX} = \frac{q_{DOM}}{\epsilon_{DOM}} \cdot f \cdot \begin{cases} d_0 & d_{DOM} < d_0 \\ d_{DOM} \cdot e^{(d_{DOM}-d_0)/\lambda_{att}(z)} & d_{DOM} > d_0 \end{cases} \tag{5.21}$$

Here ϵ_{DOM} is the DOM efficiency, f = 0.020 GeV/(m$^2\cdot$ p.e.) the conversion factor obtained from simulations and d_{DOM} the perpendicular distance from the DOM to the track. The attenuation constant λ_{att} is defined for each horizontal layer in the ice, therefore it depends on the height z with respect to the center of the detector. It shows a great accordance with the properties of the ice [146]. Due to reasons of computation time and statistical fluctuations only DOMs within a maximal perpendicular distance of 70 m(red line), 100 m(green) or 150 m (blue) from the track are taken into account. One can choose between these three settings, but in the standard Level 3 processing a maximal distance of 100 m is used. Also DOMs at a lateral distance closer than 25 m from the track are discarded, which makes the constant region close to the track less important.
The reconstructed energy losses of each DOM projected on the track are grouped in longitudinal bins of 50 m along the track.
The result of such a DDDDR energy loss reconstruction for a real data event is shown in Figure 5.26 (right). It should be noted that here a very inclined event is taken, which is probably only one very energetic muon. The energy losses obtained in every DOM are shown, together with the averaged values in the 50 m longitudinal bins using the three different cutoffs. The peak in the reconstructed energy loss profile and the median are also given. The sensitivity of this median or also the mean energy loss to the number of muons in an air shower and thus to the primary particle type is comparable to the $\frac{dE}{dX}$(X=1500 m) obtained from the fit to the millipede output (Eq. 5.18).

5.4.3 Reconstruction of direction and energy with the IceCube array

As described above, for air showers that hit the surface with a core outside the IceTop array it cis useful to try to reconstruct the direction with the deep IceCube detector. Although the achieved resolution is worse, it sufffices to perform a reliable reconstruction of the energy loss along the track and might help for a surface reconstruction. The directional reconstruction is entirely decoupled from the subsequent reconstruction of the energy loss profile. The SeededRT cleaned IceCube pulses (section 5.4.1) are used as input.

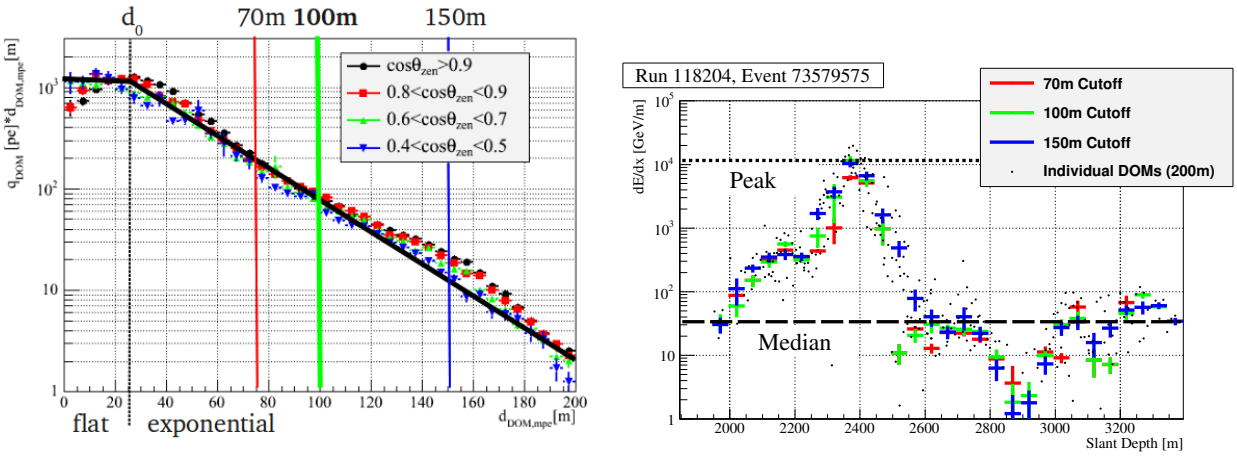

Figure 5.26: Illustration of the DDDDR algorithm to reconstruct the energy loss of muons or muon bundles. Left: illustration of the exponential attenuation of the photon light yield due to absorption and scattering in the ice, derived from data. Various primary zenith angles are shown and some important minimal and maximal distances are indicated. Right: reconstruction of the energy loss profile for one data event using the DDDDR method. [146]

Directional reconstruction

While the energy loss is mainly determined by the total charge, the directional reconstruction strongly depends on the time distribution of the detected pulses. The large uncertainties on the path followed by the Cherenkov photons due to scattering processes make this a difficult task. The track is defined by six free parameters for position, time and direction ($\mathbf{x}$, t_0, θ, ϕ). Similar to the IceTop reconstruction, a likelihood minimization technique is used to find the right parameters. This is done in several steps due to the complex 6-parameter space which could result in a wrong local minimum. The procedure is developed specifically for muon tracks [229, 230], but can also be applied to muon bundles.

A likelihood minimization takes a big advantage out of a reliable seed. The first guess procedure for a track reconstruction in IceCube, called ”LineFit” [231], approximates the Cherenkov light radiation as a plane wave travelling along the particle track. The time of the first hit of each pulse in a DOM is as such related to the track hypothesis and a least squares minimization is used to obtain the track. The ”improvedLineFit” method [232], which replaced LineFit, meanwhile removes noise hits further improving the first guess procedure.
The seed is used for the first likelihood minimization procedure, called single-photoelectron (”SPE”) fit. In this SPE fit, the actual radiation angle of the Cherenkov emission is taken into account, as well as the scattering and absorption in the ice. The time delay of a scattered photon with respect to the unscattered path is modelled in this minimization using a Gaussian-smeared Pandel function [233, 234]. In the SPE Fit, only the time of the first photon arriving at the DOM is used, of which there is a larger chance compared to the other photons that it is a direct photon. This seems to provide a good track reconstruction, while it is also computationally favourable. It however entirely neglects that multiple photons hit the DOM. This is taken into account in the following multi-photoelectron (”MPE”) fit. In the MPE fit a binomial probability is added to compute the chance to observe the first photon out of all photons detected at the DOM. This also narrows the width of the arrival time distribution [229]. The MPE fit uses the SPE fit as an input and is the final reconstruction of the direction performed in the ice.

Energy loss profile along the track

Three different algorithms are implemented in the Level 3 processing to reconstruct the energy losses along the track reconstructed with the MPE fit. This is done in order to keep consistency with what is used in

online and offline processing by muon analyses. Due to computation time limitations it was chosen to not run millipede on these tracks reconstructed with IceCube. The DDDDR algorithm on the other hand is ran since it is used in the measurement of the muon multiplicity with the deep IceCube detector [146], also relies on the IceCube track reconstruction. It is ran with the exact same settings as when the track is reconstructed using IceTop. On top, two extra algorithms are used: MuEx [65, 235] and Truncated Energy [65, 236]. MuEx uses a parametrization of the number of photons as function of distance to the muon track to convert the measured photon number to the average number of emitted photons, following a poissonian distribution. This can then on its turn be converted to a muon energy. This is similar to DDDDR, but obtained from theory as compared to parametrized from data. In MuEx however no segmentation of the track occurs. In the Truncated energy method the track is subdivided into segments with a length of 120 m, and only DOMs within a perpendicular distance of 10 to 80 m from the track are taken into account. Within the hollow cilinder around the track segment the total measured number of PEs in all the DOMs are summed. This value is then compared to the expected number of PEs for a muon following the same path but an energy loss of 1 GeV/m. The obtained ratio provides the energy loss dE/dX in this segment. The mean of all of those segments could be used as an estimate of the energy of the muon or number of muons, but it was found that the result is more reliable when some fraction of the segments with highest reconstructed energy losses are omitted in the calculation of the average ("Truncated"). When the track is shorter than 360 m, i.e. 3 track segments, the method is unreliable.
All of these algorithms can provide an estimate of the muon energy or number of muons in a bundle and perform rather well. These tools are available in the cosmic ray Level 3 processing and it seems up to the user or to a specific analysis to use and improve a certain method.

5.4.4 Event quality description

Similar to the IceTop part (section 5.3.6), cuts are implemented to ensure a good quality of the IceCube reconstructions. This event selection is only based on the energy loss reconstructions using the IceTop track (section 5.4.2). For the directional reconstruction with IceCube (section 5.4.3), which is not used in the further analysis described here, no cuts are defined yet.

All the implemented cuts are used to ensure a good quality of the energy loss reconstruction using millipede. At first, one needs sufficient hits related to the muon bundle. This in practice translates to a requirement that 8 different DOMs need to be present in the cleaned pulses (section 5.4.1), i.e. in the coincident time window and around the IceTop track. This is followed by two cuts on the output of the millipede algorithm. The reduced loglikelihood of the minimization is required to be smaller than 2. A second signature of a wrong solution in the millipede minimization is the fact that the total charge in a forward folding of the reconstructed energy losses in the various segments is significantly smaller as compared to the measured total charge. A threshold of $\log_{10}$(forward folded charge/measured charge)> -0.03 is chosen. Finally also the fit to the binned energy losses as function of the slant depth (Eq. 5.18) needs to be succeeded. In order to ensure this further, at least three bins need to contain energy losses after the removal of the energy losses in the dust layer and outside the detector. By posing these requirements, the track of the muon bundle needs to intersect significantly with the IceCube detector. This removes corner-clipping trajectories or muon bundles at the edge of the IceCube array.

5.5 Environmental effects

Ideally, the circumstances in which a telescope operates do not change. If they do vary, it would be convenient that they do not alter the data-taking significantly. However, due to its specific location the situation at South Pole is so extreme, that one can observe variations that are important to consider. In section 5.2.2 it was already seen that the calibration of the IceTop tanks depends on the temperature of the DOM, which changes throughout the year. In the current section the two main environmental effects on cosmic ray measurements

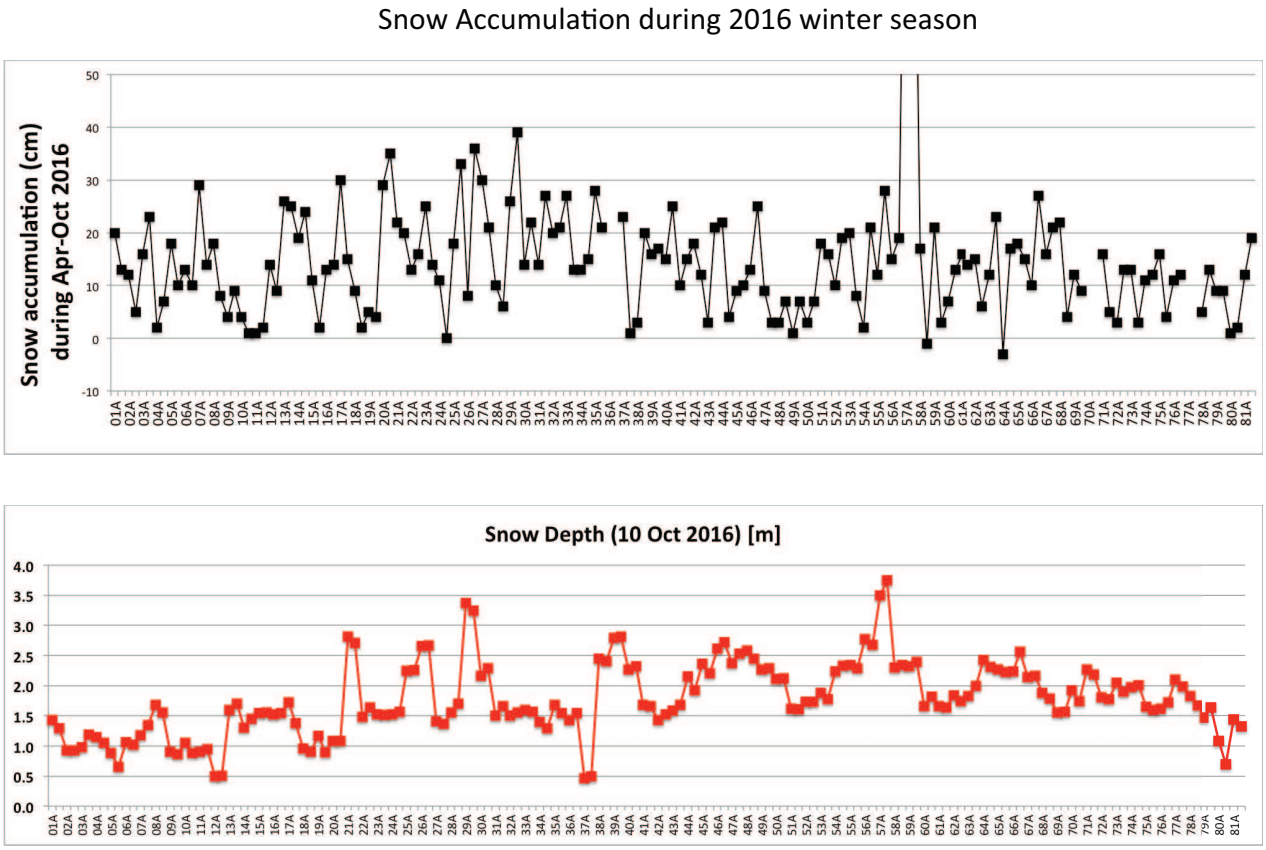

Figure 5.27: Top: snow accumulation from April 2016 to October 2016 for all IceTop tanks. Bottom: snow depth in October 2016 on top of all tanks. Credits: Serap Tilav

with IceTop and IceCube are discussed. As will be shown in section 5.5.2, also the atmospheric temperature at heights of $\mathcal{O}(10)$ km significantly influences the measurements, i.e. of the high-energy muon bundles with the deep detector. The main effect on the response of the IceTop tanks on the other hand is the accumulation of snow on top of the tanks (section 5.5.1).
All these variations that alter the response of the detector need to be taken into account if one wants to reconstruct the properties of the primary cosmic ray properly. These corrections are either included in the Level 3 processing (for snow) or done a posteriori (for the HE muon bundle).

5.5.1 Snow

If one stands at the geographic South Pole and neglects the recent man-built research stations, all one sees is a gigantic plain of snow, more snow and even more snow. Yet the snowfall is very small, only 1-2 cm of snow is actually caused by precipitation. Due to the remote location, far from any sea, Antarctica is a frozen desert and the South Pole is one of the dryest places on Earth. However, strong winds blow from the shores to the center of Antarctica, predominantly from the northeast direction, with a speed of $\sim$5 m/s [87]. The wind carries the snow along and causes a significant snow acculumation in the entire area. This increase of the average snow height influences the data-taking significantly, as discussed below.

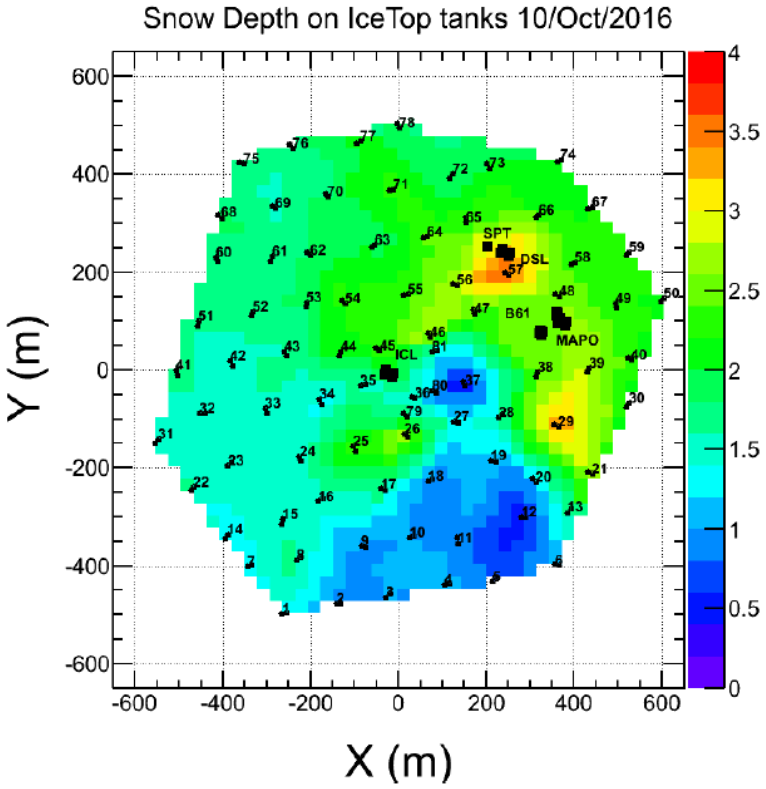

Figure 5.28: Map of the snow height level (in meters) on the IceTop array. Also the main buildings in the array are indicated. Credits: Serap Tilav

Snow heights

At the time of deployment, the tanks were deployed with their lid flush with the snow surface (Figure 2.10). In the meantime, they are all covered with a snow layer. Per year, the snow drift gives rise to an average snow accumulation of 22-23 cm in the entire area, thus also on top of the IceTop tanks. As an example, the snow accumulation from April 2016 to October 2016 on top of each tank is shown in Figure 5.27 (top). This illustrates the above given yearly average snow build-up, although a few more centimeters are added during the austral summer months. It also shows that the accumulation is far from uniform: while on some tanks almost no snow accumulates, it can reach up to 40 cm or more for others. This is mostly due to the slope in the terrain and the vicinity of buildings. The snow accumulation on top of station 57 is extreme since it is located very close to the SPT and BICEP experiments. From time to time some snow gets removed from those tanks, which is accompanied by a more than usual amount of snow piling up during the winter months. The total snow accumulation from deployment to October 2016 is shown on the bottom figure of Figure 5.27. The snow heights in October 2016 thus range from $\sim$0.5 m to as much as $\sim$3.5 m. Next to the slope in the terrain and the approximity of buildings, this large spread in snow heights is also caused by the deployment of tanks in earlier seasons compared to others (Table 2.1). A map of the snow depth across the array in October 2016 can be seen in Figure 5.28.

The snow heights are obtained from measurements using the length of the marker pole attached to each tank, performed by the IceCube researchers at South Pole. Due to the cold and darkness during the long winter, these measurements only occur two or three times per year: once at the start of the austral summer (October or November) and once at the end of the summer (February, March or April). Sometimes one extra measurement is performed around January.

The snow accumulation during the other months is unknown and can only be estimated. One possibility is to guess the snow height using the signal of muons versus the electromagnetic signal in a tank. While muons penetrate the snow almost unaffected, the electrons lose their energy very fast. This thus relates to the estimation of the VEMCal values (section 5.3.2), and is deduced from the ratio of the muonic signal over EM background in Figure 5.9 [237]. The relation between the snow height and this ratio can be seen in Figure 5.32. Although a clear linear relationship is observed, it was found that this method does not provide the required accuracy. As can be seen on this figure, the spread in observed snow heights that agree with a certain VEMCal estimation can reach $\sim$50 cm. This is almost double of the average yearly accumulation. While this method was used in the main previous analyses [139, 142], in Level 3 instead a simple linear interpolation between the measurements is used. This method also has a certain uncertainty, but no unexpected variations can appear.
The reliablity of this linear interpolation was studied using snow height measurements at a snow stake field (containing 50 stakes) at South Pole, maintained by the AMRC [87]. Every month, scientists from the AMRC who winterover at South Pole measure the snow heights at these 50 stakes. Fourteen years (2000 to 2014) of according snow stake data was used to study whether the snow accumulation is more significant during certain months or the linear interpolation describes the behaviour in a satisfying manner. On top, this also allows to study variations in the snow accumulution between several locations. The deviations from a linear interpolation are, as an example, shown for the measurements in 2000 and 2002 in Figure 5.29. As a study, the snow heights are interpolated between January and December and are compared with the actual measurements. In 2000 the interpolated heights seem to slightly overestimate the real snow heights during the entire period. The snow accumulation during the first months of this year seemed to be small. In contradication, in 2002 the average of the measurements fluctuates around the interpolated curve. In general, from these studies it was found that the snowdrift is not particularly dominant during certain months. Hence, this linear interpolation seems to be adequate and can be used for the snow height estimation of the IceTop tanks. However, large stake-to-stake and year-to-year variations, i.e. deviations from the linear interpolation, do are observed. This is shown by the error bars in Figure 5.29. These deviations with regard to the interpolation are, as expected, smallest close to the start and end dates of the interpolation and largest in the middle of this period. These fluctuations should also be taken into account in the determination of the snow heights for IceTop: the interpolated values are not the truth, but the heights should be smeared around the interpolated values. To obtain a rough estimation, the standard deviations obtained from the gaussian fit to the relative difference between the interpolated and measured values (per monthly measurement) are all considered. Their distribution is shown in Figure 5.30. The mean of the gaussian fit to these values (black line) is then used as an estimate to introduce a smearing around the interpolated values. Hence, due to the interpolation an extra smearing of the snow heights of $0.27 \cdot (d_{\mathrm{end}} - d_{\mathrm{start}})$ is introduced, where 0.27 is the mean of the gaussian fit in Figure 5.30.
Also locally on top of the tanks the snow level varies slightly, mainly due to sastrugi (see for example Figure 5.31). The standard deviation of the gaussian variation due to sastrugi was quantified as 4 cm. Summarized, first the interpolated snow height for a certain tank is calulated. This height is then gaussian smeared with a standard deviation σ of:

$$\sigma = \sqrt{4^2 + (0.27 \cdot (d_{\mathrm{end}} - d_{\mathrm{start}}))^2} \tag{5.22}$$

where d_{start} and d_{end} are the snow depth at respectively the start and end measurement of the interpolation. As such, a larger smearing is applied when more snow accumulated during the entire interpolation period on top of a tank. The snow height smearing is not yet used in the current Level 3, but this is work in progress.
In 2017, a sensor to measure the snow height was installed above tank 37A [238]. This was only a prototype, but it is possible that more of these sensors are installed in the future. The uncertainty of the snow height measurement using this sensor seems to be ± 1 cm, which is an important improvent compared to the current situation.

The total amount of snow is not only determined by the height, but also by the density. This was measured

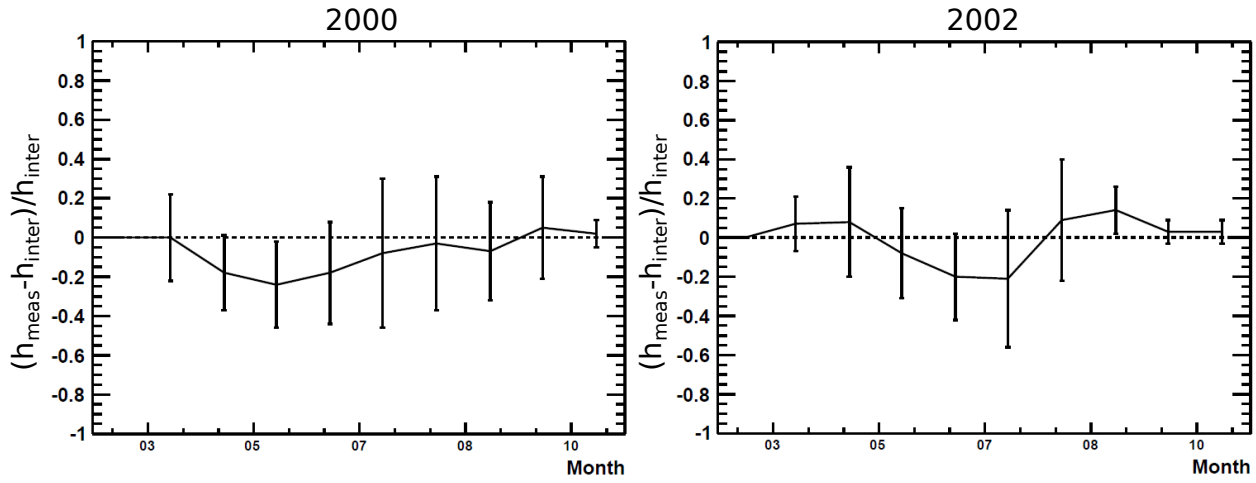

Figure 5.29: Difference between the measured snow height (h_{meas}) and the interpolated snow height (h_{inter}) as function of the time of the year, relatively to the amount of snow accumulation during this entire period (from January to December). The data is obtained from the snow stake field maintained by AMRC. The solid line indicates the gaussian-fitted average for all 50 snow stakes, while the error bars shows the standard deviation of the distribution (per month) for all 50 now stakes. This is shown for the measurements in 2000 in the left panel and 2002 in the right panel.

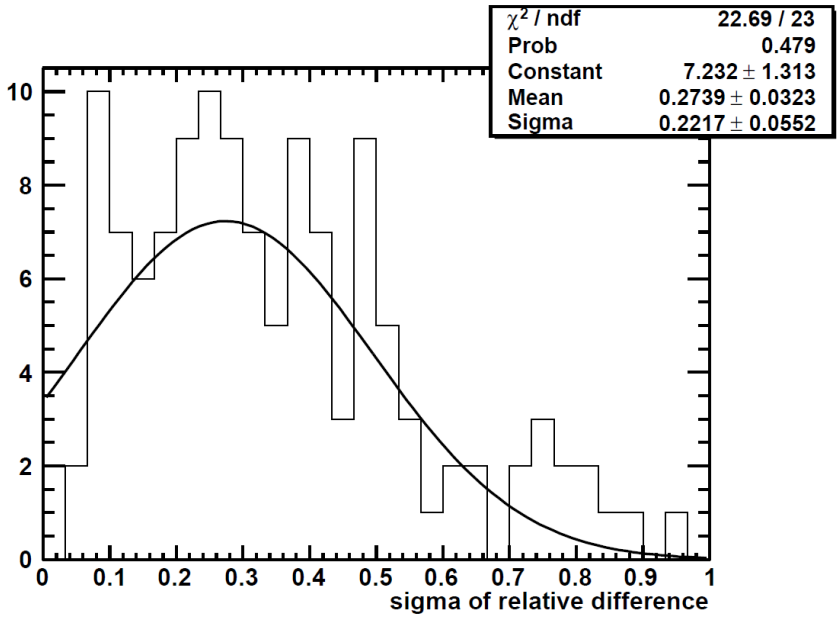

Figure 5.30: Distribution of the standard deviations of the gaussian fits to the relative difference between the measured and interpolated snow heights (Figure 5.29). Per month one gaussian fit is used, which is based on the relative difference for 50 (snow) stakes.

Figure 5.31: Picture taken at South Pole in January 2015, illustrating the sastrugi (in and around the IceTop array).

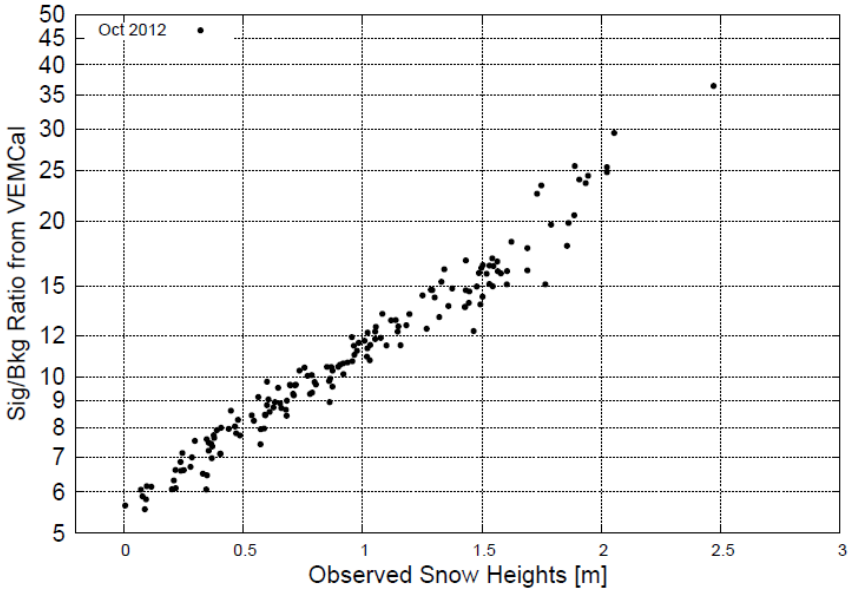

Figure 5.32: The ratio of the muonic signal over the electromagnetic ratio from VEMCal related to the observed snow heights in October 2012. Figure made by Takao Kuwabara.

in-situ at South Pole at several locations and depths [239]. The density was found to vary from 0.34 g/cm^3 to 0.42 g/cm^3, slightly related to depth and the compactification due to for example machines running over the snow. The snow density used in simulation is chosen to be 0.38 g/cm^3. Using this value, a snow depth of 1 m thus corresponds to 38 g/cm^2 of material that has to be crossed, while 2 m of snow is roughly equal to 76 g/cm^2. Since the absorption length of the EM particle population is $\sim$85 g/cm^2 [3], i.e. 1/e$\approx$ 63 % of the EM particles is stopped after this length, this significantly reduces the electromagnetic signal in the IceTop tanks.

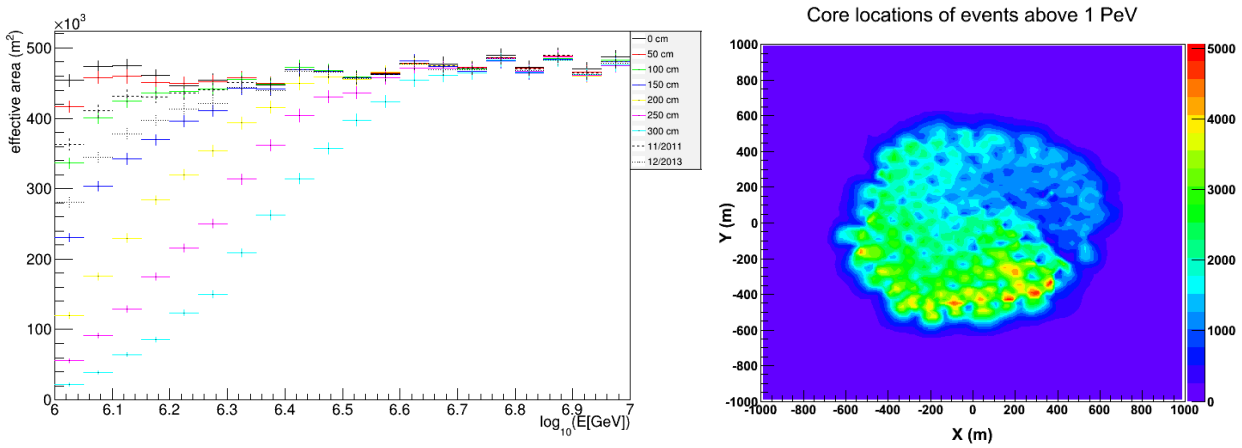

Figure 5.33: Influence of the snow accumulation on the number of air showers observed with IceTop. Left: The effective area, or efficiency, for the detection of proton initiated air showers as function of the primary energy in a specific snow simulation study [240]. The various colours and dotted lines indicate different snow heights. Right: the reconstructed core position of observed air showers with a reconstructed energy >1 PeV, for data of May-June-July 2013.

Energy threshold

A first effect of the snow is the fact that air showers trigger less and less tanks with increasing snow height. At the lowest energies, this causes that EAS which were able to hit sufficient tanks to pass the filter when the amount of snow was low, fall below the detection threshold with higher snow levels. The energy threshold of the IceTop array thus constantly increases, due to the accumulation of snow. This is seen in both simulations as data, as shown in Figure 5.33. The left figure indicates the increase in the energy at which the IceTop array becomes fully efficient with increasing snow height (flat region), for proton initiated showers with $\cos\theta > 0.8$ (θ is the primary zenith angle). This simulation study was dedicated to investigate the influence of snow, therefore a constant snow level was used among all tanks. It can be observed that for each 50 cm of snow accumulation, the energy at which the array becomes fully efficient moves roughly 0.1 in $\log_{10}$(E/GeV). On top, also the real snow heights of November 2011 and December 2013 were used, in order to have a comparison with realistic snow heights. In these months, the average snow heights were respectively $\sim$77 and $\sim$120 cm.
Figure 5.33 (right) shows the number of reconstructed locations of the shower core of EAS with a (reconstructed) primary energy exceeding 1 PeV, in the period from May 2013 to July 2013. When compared with Figure 5.28, the lower number of showers can be related to the region of the array where the tanks are buried deeper in the snow (top-right).

Snow correction

The increasing snow level on top of the IceTop tanks does not only cause a lower trigger rate due to the loss of EAS detections at the lowest energies, it also modifies the signals deposited by the EAS which still trigger the array. As the snow could be seen as an extra shielding, it mostly reduces the signal that is detected. The larger the path length of the particles through the snow, the more the EM particles lose their energy and are even absorbed in the snow. The muonic component of the air shower on the other hand is mostly unaffected and muons still roughly deposit their typical 1 VEM signal in the tank. Since the reconstruction of the primary energy highly depends on the deposited signals, one needs to account for this snow attenuation of the signal.

Since the (average) path length of the particles through the snow depends on the zenith angle, the snow correction is applied during the iterative reconstruction described in section 5.3.4. At this moment, the expected signal according to the LDF S_i^{exp} is corrected using a straightforward exponential correction. The

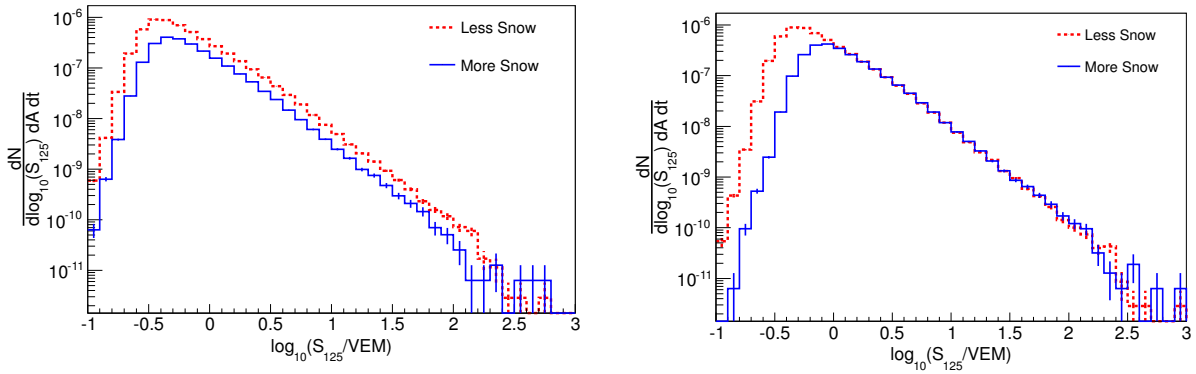

Figure 5.34: The reconstructed $\log_{10}(S_{125})$ spectrum in two parts of the array, with less (red) and more snow (blue). Left: without snow correction. Right: with a snow correction with λ_{eff}= 2.1 m. [139]

signal of tank i in the LDF is reduced (S_i^{corr}) for the snow depth d_i on top of the tank:

$$S_i^{corr} = S_i^{exp} \cdot \exp\left(-\frac{d_i}{\lambda_{eff}\cos\theta}\right) \tag{5.23}$$

This function thus uses the entire signal, deposited by all components of the EAS. Accordingly, λ_{eff} is the effective snow attenuation length, which takes both the large attenuation of the EM component and the negligible attenuation of the muonic component into account.

The effective attenuation length can thus not easily be determined from theory, since the unknown muonic fraction has to be taken into account. Instead, it was obtained from a data study using the IT73 configuration. In this study the array was divided in two parts, based on the snow coverage (Figure 5.28). In both parts the $\log_{10}(S_{125})$ (linearly related to $\log_{10}(E_{\text{prim}})$) spectrum was reconstructed with attenuation lengths ranging from 1.5 m to 4.0 m. The optimal attenuation length then results in an agreement between the $\log_{10}(S_{125})$ spectra reconstructed in both parts. An attenuation length λ_{eff} of 2.1 m was found in this study [241]. The uncorrected spectra of the two parts of the array are shown in Figure 5.34 (left), while the right plot shows the spectra when a correction with λ_{eff} is used. This shows the importance of the correction, where an agreement is seen above the threshold. Due to the slightly varying λ_{eff} with zenith angle and primary energy range, a systematic error of 0.2 m was appointed to λ_{eff}. This is the most important systematic uncertainty on the energy spectrum measurement with IceTop [139, 143].

When multiple years of data were combined to obtain the 3 year spectrum and composition result [143], it was however observed that this λ_{eff} of 2.1 m does not provide an agreement between the various years of data. Instead, λ_{eff} should increase over time. This is caused by the fact that IceTop does not distinguish between muonic and electromagnetic particles an the snow correction corrects the entire signal deposited by all particles. With increasing snow height, the muonic signal is more and more corrected. Hence, when the snow height increases, the effective attenuation length should increase to compensate for this overcorrection of the muons. In the Level 3 processing an attenuation length of 2.25 m is used for IC86.2011 and IC86.2012, and λ_{eff}=3.0 m for the following data-taking years.

Next to the variation according to the snow height, this simple snow correction should in fact also be adapted when the muonic to electromagnetic contribution to the signal changes. Since showers initiated by heavier primary cosmic rays contain more muons, this attenuation length could be different for various primaries. This effect was studied in a dedicated simulation study concerning the influence of snow on the IceTop data taking [240]. Table 5.3 summarizes the attenuation lengths for proton and iron initiated showers with increasing snow heights. This clearly shows that iron showers require an effective attenuation length which is 0.2-0.3 m higher compared to proton showers. Since in data only one attenuation length is used, this causes

Table 5.3: The effective attenuation length in snow (λ_{eff}) for proton and iron air showers between 1 and 10 PeV, while the tanks are covered with increasing snow depths. These values are obtained from a dedicated simulation study [240].

Snow height [cm]	Proton λ_{eff} [m]	Iron λ_{eff} [m]
50	1.9	2.2
100	1.9	2.2
150	1.9	2.2
200	2.0	2.2
250	2.0	2.3
300	2.0	2.3

that EAS initiated by heavier primaries are reconstructed with a slightly higher energy compared to proton initiated air showers with the same primary energy. This is clearly an undesired behaviour.
Since the muon to EM particle abundance in air showers also changes with changing zenith angle and energy of the primary, the attenuation length should in fact also change with these parameters. Furthermore, since the muonic LDF is flatter than the EM LDF, the effective attenuation length should increase with distance to the shower core.
It thus became clear that this snow correction procedure is not perfect.

Future snow correction

Due to the limitations of the simple snow correction (Equation 5.23), a more advanced snow correction is being developed [242]. Since this is still work in progress, it is however not yet used in the Level 3 processing of the data and the analysis described in this work.

In the current implementation this correction consists of two main parts. In the first step the muonic contribution to the signal in each tank is estimated, which will then be omitted in the correction. Currently, the muonic fraction is estimated via the reconstruction of the shower age (Eq. 3.15): close to the depth of shower maximum the EM particles greatly outnumber the muons, while in old showers the electromagnetic fraction is largely reduced. The deduction of the shower age itself is based on reconstructed parameters, like for example the slope β of the LDF and the zenith angle. These parameters however on their turn depend on the snow correction. Hence, multiple iterations are currently used. This part of the future snow correction was studied in detail in [243], but no satisfying result has been achieved yet.
In the second part of this snow correction procedure only the decoupled electromagnetic signal is corrected. Due to the changing energy of the electromagnetic particles with distance to the shower axis, the correction formula depends on this distance between the tank and the shower axis. Furthermore, it also depends on the estimated shower age. The parameters used in this correction formula were deduced in a special ring simulation, therefore this snow correction was given the name ”BORS”: based on ring simulations.

This new correction seems the way forward, but however still some problems need to be resolved before it can be used in the reconstructions.

5.5.2 Atmosphere

In indirect air shower measurements, the atmosphere can be regarded as part of the detection mechanism. Changes in the atmosphere can therefore also alter the response of the detector to the primary particle. At South Pole, the atmospheric variations are extreme: during austral summer, the sun heats the atmosphere for 6 months, while from roughly April to October the sun is below the horizon, resulting in very cold winter months. This temperature difference can be seen in Figure 5.35, which shows the atmosphere during one austral summer month (February) as compared to one winter month (July). Around heights of 10-20 km, the temperature difference can range up to 50 °C. This is also seen in Figure 5.36 (top), where the temperature

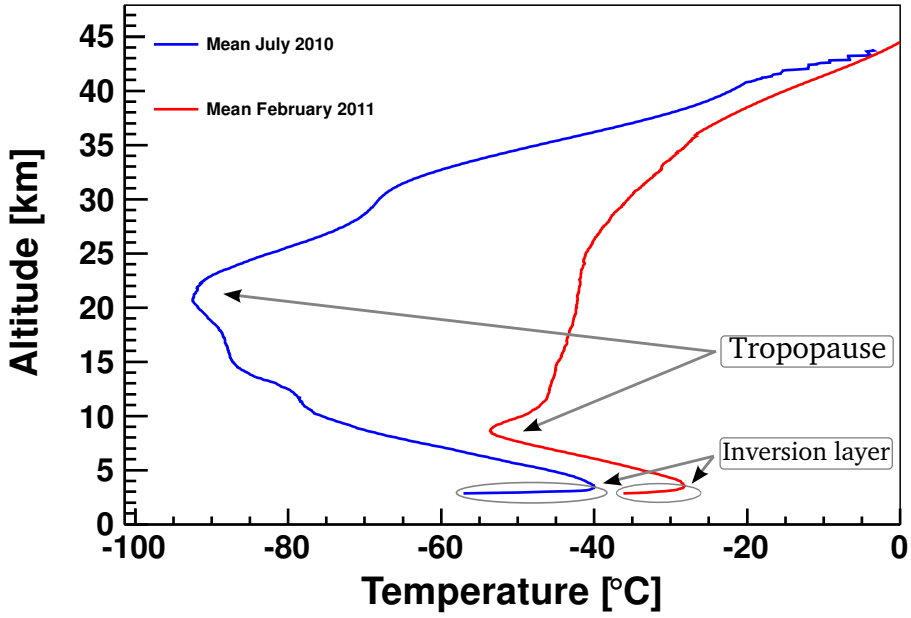

Figure 5.35: The average atmospheric temperature profile at South Pole in July 2010 and February 2011. Data obtained from AMRC [87].

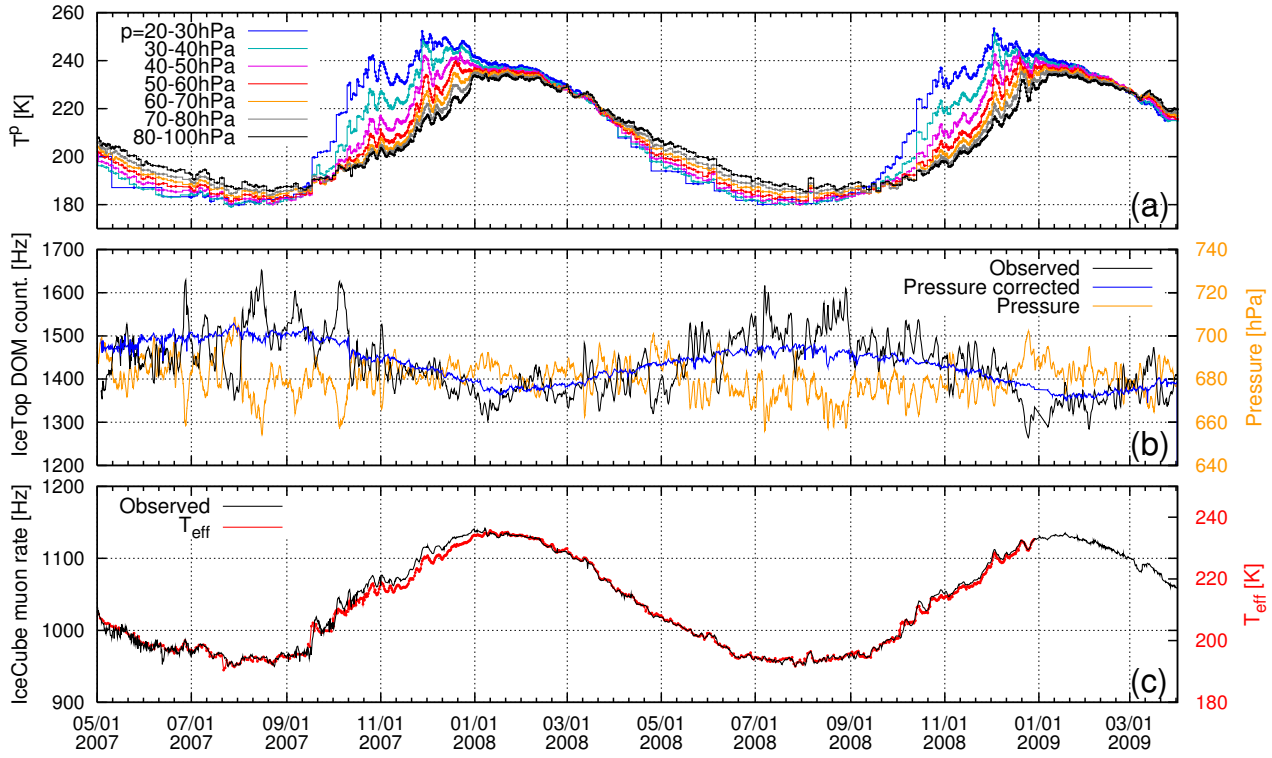

Figure 5.36: Top: atmospheric temperature at various pressure levels. Center: Surface pressure, IceTop DOM count and pressure corrected DOM count. Bottom: muon rate in IceCube together with the effective temperature for this muon analysis. [244]

variation along the year is shown along fixed pressure levels. This temperature variation has an effect on the local atmospheric densities, with an increased temperature resulting in a lower density (section 3.1).

Also typical to this South Pole atmosphere is the layer close to the surface where the temperature decreases with decreasing altitude. This "inversion layer" is due to the presence of the large ice sheet. As covered in detail in [245], the corresponding larger density in the inversion layer compared to the same heights in subpolar regions (next to the ice sheet) causes large catabatic winds. The more prominent inversion layer in winter results in an increased density (Eq. 3.1), which causes a net flux of material from the South Pole to the subpolar regions [246]. This in the end results in a (small) decrease in surface pressure in winter. The entire average density and atmospheric depth profiles in July 2010 and February 2011 were given in Figure 4.3.
On top of the seasonal variations, also daily variations occur. These are mainly present in the chaotic regions close to the surface of the Earth, therefore affect the surface pressure. These large daily variations can be seen in the central panel of Figure 5.36. The bottom plot shows a clear correlation between the (mostly) single HE muon rate measured by the IceCube array and an effective temperature (T_{eff}) which is related to the typical creation heights of these muons (around the pressure levels indicated in the top plot) [244].
In this section the influence of the atmosphere on the actual cosmic ray observations reconstructed with IceTop and IceCube is discussed.

Influence on cosmic ray reconstruction with IceTop

A changing surface pressure causes that an air shower is detected in a slightly different stage of its development. This could cause a change in the measured shower size, and possibly also in other variables. This was studied in data and simulations [225, 246]. In these studies an effect was observed, although small: the seasonal effect of the surface pressure on the shower size $\log_{10}(S_{125}/VEM)$ is ~ 0.01. This is significantly below the uncertainty induced by the snow. Therefore, no correction is applied. In [246] also a small but existing variation of β, the slope of the LDF at 125 m from the shower axis, is reported. This could be related to both changes in the lower atmosphere as around the tropopause.
Since the simulations occur with an average surface pressure (section 4.1.1), the surface pressure variations only introduce a smearing of the data.

Influence on HE muon bundle measurements

During the air shower development the competition between decay (to muons) and interaction of the secondary mesons highly depends on the local density (Eqs. 3.7 and 3.8). With a higher density ρ the chance that mesons interact grows ($\lambda_{int} = \frac{1}{\rho}$) as compared to the decay to muons. Therefore, the number of HE muons and thus the measured IceCube energy loss are highly affected by the large temperature variations at heights were these high energetic muons are created. This is seen in Figure 5.37 (left). The average reconstructed energy loss $\frac{dE}{dX}$ (X=1500 m) as function of the primary energy is shown for simulated proton and iron initiated showers. The mean values obtained in July 2010 are shown as the black points, and the seasonal variations on these values are shown by the grey band. At the highest energies, the statistics is limited. This variation reaches maximally $\sim$15 % of the difference between proton and iron, which can be seen in the upper right panel. Hence, this is a significant variation. If one wants to use an entire year of data, a correction needs to be applied such that the number of muons would agree with the ones in simulations. The correction is described in detail in [247], but a short discussion is provided here.

In order to relate the variation in the muon multiplicity to a change in the atmospheric temperature profile, a new effective temperature T_{eff} is defined. This temperature should represent the temperatures at the depths where the HE muons are produced. Hence, the atmospheric temperature profile $T(X)$, obtained from AMRC [87], is weighted with the (normalized) HE muon production profiles:

$$T_{eff}(E_0, A) = \frac{\int\int \frac{dN_\mu}{dX\,dE_\mu}(E_0, A) T(X) dX dE_\mu}{\int\int \frac{dN_\mu}{dX\,dE_\mu}(E_0, A) dX dE_\mu} \tag{5.24}$$

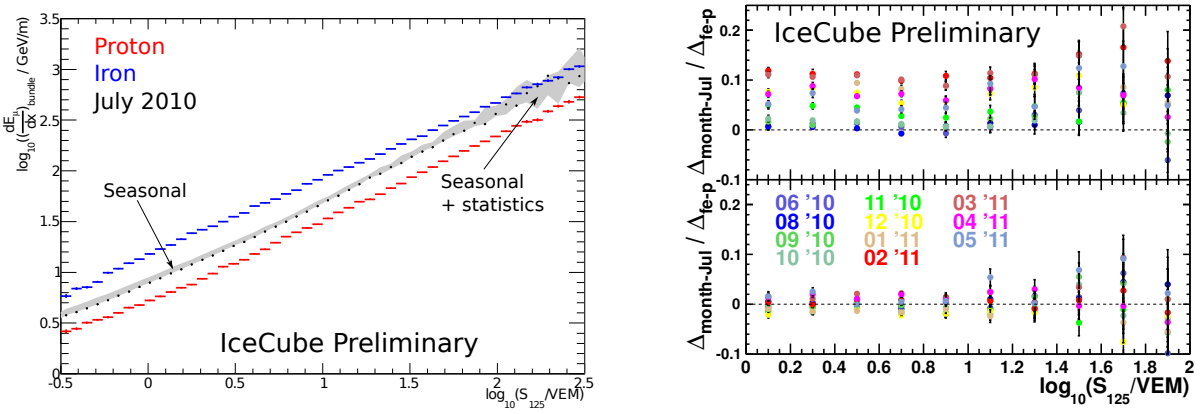

Figure 5.37: Left: logarithm of the mean reconstructed IceCube energy loss ($\frac{dE}{dX}$) (X=1500 m) as function of $\log_{10}(S_{125})$. Proton and iron simulations are shown, together with the averages obtained in July 2010 (black points). The seasonal variations are indicated by the grey band. Right: uncorrected (top) and corrected (bottom) $\log_{10}(\frac{dE}{dX})$ variation between the months (July as a base) relative to the proton-iron difference.

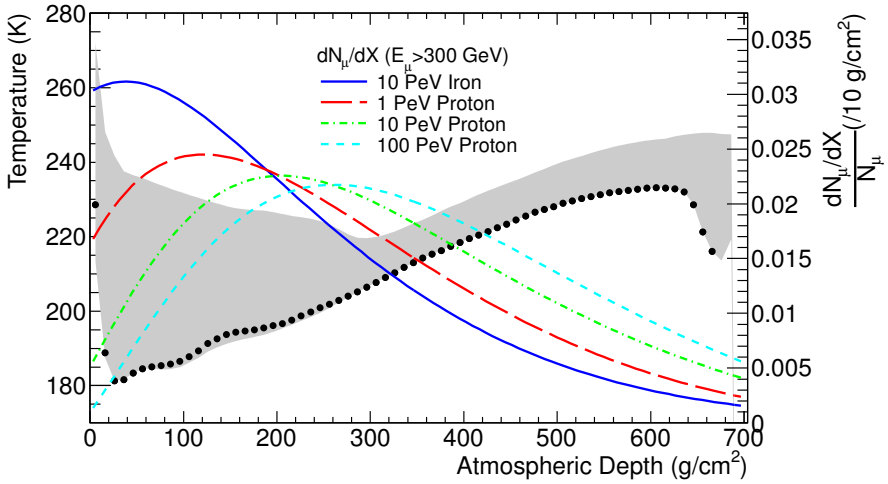

Figure 5.38: The black points show the average atmospheric temperature profile in July 2010, while the grey band indicates the maximal variation. The coloured lines describe the longitudinal production profile of HE muons for proton initiated showers with primary energies of 1, 10 and 100 PeV.

As an illustration, both the atmospheric temperature profiles and normalized muon production profiles initiated by proton showers of 1, 10 an 100 PeV and iron showers of 10 PeV are shown in Figure 5.38. The higher the energy E_0 of the primary particle, the deeper in the atmosphere the muons are produced. In showers produced by heavier nuclei the muons are produced higher in the atmosphere.
In simulation T_{eff} is then directly related to the observed muon number N_μ in a certain month m:

$$\frac{N_\mu^m - N_\mu^{July}}{N_\mu^{July}} = \alpha \frac{\Delta T_{eff}^m - T_{eff}^{July}}{T_{eff}^{July}} \,, \tag{5.25}$$

where α is the temperature coefficient.
In data a similar relationship is deduced, using the reconstructed energy loss instead of the number of muons. In order to relate this to an effective temperature S_{125} is converted to the primary energy using the relationship from [139]. In simulations it was found that T_{eff} rises linearly with the log of the energy per nucleon

($\log_{10}(E_0/A)$), such that a composition assumption allows to convert S_{125} to T_{eff}. The average mass A in this energy region is modelled as in the H4a model [207].
In simulation a temperature coefficient of 0.84 ± 0.10 was deduced, while $\alpha \approx 0.81 \pm 0.28$ in data. This large uncertainty in data is mainly caused by the fact that the coefficient still seems to be slightly energy dependent, despite that the energy dependence should already be taken into account. Many explanations for this energy dependence were investigated, but no reason was found. Since it is not desired to apply a corrrection which provides an energy dependent solution, the temperature coefficient α is made energy dependent. As such, the correction works well for all primary energies. The remaining variation of $\log_{10}(dE/dX)$ after the correction for the various months is ± 3 %, as seen on the bottom plot of Figure 5.37 (right). At the highest energies the statistical error dominates. It is important though that the remaining variation is symmetric with regard to the reference atmosphere (here July). Hence, the data is smeared, but it does not result in a systematic error.

5.6 Level3 performance

In this section the performance and quality of the cosmic ray Level 3 processing is described. In sections 5.6.1 and 5.6.2 the event selection, efficiency and the precision of the reconstructions are investigated. For this purpose proton and iron simulations performed for the IC79 configuration are used. The derivation of the livetime in data and the data rates for various cut levels are discussed in section 5.6.3. This allows to perform detailed comparisons between data and simulations (section 5.6.4). Finally the implementation of checks in the Level 3 processing is shortly described in section 5.6.5.

5.6.1 Containment and effective area

Most existing analyses, including the one described in this work, only use air showers which have their core contained inside the IceTop array. Current IceTop reconstruction algorithms are neither able to describe the uncontained events properly. Many uncontained air showers however still trigger the IceTop array and one needs to ensure that these are removed in order to have a reliable reconstruction. This is done by the quality cuts described in sections 5.3.6 and 5.4.4 and illustrated in Figure 5.39. This figure is based on proton simulations for the IC79 configuration ($5 < \log_{10}$(E/GeV)$< 9.5;\ \cos\theta < 0.8$) and shows the distribution of the true shower core distances from the IceTop center. In simulations the shower cores are randomly distributed in a circle arround the center of the IceTop array. The radius of this circle increases with every decade in primary energy (section 4.3.1). The top left panel of Figure 5.39 shows the distribution for all showers that passed one of the IceTop filters (section 5.2.3). This indicates up to which distance EAS of a certain energy are able to trigger the IceTop array. The distribution remaining after the IceTop event selection is shown in the top right panel, while a map of these core positions (after these IceTop cuts) is given in the lower right panel. A large fraction of the contained events is kept, while most uncontained events are removed. Some outliers with a remote core however remain in the event collection even after these cuts. These events also cause the low reconstructed S_{125} values for a certain energy (seen in the lower right corner of Figure 5.14). An analysis using only IceTop should thus develop extra cuts to remove these rare events. In a coincident analysis these events are removed by the IceCube part. Since the reconstructed shower axis is far from the truth, no hits in the InIce detector are selected around the track. Hence, no succesful reconstruction can be performed and the events do not pass the IceCube event selection. In the bottom left panel of Figure 5.39, which shows the shower core distrubution after both IceTop and IceCube cuts, these events disappeared. This is a reassuring result for the further analysis.

The removal of all uncontained events results in a flat detection efficiency as function of the primary energy, at least above the threshold region. This translates into a stable effective detection area, which is shown in Figure 5.40 for proton (left) and iron (right) showers that survive the IceTop event selection. The influence of the increasing cut levels can be seen as the different colours. The rare kept uncontained events do not influence this distribution significantly. After all of these cuts, the effective area is $\sim$600 m^2 above an energy

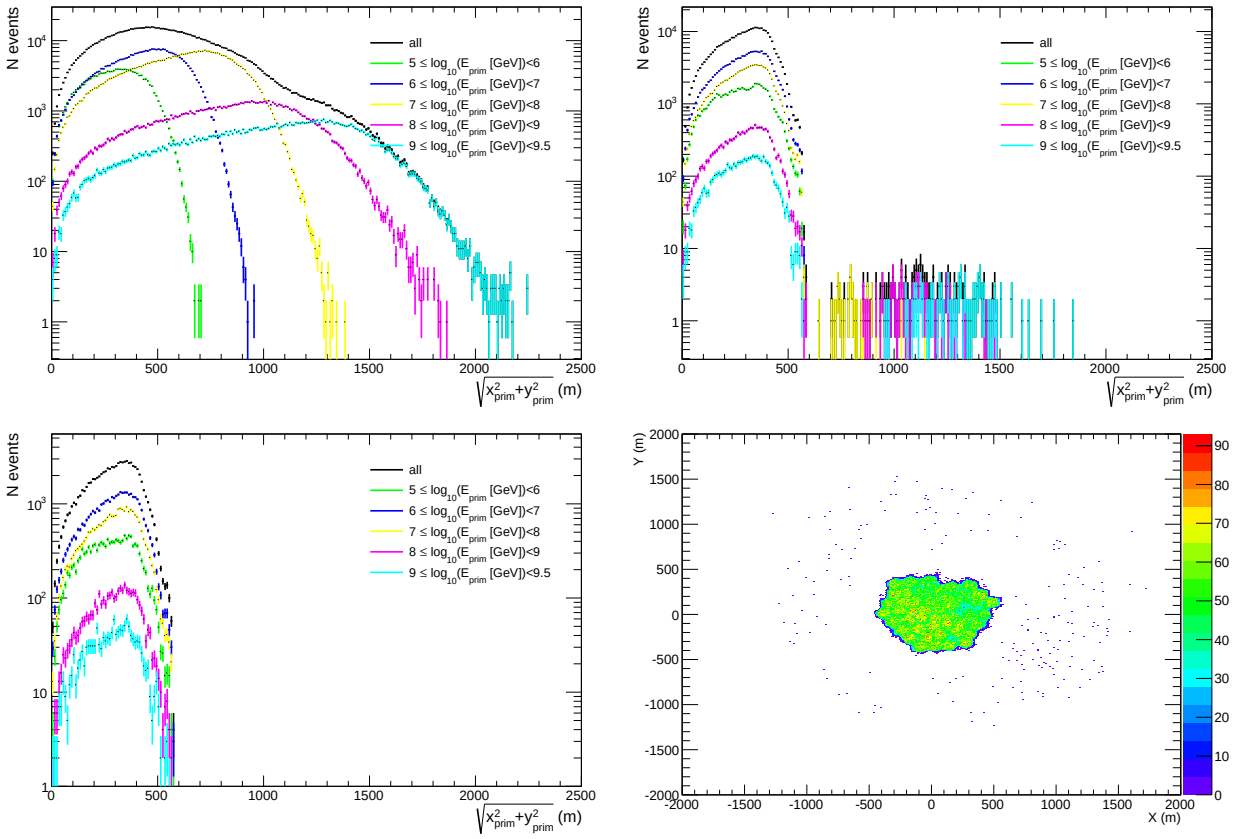

Figure 5.39: The first three plots show the number of proton showers as function of the distance from the true shower core position to the center of the IceTop array, divided into energy decades (from IC79 simulations). The upper left figure provides the distribution of all the events kept in the Level 3 processing (which requires one cosmic ray filter to be passed), while the upper right figure shows the distribution after all the IceTop cuts (section 5.3.6) and the lower left after both the IceTop and IceCube quality cuts 5.4.4. The bottom right plot shows a map of the reconstructed shower cores after IceTop cuts.

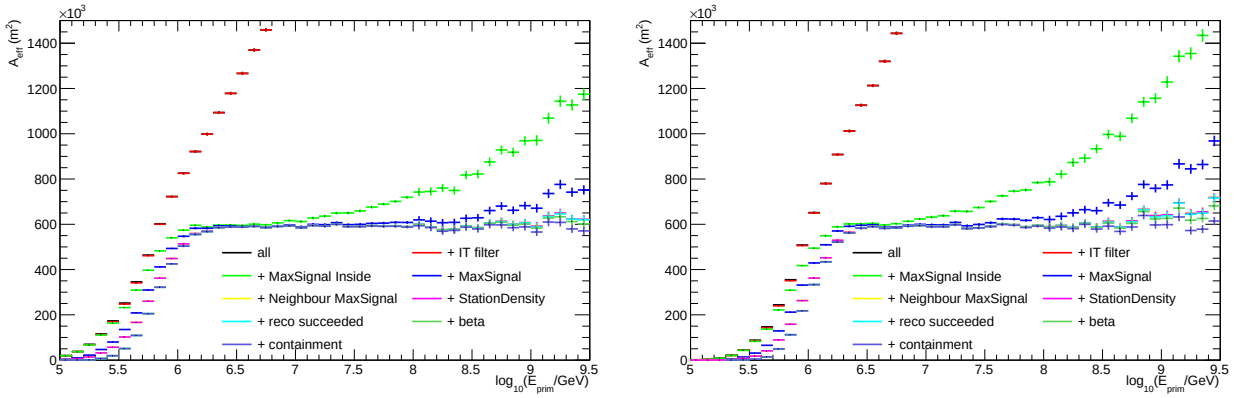

Figure 5.40: Effective area as function of the primary energy, for proton (left) and iron (right) initiate showers, obtained from the IC79 simulations. The change in the effective area with increasing number of quality cuts is shown with the various colours, starting from all events in black to the final containment cut in blue.

of $\log_{10}$(E/GeV)$\approx$ 6.4. As desired, it is independent of the primary particle type. This also defines the threshold energy above which most analyses start.

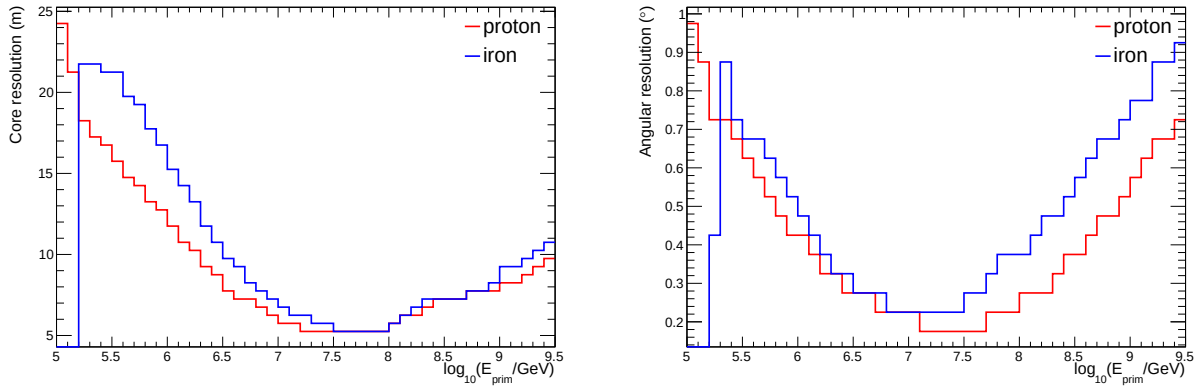

Figure 5.41: Core (left) and angular (right) resolution for proton and iron initiated air showers reconstructed with IceTop, after the quality cuts described in section 5.3.6. The resolution has been defined as 68.3 % of the events which have a better reconstruction than this number.

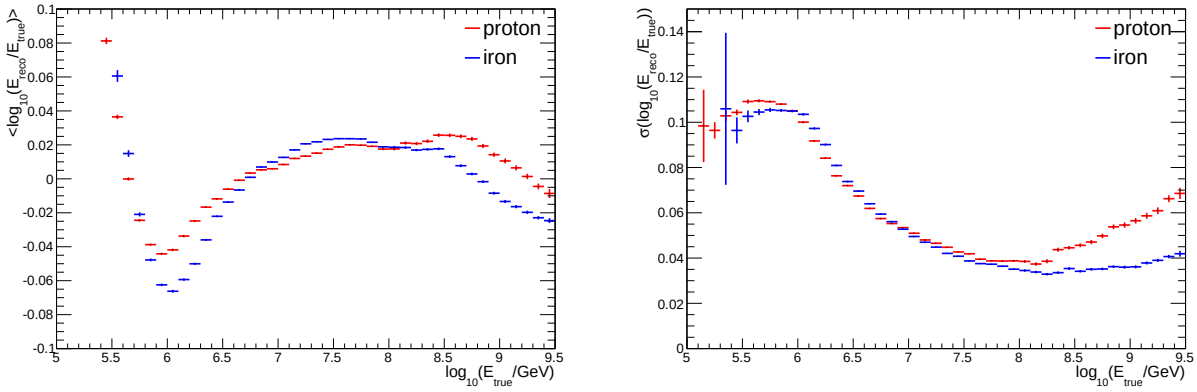

Figure 5.42: Estimate of the energy bias (left) and resolution (right) as function of the true energy, for proton and iron showers after the IceTop event selection.

5.6.2 Resolution

The stringent event selection also results in an overall accurate and reliable reconstruction. The resolution of the core and angular reconstruction with IceTop (section 5.3.4) after IceTop quality cuts is shown in Figure 5.41 as function of the primary energy. The resolution is defined as the value for which 68.3 % of the events have a better accuracy. Above the threshold ($\log_{10}(\mathrm{E_{prim}/GeV}) > 6.4$), the core resolution is below 10-12 m, reaching a minimum of $\sim$5 m between 30 and 100 PeV. The angular resolution is well below 1° over the entire energy, while an accuracy of 0.2-0.3° is reached around 10 PeV. The resolution gets worse at higher energies due to the saturation of the tanks at the center of the EAS.

With the functions derived in the IceTop-only analysis of the IT73 data [139], the reconstructed S_{125} can be converted to an energy. Using this relation, we can get an estimate of the energy resolution and bias obtained with the Level 3 processing. This is shown in Figure 5.42 for proton and iron showers over the entire energy range. In the primary energy range $6.5 < \log_{10}(\mathrm{E_{prim}/GeV}) < 8.5$ the bias (left) is below 0.02 in $\log_{10}$(E). Outside of this energy range, the bias is slightly larger. The energy resolution is below 20 % above the threshold. A very similar change is obtained for both primaries, which is the desired behaviour.

Figure 5.43 shows the core and directional resolution obtained with the reconstructions using the IceCube detector. All events kept in the Level 3 processing for which the MPE reconstruction (section 5.4.3) succeeded

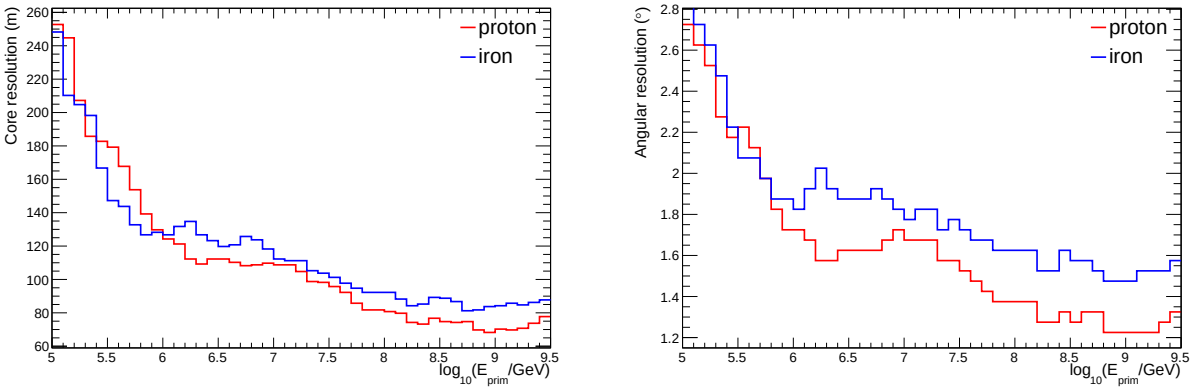

Figure 5.43: Core (left) and angular (right) resolution of the IceCube directional reconstruction, for proton and iron initiated air showers. All events which passed one of the IceTop filters and of which the directional reconstruction converged are taken into account.

are taken into account here and no further optimization is performed. The core resolution, the distance on the ice surface between the true and reconstructed shower core, decreases from ∼140 m at 1 PeV to 80 m around 1 EeV. The angular resolution is ∼2° at 1 PeV and ∼1.4° at 1 EeV. This resolution is worse than the one achieved with IceTop. However, it can suffice to have a reliable reconstruction for showers with a shower axis that intersects the surface outside the icetop array.

5.6.3 livetime and rates

To convert the number of events detected in data into a rate or finally a flux one needs to account for the duration over which the data is taken. The detector livetime for a certain run can be deduced from the time difference between the first and last event observed during the run. The livetime of a longer period, for example a certain month, can then be obtained by summing up the livetimes of all runs taken during this time. This method is however amenable to errors like unknown detector downtime. Instead, the livetime can also be obtained from the poisson distributed arrival times of all events that survive the quality cuts. The number of events as function of the time difference t between subsequent events decays exponentially according to $\exp(-t/\tau)$, where τ is the average time difference between the events. Hence, the livetime is obtained by the multiplying τ with the number of events used in this distribution, which is given by the integral of the curve. An example of such a livetime calculation is given in Figure 5.44, for the data detected during July 2010. The obtained livetime for this month is 29.18 days.

Using the livetime of each individual run, the event rate as function of time can be displayed. This allows to check for the stability of the detector and the analysis over time. The event rate per run is shown in Figure 5.45 for the Level 3 processed data of the IC79 to IC86.2015 season, so six years of data. The top two plots respectively show the rate of events that pass the five station (STA5) and the InFill filter, after the refiltering performed in the Level 3 processing. The rate of events that pass all IceTop quality cuts is shown in the third panel, while the bottom plot indicates the event rate after both IceTop and IceCube quality cuts. One can clearly observe that all rates decrease, which is due to the increasing snow heights and thus the decreasing number of event detections. The transition from the IC79 to the IC86 configuration, mainly the introduction of the extra stations in the InFill array, occurs at run 118175. The lack of other jumps from one data-taking season to another, especially from IC86.2011 to IC86.2012 where many filters changed, provides confidence in the data processing. Small run-to-run variations are probably due to daily and/or seasonal atmospheric changes. Only a few runs have deviant lower rates, mostly present in the last data-taking years. These (often short) runs need to be further investigated towards detector downtime. These kind of stability studies over time provide an excellent tool to detect this type of problems. In the IC79-IC86.2012 seasons these runs have

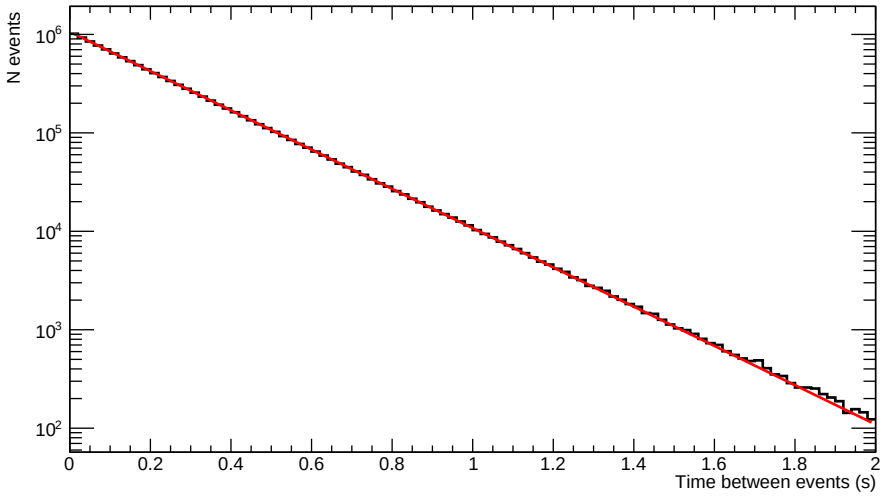

Figure 5.44: Livetime calculation for July 2010 data based on the time difference between subsequent events. The red line shows the exponenital fit to the data (black).

already been removed, while it still needs to be done for the IC86.2013 to IC86.2015 seasons.

5.6.4 Data-MC comparison

A deviation between the data and simulation could point to possible problems in the simulations. Therefore it is important to compare the data-MC distributions for as many parameters as possible. The optimization of the cuts, the inclusion of the livetime for data and the reweighting of the simulations (section 4.4.3) now provide all the necessary tools to perform a reliable comparison.

Some sample comparison plots are given in Figures 5.46 to 5.48, where the bottom panel provides more detail with the data/MC ratio. The simulations assume a pure (proton or iron) composition and are reweighted to a flux at 1 PeV as determined in the H4a model [207], while an energy spectrum decreasing as $E^{-2.7}$ is assumed below 1 PeV and following E^{-3} at higher energies. Since data is a mixture of all elements between proton and iron, data should roughly lie between the proton and iron curves. A first important variable where the data and simulations should be compared is the shower size S_{125} (Figure 5.46). The data-MC agreement in the main energy range confirms the correct weighting procedure of the simulations. The lower rate in data at the lowest energies is caused by a higher snow level in data as compared to MC. Differences at higher energies point to a deviation in the measured energy spectrum as compared to the simple power law assumption.
If one wants to compare the distributions in other variables only events with $\log_{10}(S_{125}/\mathrm{VEM}) > 0.4$ are selected, due to the difference in the threshold region between data and simulations. In Figures 5.47 and 5.48 more low level variables are shown for events with an energy above the threshold. Figur 5.47 compares the number of hit tanks per event (left) and the total measured charge in the tanks (right), after event cleaning algorithms. The lower number of participating tanks per shower in data can again be explained by the higher snow level in data, while the decrease in measured charge is smaller compared to the proton-iron difference. The comparison of the number of hit IceCube DOMs and the total charge measured per event in the ice is given in Figure 5.48. These are obtained from the pulses that are kept after the hit cleaning around the icetop track and indiacate a good data-MC comparison.
A good agreement of these high- and low-level variables provides trust in the simulations and existing analysis software: both the online and offline software and Level 3 processing.

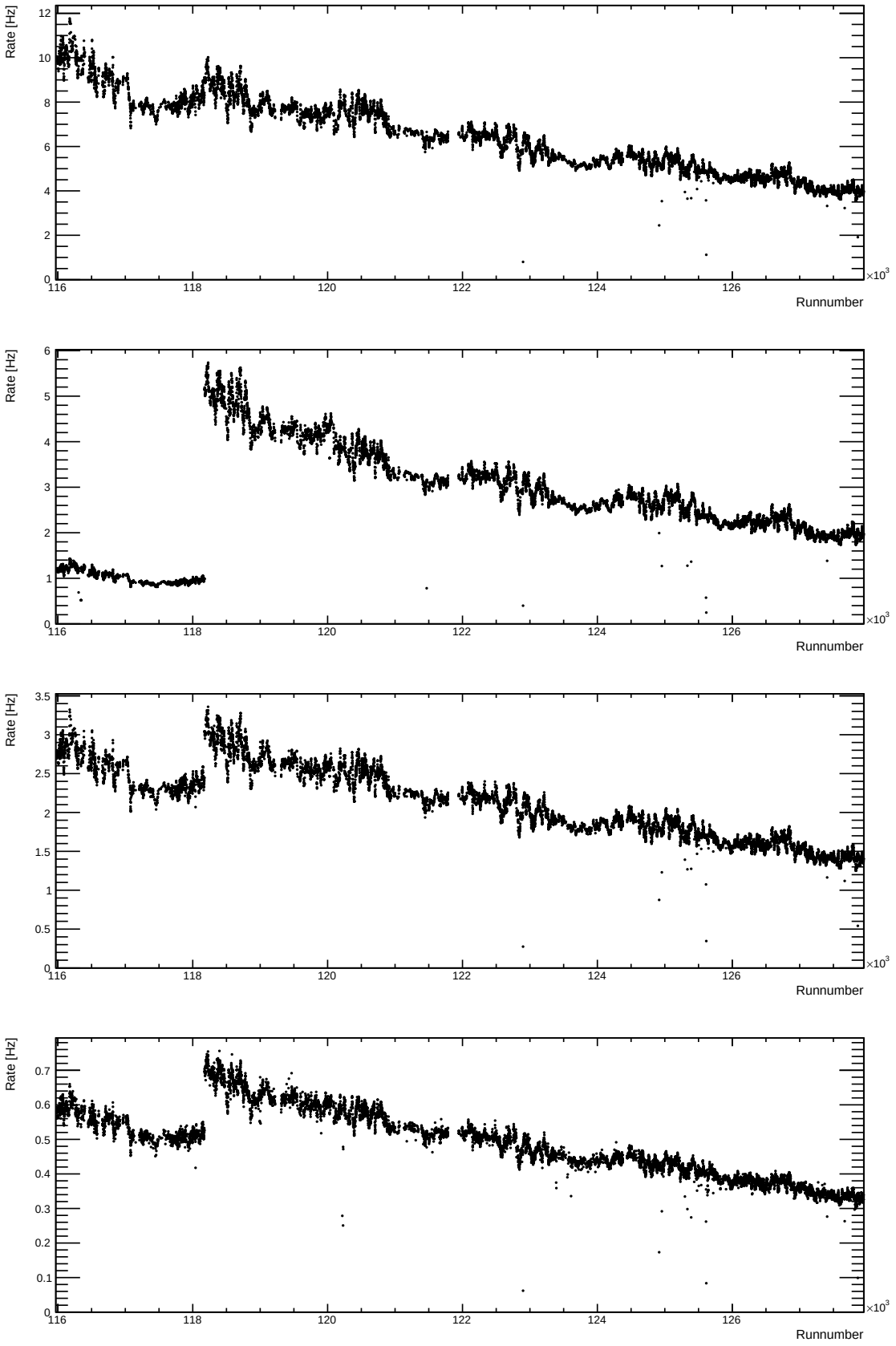

Figure 5.45: Various rates as function of the run number. Respectively shown from top to bottom are the icetop 5 station filter rate, the InFill filter, the rate after all icetop quality cuts and the event rate of passing all IceTop and IceCube quality cuts.

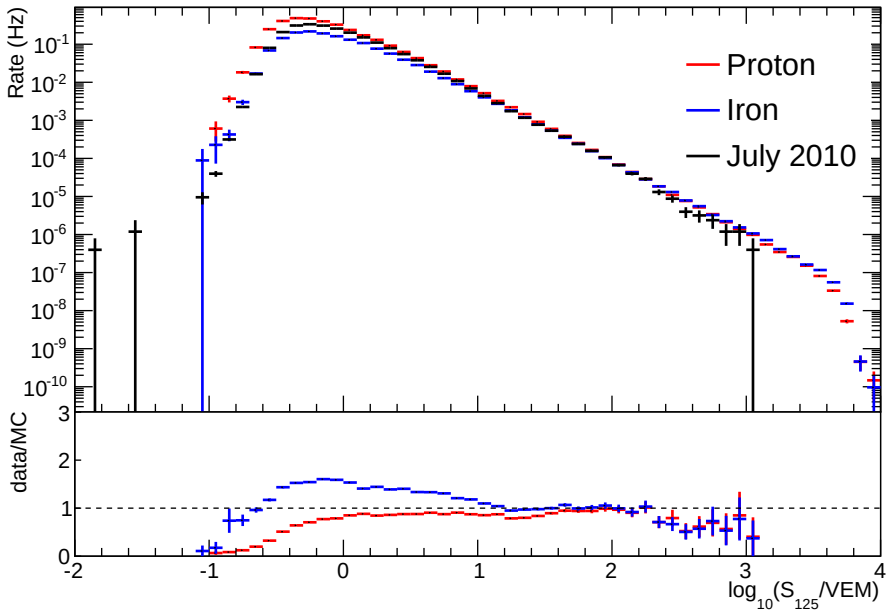

Figure 5.46: Raw $\log_{10}(S_{125})$ spectrum after quality cuts for data of July 2010 and proton and iron IC79 simulations. The bottom figure shows the ratio between data and simulations.

5.6.5 Verification histograms

The above studies indicate that the current analysis has been carried out reliably. With the implementation of consistent checks at the end of each processing chain, one can also try to limit the amount of errors in future analyses. These could for example arise from small changes in the code. To avoid this a method was developed in the IceCube collaboration to produce some standard histograms during the analysis chain. These ”production histograms” are now also implemented in the cosmic ray Level 3 processing. For every 10th DAQ event and 10th (physics) event, some selection of variables prone to errors is kept. These can then be easily accessed to perform comparisons for new datasets or a new processing of the data after an update of the software. It should be noted though that these distributions are very rough, since no prescales, cuts or reweighting are applied. Two example distributions are given in Figure 5.49, where the data during June 2010 is compared to June 2011 (chosen as a reference). Only the livetime of each month is taken into account, to be able to compare the rates adequate. The left plot shows the comparison in hit rate of each station in the seeded RT cleaned pulses. The total energy deposition (in VEM) per event, is shown in the right panel, where a rough correction for the amount of snow on top of a tank is taken into account.

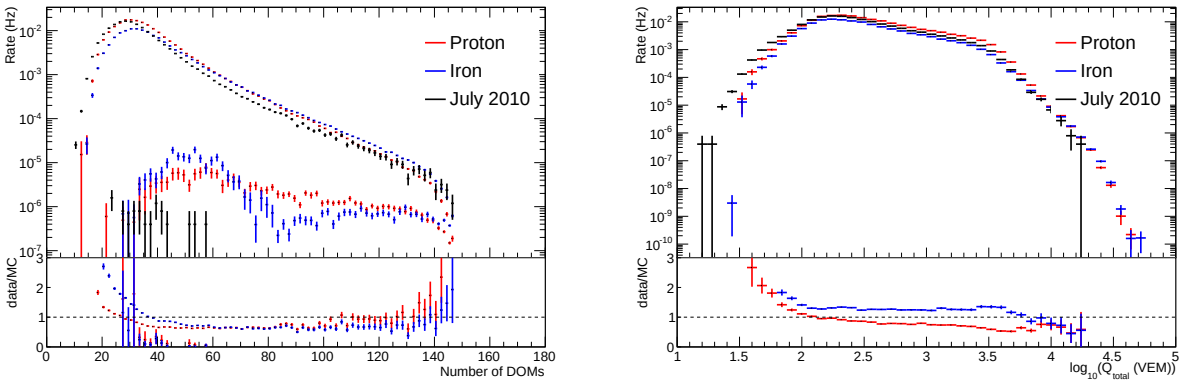

Figure 5.47: Number of hit tanks and the logarithm of the total measured charge in de SeededRT IceTop pulses. Only events which survive the IceTop event selection and have a reconstructed S_{125} above the threshold ($\log_{10}(S_{125}) > 0.4$) are taken into account.

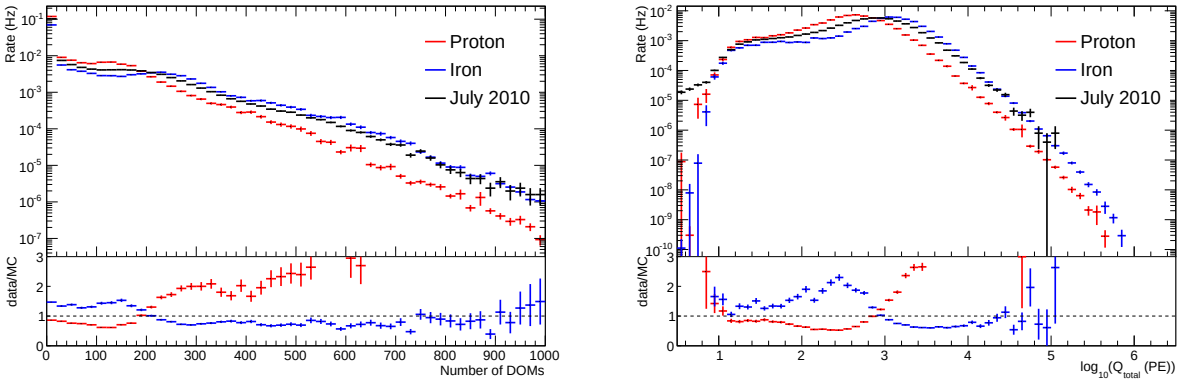

Figure 5.48: Number of hit tanks and the logarithm of the total measured charge in de InIce pulses after the pulse cleaning around the IceTop reconstructed track. Only events which survive the IceTop event selection and have a reconstructed S_{125} above the threshold ($\log_{10}(S_{125}) > 0.4$) are taken into account.

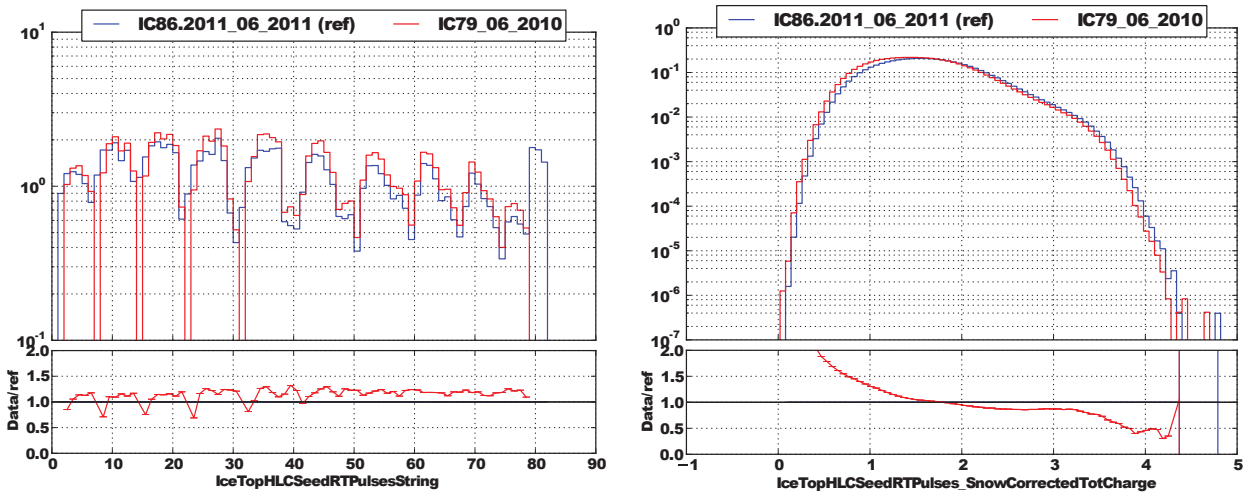

Figure 5.49: Examples of histograms produced during Level 3 processing to evaluate the data processing. Left: pulse rate in each station after SeededRT cleaning of the IceTop pulses. Right: total IceTop charge per event, expressed in VEM and a rough correction of the signal for the snow.

6

Analysis

Of all the paths you take in life, make sure a few of them are dirt.

John Muir

6.1 Goal and method of the analysis

The recent experimental results of the energy spectrum and composition of cosmic rays have been discussed in section 3.4.3. While a rough agreement is obtained between the various experiments concerning the energy spectrum, significant discrepancies arise for the indirect measurements of the composition. Between the knee of the spectrum and 100 PeV all experiments measure an increasing composition, but beyond this energy major differences exist. Here we want to focus on the important discrepancy in the composition result between the IceCube Neutrino Observatory and the other experiments. Compared to the other experiments like KASCADE-Grande, the Pierre Auger Observatory (PAO) or the Telescope Array (TA), a heavier compostion is measured with IceCube in an energy range from 100 PeV to 1 EeV (Figures 3.14 and 3.15). In the IceCube data there is no clear indication of an extragalactic component, while it would have been expected with a light proton-like composition at the ankle (around 1 EeV) measured by PAO and TA. This is one of the main discussion points within the experimental cosmic ray community.
In section 3.4.3 it was suggested that the reason for this reconstructed composition difference could lie within the use of different measurement techniques to find the primary composition. KASCADE-Grande based its composition reconstruction on the number of muons at roughly sea level, the PAO and TA used the depth of shower maximum (section 3.2.2) and IceCube used the number of muons in the deep in-ice detector. While KASCADE-Grande detects muons with an energy of $\mathcal{O}(1)$ GeV, which are created after many interactions in the air shower development, the muons that are able to penetrate down to the IceCube detector need to have an energy of at least 300-400 GeV. They are created in the first interactions of the air shower development. The use of different mass sensitive observables could lead to a different conclusion if the relation between the observations and the properties of the primary particle are deduced from imperfect air shower simulations. Most probably this is due to the modelling of the high-energetic collisions between the air shower particles and atmospheric nuclei, since these occur at energies beyond reach of man-built accelerator experiments.

Cosmic ray experiments have now reached an accuracy where they can pinpoint problems in the hadronic interaction models (section 3.4.4). The joint effort from cosmic ray experiments, accelerator experiments and theorists to improve the models is one of the main goals of current cosmic ray studies. In this work we study to which extent a measurement using the deep muon bundles with IceCube could result in a different composition reconstruction as compared to when other observables are used. More specifically the composition estimate with IceCube is compared with a mass measure from the IceTop surface array. An estimation of the primary energy of the shower is also performed using the IceTop surface array. A comparison of the composition obtained with both measurement techniques could -possibly- explain the

disagreement of the reconstructed composition between IceCube and the other experiments. It is furthermore an important contribution to the experimental check of the internal consistency of the various hadronic interaction models.

The main analysis method, i.e. the IceTop and IceCube mass sensitive variables used in this analysis, is described in section 6.2. In section 6.3 the effect of the systematic uncertainties that need to be taken into account on the variables is discussed. Simulations using the various hadronic interaction models under study all result in slightly varying secondary muon spectra. This is shown in section 6.4, together with how this changes the distributions of the used variables. The final result, the average mass interpretation and consistency check between the two measurements for all interaction models is provided in the following chapter.

6.2 Composition sensitivity of reconstructed observables

The observables used in this analysis are all obtained from the Level 3 processing, extensively treated in the previous chapter. In this study the separate pieces are put together into one analysis. The reconstruction of the air shower with IceTop, i.e. of the core, direction and lateral distribution function (LDF) is performed as described in section 5.3.4. This track reconstructed with IceTop is propagated to the IceCube array, where the energy loss profile of the muon bundle along this track is obtained. The event selection is applied exactly as defined in the Level 3 IceTop and IceCube quality cuts (sections 5.3.6 and 5.4.4). Hence, the selected air showers have their shower axis contained in both the IceTop and IceCube array and a zenith angle θ with $\cos\theta < 0.8$ is required. The effective area of the analysis hence corresponds the the effective area obtained after the Level 3 processing and quality cuts, and is shown in Figure 5.40.

For the study of the composition sensitivity of the used variables (sections 6.2.1 and 6.2.2), simulations produced for the IC79 simulations are utilized (Table 4.5) with Sibyll 2.1 as hadronic interaction models, since these cover the full primary energy range. Simulations with the post-LHC hadronic interaction models and Sibyll 2.1 are performed for analyses with the IC86.2012 configuration. The further analysis, starting with the data-MC comparison in section 6.2.3, thus uses these latter simulations. Sibyll 2.1 is used as hadronic interaction model for the full (base) datasets, while smaller (systematic) datasets are produced for the post-LHC handronic interaction models. The choice for Sibyll 2.1 as hadronic model for the base processing is caused by the unavailibility of the post-LHC models when the mass simulations were started. The simulations with the post-LHC models were produced later. The details of the IC86.2012 simulation datasets are given in Table 4.6.

6.2.1 IceTop: slope of the lateral distribution function β

The main composition sensitivity of a surface array to cosmic rays arises from the number of muons present in the shower: extensive air showers (EAS) initiated by heavier nuclei on average contain more muons (section 3.3.2). This could be measured with the reconstruction of a separate electromagnetic (EM) and muon lateral distribution function (LDF), but is work in progress for the IceTop group [220]. It is also difficult to tag the muons and count the total number of muons, since, at the stage of the shower development where most EAS are detected with IceTop, the number of EM particles greatly outnumbers the muons. However, since the lateral distribution of the muons as function of distance to the shower axis falls less steeply as compared to the EM component (Figure 3.10), the muon density can be reconstructed far from the shower core. This is done in [227], where the data is also compared to simulations to obtain a rough reconstruction of the average composition.

Instead, in this work we use the tools defined and verified in the Level 3 processing. The shower size S_{125}, the signal of the LDF at a pependicular distance of 125 m of the shower axis, is an excellent parameter to estimate

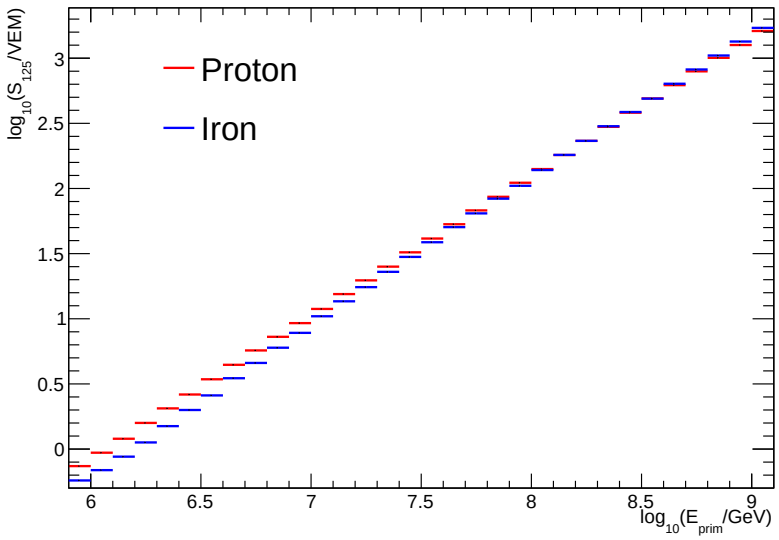

Figure 6.1: Average $\log_{10}(S_{125}/\text{VEM})$ as function of the primary energy, for proton (red) and iron (blue) initiated showers (same as Figure 5.14).

the primary energy. The relation between ($\log_{10}$)primary energy and ($\log_{10}$)S_{125} is shown in Figure 6.1 for proton and iron initiated simulations. One could thus roughly imagine that $\log_{10}(S_{125}/\text{VEM})$=0 is around 1 PeV and with every decade in S_{125} also the energy increases with a decade. A $\log_{10}(S_{125}/\text{VEM})$ of 2 hence roughly agrees with a primary energy of 100 PeV. S_{125} also slightly depends on the mass of the primary particle, however, the difference is small. In this analysis, however, S_{125} is not converted to the primary energy since the goal is not to obtain an energy spectrum, but to scrutinize the hadronic models based on reconstructed variables.
The signal in the IceTop tanks is a combination of an electromagnetic and muonic contribution. The fit to the lateral distribution of the tank charges is then also performed to the entire, combined, tank signal. Due to the significantly higher number of EM particles as compared to muons this close to the shower axis, S_{125} is mainly determined by the amount of EM particles in the shower. The properties of the obtained lateral distibution function (LDF) are however also affected by the number of muons, i.e the steepness of the fitted LDF is influenced by the dominant muonic signal at the edge of the shower. The slope of the LDF at a perpendicular distance of 125 m from the shower axis (β), is used in this work to provide an estimate of the primary composition with IceTop. β and S_{125} are the two free parameters in the LDF fitted to the tank charge distribution (Eq. 5.8).

The distribution of the obtained β values as function of the energy estimator $\log_{10}(S_{125})$ is shown in Figure 6.2(left), for proton initiated air showers. As discussed above, simulations for the IC79 configurations are used. A large spread in β values can be seen for a fixed S_{125} value, especially at the lowest energies. This is due to the large shower-to-shower variations and equivalent fluctuations of the measured tank charges. The average β however remains rather stable with increasing S_{125} (energy) around a value of 3.15, up to an $\log_{10}(S_{125}) \approx 2$. This average β curve for proton showers is shown in the right panel of Figure 6.2. At a $\log_{10}(S_{125})$ around two the average β suddenly starts to increase, reaching 3.4 around $\log_{10}(S_{125}) \approx 2.4$, above which it seems stable again. This sudden increase is not present in data and currently not understood. For a while it was thought that this is related to the thinning and (possibly worrying) dethinning of air showers (sections 4.1.2 and 4.3.3), as also the thinning settings rise with a similar curve. Both the thinning energy and the maximal weight appointed to particles increase fast between 100 and 273 PeV, which roughly correspond to $\log_{10}(S_{125})$ respectively around 2 and 2.4. However, this is not proven. Further studies have been performed but more work is needed [196]. In the final analysis only air showers without thinning, thus

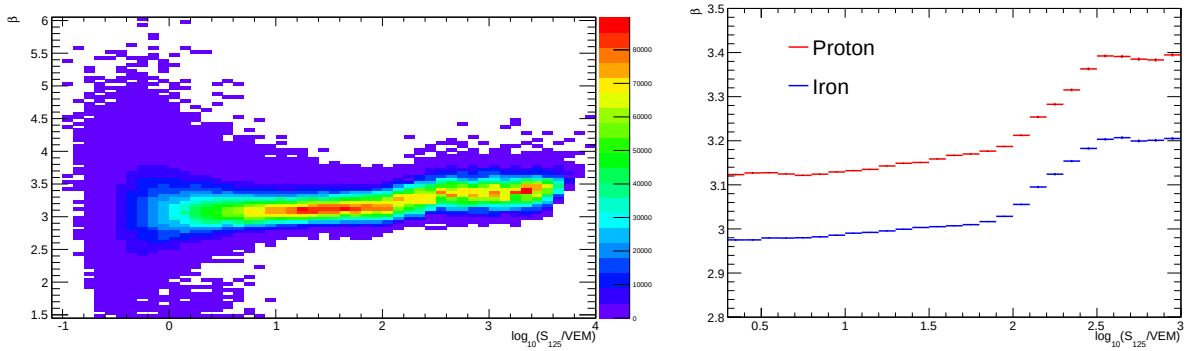

Figure 6.2: Left: reconstructed β as function of $\log 10(S_{125}/\text{VEM})$ for proton initiated showers with $\cos\theta > 0.8$, after the IceTop event selection. Simulations for the IC79 configuration are used. Right: mean of the gaussian fit to the distribution in the left figure in red (proton), while the average values obtained for iron are shown in blue.

with a $\log_{10}(S_{125}) < 2$, are used. Therefore this is not a problem for the current work. This should be investigated in more detail though for an extension of the analysis to higher energies.

A similar β ($\log_{10}(S_{125})$) distribution is obtained for air shower initiated by heavier primaries. Due to the large scatter in reconstructed β values, even the distributions for the extreme nuclei (proton and iron) largely overlap. Despite these overlapping distributions, a siginifcant difference can be seen in their average β values, as shown in Figure 6.2 (right). Over the entire energy range a stable separation of 0.15 of the mean β between proton and iron showers is obtained. This indicates the composition sensitivity of β.

The sensitivity to the primary mass is mainly introduced by two differences in the air shower development for lighter and heavier primary nuclei. Air showers caused by higher mass primaries on average develop faster, since the interaction cross section of the primary is larger and the primary energy is distributed over more nucleons. This means that the depth of shower maximum X_{max} is reached higher up in the atmosphere and showers are detected at a later stage in their development (section 3.2.3). At the observation depth the average "shower age s" (as computed in Eq. 3.15) is on average larger for showers initiated by heavier primaries. The lateral spread of the particles is larger in an older shower (discussed in section 3.3.3), which results in a smaller steepness of the lateral distribution function.
This is illustrated in Figure 6.3. The left panel shows the distribution of reconstructed β values as function of the shower age for proton showers, within a restricted energy range of $1.6 < \log_{10}(S_{125}) < 2.0$. EAS have a shower age around 0 when the shower maximum occurs close to the surface, while older showers have a more positive age. Negative shower ages correspond to reconstructed depths of shower maximum below the Antarctic surface. Again a broad β scatter is seen for a certain shower age, but also the negative correlation between shower age and LDF slope β is observed. This is especially clear for positive shower ages and was explained above with the larger particle spread for older showers. The average β as function of the shower age can be seen for proton showers in red in Figure 6.3(right). The blue curve shows the values obtained for iron initiated showers. This indicates the later stage of the shower development at which iron initiated EAS are detected. This on its turn results in a smaller average β.
Clearly a 2nd effect should cause an even lower average β for iron showers. This can be explained by the higher number of GeV muons in iron showers, as discussed before (section 3.3.2). The dominance of the muonic signal far from the shower core decreases the steepness of the LDF even more.

6.2.2 IceCube: differential energy loss dE/dX_{1500}

Based on the track reconstructed with IceTop, the energy loss profile of the high-energy (HE) muon bundle along the track is reconstructed using millipede (section 5.4.2). The differential energy losses are then fitted

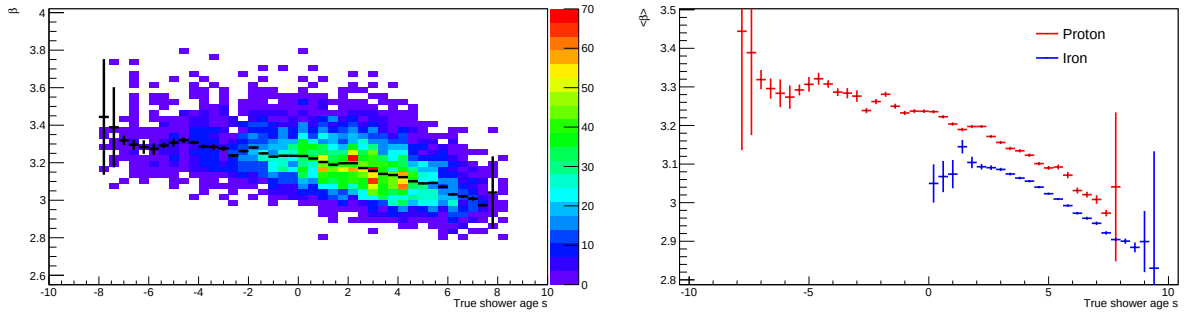

Figure 6.3: Reconstructed slope of the LDF β at a lateral distance of 125 m from the shower core, as function of the (true) shower age s, for events with $1.6 < \log_{10}(S_{125}) < 2.0$ and $\cos\theta > 0.8$. Also the IceTop event selection was applied. Left: 2D distribution for proton initated air showers, where the black curve indicates the mean of a gaussian fit to each vertical bin. Right: the mean of the gaussan fit for proton and iron showers.

(Eq. 5.18), as illustrated in Figure 5.24. The energy loss at a slant depth of 1500 m dE/dX_{1500}(GeV/m) provides an excellent sensitivity to the HE muon number. The relation between dE/dX_{1500} and the number of muons with a muon energy exceeding 400 GeV was given in Figure 5.25.
Not only the number of surface (GeV) muons changes with primary composition, but also these HE muons. This was discussed in section 3.3.2 and shown by the comparison of the secondary muon spectra for proton and iron showers (Figures 3.8 and 3.9). Therefore, the reconstructed energy loss in the ice provides an excellent measure for the mass of the primary particle. It is important to see that this provides a different observable independent from the measurement of the surface muons, since various parts of the shower development are sampled.

Figure 6.4 illustrates the composition sensitivity of dE/dX_{1500} to the primary composition for all energies. The left panel shows, similar to Figure 6.2, $\log_{10}(dE/dX_{1500})$ as function of $\log_{10}(S_{125})$ for proton initiated air showers in a primary energy range $5 < \log_{10}(E_{prim}/GeV) < 9.5$. Due to the intrinsic shower-to-shower fluctuations also for this variable a broad distribution is obtained with a large overlap between various primaries. Therefore also entire destributions are required to acquire a composition sensitivity. The separation of the mean $\log_{10}(dE/dX_{1500})$ in each $\log_{10}(S_{125})$ bin between proton and iron is shown in the right panel of Figure 6.4. This separation is clear and larger as compared to the difference in β between the two particle types (log scale). The difference between the two nuclei decreases slighltly with energy.
It should also be noted that showers initiated by heavier primaries possess smaller shower-to-shower fluctuations compared to lighter primaries (Figure **??**, which results in a narrower $\log_{10}(dE/dX_{1500})$ distribution per energy bin. This could -in principle- be used as an extra composition sensitivity. In the analysis presented here this is not used, while it is important in the mass reconstruction of the coincident IceTop-IceCube analysis ([142]).

6.2.3 Data-MC comparison

Because the simulations that are used in this study are produced for the IC86.2012 configuration, also the data is selected between the start and end date of this data-taking season. The first run of this configuration was taken on April 26, 2012 and the last one at May 2, 2013. As can be seen in Table 4.6, no thinned datasets were produced yet at the time of this analysis and a maximum primary energy of 100 PeV is reached. In order to have sufficient statistics up to this energy, one does not need to use all data and only one month is required. Since the simulations were produced using the average April atmosphere (section 4.1.1), it was chosen to only use the April 2013 data (part of the IC86.2012 data-taking season). The atmosphere in April 2013 is very similar to the April atmosphere used to produce the simulations, and thus no seasonal correction of the in-ice energy loss needs to be performed (section 5.5.2). Using the method described in section 5.6.3,

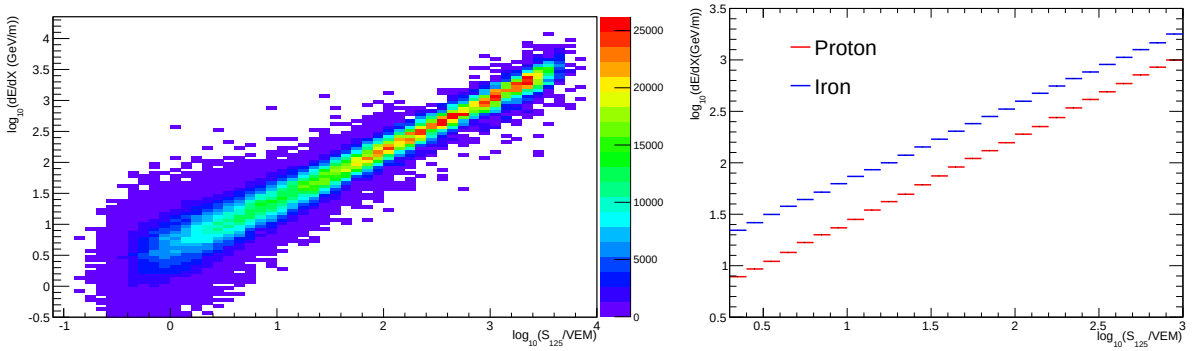

Figure 6.4: Left: the logarithm of the reconstructed energy loss at a slant depth of 1500 m ($\log_{10}(dE/dX_{1500})$) as function of $\log 10(S_{125})$, for proton initiated showers with $\cos\theta > 0.8$, after the IceTop and IceCube event selection. Also these events are obtained from simulations for the IC79 configuration. Right: mean of the gaussian fit to the distribution in the left figure in red (proton events), while the averages obtained for iron are shown in blue.

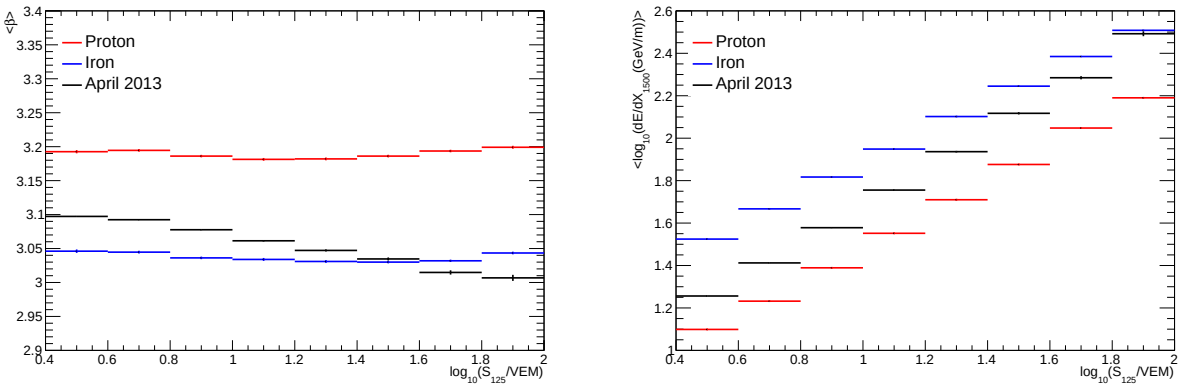

Figure 6.5: Comparison between April 2013 data and proton and iron simulations of the average reconstructed β (left) and ($\log_{10}(dE/dX_{1500})$), as function of the energy sensitive variable $\log_{10}(S_{125})$. Simulations for the IC86.2012 configuration are used, with Sibyll 2.1 as hadronic interaction model. The IceTop and IceCube quality cuts are applied to the events and a minimum reconstructed zenith angle θ of $\cos\theta > 0.8$ is required.

the total livetime of the data taken in this month was found to be 27.68 days. The snow heights put in the simulations are the in-situ measurements from October 2012.

The average β and $\log_{10}(dE/dX_{1500})$ as function of $\log 10(S_{125})$ obtained in April 2013 data are compared to the proton and iron simulations in Figure 6.5. As opposed to Figures 6.2 and 6.4, the $\log 10(S_{125})$ range is restricted to the one used in the analysis. The lower value is defined by the energy threshold at which the analysis becomes fully efficient: $\log_{10}(E_{\rm prim}) \approx 6.4$ (section 5.6.1), which roughly corresponds to $\log_{10}(S_{125}) = 0.4$. No simulations are available beyond 100 PeV, which roughly agrees with $\log_{10}(S_{125})$=2. The $\log_{10}(S_{125})$ range used in this analysis is thus 0.4 to 2, which corresponds to the energy range from a few to 100 PeV.
It can be seen that, for most $\log_{10}(S_{125})$ bins, the data is in between proton and iron. This indicates that the simulations describe the data rather well and no obvious problems exist. Checks of lower-level observables are extensively performed, as described in section 5.6.4. At the highest bins the average β in data is outside the proton-iron range. It will be shown further on that this is highly probably due to the used hadronic interaction model in the simulations (Sibyll 2.1).
Further interpretation of these data-MC comparison plots is postponed to the following chapter, where the results are discussed.

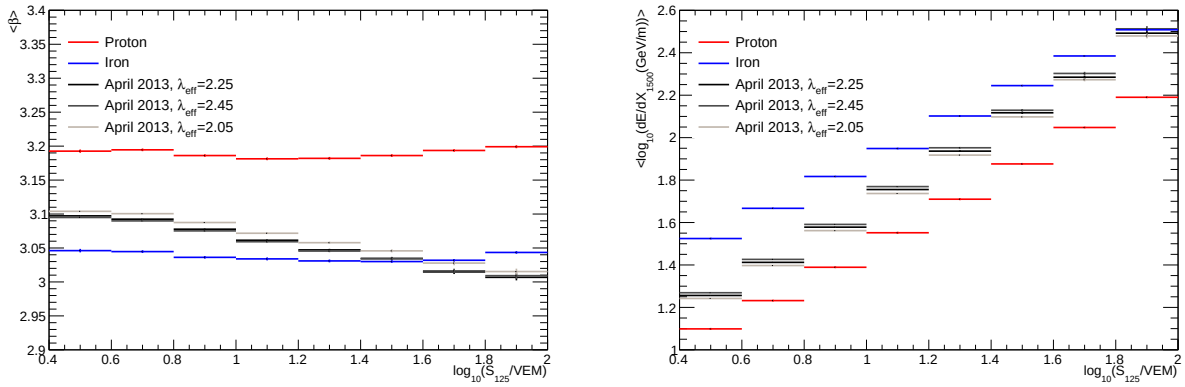

Figure 6.6: Systematic error on the data curves due to the uncertainty on the effective attenuation length λ_{eff} in the snow correction procedure (grey lines).

6.3 Systematic uncertainties

In this study three sources of systematic uncertainties need to be taken into account: the uncertainty on the snow correction and VEM calibration for the IceTop part, and the total light yield measured in the deep ice.

6.3.1 Snow

The signal in each tank is corrected for the snow on top of it using a simple exponential attenuation function (Eq. 5.23). It is known that this function is far from perfect, mainly due to the fact that it corrects the combined signals deposited by muons and EM particles. The effective attenuation length λ_{eff} was deduced as 2.1 m for the snow heights during the IC79 configuration, 2.25 m for IC86.2011 and IC86.2012 and 2.3 m for the later years. However, it varies with energy, zenith angle and also mass of the primary particle. Therefore, an uncertainty of 0.2 m was appointed to the effective attenuation length [241]. An increased (decreased) attenuation length results in a smaller (higher) reconstructed signal per tank. The effect is similar for all tanks, although it is larger for the tanks with more snow. It thus mainly affects the reconstructed shower size S_{125}, while β might change slightly. The effect on the in-ice reconstruction is entirely negligble. However, since it changes S_{125}, events move to different $\log_{10}(S_{125})$ bins and the curves of $< \beta >$ and $< dE/dX_{1500} >$ as function of $\log_{10}(S_{125})$ might change. This is shown in Figure 6.6 for $< \beta >$ (left) and $< dE/dX_{1500} >$ (right). These plots are similar to Figure 6.5, but also indicate the curves that are obtained when the data is corrected with an attenuation length of 2.45 m (dark grey) and 2.05 m (light gray) instead of 2.25 m.

6.3.2 VEMCal

The calibration of the IceTop tanks is performed based on the signal deposition of vertical (equivalent) muons (VEM). This calibration procedure is described in detail in section 5.2.2. The conversion from number of photo-electrons to the VEM charge unit is determined on a tank-by-tank base and is reproduced in simulations up to a 2-3 % level [192]. Hence, this uncertainty is propagated to the analysis and the charges in data are shifted by ± 3 % to obtain an estimate of the error. Similar to the snow correction uncertainty, it mainly influences the reconstructed shower size S_{125}. The systematic errors on the analysis introduced by this VEMCal uncertainty are shown in Figure 6.7 as alternative data curves. It can be seen that the effect is slightly smaller compared to the error imposed by the snow correction. These errors can be quadratically summed into one combined uncertainty on the IceTop charge since they are uncorrelated.

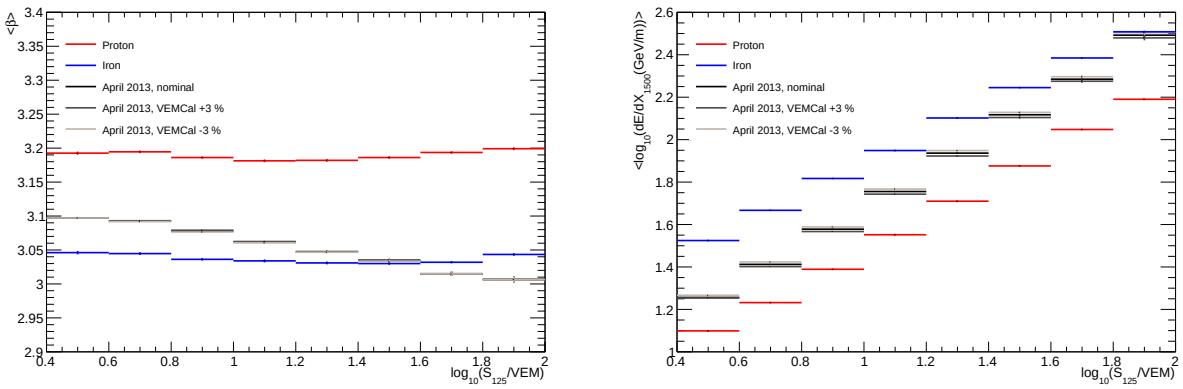

Figure 6.7: The effect of the ± 3 % VEM calibration uncertainty on the obtained distributions for data (grey lines).

6.3.3 Light yield

The charge measured in the ice introduces the largest uncertainty on a composition analysis with the in-ice component of the IceCube Neutrino Observatory, since it directly affects the reconstructed energy losses.

A first uncertainty is introduced by the photon detection efficiency of the DOMs. Due to important calibration efforts in the collaboration, this uncertainty on the DOM efficiency is currently reduced to ± 3 %. This linearly translates to a ± 3 % uncertainty on the charge.
In the reconstruction of the differential energy losses along the muon bundle track (section 5.4.2) from the charges measured in the DOMs, one further has to make an assumption about the ice properties. The description of the photon scattering and absorption in the ice is currently performed with the SPICE-Mie model (section 2.1.3). The 1 σ uncertainty on these scattering and absorption parameters is shown with the error ellipse in Figure 2.8. The systematic values used to comprise these errors are +10 % scattering, -10 % scattering, -7.1 % scattering and absorption. Work is ongoing to further minimize these errors and it is known that the current values overestimate the uncertainties. The effective scattering length in the "Hole" ice, the refrozen ice around the DOM, is modelled with a baseline of 50 cm, while 30 cm and 100 cm are used to describe the possible error.

The influence of these ice parameter uncertainties on the in-ice light yield has been investigated in a dedicated simulation study [248]. For each of the systematic values a specific simulation set was produced, and the change in the observed light yield was studied. This was performed for various zenith angle regions, where in this analysis only the results for the zenith angle range $0^\circ < \theta < 30^\circ$ are used. The measured charge difference of each set with regard to the baseline is given in Table 6.1.
When the approximation is made that all these systematic errors are uncorrelated, the errors that either increase or decrease the total light yield are gathered, and these sets of increasing/decreasing errors can be summed up quadratically. This is done here, although it is known that this again overestimates the error slightly. To reduce this error new simulations are required, which takes time.
The total systematic uncertainty on the in-ice light yield is +9.6 % and -12.5 %. This is applied as a shift to the observed charge in data. The influence on the reconstructed energy loss $< \log_{10}(dE/dX_{1500}) >$ is shown in Figure 6.8. Similar to the snow and vemcal systematic error it is indicated by the grey lines. This total light yield uncertainty is clearly the largest systematic error in the analysis.

Table 6.1: Overview of the various contributions to the systematic uncertainties on the in-ice light yield, obtained from dedicated simulation studies [248].

	Systematics uncertainty
DOM efficiency	$\pm$ 3%
Hole ice 30 cm	+ 4.5%
Hole ice 100 cm	- 2.9%
+ 10 % scattering	+ 3.6 %
- 10 % scattering	-11.8 %
-7.1 % scattering and absorption	+ 7%
Total	+9.6%,-12.5%

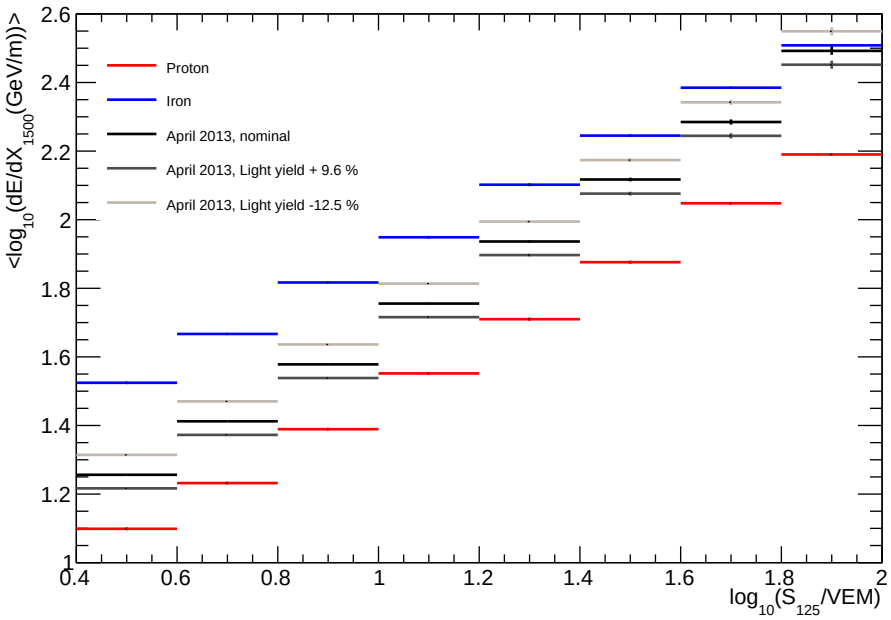

Figure 6.8: Uncertainty in the average reconstructed energy loss for data in every $\log_{10}(S_{125})$ bin, implied by the combined in-ice light yield systematic error (grey lines).

6.4 Hadronic interaction models

Since the post-LHC models were not yet available at the start of the production, the main sets of (cosmic ray) IC86.2012 simulations use Sibyll 2.1 as hadronic interaction model. These sets are also used in all previous figures and studies. Afterwards smaller datasets were produced with Sibyll 2.3, QGSJet-II.04 and EPOS-LHC. The datasets of the three post-LHC hadronic interaction models have a 10 times smaller statistics as compared to the Sibyll 2.1 dataset. The properties of all of these datasets are listed in Table 4.6.
The hadronic interaction models have been described in section 4.2, which contains a discussion of the upgrades of the models to include LHC and other recent data. The most important difference of the new models with regard to Sibyll 2.1 for IceCube analyses is the increased production rate of GeV muons.
In section 6.4.1 the muon spectra in the simulations produced with the various hadronic models are compared. The influence of these different muon spectra on the observables used in this analysis (β and dE/dX_{1500}) are investigated in section 6.4.2.

6.4.1 Muon spectra

Figures 6.9 and 6.10 depict the resulting muon spectra that are obtained after simulations down to an atmospheric depth corresponding to the IceTop altitude (2835 m a.s.l, which results in an average atmospheric depth of 692 g/cm^2). The muon spectra are shown starting from a muon energy of 0.1 GeV, which is roughly the threshold for muons to create a signal in the IceTop tanks, up to 10 PeV. They are respectively shown for proton and iron initiated air showers, in the lowest and highest primary energy bins in the analysis: from 6.4$<\log_{10}(E_{\rm prim}/{\rm GeV})<$6.6 and 7.8$<\log_{10}(E_{\rm prim}/{\rm GeV})<$8.0. The curves show the average over many showers and error bars describe the error on the average. The various colours indicate the spectra produced in the different hadronic interaction models. More detail is provided in the bottom plots, which show the ratio of the post-LHC models results to the Sibyll 2.1 spectra.
The number of low-energy muons increases for all new hadronic models, for both primaries and energy bins. This is expected, due to the increased number of charged secondary at the expense of the neutral particles (section 4.2). The largest increase in low-energy (surface) muon number is observed for EPOS-LHC ($> 40\%$). This number increases by $\sim$30 % and $\sim$20 % for respectively Sibyll 2.3 and QGSJet-II.04. The change in the number of high-energy muons (> 300 GeV) is smaller. On average there seems to be a decrease of $5-10\%$ for simulations using EPOS-LHC, while both QGSJet-II.04 and SIBYL 2.3 only show a very small, nearly negligible, increase in HE muon number relative to Sibyll 2.1.

6.4.2 Influence on measured observables

Similar to as is done for simulations using Sibyll 2.1 (Figures 6.2 and 6.4), also for the simulations with the post-LHC models the average β and $\log 10(dE/dX_{1500})$ are reconstructed in the $\log_{10}(S_{125})$ range from 0.4 to 2. The results obtained with the various hadronic models are shown in Figures 6.11 and 6.12. The change with respect to Sibyll 2.1 is displayed in the bottom two panels.

A decrease in β with regard to Sibyll 2.1 is observable for all post-LHC hadronic interaction models with regard to Sibyll 2.1. This decrease is caused by the increased number of surface muons in all models, which flattens the LDF since they dominate the signal at the edge of the shower. The smallest $<\beta>$ is obtained in simulations with EPOS-LHC, consistent with the largest increase in GeV muon multiplicity. As described in section 4.2, simulations with the post-LHC models result in a depth of shower maximum deeper in the atmosphere. From a deeper depth of shower maximum a lower shower age naturally follows. In section 6.2.1 it was seen that this would cause β to increase. The opposite effect is observed, which leads to the conclusion that this effect is less important and the change in β is dominated by the different surface muonn number.

The difference between QGSJet-II.04, Sibyll 2.3 and Sibyll 2.1 concerning the number of high-energy muons is small, which results in a negligible change in the measured average energy loss in the ice. For EPOS-LHC

on the other hand a significant reduction can be observed at all energies, due to the 5 to 10 % decrease of the HE muon multiplicity. It should be noted though that the statistics are low and significant bin-to-bin variations are visible. Hopefully more simulations for the post-LHC hadronic models can be added in the future.

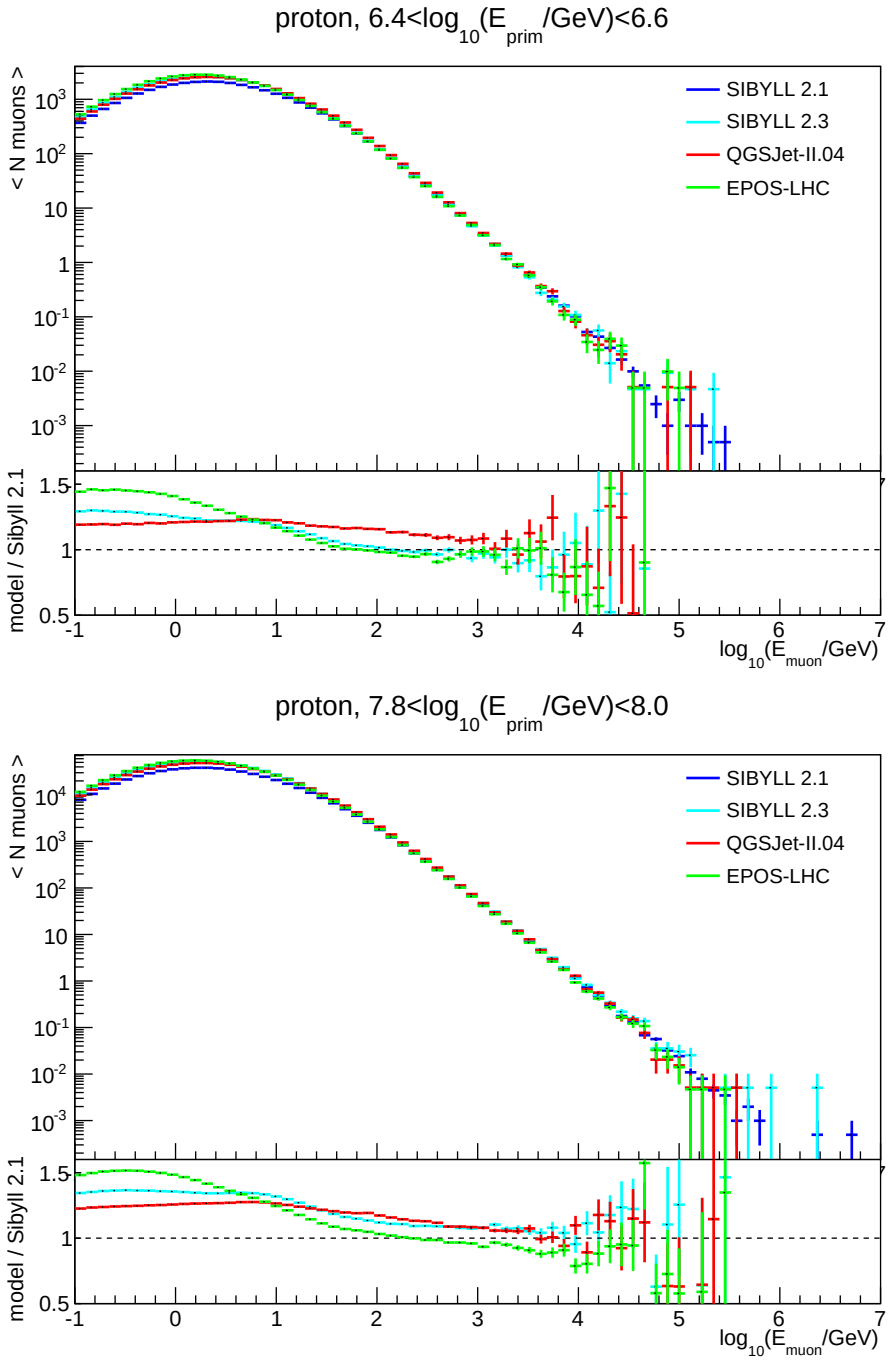

Figure 6.9: Average secondary muon spectra at the IceTop atmospheric depth in simulations (692 g/cm^2, April 2011 South Pole atmosphere), for proton showers with zenith angles $< 40°$ in two energy ranges (around 3 and 80 PeV). The spectra obtained with various hadronic models are shown, together with the ratio with respect to Sibyll 2.1.

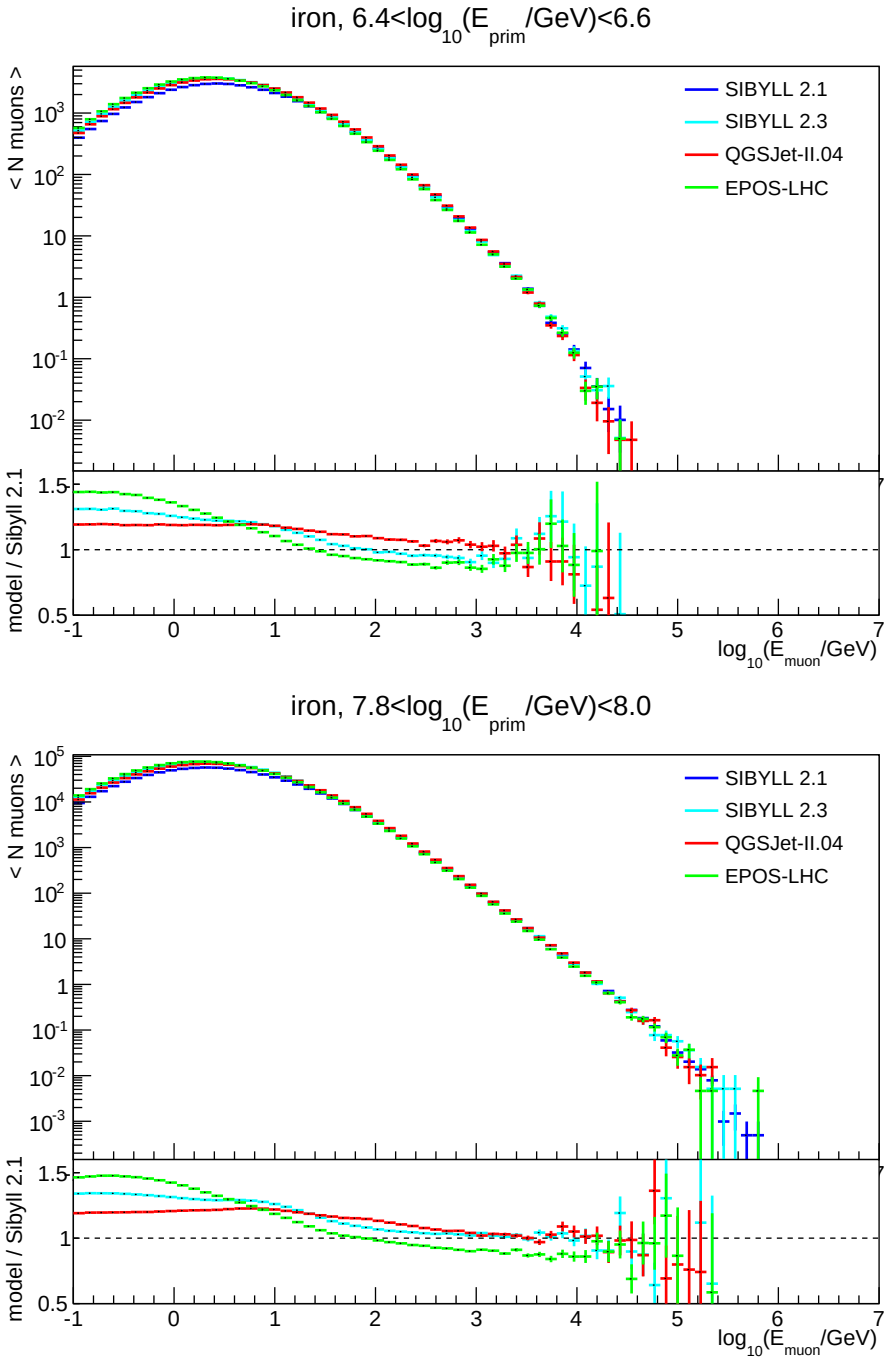

Figure 6.10: Average secondary muon spectra at the IceTop atmospheric depth in simulations (692 g/cm^2, April 2011 South Pole atmosphere), for iron showers with zenith angles $< 40^\circ$ in two energy ranges (around 3 and 80 PeV). The spectra obtained with various hadronic models are shown, together with the ratio with respect to Sibyll 2.1.

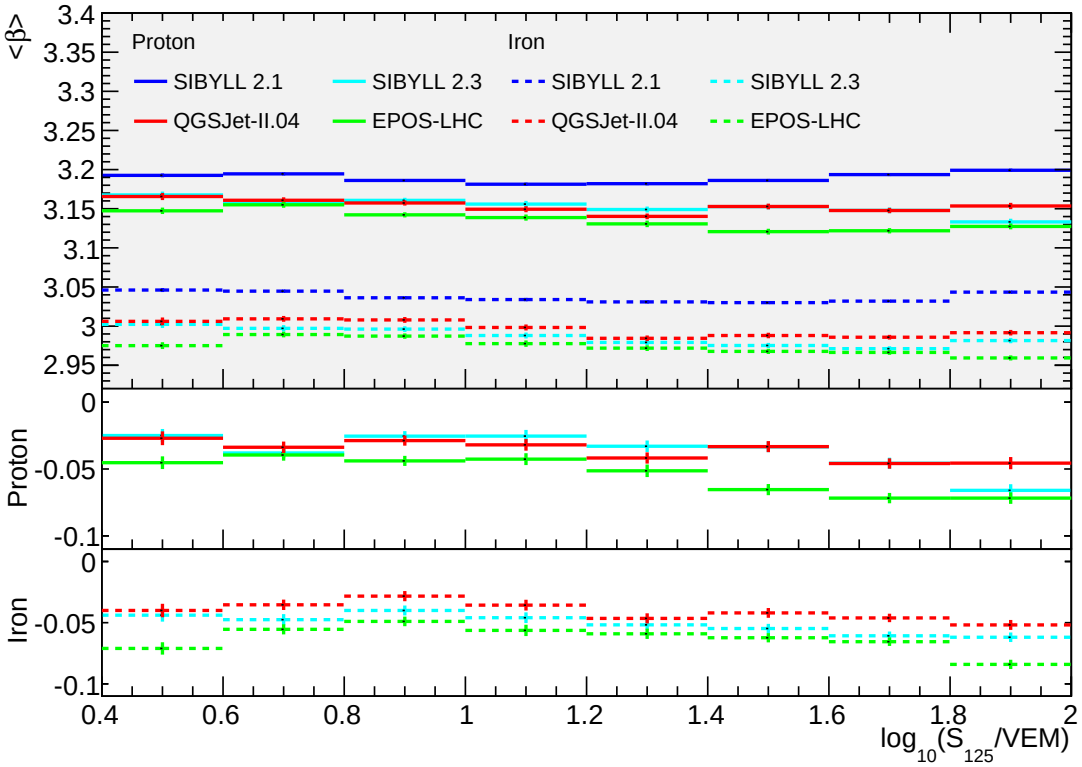

Figure 6.11: The average LDF slope β at 125 m from the shower axis as function of S_{125}, for proton (solid) and iron showers (dashed), for various hadronic interaction models. The bottom panels indicate the shift of the new models with respect to Sibyll 2.1.

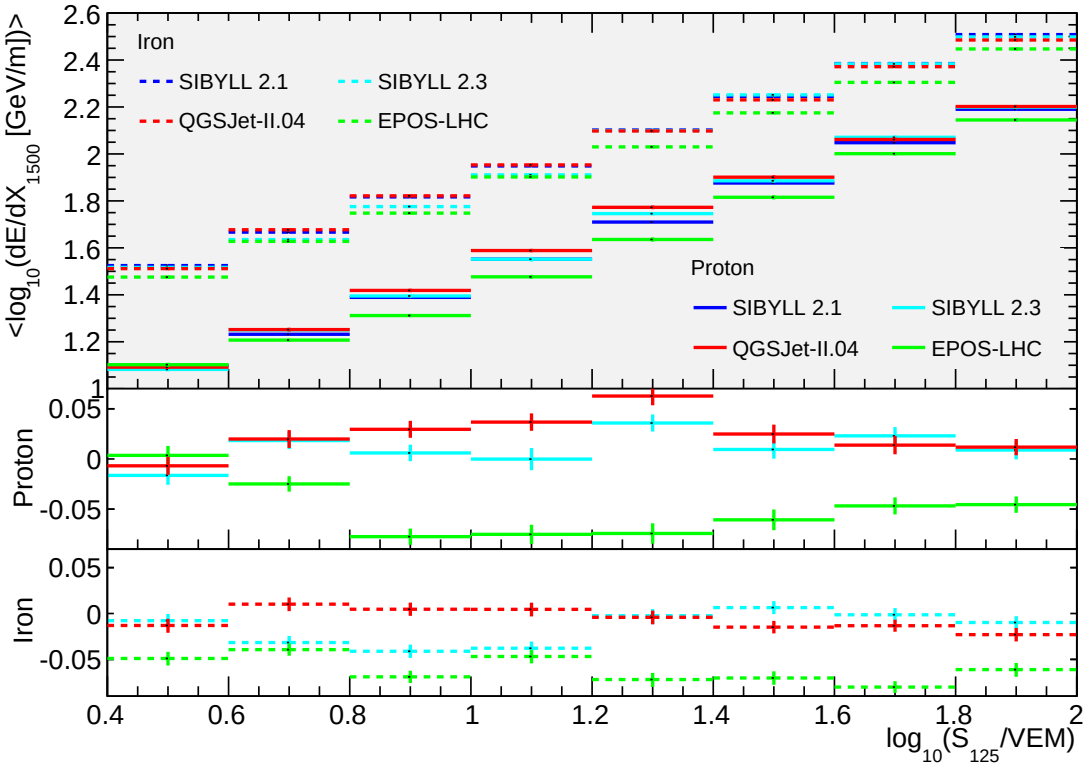

Figure 6.12: The mean energy loss at a slant depth of 1500 m as function of S_{125}, for proton (solid) and iron showers (dashed), for various hadronic interaction models. The bottom panels indicate the shift of the new models with respect to Sibyll 2.1.

7

Results

Knowledge is power. Information is liberating. Education is the premise of progress, in every society, in every family.

Kofi Annan

7.1 Results

With the analysis outlined in the previous chapter one can investigate the internal consistency of the hadronic interaction models. Simulations with these models (the pre-LHC model Sibyll 2.1 and the post-LHC models Sibyll 2.3, QGSJet-II.03 and EPOS-LHC) can result in a different relationship between observations and the primary particle properties if the simulations do not describe the extensive air shower (EAS) propagation in a realistic manner. The use of multiple observables, sensitive to complementary parts of the air shower development, then allows to verify whether a consistent picture is obtained with a certain hadronic interaction model.

In this specific analysis, the average cosmic ray composition reconstruction with the IceTop surface array is compared to the average mass obtained with the in-ice IceCube array. The composition sensitivity with IceTop is gained from the measurement of the average slope β of the LDF at a perpendicular distance of 125 m from the shower axis (section 6.2.1), which is correlated to the age of the shower and the number of low-energy (LE) muons at the surface ($E_\mu \approx \mathcal{O}(1\text{ GeV})$). The energy loss dE/dX_{1500} of the high-energy (HE) muon bundle at a slant depth of 1500 m in the ice is an excellent measure for the number of muons with energies exceeding 400 GeV in the shower (section 6.2.2). These muons are created in the first interactions of the air shower, while the GeV muons detected with IceTop are created after many particle interactions in the atmosphere. Both the GeV muon multiplicity, combined with the shower age, and the number of HE muons provide an excellent sensitivity to the primary mass of the cosmic ray. Hence, these variables can be converted into an independent measurement of cosmic ray composition.
The reconstruction of the composition with the two variables is performed as function of the shower size S_{125}, related to the primary energy of the shower. The analysis reported upon here is only done for $\log_{10}(S_{125})$ values between 0.4 and 2, with a binwidth of 0.2. This roughly corresponds to a primary energy range between 2.5 and 100 PeV (Figure 6.1). The required simulations were not available at higher energies, while at lower energies the detector is not fully efficient.

The average β and $\log_{10}(dE/dX_{1500})$ as function of $\log_{10}(S_{125})$ obtained in April 2013 data were shown in Figure 6.5 (black). The red and blue curves indicate the means obtained with respectively pure proton and iron simulations, where Sibyll 2.1 was used as hadronic interaction model. Due to the differences in the created muon spectra between the hadronic interaction models (section 6.4.1), the average β and $\log_{10}(dE/dX_{1500})$ curves differ in simulations with changing hadronic interaction model. This was shown

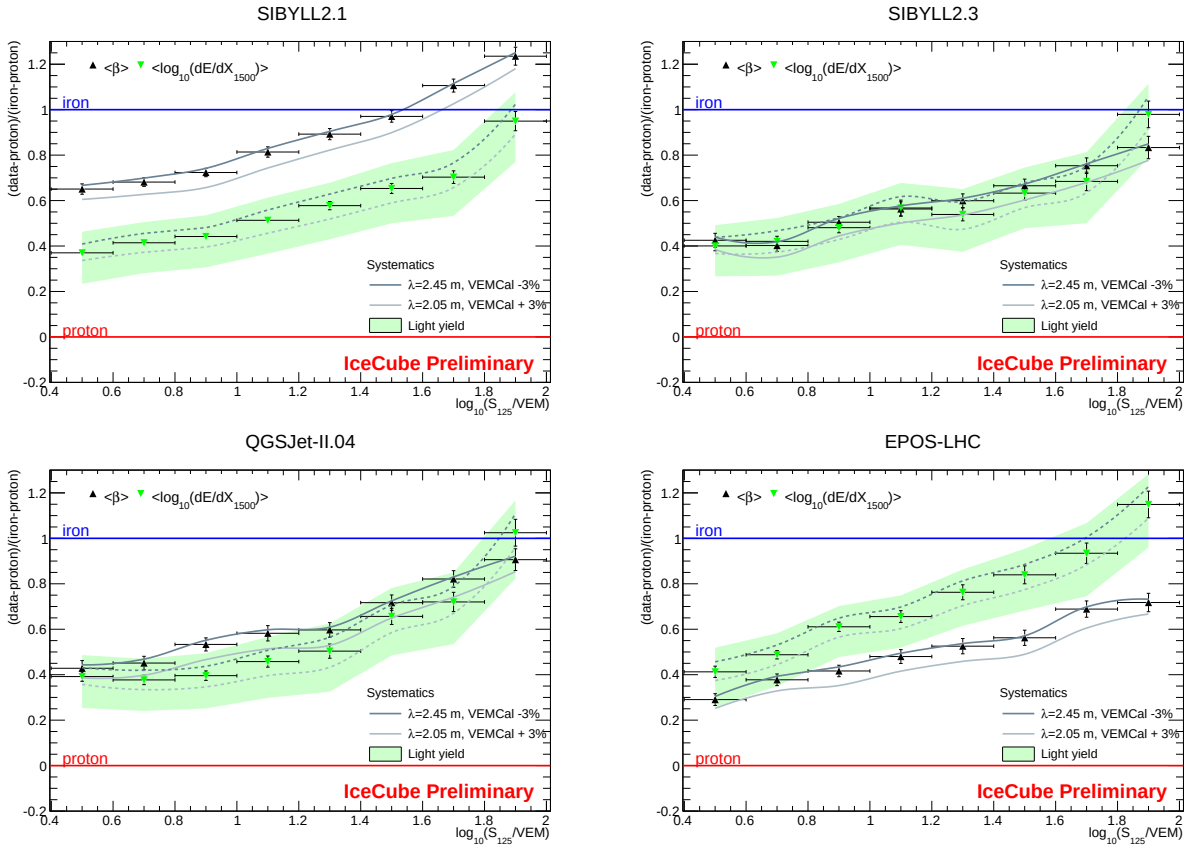

Figure 7.1: Distribution of the average reconstructed β and $\log_{10}(dE/dX_{1500})$ measurements as function of S_{125} in the proton-iron space. Each panel shows the results obtained with a certain hadronic model. The green band shows the in-ice light yield systematic, while the solid and dotted grey curves indicate the combined uncertainties from snow and energy considerations in the IceTop reconstructions.

in Figures 6.11 and 6.12.

Simulations should describe the development of the air shower accurately, as close to the reality as possible. If this is the case, measured data curves should be somewhere in between simulated proton and iron curves (or at least very close to them). To compare the data results of the two variables (β and $\log_{10}(dE/dX_{1500})$), we plot the relative position of data within the proton-iron space for each variable. When data is similar to proton (iron) for a certain variable, it has a value close to 0 (1). If a consistent, i.e. agreeing within the error bars, composition is measured between the two variables, the two curves should roughly overlap.
The resulting comparison of the mean β and $\log_{10}(dE/dX_{1500})$ obtained in data with respect to simulations is shown in Figure 7.1, for each of the hadronic interaction models. The black triangles indicate the relative position of the surface measurement (β) and the green triangles the in-ice energy loss measurement. The systematic error induced by the snow correction and the VEM calibration are summed up quadratically and shown as the grey solid (for β) and dotted (for $\log_{10}(dE/dX_{1500})$) lines (sections 6.3.1 and 6.3.2). These have a similar effect on the surface and the in-ice measurements. The total light yield systematic uncertainty (section 6.3.3) only affects the in-ice measurement and is indicated with the green area. The light yield uncertainty in the ice clearly dominates the systematics. Also the statistical error bars are shown, which logically increase with increasing S_{125} or energy. However, they do not dominate this measurement.

A manifest behaviour that can be seen in all of these plots is that, for both observables, the data curves move closer towards iron with increasing S_{125} and thus with energy, indicating a rising average composition. Depending on which hadronic interaction model is used, these plots do show a varying agreement between

the two observables. For both Sibyll 2.3 and QGSJet-II.04, a consistent interpretation is obtained between the two parameters. In this case a composition measurement using an observable sensitive to the shower age and the muonic component on the surface agrees with a measurement of the in-ice energy loss caused by the HE muons, which is of great importance. Results obtained with simulations using Sibyll 2.1 and EPOS-LHC on the other hand show some discrepancy concerning these measurements. Namely the lower number of LE muons on the surface in the pre-LHC model Sibyll 2.1 causes the measured slope of the LDF to give a heavier composition than the signal in deep ice. In the case of EPOS-LHC, the decreased number of HE muons combined with the $\sim$50 % increase in the LE muon number leads to the opposite inconsistency. A heavier composition is reconstructed with the in-ice measurement as compared to the IceTop reconstruction of the slope of the LDF.

As summarized, consistent results are obtained with Sibyll 2.3 and QGSJet-II.04, while for Sibyll 2.1 and EPOS-LHC a different compostion interpretation would be obtained depending on which observable is used. Generally, it should also be concluded that it is of crucial importance to understand and take into account the variations within certain models and in between models, especially when cosmic ray composition results are compared where different properties of the extensive air showers are used to reconstruct the primary cosmic ray mass.

7.2 Comparison to other results and discussion

The rising average mass in this energy range (from roughly 2.5 to 100 PeV) is observed before by IceCube and other experiments. The IceCube Neutrino Observatory measured this rise in the average mass in both a (LE) muon density analysis [227] and a measurement of the elemental spectra mainly using the HE muon bundle energy loss [142] (the same parameter as used in the analysis described in this work), In the 3 year update of this latter composition analysis [144], the post-LHC hadronic interaction models are used to derive alternative results. This is performed based on the shifts between the post-LHC models and Sibyll 2.1, as deduced during the work presented here. The obtained shifts are given and described in Appendix B. While Sibyll 2.3 and QGSJet-II.04 result in a similar composition reconstruction as Sibyll 2.1, mainly the use of EPOS-LHC would give a heavier average mass over the entire energy range. Alternative elemental spectra with Sibyll 2.3 and QGSJET-II.04 are close to the result obtained with Sibyll 2.1. In the muon density measurement with IceCube a lighter average mass is obtained compared to both methods presented in this work, systematically for all post-LHC hadronic interaction models.
As shown in section 3.4.3, more specifically in Figure 3.14, also KASCADE(-Grande), the Yakutsk Array and Tunka measure this increasingly heavy composition in the energy region from the knee in the spectrum (around a few PeV) to the second knee ($\sim$100 PeV). Although the measurements all show the rising average mass in this energy region, the measurements do cover a broad band in the average mass with respect to each other. Therefore, experiments need to scrutinize their energy and mass measurement, but we should also take into account that this disagreement between the experiments is due to the different observables used and the uncertainty in the hadronic interaction models. It would be furthermore great if other methods to extract the composition in this energy range (and above) are added: the reconstruction of X_{max} using fluorescence telescopes at the low-energy extension of the Telescope Array experiment (TALE), air Cherenkov or radio measurements.
Above 100 PeV, the measurements start to diverge more and more, probably due to the uncertainty in the simulations at these high energies. One of the reasons the work described here was started was the discrepancy between the IceCube composition measurement and other experiments in the energy range between 100 PeV and 1 Eev. A heavier composition was obtained with IceCube compared to for example KASCADE-Grande. Around the ankle it is also difficult to match the composition obtained with IceCube with the Pierre Auger Observatory and Telescope Array measurements (Figure 3.15). As concluded in the previous section, it seems possible that this discrepancy is caused by the different measurement techniques combined with the uncertainties in the hadronic models. However, the current analysis needs to be extended

to higher energies to be able to make a final conclusion.

As described in section 3.4.4, also other experiments performed investigations of the hadronic interaction models. These mostly focus on the number of GeV muons on the surface and compare the number of muons in the simulations with respect to the data. In the energy range under investigation in this work, the KASCADE(-Grande) collaboration did not observe a muon deficit in simulations with post-LHC hadronic interaction models [249]. This means, in practice, that data is found within the proton-iron band. This is comparable to the result obtained in this work, where also no clear muon problem is observed. When, more in detail, the IceTop composition reconstruction is compared to the one with the in-ice detector, one does observe a discprency for Sibyll 2.1 and EPOS-LHC. Furthermore, in the KASCADE-Grande study, the evolution of the muon density with increasing zenith angle in data is found to be not accurately reproduced by simulations. The muon density measurement performed in IceCube [227] provides a complementary measurement to the ones presented in the work presented here. Since in that measurement the average mass would be reconstructed slightly lighter when the post-LHC hadronic models are used, combined with the presented analysis it would result in a further disagreement of these models. A measurement of the lateral separation of high-energy muons from the muon bundles in IceCube shows some incosistency for EPOS-LHC and QGSJET-II.04 [250]. Hence, at these energies, no clear muon deficit or any other obvious data-MC discrepancy is seen. However, when one scrutinizes the details like the zenith dependence or using multiple observables, inconsistensies are seen for most hadronic models.
With increasing primary energy, an increasing muon deficit in simulations as compared to data is observed, even with post-LHC hadronic models. At 10^{19} eV, a significant muon deficit is seen by the Pierre Auger Observatory [157, 251] and the Telescope Array[252], especially for inclined events. The Pierre Auger Observatory also found that a higher mass would be reconstructed if the rise-time of the signals oberved in the detectors is used as mass-measure [158] or if the muon production depth is used to reconstruct the mass [159].
Important work in gathering these measurements was recently done in [253]. Next to the overview, this also gathers all GeV muon number measurements to provide a clear picture for every hadronic interaction model over the entire energy range covered by indirect air shower experiments.

Summarized, measurements more and more show the imperfect modelling of the air shower by simulations, at least in some parts of the shower. The GeV muons seem to be inadequately modeled, especially at the highest energies and inclinations, but apart from this also other problems are observed. Especially when one combines multiple observables to investigate the hadronic models or to compare the obtained composition, important inconsistencies are seen. More studies are needed to pinpoint to the exact limitations in the models and to find out which parts of the air shower are well modelled and can be trusted to reconstruct the primary mass. In this view, the measurement described in this work is an important addition to the existing studies concerning the hadronic interaction models.

7.3 Further improvements

This analysis has shown its potential to find problems in the hadronic interaction models. To finalize the work, some updates and improvements are desired.

The most important goal should be to extend the analysis to higher energies, i.e. to reach a primary energy of (almost) 1 EeV. This would allow to investigate whether the disagreement between the composition reconstruction using IceCube and other experiments (section 3.4.3) is due to the modelling of the hadronic interactions in simulations. Since these energies cannot be reached at human-made accelerator facilities the hadronic models need to rely on extrapolations, which increases the chance of problems in the models. Experiments sensitive at these high cosmic ray energies previously reported on a muon deficit in simulations. The extension of this current analysis seems a valuable input to solve this ”muon problem”. In the end, this

hopefully helps to reach an agreement between the various experiments concerning the composition, which would result in a better understanding of the sources of these high-energetic cosmic rays.
The main bottleneck at this point for an extension to higher energies is the lack of thinned simulation datasets with energies ranging up to $\log_{10}(E_{prim}/\text{GeV})$=9.5. For this analysis these have to be created for proton and iron primaries, using all four used hadronic interaction models. It takes at least several months, up to one year, to produce the CORSIKA simulations and simulate the detector response.
However, before this energy range can be added to the analysis also the reason of the sudden increase of the average β in simulations has to be found (Figure 6.2). This feature is not visible in data and therefore the simulations need to be scrutinized. My personal suspicion still goes towards the thinning and unthinning of air showers, possibly together with the imperfect description of the shower fluctuations. In new simulations for future analyses this feature seems to have disappeared, but the reason for this is currently under study [254].

On top of extending the analysis to higher energies, a significant decrease of the error could be achieved with an update of the in-ice uncertainty study. The knowledge of the ice properties greatly improved in the meantime and it is known that the currently quoted error overestimates the uncertainty significantly. Also an improved snow correction would help IceTop analyses, but is of minor importance here.
In the near feature, certainly in view of a publication of the work, the direct measurement of the muon density far from the shower core [227] can be added to this study. This muon density is correlated to the slope of the reconstructed LDF, but is less influenced by the age of the shower. Furthermore, also the lateral distribution of the muons does not seem to match well between simulations and data. Therefore one could also expect a slightly different composition reconstruction between the two observables. This would thus be extra important input for the hadronic models.
In the longer future, possible additions to the IceCube Neutrino Observatory such as a scintillator array [83], the Imaging Air Cherenkov Telescopes (”IceAct”) [255] or a radio antenna array could be used to investigate air showers using a variety of observables. This would allow a broad check of the hadronic interaction models.

8

Discussion

All the freaky people make the beauty of the world. Stay human.
Michael Franti & Spearhead - Stay Human

The thesis work presented here contributes to the analysis of cosmic rays with the IceCube Neutrino Observatory. In general, it also aims to improve the understanding of the air shower development, the giant cascade of particles created when an energetic cosmic ray hits the top of the atmosphere. The IceCube Neutrino Observatory, primarily built for neutrino astronomy, is one of few currently active arrays that performs measurements of high-energetic cosmic rays. Combined with neutrinos, gamma rays and gravitational waves as other messenger particles, these cosmic rays help to gain understanding of the extremely energetic phenomena in the Universe.

A lot of effort has been put in various parts of cosmic ray analyses with IceTop and IceCube. Improvements were made in a diversity of topics, such as the development of a realistic atmosphere for simulations (section 4.1.1), the determination of the snow heights and correction (section 5.5.1), the influence of atmospheric variations on the data (section 5.5.2), unthinning of air showers (section 4.3.3), calibration (section 5.3.2), etc.
However, beyond any doubt the main contribution of this work lies in the development of an advanced event processing for cosmic ray analyses with IceTop and IceCube (Chapter 5). Following the Level 1 (Online) and Level 2 (Offline) processing, respectively the first data processing at South Pole and in the North, the developed software chain is referred to as Level 3 (L3). This provides a high-level reconstruction of the observed cosmic ray events, suited for a large variety of analyses. While before the development of these scripts all data analyzers had to start from the Level 2 processed data and develop their own analysis chain, one can now start from this high-level verified data. This seems a giant leap forward for the cosmic ray studies with IceTop and IceCube. It furthermore also serves as a collection of scripts easily accessible for any collaborator for use in its own study.
Primarily, the Level 3 processing is based on the IT73/IC79 energy spectrum and composition analyses, but it was heavily extended and optimized. Currently all data-taking years from the IC79 to IC86.2015 configurations can be processed. While the Level 2 output differs from configuration to configuration, it is unified in Level 3. This is followed by extra recalibrations and updated cleaning procedures. The IceTop reconstructions are similar to the IT73/IC79 analyses, but afterwards an extra pulse cleaning procedure based on the reconstructed track is implemented. This also selects and removes the isolated soft local coincidence pulses. The energy loss reconstruction in the ice is performed along the track reconstructed by IceTop, after pulse selection procedures. The method is similar to the IT73/IC79 analysis, with small modifications to mainly increase the accepted zenith angle range. However, an extra branch of the IceCube part of the cosmic ray Level 3 processing is created to also reconstruct the track direction in the ice, followed by the determination of the energy loss profile. These in-ice track reconstructions could be used for events with a shower core outside the IceTop array to increase the acceptance of the detector. For both the IceTop and

IceCube part a set of standard event quality cuts are implemented to select events for which their shower axis is contained in both IceTop and IceCube. This provides a set of well-described high-level events that can be used for a large diversity of topics.

Of course this is only a first implementation of an advanced event processing and parts will hopefully be updated in the future. Some of these possible updates are listed here, and most of them are already work in progress. From the detailed snow study, performed in this and previous work, it became apparent that an urgent need exists to update the snow correction procedure. The BORS snow correction seems to be the way forward, but still needs intensive work. The snow heights also need to be known in more detail, for which currently a sensor is tested at one of the IceTop tanks. Furthermore, the parametrization of the curvature of the shower front and the charge and time fluctuations were studied using the 26-station configuration of IceTop and therefore seem to describe the behaviour of higher energetic showers ($\mathcal{O}$(100) PeV) imperfect. A last significant improvement in the IceTop part would be the development of a separate fit to the electromagnetic and muonic contribution of the signal.
A better sensitivity to the primary composition using high-energy muon bundles might be reached with the development of an energy loss reconstruction specific for large muon bundles. The currently used algorithms are developed for single muons, which can obviously be improved.
A final, and probably most important, gain for cosmic ray physics with IceTop and IceCube would come from a combined IceTop-IceCube track reconstruction for showers with a shower core outside the IceTop array. This would highly improve the detection efficiency and thus the statistics at the highest energies.

The second part of this thesis work consisted of the study of the sensitivity of IceCube cosmic ray measurements to the hadronic interaction models (Chapters 6 and 7). Motivated by the disagreement in the reconstructed composition between IceCube and the other experiments in the 100 PeV to 1 EeV primary energy region, for the first time an average mass reconstruction is performed with both the IceTop and the IceCube array. A comparison of the mass sensitive observables between data and simulations ran with a variety of hadronic interaction models allows to investigate the cause of the discrepancy and the dependence on the assumed hadronic model.

In the analysis of the cosmic ray composition with IceCube, in conflict to the other experiments, the mass sensitivity is based on the energy loss profile of the high-energy muon bundle in the ice. This measurement is now compared to a mass reconstruction based on the steepness of the lateral distribution function (LDF) fitted to the charges in the IceTop tanks. The LDF slope β is obtained at a distance of 125 m from the shower axis, while the shower size at this distance S_{125} provides the measure of the primary energy. In this analysis $\log_{10}(S_{125})$ values between 0.4 and 2 are used, which roughly corresponds to a primary energy range from 2.5 PeV to 100 PeV. The slope of the lateral distribution function is mainly influenced by the age of the shower and the number of muons in a muon energy range around 1 GeV, while the in-ice measurements are correlated to the multiplicity of muons with an energy exceeding 400 GeV. Therefore, the two observables result in an independent reconstruction of the primary mass. This mass sensitivity arises from the increase of the muon number, over almost the entire muon energy range, with the mass of the primary cosmic ray. The produced muon spectra furthermore differ among the used hadronic interaction model. The dependence of the two mass sensitive observables to different parts of the muon spectra thus also provides the possibility to check the internal consistency of the models.

When the composition reconstruction with IceTop and IceCube is compared, simulations performed with Sibyll 2.3 and QGSJet-II.04 show an internal consistency. The pre-LHC model Sibyll 2.1 would result in a heavier composition obtained with IceTop as compared to IceCube, which is due to the (known) fact that it produces too few GeV muons. This GeV muon number was increased in the post-LHC models. Simulations ran with the EPOS-LHC model result in the highest number of GeV muons. The high-energy muon multiplicity in EPOS-LHC is however lower with regard to the other models, which also results in

a disagreement of the composition measurement between the IceTop surface array and the deep IceCube detector. Therefore, most satisfying results are obtained with the Sibyll 2.3 and QGSJet-II.04 models. All hadronic models result in a rising composition measurement with both variables in the energy range under study.
This specific analysis can hopefully be updated soon to higher energies. By doing so, the different composition result obtained with IceCube as compared to the other experiments can be investigated and the hadronic interaction models can be scrutinized at energies above the one reached at accelerator facilities.
Generally, from this study the conclusion is drawn that one has to be cautious when an observable, related by simulations to the properties of the primary particle, is used for a composition reconstruction. This is of course all one can do, but it should be kept in mind that a different observable could result in a varying result of the primary mass. With the type of analysis performed here we can point to problems within certain hadronic interaction models, as is also done before by other experiments.

Thanks to the strong rise of new technologies, indirect cosmic ray experiments gained enormous accuracy during the last decades. With the resolution that is now achieved, it seems that the hadronic interaction models are currently the bottleneck to obtain a more detailed view of the composition of cosmic rays. With this in mind it is important that observatories have started to include a large variety of experimental measurement techniques. The results of the combined measurements will keep providing input to the models that describe the highest energetic particle collisions on Earth. As such, 65 years after the conclusion of Leprince-Ringuet concerning the interplay between particle and cosmic ray physics and the importance of further cosmic ray studies, it still seems valid: *But probably this point of view should be tempered by the fact that we have the uniqueness of some phenomena, quite rare it is true, for which the energies are much larger*.
Interesting times lie ahead in astroparticle physics, to further explore the extreme universe.

Appendix A

Monthly atmosphere parameters for simulations

Table A.1: January

Layer i	Height (km)	a_i	b_i	c_i
1	2.835-7.800	-91.69560000	1125.710	821621
2	7.800-16.400	7.01491000	1149.810	635444
3	16.400-40.400	0.50545200	1032.680	682968
4	40.400-100.000	-0.00181302	490.789	807327
5	100.000-112.800	0.00207722	1.000	5430320300

Table A.2: February

Layer i	Height (km)	a_i	b_i	c_i
1	2.835-8.000	-72.19880000	1108.190	786271
2	8.000-10.600	22.70020000	1159.770	599986
3	10.600-40.400	0.43017100	1079.250	667432
4	40.400-100.000	-0.00120300	523.956	780919
5	100.000-112.800	0.00207722	1.000	5430320300

Table A.3: March

Layer i	Height (km)	a_i	b_i	c_i
1	2.835-6.700	-63.72900000	1102.660	764831
2	6.700-22.400	-1.02799000	1093.560	660389
3	22.400-40.400	0.32441400	1198.930	636118
4	40.400-100.000	-0.00049077	589.827	734909
5	100.000-112.800	0.00207722	1.000	5430320300

Table A.4: April

Layer i	Height (km)	a_i	b_i	c_i
1	2.835-7.600	-69.72590000	1111.700	766099
2	7.600-22.000	-2.79781000	1128.640	641716
3	22.000-40.400	0.26269200	1413.980	588082
4	40.400-100.000	-0.00008417	587.688	693300
5	100.000-112.800	0.00207722	1.000	5430320300

Table A.5: May

Layer i	Height (km)	a_i	b_i	c_i
1	2.835-8.400	-78.55510000	1118.460	776648
2	8.400-20.000	-5.33239000	1169.090	626683
3	20.000-39.700	0.31288900	1577.710	553087
4	39.700-100.000	-0.00009205	452.177	696835
5	100.000-112.800	0.00152236	1.000	7409569900

Table A.6: June

Layer i	Height (km)	a_i	b_i	c_i
1	2.835-8.500	-92.61250000	1129.880	791177
2	8.500-17.900	-8.56450000	1191.980	618840
3	17.900-38.400	0.36398600	1619.820	535235
4	38.400-100.000	0.00001652	411.586	692253
5	100.000-112.800	0.00207722	1.000	5430320300

Table A.7: July

Layer i	Height (km)	a_i	b_i	c_i
1	2.835-8.500	-89.96390000	1125.730	784553
2	8.500-15.900	-13.96970000	1180.470	628042
3	15.900-37.500	0.44163100	1581.430	531652
4	37.500-100.000	-0.00001465	373.796	703417
5	100.000-112.800	0.00207722	1.000	5430320300

Table A.8: August

Layer i	Height (km)	a_i	b_i	c_i
1	2.835-8.500	-90.42530000	1125.010	781628
2	8.500-14.400	-18.71540000	1175.600	633793
3	14.400-37.500	0.51393000	1518.030	533269
4	37.500-100.000	-0.00021565	299.006	737794
5	100.000-112.800	0.00152236	1.000	7409569900

Table A.9: September

Layer i	Height (km)	a_i	b_i	c_i
1	2.835-8.500	-91.68600000	1125.530	786017
2	8.500-13.000	-23.35190000	1169.770	645241
3	13.000-36.200	0.89130200	1431.260	545022
4	36.200-100.000	-0.00076567	247.030	805419
5	100.000-112.800	0.00207722	1.000	5430320300

Table A.10: October

Layer i	Height (km)	a_i	b_i	c_i
1	2.835-3.100	451.61600000	849.239	225286
2	3.100-10.100	-85.54560000	1113.160	789340
3	10.100-31.500	2.06082000	1322.280	566132
4	31.500-100.000	-0.00107600	372.242	796434
5	100.000-112.800	0.00207722	1.000	5430320300

Table A.11: November

Layer i	Height (km)	a_i	b_i	c_i
1	2.835-8.500	-152.85300000	1174.090	891602
2	8.500-22.400	4.22741000	1272.490	582119
3	22.400-32.400	1.38352000	975.906	643130
4	32.400-100.000	-0.00115014	481.615	783786
5	100.000-112.800	0.00207722	1.000	5430320300

Table A.12: December

Layer i	Height (km)	a_i	b_i	c_i
1	2.835-8.500	-100.38600000	1128.710	829352
2	8.500-22.000	5.43849000	1198.100	612649
3	22.000-40.400	0.39946500	858.522	706104
4	40.400-100.000	-0.00175472	480.142	806875
5	100.000-112.800	0.00207722	1.000	5430320300

Appendix B

Parameter shifts between hadronic models

In order to obtain a very rough estimation of alternative results with the post-LHC hadronic interaction models for the 3 year energy spectrum and composition analysis [144], the average shift of $\log 10(S_{125})$ and dE/dX_{1500} between the post-LHC models and Sibyll 2.1 were quantified. The fits are not used in the analysis presented in this thesis.

B.1 $\log_{10}(S_{125})$

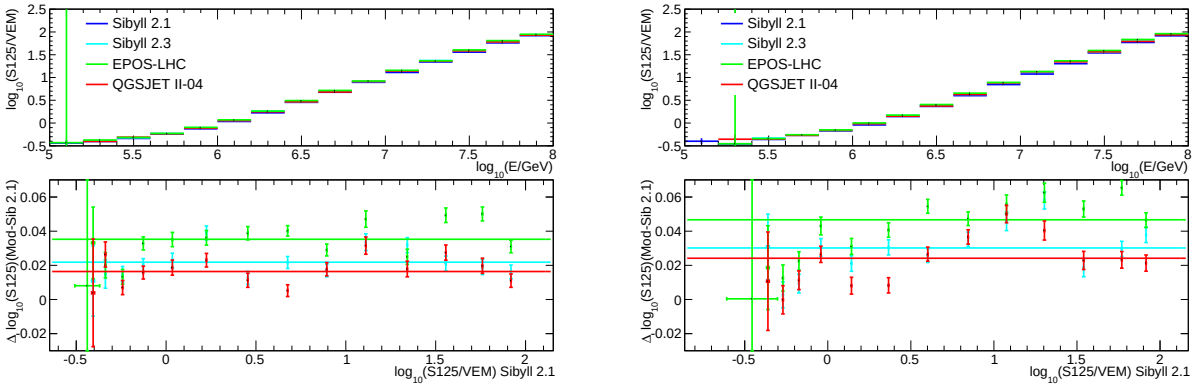

Figure B.1: $\log_{10}(S_{125})$ as function of the primary energy (top) for proton (left) and iron (right) initiated simulations. On the bottom panels the shift in $\log_{10}(S_{125})$ between the post-LHC hadronic models en Sibyll 2.1 is shown, as function of the $\log_{10}(S_{125})$ in using Sibyll 2.1.

In Figure B.1 the change in average $\log_{10}(S_{125})$ between the post-LHC hadronic models and Sibyll 2.1 is shown, as function the $\log_{10}(S_{125})$ obtained with Sibyll 2.1. Although the bin-to-bin variations are large, a constant function is fitted to these obtained shifts. The fit is performed for $0 < \log_{10}(S_{125})(\text{Sibyll 2.1}) < 2$. The obtained shifts are listed in Table B.1.

Table B.1: Average difference between the obtained $\log_{10}(S_{125})$ between the post-LHC hadronic models and Sibyll 2.1, for proton and iron initiated simulations. ($< \log_{10}(S125) >$(model)- $< \log_{10}(S125) >$(sibyll 2.1)

Post-LHC hadronic model	proton	iron
Sibyll 2.3	0.022	0.030
QGSJet-II.04	0.016	0.024
EPOS-LHC	0.035	0.047

B.2 dE/dX_{1500}

The shift of the average in-ice energy loss at a slant depth of 1500 m ($\log_{10}(dE/dX)1500$) is not obtained via a direct study of the difference within this variable between the hadronic interaction models. Instead, it is obtained via a study of the difference in the number of high-energy muons and the relation between the number of muons and the in-ice energy loss. This relation was defined in the study of the seasonal variations of the muon multiplicity [247].

The ratio of the muon multiplicity produced in simulations with post-LHC hadronic models with regard to Sibyll 2.1 is shown in Figure B.2, for proton and iron initiated showers in the energy range from 1 to 100 PeV. The dotted lines show a constant fit in this energy range, for the various hadronic interaction models.

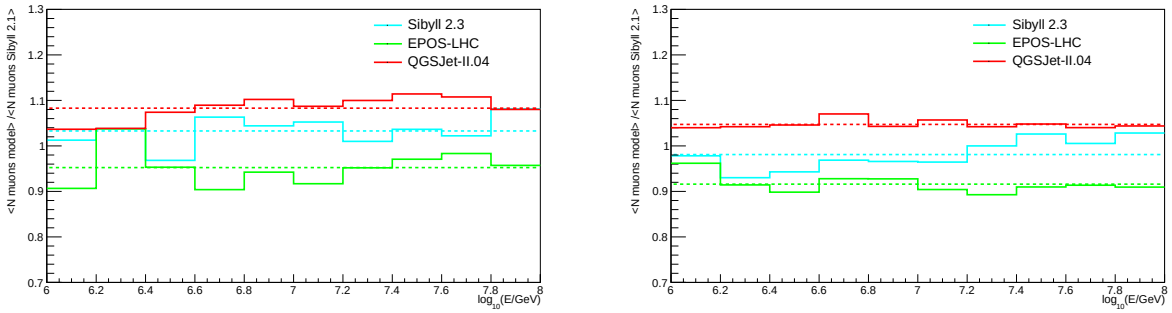

Figure B.2: Ratio of the high-energy muon multiplicity (> 400 GeV) in simulations using the post-LHC hadronic interaction models with respect to Sibyll 2.1, for proton (left) and iron (right) initiated air showers, as function of the primary energy. The dotted line indicates the constant fit to the histograms.

The fit results are listed in Table B.2.

Table B.2: Ratio between the average muon multiplicity produced with post-LHC hadronic models with regard to Sibyll 2.1, from the fit to the primary energy region from 1 PeV to 100 PeV (Figure B.2).

Post-LHC hadronic model	proton	iron
Sibyll 2.3	1.033	0.981
QGSJet-II.04	1.083	1.047
EPOS-LHC	0.952	0.916

The relation between the muon multiplicity $\log_{10}(N_\mu)$ and $\log_{10}(dE/dX)1500$ was found to be [247] for respectively proton and iron initiated showers:

$$\frac{dE}{dX_{1500}} = -0.202 + 0.937 * \log 10(N_\mu) \quad (\text{proton}) \tag{B.1}$$

$$\frac{dE}{dX_{1500}} = -0.028 + 0.894 * \log 10(N_\mu) \quad (\text{iron}) \tag{B.2}$$

As such, the in-ice energy loss can be converted to the number of muons using the (inverse of the) above relation. Then one can apply the correction factor for a certain hadronic model (and primary) as listed in Table B.2. This new muon multiplicity can then be again converted to $\log_{10}(dE/dX)1500$ using the above relation.

As such, one can -very roughly- estimate the influence of the post-LHC hadronic interaction models on, for example, a composition analysis using the high-energy muon bundles.

Bibliography

[1] K. G. Jansky, "Electrical Disturbances Apparently Of Extraterrestrial Origin,".

[2] S. Lafebre, "Cosmic ray flux versus particle energy." https://commons.wikimedia.org/wiki/File:Cosmic_ray_flux_versus_particle_energy.svg.

[3] T. Gaisser, R. Engel, and E. Resconi, *Cosmic Rays and Particle Physics*. Cambridge University Press, 2 ed., 2016.

[4] T. K. Gaisser, T. Stanev, and S. Tilav, "Cosmic Ray Energy Spectrum from Measurements of Air Showers," *Front. Phys.(Beijing)* **8** (2013) 748–758, arXiv:1303.3565 [astro-ph.HE].

[5] T. K. Gaisser and T. Stanev, "High-energy cosmic rays," *Nuclear Physics A* **777** (2006) 98 – 110. http://www.sciencedirect.com/science/article/pii/S0375947405000540.

[6] C. A. Coulomb, *Mémoires sur l'électricité et la magnétisme*. Académie Royale du Sciences, 1789.

[7] V. Hess, "Über Beobachtungen der durchdringenden Strahlung bei sieben Freiballonfahrten.," *Z. Phys.* **XIII** (1912) 1084–1091.

[8] A. D. Angelis, "Cosmic rays: Increase of ionization with height as measured by Hess in 1912 and by Kolhörster in 1913 and 1914." https://commons.wikimedia.org/wiki/File:HessKol.jpg.

[9] B. Rossi, "On the Magnetic Deflection of Cosmic Rays," *Phys. Rev.* **36** (Aug, 1930) 606–606. https://link.aps.org/doi/10.1103/PhysRev.36.606.

[10] B. Rossi, "Misura sulla distribuzione angolare di intensia della radiazione penetrante all' Asmara," *Supplemento a la Ricerca Scientifica* **1** (1934) 579.

[11] P. Auger, P. Ehrenfest, R. Maze, J. Daudin, Robley, and A. Fréon, "Extensive Cosmic-Ray Showers," *Rev. Mod. Phys.* **11** (1939) 288–291.

[12] C. D. Anderson, "The apparant existence of easily deflectable positives," *Science* **76** no. 1967, (1932) 238–239. http://science.sciencemag.org/content/76/1967/238.

[13] S. H. Neddermeyer and C. D. Anderson, "Note on the nature of cosmic-ray particles," *Phys. Rev.* **51** (May, 1937) 884–886. https://link.aps.org/doi/10.1103/PhysRev.51.884.

[14] H. Yukawa, "On the Interaction of Elementary Particles I," *Proc. Phys. Math. Soc. Jap.* **17** (1935) 48–57. [Prog. Theor. Phys. Suppl.1,1(1935)].

[15] G. D. Rochester and C. C. Butler, "Evidence for the Existence of New Unstable Elementary Particles," *Nature* **160** (1947) 855–857.

[16] J. W. Cronin, "The 1953 Cosmic Ray Conference at Bagnères de Bigorre: the Birth of Sub Atomic Physics," *The European Physical Journal H* **36** no. 2, (2011) 183.

[17] **Super-Kamiokande** Collaboration, Y. Fukuda *et al.*, "Evidence for oscillation of atmospheric neutrinos," *Phys. Rev. Lett.* **81** (1998) 1562–1567, arXiv:hep-ex/9807003 [hep-ex].

[18] W. Baade and F. Zwicky, "On Super-novae," *Proceedings of the National Academy of Science* **20** (May, 1934) 254–259.

[19] W. Baade and F. Zwicky, "Cosmic Rays from Super-Novae," *Proceedings of the National Academy of Sciences* **20** no. 5, (1934) 259–263, % ttfamily http://www.pnas.org/content/20/5/259.full.pdf. http://www.pnas.org/content/20/5/259.short.

[20] J. A. Simpson and M. Garcia-Munoz, "Cosmic-ray lifetime in the galaxy: Experimental results and models," *Space Science Reviews* **46** no. 3, (1988) 205–224. http://dx.doi.org/10.1007/BF00212240.

[21] V. L. Ginzburg and S. I. Syrovatsky, "Origin of Cosmic Rays," *Progress of Theoretical Physics Supplement* **20** (1961) 1. +http://dx.doi.org/10.1143/PTPS.20.1.

[22] E. Fermi, "On the Origin of the Cosmic Radiation," *Phys. Rev.* **75** (Apr, 1949) 1169–1174. https://link.aps.org/doi/10.1103/PhysRev.75.1169.

[23] P. O. Lagage and C. J. Cesarsky, "The maximum energy of cosmic rays accelerated by supernova shocks," *Astronomy and Astrophysics* **125** (Sept., 1983) 249–257.

[24] A. R. Bell, "Turbulent amplification of magnetic field and diffusive shock acceleration of cosmic rays," *Monthly Notices of the Royal Astronomical Society* **353** (Sept., 2004) 550–558.

[25] **Fermi-LAT** Collaboration, M. Ackermann *et al.*, "Detection of the Characteristic Pion-Decay Signature in Supernova Remnants," *Science* **339** (2013) 807, arXiv:1302.3307 [astro-ph.HE].

[26] **IceCube** Collaboration, M. G. Aartsen *et al.*, "Neutrinos and Cosmic Rays Observed by IceCube," arXiv:1701.03731 [astro-ph.HE].

[27] A. M. Hillas, "The Origin of Ultra-High-Energy Cosmic Rays," *Annual review of astronomy and astrophysics* **22** (1984) 425–444.

[28] Felicia Krauß after Urry and Padovani (1995). https://staff.fnwi.uva.nl/f.s.l.krauss/resources.html.

[29] C. M. Urry and P. Padovani, "Unified Schemes for Radio-Loud Active Galactic Nuclei," *Publications of the Astronomical Society of the Pacific* **107** (Sept., 1995) 803, astro-ph/9506063.

[30] European Southern Observatory, "Centaurus A." http://www.eso.org/public/images/eso0903a.

[31] K. Kotera and A. V. Olinto, "The Astrophysics of Ultrahigh Energy Cosmic Rays," *Ann. Rev. Astron. Astrophys.* **49** (2011) 119–153.

[32] M. J. Hardcastle, "Which radio galaxies can make the highest energy cosmic rays?," *Monthly Notices of the Royal Astronomical Society* **405** no. 4, (2010) 2810. +http://dx.doi.org/10.1111/j.1365-2966.2010.16668.x.

[33] M. Kachelriess, S. Ostapchenko, and R. Tomas, "High energy radiation from Centaurus A," *New J. Phys.* **11** (2009) 065017, arXiv:0805.2608 [astro-ph].

[34] B. Peters, "Primary cosmic radiation and extensive air showers," *Il Nuovo Cimento (1955-1965)* **22** no. 4, (1961) 800–819. http://dx.doi.org/10.1007/BF02783106.

[35] C. J. Cesarsky, "Cosmic-ray confinement in the galaxy," *Annual review of astronomy and astrophysics* **18** (1980) 289–319.

[36] **AMS Collaboration** Collaboration, M. Aguilar *et al.*, "Precision Measurement of the Boron to Carbon Flux Ratio in Cosmic Rays from 1.9 GV to 2.6 TV with the Alpha Magnetic Spectrometer on the International Space Station," *Phys. Rev. Lett.* **117** (Nov, 2016) 231102. https://link.aps.org/doi/10.1103/PhysRevLett.117.231102.

[37] P. Blasi, "Origin of Galactic Cosmic Rays," *Nuclear Physics B - Proceedings Supplements* **239-240** (2013) 140 – 147. http://www.sciencedirect.com/science/article/pii/S0920563213004003.

[38] **IceCube** Collaboration, M. G. Aartsen *et al.*, "Observation of Cosmic Ray Anisotropy with the IceTop Air Shower Array," *Astrophys. J.* **765** (2013) 55, arXiv:1210.5278 [astro-ph.HE].

[39] V. L. Ginzburg, Y. M. Khazan, and V. S. Ptuskin, "Origin of cosmic rays: Galactic models with halo," *Astrophysics and Space Science* **68** no. 2, (1980) 295–314. http://dx.doi.org/10.1007/BF00639701.

[40] P. Blasi and E. Amato, "Diffusive propagation of cosmic rays from supernova remnants in the Galaxy. II: anisotropy," *JCAP* **1201** (2012) 011, arXiv:1105.4529 [astro-ph.HE].

[41] K. Greisen, "End of the Cosmic-Ray Spectrum?," *Phys. Rev. Lett.* **16** (1966) 748–750.

[42] G. T. Zatsepin and V. A. Kuz'min, "Upper Limit of the Spectrum of Cosmic Rays," *J. Exp. Theor. Phys. Lett.* **4** (1966) 78–80.

[43] R. Aloisio, V. Berezinsky, and S. Grigorieva, "Analytic calculations of the spectra of ultra-high energy cosmic ray nuclei. I. The case of CMB radiation," *Astropart. Phys.* **41** (2013) 73–93, arXiv:0802.4452 [astro-ph].

[44] **ANTARES** Collaboration, E. Aslanides *et al.*, "A deep sea telescope for high-energy neutrinos," arXiv:astro-ph/9907432 [astro-ph].

[45] S. Adrin-Martnez *et al.*, "Letter of intent for km3net 2.0," *Journal of Physics G: Nuclear and Particle Physics* **43** no. 8, (2016) 084001. http://stacks.iop.org/0954-3899/43/i=8/a=084001.

[46] **Baikal-GVD** Collaboration, A. D. Avrorin *et al.*, "Baikal-GVD: status and prospects," *EPJ Web Conf.* **191** (2018) 01006, arXiv:1808.10353 [astro-ph.IM].

[47] **AMANDA** Collaboration, E. Andres *et al.*, "The AMANDA Neutrino Telescope: Principle of Operation and First Results," *APP* **13** (2000) 1–20, astro-ph/9906203.

[48] **AMANDA** Collaboration, E. Andres *et al.*, "Observation of high-energy neutrinos using Cherenkov detectors embedded deep in Antarctic ice," *Nature* **410** (2001) 441–443.

[49] P. A. Čerenkov, "Visible Radiation Produced by Electrons Moving in a Medium with Velocities Exceeding that of Light," *Phys. Rev.* **52** (Aug, 1937) 378–379. https://link.aps.org/doi/10.1103/PhysRev.52.378.

[50] I. M. Frank and I. E. Tamm, "Kogerentnoe izluchenie bystrogo elektrona v srede ("the coherent radiation of a fast electron in a medium")," *Dokl. Akad. Nauk. SSSR* **14** (1937) 107.

[51] J. V. Jelley, *Cerenkov radiation and its applications*, vol. 6. 07, 1955.

[52] C. Spiering, "Towards High-Energy Neutrino Astronomy. A Historical Review," *Eur. Phys. J.* **H37** (2012) 515–565, arXiv:1207.4952 [astro-ph.IM].

[53] P. H. Barrett, L. M. Bollinger, G. Cocconi, Y. Eisenberg, and K. Greisen, "Interpretation of Cosmic-Ray Measurements Far Underground," *Rev. Mod. Phys.* **24** (Jul, 1952) 133–178. https://link.aps.org/doi/10.1103/RevModPhys.24.133.

[54] **IceCube** Collaboration, R. Abbasi *et al.*, "IceTop: The surface component of IceCube," *Nucl. Instrum. Meth.* **A700** (2013) 188–220, arXiv:1207.6326 [astro-ph.IM].

[55] **IceCube** Collaboration, R. Abbasi *et al.*, "Calibration and Characterization of the IceCube Photomultiplier Tube," *Nucl. Instrum. Meth.* **A618** (2010) 139–152, arXiv:1002.2442 [astro-ph.IM].

[56] **IceCube** Collaboration, M. Aartsen *et al.*, "The IceCube Neutrino Observatory: instrumentation and online systems," *Journal of Instrumentation* **12** no. 03, (2017) P03012. http://stacks.iop.org/1748-0221/12/i=03/a=P03012.

[57] **IceCube** Collaboration, R. Abbasi *et al.*, "The IceCube Data Acquisition System: Signal Capture, Digitization, and Timestamping," *Nucl. Instrum. Meth.* **A601** (2009) 294–316, arXiv:0810.4930 [physics.ins-det].

[58] R. C. Bay *et al.*, "South Pole paleowind from automated synthesis of ice core records," *J. Geophys. Res.* **115** (2010) D14126.

[59] **IceCube** Collaboration, M. G. Aartsen *et al.*, "Measurement of South Pole ice transparency with the IceCube LED calibration system," *Nucl. Instrum. Meth.* **A711** (2013) 73–89, arXiv:1301.5361 [astro-ph.IM].

[60] G. Mie, "Beiträge zur Optik trüber Medien, speziell kolloidaler Metallösungen," *Annalen der Physik* **330** (1908) 377–445.

[61] P. B. Price, K. Woschnagg, and D. Chirkin, "Age vs depth of glacial ice at South Pole," *Geophysical Research Letters* **27** no. 14, (2000) 2129–2132. http://dx.doi.org/10.1029/2000GL011351.

[62] M. Rongen, "Measuring the optical properties of IceCube drill holes," in *European Physical Journal Web of Conferences*, vol. 116 of *European Physical Journal Web of Conferences*, p. 06011. Apr., 2016.

[63] **IceCube** Collaboration, V. Baum, D. Heereman, and R. Bruijn, "An improved data acquisition system for supernova detection with IceCube," in *Proceedings, 33rd International Cosmic Ray Conference (ICRC2013): Rio de Janeiro, Brazil, July 2-9, 2013*, p. 0444. http://www.cbpf.br/%7Eicrc2013/papers/icrc2013-0444.pdf.

[64] G. de Wasseige, P. Evenson, K. Hanson, N. van Eijndhoven, and K.-L. Klein, "Evaluation of expected solar flare neutrino events in the IceCube observatory," in *Proceedings, 34th International Cosmic Ray Conference (ICRC 2015): The Hague, The Netherlands, July 30-August 6, 2015*, vol. ICRC2015, p. 1049. 2016.

[65] **IceCube** Collaboration, M. G. Aartsen *et al.*, "Energy Reconstruction Methods in the IceCube Neutrino Telescope," *JINST* **9** (2014) P03009, arXiv:1311.4767 [physics.ins-det].

[66] **IceCube** Collaboration, J. Kiryluk, M. V. D'Agostino, S. R. Klein, C. Song, and D. R. Williams, "IceCube performance with artificial light sources: The road to cascade analyses," in *Proceedings, 30th International Cosmic Ray Conference (ICRC 2007): Merida, Yucatan, Mexico, July 3-11, 2007*, vol. 3, pp. 1233–1236. 2007.

[67] **IceCube** Collaboration, M. G. Aartsen *et al.*, "First observation of PeV-energy neutrinos with IceCube," *Phys. Rev. Lett.* **111** (2013) 021103, arXiv:1304.5356 [astro-ph.HE].

[68] **IceCube** Collaboration, M. G. Aartsen *et al.*, "Evidence for High-Energy Extraterrestrial Neutrinos at the IceCube Detector," *Science* **342** (2013) 1242856, arXiv:1311.5238 [astro-ph.HE].

[69] **IceCube** Collaboration, M. G. Aartsen *et al.*, "Observation of High-Energy Astrophysical Neutrinos in Three Years of IceCube Data," *Phys. Rev. Lett.* **113** (2014) 101101, arXiv:1405.5303 [astro-ph.HE].

[70] **IceCube** Collaboration, M. G. Aartsen *et al.*, "Atmospheric and astrophysical neutrinos above 1 TeV interacting in IceCube," *Phys. Rev.* **D91** no. 2, (2015) 022001, arXiv:1410.1749 [astro-ph.HE].

[71] **IceCube** Collaboration, M. G. Aartsen *et al.*, "The IceCube Neutrino Observatory - Contributions to ICRC 2015 Part II: Atmospheric and Astrophysical Diffuse Neutrino Searches of All Flavors," in *Proceedings, 34th International Cosmic Ray Conference (ICRC 2015): The Hague, The Netherlands, July 30-August 6, 2015*. 2015. arXiv:1510.05223 [astro-ph.HE]. https://inspirehep.net/record/1398539/files/arXiv:1510.05223.pdf.

[72] **IceCube** Collaboration, M. G. Aartsen *et al.*, "Observation and Characterization of a Cosmic Muon Neutrino Flux from the Northern Hemisphere using six years of IceCube data," *Astrophys. J.* **833** no. 1, (2016) 3, arXiv:1607.08006 [astro-ph.HE].

[73] **IceCube** Collaboration, M. G. Aartsen *et al.*, "Neutrinos and Cosmic Rays Observed by IceCube," arXiv:1701.03731 [astro-ph.HE].

[74] **IceCube** Collaboration, M. G. Aartsen *et al.*, "All-sky search for time-integrated neutrino emission from astrophysical sources with 7 years of IceCube data," *Astrophys. J.* **835** no. 2, (2017) 151, arXiv:1609.04981 [astro-ph.HE].

[75] **Liverpool Telescope, MAGIC, H.E.S.S., AGILE, Kiso, VLA/17B-403, INTEGRAL, Kapteyn, Subaru, HAWC, Fermi-LAT, ASAS-SN, VERITAS, Kanata, IceCube, Swift NuSTAR** Collaboration, M. G. Aartsen *et al.*, "Multimessenger observations of a flaring blazar coincident with high-energy neutrino IceCube-170922A," *Science* **361** no. 6398, (2018) eaat1378, arXiv:1807.08816 [astro-ph.HE].

[76] **IceCube** Collaboration, M. G. Aartsen *et al.*, "Neutrino emission from the direction of the blazar TXS 0506+056 prior to the IceCube-170922A alert," *Science* **361** no. 6398, (2018) 147–151, arXiv:1807.08794 [astro-ph.HE].

[77] **IceCube** Collaboration, M. G. Aartsen *et al.*, "Measurement of the Atmospheric ν_e Spectrum with IceCube," *Phys. Rev.* **D91** (2015) 122004, arXiv:1504.03753 [astro-ph.HE].

[78] **Super-Kamiokande** Collaboration, Y. Fukuda *et al.*, "Evidence for oscillation of atmospheric neutrinos," *Phys. Rev. Lett.* **81** (1998) 1562–1567, arXiv:hep-ex/9807003 [hep-ex].

[79] **IceCube** Collaboration, M. G. Aartsen *et al.*, "Determining neutrino oscillation parameters from atmospheric muon neutrino disappearance with three years of IceCube DeepCore data," *Phys. Rev.* **D91** no. 7, (2015) 072004, arXiv:1410.7227 [hep-ex].

[80] **IceCube** Collaboration, M. G. Aartsen *et al.*, "First search for dark matter annihilations in the Earth with the IceCube Detector," *Eur. Phys. J.* **C77** no. 2, (2017) 82, arXiv:1609.01492 [astro-ph.HE].

[81] **IceCube** Collaboration, M. G. Aartsen *et al.*, "Search for annihilating dark matter in the Sun with 3 years of IceCube data," arXiv:1612.05949 [astro-ph.HE].

[82] **IceCube** Collaboration, M. G. Aartsen *et al.*, "IceCube-Gen2: A Vision for the Future of Neutrino Astronomy in Antarctica," arXiv:1412.5106 [astro-ph.HE].

[83] **IceCube-Gen2** Collaboration, T. Huber, J. Kelley, S. Kunwar, and D. Tosi, "The IceTop Scintillator Upgrade," *PoS* **ICRC2017** (2017) 401.

[84] National Space Science Data Center, NSSDC, NASA, "Earth Fact Sheet." http://nssdc.gsfc.nasa.gov/planetary/factsheet/earthfact.html.

[85] B. Keilhauer, "Atmosphere Physics, Fluorescence Light and Atmospheres in CORSIKA,". CORSIKA school.

[86] M. E. Wieser and T. B. Coplen, "Atomic weights of the elements 2009 (IUPAC Technical Report)," *Pure. Appl. Chem.* **83** (2011) 359–396.

[87] Space Science and Engineering Center, UW-Madison, "Antarctic meteorological research center and automatic weather stations project." https://amrc.ssec.wisc.edu/.

[88] NASA, "Atmospheric Infrared Sounder." https://airs.jpl.nasa.gov/.

[89] Johannes Knapp and Fabian Schmidt, "CORSIKA shower images: Proton showers." https://www-zeuthen.desy.de/~jknapp/fs/proton-showers.html.

[90] **Pierre Auger** Collaboration, P. Abreu *et al.*, "Measurement of the proton-air cross-section at $\sqrt{s} = 57$ TeV with the Pierre Auger Observatory," *Phys. Rev. Lett.* **109** (2012) 062002, arXiv:1208.1520 [hep-ex].

[91] G. D. Westfall, L. W. Wilson, P. J. Lindstrom, H. J. Crawford, D. E. Greiner, and H. H. Heckman, "Fragmentation of relativistic Fe-56," *Phys. Rev.* **C19** (1979) 1309–1323.

[92] P. Grieder, *Extensive air showers*. Springer, 1 ed., 2010.

[93] W. Heitler, *Quantum Theory of Radiation*. Oxford: Oxford Univ. Press. 2nd ed., 1944.

[94] *Review of Particle Physics*. Particle Data Group, 2010.

[95] R. Ulrich, J. Blumer, R. Engel, F. Schussler, and M. Unger, "On the measurement of the proton-air cross section using air shower data," *New J. Phys.* **11** (2009) 065018, arXiv:0903.0404 [astro-ph.HE].

[96] J. Matthews, "A Heitler model of extensive air showers," *Astropart. Phys.* **22** (2005) 387–397.

[97] T. K. Gaisser and A. M. Hillas, "Reliability of the method of constant intensity cuts for reconstructing the average development of vertical showers," *International Cosmic Ray Conference* **8** (1977) 353–357.

[98] D. Heck *et al.*, "CORSIKA: A monte carlo code to simulate extensive air showers," tech. rep., 1998.

[99] D. Heck, "Influence of hadronic interaction models on simulated showers: a phenomenological comparison," CORSIKA school 2008. https://web.ikp.kit.edu/corsika/corsika-school2008/program.htm.

[100] E.-J. Ahn, R. Engel, T. K. Gaisser, P. Lipari, and T. Stanev, "Cosmic ray interaction event generator SIBYLL 2.1," *Phys. Rev. D* **80** (Nov, 2009) 094003.

[101] T. Feusels, *Measurement of cosmic ray composition and energy spectrum between 1PeV and 1EeV with IceTop and IceCube.* PhD thesis, Ghent University, 2013.

[102] J. W. Elbert, "Multiple muons produced by cosmic ray interactions," in *Proc., DUMAND Summer Workshop*, vol. 2, pp. 101–119, La Jolla, CA. 1978.

[103] T. K. Gaisser and T. Stanev, "Muon bundles in underground detectors," *Nucl. Instrum. Meth.* **A235** (1985) 183–192.

[104] K. Greisen, "Cosmic ray showers," *Ann. Rev. Nucl. Sci.* **10** (1960) 63–108.

[105] K. Kamata and J. Nishimura, "The Lateral and the Angular Structure Functions of Electron Showers," *Progress of Theoretical Physics Supplement* **6** (1958) 93–155.

[106] K.-H. Kampert, A. A. Watson, and A. A. Watson, "Extensive Air Showers and Ultra High-Energy Cosmic Rays: A Historical Review," *Eur. Phys. J.* **H37** (2012) 359–412, `arXiv:1207.4827 [physics.hist-ph]`.

[107] H. E. Bergeson, J. C. Boone, and G. L. Cassiday, "The Fly's Eye. A Novel Technique for Sensing Extensive Air Showers," *International Cosmic Ray Conference* **8** (Aug., 1975) 3059.

[108] **PIERRE AUGER** Collaboration, M. J. Tueros, "Estimate of the non-calorimetric energy of showers observed with the fluorescence and surface detectors of the Pierre Auger Observatory," in *Proceedings, 33rd International Cosmic Ray Conference (ICRC2013): Rio de Janeiro, Brazil, July 2-9, 2013*, p. 0705.

[109] A. M. Hillas, "The sensitivity of Cerenkov radiation pulses to the longitudinal development of cosmic-ray showers," *Journal of Physics G: Nuclear Physics* **8** no. 10, (1982) 1475. `http://stacks.iop.org/0305-4616/8/i=10/a=017`.

[110] T. Huege, "The renaissance of radio detection of cosmic rays," *Braz. J. Phys.* **44** (2014) 520–529, `arXiv:1310.6927 [astro-ph.IM]`.

[111] **AMS Collaboration** Collaboration, "Precision Measurement of the Proton Flux in Primary Cosmic Rays from Rigidity 1 GV to 1.8 TV with the Alpha Magnetic Spectrometer on the International Space Station," *Phys. Rev. Lett.* **114** (Apr, 2015) 171103. `https://link.aps.org/doi/10.1103/PhysRevLett.114.171103`.

[112] **AMS** Collaboration, M. Aguilar *et al.*, "Observation of the Identical Rigidity Dependence of He,C, and O Cosmic Rays at High Rigidities by the Alpha Magnetic Spectrometer on the International Space Station," *Phys. Rev. Lett.* **119** no. 25, (2017) 251101.

[113] **AMS** Collaboration, M. Aguilar *et al.*, "Observation of New Properties of Secondary Cosmic Rays Lithium, Beryllium, and Boron by the Alpha Magnetic Spectrometer on the International Space Station," *Phys. Rev. Lett.* **120** no. 2, (2018) 021101.

[114] H. S. Ahn *et al.*, "Discrepant hardening observed in cosmic-ray elemental spectra," *Astrophys. J.* **714** (2010) L89–L93, `arXiv:1004.1123 [astro-ph.HE]`.

[115] "Cosmic Ray Energetics And Mass for the International Space Station (ISS-CREAM)," *Advances in Space Research* **53** no. 10, (2014) 1451 – 1455.

[116] P. Maestro, "Cosmic rays: direct measurements," *PoS* **ICRC2015** (2016) 016, arXiv:1510.07683 [astro-ph.HE]. [34,16(2015)].

[117] A. M. Galper *et al.*, "The PAMELA experiment: a decade of Cosmic Ray Physics in space," *Journal of Physics: Conference Series* **798** no. 1, (2017) 012033. http://stacks.iop.org/1742-6596/798/i=1/a=012033.

[118] E. C. Stone *et al.*, "The advanced composition explorer," *AIP Conference Proceedings* **203** no. 1, (1990) 48–57.

[119] T. Guzik *et al.*, "The ATIC long duration balloon project," *Advances in Space Research* **33** no. 10, (2004) 1763 – 1770. http://www.sciencedirect.com/science/article/pii/S0273117703011566. The Next Generation in Scientific Ballooning.

[120] **ARGO-YBJ** Collaboration, G. Di Sciasco, "Measurement of the Cosmic Ray Energy Spectrum with ARGO-YBJ," in *Proceedings, Vulcano Workshop 2014: Frontier Objects in Astrophysics and Particle Physics: Vulcano, Italy, May 18-24, 2014*. 2014. arXiv:1408.6739 [astro-ph.HE]. https://inspirehep.net/record/1312743/files/arXiv:1408.6739.pdf.

[121] **HAWC** Collaboration, A. U. Abeysekara *et al.*, "The HAWC Gamma-Ray Observatory: Design, Calibration, and Operation," arXiv:1310.0074 [astro-ph.IM].

[122] **LHAASO** Collaboration, G. Di Sciascio, "The LHAASO experiment: from Gamma-Ray Astronomy to Cosmic Rays," *Nucl. Part. Phys. Proc.* **279-281** (2016) 166–173, arXiv:1602.07600 [astro-ph.HE].

[123] **GRAPES-3** Collaboration, S. K. Gupta *et al.*, "GRAPES-3: A high-density air shower array for studies on the structure in the cosmic-ray energy spectrum near the knee," *Nucl. Instrum. Meth.* **A540** (2005) 311–323.

[124] **H.E.S.S.** Collaboration, W. Hofmann, "The High Energy Stereoscopic System (HESS) project," *AIP Conf. Proc.* **515** no. 1, (2000) 500.

[125] C. Baixeras *et al.*, "Magic Phase II," *International Cosmic Ray Conference* **5** (2005) 227.

[126] V. Verzi, "Cosmic rays: air showers from low to high energies," *PoS* **ICRC2015** (2016) 015.

[127] **KASCADE** Collaboration, T. Antoni *et al.*, "KASCADE measurements of energy spectra for elemental groups of cosmic rays: Results and open problems," *Astropart. Phys.* **24** (2005) 1–25, arXiv:astro-ph/0505413 [astro-ph].

[128] **LOPES** Collaboration, H. Falcke *et al.*, "Detection and imaging of atmospheric radio flashes from cosmic ray air showers," *Nature* **435** (2005) 313–316, arXiv:astro-ph/0505383 [astro-ph].

[129] V. V. Prosin *et al.*, "Results from Tunka-133 (5 years observation) and from the Tunka-HiSCORE prototype," *EPJ Web Conf.* **121** (2016) 03004.

[130] **Tunka-Rex** Collaboration, P. A. Bezyazeekov *et al.*, "Radio measurements of the energy and the depth of the shower maximum of cosmic-ray air showers by Tunka-Rex," *JCAP* **1601** no. 01, (2016) 052, arXiv:1509.05652 [hep-ex].

[131] M. Amenomori *et al.*, "The All-Particle Spectrum of Primary Cosmic Rays in the Wide Energy Range from 1014 to 1017 eV Observed with the Tibet-III Air-Shower Array," *The Astrophysical Journal* **678** no. 2, (2008) 1165. http://stacks.iop.org/0004-637X/678/i=2/a=1165.

[132] A. A. Ivanov, S. P. Knurenko, and I. Y. Sleptsov, "Measuring extensive air showers with Cherenkov light detectors of the Yakutsk array: the energy spectrum of cosmic rays," *New Journal of Physics* **11** no. 6, (2009) 065008. http://stacks.iop.org/1367-2630/11/i=6/a=065008.

[133] **Pierre Auger** Collaboration, A. Aab *et al.*, "The Pierre Auger Cosmic Ray Observatory," *Nucl. Instrum. Meth.* **A798** (2015) 172–213, arXiv:1502.01323 [astro-ph.IM].

[134] **Telescope Array** Collaboration, T. Abu-Zayyad, "Cosmic Rays Energy Spectrum observed by the TALE detector using Cerenkov light," *PoS* **ICRC2015** (2016) 422.

[135] S. Buitink *et al.*, "A large light-mass component of cosmic rays at 10^{17} - $10^{17.5}$ eV from radio observations," *Nature* **531** (2016) 70, arXiv:1603.01594 [astro-ph.HE].

[136] T. Huege *et al.*, "Ultimate precision in cosmic-ray radio detection the SKA," *EPJ Web Conf.* **135** (2017) 02003, arXiv:1608.08869 [astro-ph.IM].

[137] G. Cataldi, "Towards AugerPrime: the upgrade of the Pierre Auger Observatory," *Nuclear and Particle Physics Proceedings* **291-293** (2017) 96 – 101. http://www.sciencedirect.com/science/article/pii/S240560141730398X. New eyes on the Universe CRIS 2016 Cosmic Rays International Seminars Proceedings of the Cosmic Rays International Seminars.

[138] "Latest results from the telescope array," *Nuclear Instruments and Methods in Physics Research Section A: Accelerators, Spectrometers, Detectors and Associated Equipment* **742** (2014) 29 – 34. 4th Roma International Conference on Astroparticle Physics.

[139] **IceCube** Collaboration, M. G. Aartsen *et al.*, "Measurement of the cosmic ray energy spectrum with IceTop-73," *Phys. Rev.* **D88** no. 4, (2013) 042004, arXiv:1307.3795 [astro-ph.HE].

[140] **KASCADE-Grande Collaboration** Collaboration, W. D. Apel *et al.*, "Kneelike Structure in the Spectrum of the Heavy Component of Cosmic Rays Observed with KASCADE-Grande," *Phys. Rev. Lett.* **107** (Oct, 2011) 171104. https://link.aps.org/doi/10.1103/PhysRevLett.107.171104.

[141] S. Knurenko, I. Petrov, Z. Petrov, and I. Sleptsov, "Mass Composition of Cosmic Rays of the energy region $10^{16} - 10^{18} eV$ by data the Small Cherenkov Array at Yakutsk. Comparison with other Arrays," *PoS* **ICRC2015** (2016) 254.

[142] **IceCube** Collaboration, T. Feusels and K. Rawlins, "Cosmic Ray Composition and Energy Spectrum between 2.5 PeV and 1 EeV with IceTop and IceCube," in *Proceedings, 33rd International Cosmic Ray Conference (ICRC2013): Rio de Janeiro, Brazil, July 2-9, 2013*, p. 0861. 2013. http://www.cbpf.br/%7Eicrc2013/papers/icrc2013-0861.pdf.

[143] **IceCube** Collaboration, K. Rawlins, "Cosmic ray spectrum and composition from three years of IceTop and IceCube," *J. Phys. Conf. Ser.* **718** no. 5, (2016) 052033.

[144] **IceCube** Collaboration, M. G. Aartsen *et al.*, "Cosmic Ray Spectrum and Composition from PeV to EeV Using 3 Years of Data From IceTop and IceCube." To appear.

[145] K.-H. Kampert, "Ultrahigh-Energy Cosmic Rays: Results and Prospects," *Braz. J. Phys.* **43** (2013) 375–382, arXiv:1305.2363 [astro-ph.HE].

[146] **IceCube** Collaboration, M. G. Aartsen *et al.*, "Characterization of the Atmospheric Muon Flux in IceCube," *Astropart. Phys.* **78** (2016) 1–27, arXiv:1506.07981 [astro-ph.HE].

[147] A. Porcelli, "Measurements of the first two moments of the depth of shower maximum over nearly three decades of energy, combining data from," *PoS* **ICRC2015** (2016) 420.

[148] **Telescope Array** Collaboration, J. Belz, "Summary of UHECR composition measurements by the Telescope Array Experiment," *PoS* **ICRC2015** (2016) 351.

[149] **Pierre Auger** Collaboration, A. Aab *et al.*, "Depth of maximum of air-shower profiles at the Pierre Auger Observatory. II. Composition implications," *Phys. Rev.* **D90** no. 12, (2014) 122006, arXiv:1409.5083 [astro-ph.HE].

[150] **Pierre Auger, Telescope Array** Collaboration, R. Abbasi *et al.*, "Report of the Working Group on the Composition of Ultra High Energy Cosmic Rays," *JPS Conf. Proc.* **9** (2016) 010016, arXiv:1503.07540 [astro-ph.HE].

[151] **HAWC** Collaboration, R. Alfaro *et al.*, "All-particle cosmic ray energy spectrum measured by the HAWC experiment from 10 to 500 TeV," *Phys. Rev.* **D96** no. 12, (2017) 122001, arXiv:1710.00890 [astro-ph.HE].

[152] G. Giacinti, M. Kachelrieß, D. V. Semikoz, and G. Sigl, "Cosmic ray anisotropy as signature for the transition from galactic to extragalactic cosmic rays," *JCAP* **7** (July, 2012) 031, arXiv:1112.5599 [astro-ph.HE].

[153] T. Gaisser, "Challenges for Cosmic-ray Experiments," *EPJ Web Conf.* **145** (2017) 18003, arXiv:1704.00788 [astro-ph.HE].

[154] H. P. Dembinski, R. Engel, A. Fedynitch, T. Gaisser, F. Riehn, and T. Stanev, "Data-driven model of the cosmic-ray flux and mass composition from 10 GeV to 10^{11} GeV," *PoS* **ICRC2017** (2017) 533, arXiv:1711.11432 [astro-ph.HE].

[155] Pierog, Tanguy, "Open issues in hadronic interactions for air showers," *EPJ Web Conf.* **145** (2017) 18002. https://doi.org/10.1051/epjconf/201614518002.

[156] **KASCADE-Grande** Collaboration, M. Bertaina *et al.*, "KASCADE-Grande energy spectrum of cosmic rays interpreted with post-LHC hadronic interaction models," *PoS* **ICRC2015** (2016) 359.

[157] **Pierre Auger** Collaboration, A. Aab *et al.*, "Testing Hadronic Interactions at Ultrahigh Energies with Air Showers Measured by the Pierre Auger Observatory," *Phys. Rev. Lett.* **117** no. 19, (2016) 192001, arXiv:1610.08509 [hep-ex].

[158] **Pierre Auger** Collaboration, A. Aab *et al.*, "Inferences on mass composition and tests of hadronic interactions from 0.3 to 100 EeV using the water-Cherenkov detectors of the Pierre Auger Observatory," *Phys. Rev.* **D96** no. 12, (2017) 122003, arXiv:1710.07249 [astro-ph.HE].

[159] **Pierre Auger** Collaboration, A. Aab *et al.*, "Muons in air showers at the Pierre Auger Observatory: Measurement of atmospheric production depth," *Phys. Rev.* **D90** no. 1, (2014) 012012, arXiv:1407.5919 [hep-ex]. [Erratum: Phys. Rev.D92,no.1,019903(2015)].

[160] J. C. Arteaga-Velzquez *et al.*, "Muon density measurements for the light and heavy mass groups of cosmic rays at the KASCADE-Grande observatory," *Nucl. Part. Phys. Proc.* **291-293** (2017) 152–157.

[161] W. R. Nelson, H. Hirayama, and D. W. O. Rogers, "The EGS4 code system," *Technical Report* **SLAC 265** (1985) . Stanford Linear Accelerator Center, http://www.slac.stanford.edu/pubs/slacreports/slac-r-265.hmtl.

[162] G. Battistoni *et al.*, "The FLUKA code: Description and benchmarking," *AIP Conference Proceeding* **896** (2007) 31–49.

[163] A. Ferrari, P. R. Sala, A. Fasso', and J. Ranft, "FLUKA: a multi-particle transport code," *CERN-2005-10* (2005) . INFN/TC_05/11, SLAC-R-773.

[164] A. M. Hillas, "Shower simulation: Lessons from MOCCA," *Nucl. Phys. Proc. Suppl.* **52B** (1997) 29–42. [,29(1997)].

[165] J. Madsen and A. Tamburro, "Simulating UHE cosmic-ray showers in IceTop." Internal Report, 2009.

[166] **ATLAS** Collaboration, G. Aad *et al.*, "The ATLAS Experiment at the CERN Large Hadron Collider," *JINST* **3** (2008) S08003.

[167] **CMS** Collaboration, S. Chatrchyan *et al.*, "The CMS Experiment at the CERN LHC," *JINST* **3** (2008) S08004.

[168] K. Kawade *et al.*, "The performance of the LHCf detector for hadronic showers," *Journal of Instrumentation* **9** no. 03, (2014) P03016. http://stacks.iop.org/1748-0221/9/i=03/a=P03016.

[169] **TOTEM** Collaboration, G. Anelli *et al.*, "The TOTEM experiment at the CERN Large Hadron Collider," *JINST* **3** (2008) S08007.

[170] F. Riehn, H. P. Dembinski, R. Engel, A. Fedynitch, T. K. Gaisser, and T. Stanev, "The hadronic interaction model SIBYLL 2.3c and Feynman scaling," *PoS* **ICRC2017** (2017) 301, arXiv:1709.07227 [hep-ph].

[171] S. Ostapchenko, "Monte Carlo treatment of hadronic interactions in enhanced Pomeron scheme: I. QGSJET-II model," *Phys. Rev.* **D83** (2011) 014018, arXiv:1010.1869 [hep-ph].

[172] T. Pierog, I. Karpenko, J. M. Katzy, E. Yatsenko, and K. Werner, "EPOS LHC: Test of collective hadronization with data measured at the CERN Large Hadron Collider," *Phys. Rev.* **C92** no. 3, (2015) 034906, arXiv:1306.0121 [hep-ph].

[173] Ostapchenko, Sergey, "Cosmic Ray Interaction Models: an Overview," *EPJ Web of Conferences* **120** (2016) 04003. https://doi.org/10.1051/epjconf/201612004003.

[174] T. Pierog, "Air Shower Simulation with a New Generation of post-LHC Hadronic Interaction Models in CORSIKA.," *PoS* **ICRC2017** (2017) 1100.

[175] V. N. Gribov, "A REGGEON DIAGRAM TECHNIQUE," *Sov. Phys. JETP* **26** (1968) 414–422. [Zh. Eksp. Teor. Fiz.53,654(1967)].

[176] H. J. Drescher, M. Hladik, S. Ostapchenko, T. Pierog, and K. Werner, "Parton based Gribov-Regge theory," *Phys. Rept.* **350** (2001) 93–289, arXiv:hep-ph/0007198 [hep-ph].

[177] K. Werner, T. Hirano, I. Karpenko, T. Pierog, S. Porteboeuf, M. Bleicher, and S. Haussler, "Gribov-Regge theory, partons, remnants, strings and the EPOS model for hadronic interactions,".

[178] **NA61/SHINE** Collaboration, M. Unger, "Results from NA61/SHINE," *EPJ Web Conf.* **52** (2013) 01009, arXiv:1305.5281 [nucl-ex].

[179] S. Ostapchenko, "Nonlinear screening effects in high energy hadronic interactions," *Phys. Rev. D* **74** (2006) 014026.

[180] S. Ostapchenko, "QGSJET-II: Towards reliable description of very high energy hadronic interactions," *Nucl. Phys. Proc. Suppl.* **151** (2006) 143–146.

[181] S. Ostapchenko, "Status of QGSJET," *AIP Conference Proceeding* **928** (2007) 118–125.

[182] K. Werner, F.-M. Liu, and T. Pierog, "Parton ladder splitting and the rapidity dependence of transverse momentum spectra in deuteron-gold collisions at the BNL Relativistic Heavy Ion Collider," *Phys. Rev. C* **74** (2006) 044902.

[183] T. Pierog and K. Werner, "EPOS Model and Ultra High Energy Cosmic Rays," *Nucl. Phys. Proc. Suppl.* **196** (2009) 102–105.

[184] F. Riehn, R. Engel, A. Fedynitch, T. K. Gaisser, and T. Stanev, "A new version of the event generator Sibyll," *PoS* **ICRC2015** (2016) 558, arXiv:1510.00568 [hep-ph].

[185] Pierog, Tanguy, "LHC data and extensive air showers," *EPJ Web of Conferences* **52** (2013) 03001. https://doi.org/10.1051/epjconf/20125203001.

[186] Engel, Ralph, Riehn, Felix, Fedynitch, Anatoli, Gaisser, Thomas K., and Stanev, Todor, "The hadronic interaction model Sibyll past, present and future," *EPJ Web Conf.* **145** (2017) 08001. https://doi.org/10.1051/epjconf/201614508001.

[187] **Pierre Auger** Collaboration, R. Engel, "Test of hadronic interaction models with data from the Pierre Auger Observatory," in *Proceedings, 30th International Cosmic Ray Conference (ICRC 2007): Merida, Yucatan, Mexico, July 3-11, 2007*, vol. 4, pp. 385–388. 2007. arXiv:0706.1921 [astro-ph]. http://lss.fnal.gov/cgi-bin/find_paper.pl?conf-07-373. [4,385(2007)].

[188] **Yakutsk, Pierre Auger** Collaboration, J. Allen *et al.*, "Air Shower Simulation and Hadronic Interactions," *EPJ Web Conf.* **53** (2013) 01007, arXiv:1306.6090 [astro-ph.HE].

[189] S. Agostinelli *et al.*, "GEANT4: a simulation toolkit," *Nuclear Instruments and Methods in Physics Research Section A: Accelerators, Spectrometers, Detectors and Associated Equipment* **506** (2003) 250–303.

[190] F. Kislat, T. Melzig, A. Van Overloop, and T. WaldenMaier, "IceTop tank simulation using g4-tankresponse." Internal Report, 2012.

[191] T. Melzig, "Verbesserung der IceTop-Detektorsimulation unter Verwendung von Geant4," Master's thesis, in German, Humboldt-Universität zu Berlin, 2011.

[192] **IceCube** Collaboration, A. Van Overloop, "Simulation of IceTop VEM calibration and the dependency on the snow layer," in *Proceedings, (ICRC 2011): Beijing, China, August 11-18, 2011*, vol. 1, pp. 97–101. http://inspirehep.net/record/1346031/files/v1_0899.pdf.

[193] S. Flis, "Fast Energy Reconstruction and Detector Simulation in IceCube," Master's thesis, Stockholm University, 2011.

[194] P. Billoir, "A sampling procedure to regenerate particles in a ground detector from a 'thinned' air shower simulation output," *Astropart. Phys.* **30** (2008) 270–285.

[195] H. Dembinski, "Unthinning Algorithm," 2016. Internal Document.

[196] J. Van Houtte, "Air shower measurements with IceTop: the effect of (un)thinning simulation techniques," Master's thesis, Ghent University, 2016.

[197] D. Chirkin and W. Rhode, "Muon Monte Carlo: A High-precision tool for muon propagation through matter," arXiv:hep-ph/0407075 [hep-ph].

[198] J.-H. Koehne, K. Frantzen, M. Schmitz, T. Fuchs, W. Rhode, D. Chirkin, and J. B. Tjus, "PROPOSAL: A tool for propagation of charged leptons," *Computer Physics Communications* **184** no. 9, (2013) 2070 – 2090. http://www.sciencedirect.com/science/article/pii/S0010465513001355.

[199] J. Lundberg, P. Miocinovic, T. Burgess, J. Adams, S. Hundertmark, P. Desiati, K. Woschnagg, and P. Niessen, "Light tracking for glaciers and oceans: Scattering and absorption in heterogeneous media with Photonics," *Nucl. Instrum. Meth.* **A581** (2007) 619–631, arXiv:astro-ph/0702108 [ASTRO-PH].

[200] C. Kopper, "CLSim." https://github.com/claudiok/clsim.

[201] D. Chirkin and IceCube Collaboration, "Photon tracking with GPUs in IceCube," *Nuclear Instruments and Methods in Physics Research A* **725** (Oct., 2013) 141–143.

[202] N. Whitehorn, J. van Santen, and S. Lafebre, "Penalized Splines for Smooth Representation of High-dimensional Monte Carlo Datasets,".

[203] M. J. Larson, "Simulation and Identification of Non-Poissonian Noise Triggers in the IceCube Neutrino Detector," Master's thesis, University of Alabama, 2013.

[204] T. DeYoung, "IceTray: A software framework for IceCube," in *Computing in high energy physics and nuclear physics. Proceedings, Conference, CHEP'04, Interlaken, Switzerland, September 27-October 1, 2004*, pp. 463–466. 2005. http://doc.cern.ch/yellowrep/2005/2005-002/p463.pdf.

[205] M. G. Aartsen *et al.*, "The IceProd Framework: Distributed Data Processing for the IceCube Neutrino Observatory," *J. Parallel Distrib. Comput.* **75** (2015) 198–211, arXiv:1311.5904 [cs.DC].

[206] D. Schultz, "IceProd 2: A Next Generation Data Analysis Framework for the IceCube Neutrino Observatory," *Journal of Physics: Conference Series* **664** no. 6, (2015) 062056. http://stacks.iop.org/1742-6596/664/i=6/a=062056.

[207] T. K. Gaisser, "Spectrum of cosmic-ray nucleons, kaon production, and the atmospheric muon charge ratio," *Astropart. Phys.* **35** (2012) 801–806, arXiv:1111.6675 [astro-ph.HE].

[208] A. A. K. Haj Ismail, *Measurement of the cosmic ray energy spectrum between 500 TeV and 100 PeV with IceTop*. PhD thesis, Ghent University, 2015.

[209] L. Demirörs *et al.*, "IceTop tank response to muons," *International Cosmic Ray Conference* **5** (2008) 1261–1264.

[210] S. De Ridder, "IceTop Level3 file structure," 2017. https://wiki.icecube.wisc.edu/index.php/IceTop_Level3_file_structure. IceCube Internal Document.

[211] J. Gonzalez, "IceTop SLC Charge Calibration," 2014. https://wiki.icecube.wisc.edu/index.php/IceTop_SLC_Charge_Calibration. IceCube Internal Document.

[212] H. Pandya, "IceTop SLC Times," 2016. https://wiki.icecube.wisc.edu/index.php/IceTop_SLC_Times. IceCube Internal Document.

[213] S. Tilav, "Vemcal monitor." `http://icecube.wisc.edu/~vemcal/monitor`. IceCube Internal Document.

[214] S. Tilav. Private Communication.

[215] H. Dembinski, "Simulation of uncorrelated background," 2016. `https://wiki.icecube.wisc.edu/index.php/Muon_LDF#Simulation_of_uncorrelated_background`. IceCube Internal Document.

[216] H. Dembinski, "Simulation of VEM drift between calibration runs," 2016. `https://wiki.icecube.wisc.edu/index.php/Muon_LDF#Simulation_of_VEM_drift_between_calibration_runs`. IceCube Internal Document.

[217] H. Pandya, "IceTop Background simulation check," 2016. `https://wiki.icecube.wisc.edu/index.php/CR_phone_call_2016-12-12`. IceCube Internal Document.

[218] S. Klepser, F. Kislat, H. Kolanoski, P. Niessen, and A. Van Overloop, "Lateral Distribution of Air Shower Signals and Initial Energy Spectrum above 1 PeV from IceTop," *International Cosmic Ray Conference* **4** (2008) 35–38.

[219] K. G. Andeen, *First Measurements of Cosmic Ray Composition from 1-50 PeV using New Techniques on Coincident Data from the IceCube Neutrino Observatory*. PhD thesis, The University of Wisconsin - Madison, 2011.

[220] **IceCube** Collaboration, J. Gonzalez, "Studying Cosmic Ray Composition with IceTop using Muon and Electromagnetic Lateral Distributions," *PoS* **ICRC2015** (2016) 338.

[221] S. Klepser, *Reconstruction of extensive air showers and measurement of the cosmic ray energy spectrum in the range of 1 - 80 PeV at the South Pole*. PhD thesis, Humboldt-Universitat zu Berlin, 2008.

[222] E. Dvorak, 2017. Private Communication.

[223] F. Kislat, "Study of charge and time fluctuations of singals in the IceTop detector," Master's thesis, Humboldt-Universitat zu Berlin, 2007.

[224] S. Klepser, F. Kislat, and A. Van Overloop, "A Lateral Distribution Function and Fluctuation Parametrisation for IceTop." IceCube Internal Report, 2007.

[225] F. Kislat, *Measurement of the energy spectrum of cosmic rays with the 26 station configuration of the IceTop detector*. PhD thesis, Humboldt-Universitat zu Berlin, Mathematisch-Naturwissenschaftliche Fakultat I, 2012.

[226] J. Gonzalez, "IceTopTankSelect." `https://wiki.icecube.wisc.edu/index.php/IceTopTankSelect`. IceCube Internal Document.

[227] **IceCube** Collaboration, J. G. Gonzalez, "Measuring the Muon Content of Air Showers with IceTop," *EPJ Web Conf.* **99** (2015) 06002, `arXiv:1501.03415 [astro-ph.HE]`.

[228] P. Hallen, "On the Measurement of High-Energy Tau Neutrinos with IceCube," Master's thesis, RWTH Aachen University, 2013.

[229] K. Jero, *A Search for Starting Tracks in IceCube: A New Window for Detecting Astrophysical Neutrinos*. PhD thesis, University of Wisconsin, Madison, 2017.

[230] L. Rädel, *Measurement of High-Energy Muon Neutrinos with the IceCube Neutrino Observatory*. PhD thesis, RWTH Aachen University, 2017.

[231] **AMANDA** Collaboration, J. Ahrens *et al.*, "Muon track reconstruction and data selection techniques in AMANDA," *Nucl. Instrum. Meth.* **A524** (2004) 169–194, arXiv:astro-ph/0407044 [astro-ph].

[232] **IceCube** Collaboration, M. Aartsen *et al.*, "Improvement in fast particle track reconstruction with robust statistics," *Nuclear Instruments and Methods in Physics Research Section A: Accelerators, Spectrometers, Detectors and Associated Equipment* **736** (2014) 143 – 149. http://www.sciencedirect.com/science/article/pii/S0168900213014654.

[233] D. Pandel, "Bestimmung von Wasser- und Detektorparametern und Rekonstruktion von Myonen bis 100 TeV mit dem Baikal Neutrinoteleskop NT-72," Master's thesis, Humboldt-Universität zu Berlin, 1996.

[234] N. van Eijndhoven, O. Fadiran, and G. Japaridze, "Implementation of a Gauss convoluted Pandel PDF for track reconstruction in Neutrino Telescopes," *Astropart. Phys.* **28** (2007) 456–462, arXiv:0704.1706 [astro-ph].

[235] D. Chirkin, "Photon propagation approximations and energy reconstruction," 2007. IceCube Internal Document.

[236] S. Miarecki and S. Klein, "I3TruncatedEnergy: using truncated mean methods to calculate the muon energy." IceCube Internal Report, 2011.

[237] T. Kuwabara, "IceTop Tank Snow Height." http://www.bartol.udel.edu/~takao/icetop/snow/index.html.

[238] G. De Wasseige, "Automated snow measurements," 2017. https://drive.google.com/drive/folders/0B61gfdEPk5BJNlhJcWR4RF82YTQ. IceCube Internal Document.

[239] **IceCube** Collaboration, T. Waldenmaier and T. Feusels, "Snow Density Measurements at the IceTop Site," *IceCube Internal Report* **201111003** (2011) 1–5.

[240] K. Erpels, "Influence of snow on cosmic rays observed by IceTop," Master's thesis, Universiteit Gent, 2015.

[241] B. Ruzybayev, *Measurement of cosmic ray energy spectrum with IceTop*. PhD thesis, University of Delaware, 2012.

[242] **IceCube** Collaboration, K. Rawlins, "The Effect of Snow Accumulation on Signals in IceTop," in *Proceedings, 33rd International Cosmic Ray Conference (ICRC2013): Rio de Janeiro, Brazil, July 2-9, 2013*, p. 1106. 2013. http://www.cbpf.br/%7Eicrc2013/papers/icrc2013-1106.pdf.

[243] J. Somville, "Towards an improved snow correction for cosmic rays observed by IceTop," Master's thesis, Universiteit Gent, 2015.

[244] **IceCube** Collaboration, S. Tilav, P. Desiati, T. Kuwabara, D. Rocco, F. Rothmaier, M. Simmons, and H. Wissing, "Atmospheric Variations as observed by IceCube," arXiv:1001.0776.

[245] T. R. Parish and D. H. Bromwich, "On the forcing of seasonal changes in surface pressure over Antarctica," *J. Geophys. Res.* **102** no. D12, (1997) 13785–13792.

[246] S. D. Ridder, "Influence of South Pole atmosphere on cosmic rays observed by IceCube," Master's thesis, Universiteit Gent, 2012.

[247] **IceCube** Collaboration, S. D. Ridder, T. Feusels, *et al.*, "Seasonal variation of the muon multiplicity in cosmic rays at South Pole," in *Proc. 33rd ICRC*, Rio De Janeiro, Brazil. 2013.

[248] D. Soldin, "IC79 in-ice systematics," 2014. `http://at-web.physik.uni-wuppertal.de/~soldin/systematics.html`.

[249] **KASCADE-Grande** Collaboration, W. D. Apel *et al.*, "Probing the evolution of the EAS muon content in the atmosphere with KASCADE-Grande," *Astropart. Phys.* **95** (2017) 25–43, `arXiv:1801.05513 [astro-ph.HE]`.

[250] **IceCube** Collaboration, D. Soldin, "Atmospheric Muons Measured with IceCube," in *20th International Symposium on Very High Energy Cosmic Ray Interactions (ISVHECRI 2018) Nagoya, Japan, May 21-25, 2018*. 2018. `arXiv:1811.03651 [astro-ph.HE]`.

[251] **Pierre Auger** Collaboration, A. Aab *et al.*, "Muons in air showers at the Pierre Auger Observatory: Mean number in highly inclined events," *Phys. Rev.* **D91** no. 3, (2015) 032003, `arXiv:1408.1421 [astro-ph.HE]`. [Erratum: Phys. Rev.D91,no.5,059901(2015)].

[252] **Telescope Array** Collaboration, R. U. Abbasi *et al.*, "Study of muons from ultrahigh energy cosmic ray air showers measured with the Telescope Array experiment," *Phys. Rev.* **D98** no. 2, (2018) 022002, `arXiv:1804.03877 [astro-ph.HE]`.

[253] H. Dembinski *et al.*, "Report on Tests and Measurements of Hadronic Interaction Properties with Air Showers." To appear.

[254] S. Verpoest, 2019. Private Communication.

[255] **IceCube-Gen2** Collaboration, J. Auffenberg, "IceAct: Imaging Air Cherenkov Telescopes with SiPMs at the South Pole for IceCube-Gen2," *PoS* **ICRC2017** (2017) 1055.